

# Dynamics of the cavitation precessing vortex rope for Francis turbines at part load operating conditions

THÈSE N° 6880 (2016)

PRÉSENTÉE LE 12 FÉVRIER 2016

À LA FACULTÉ DES SCIENCES ET TECHNIQUES DE L'INGÉNIEUR  
LABORATOIRE DE MACHINES HYDRAULIQUES  
PROGRAMME DOCTORAL EN MÉCANIQUE

ÉCOLE POLYTECHNIQUE FÉDÉRALE DE LAUSANNE

POUR L'OBTENTION DU GRADE DE DOCTEUR ÈS SCIENCES

PAR

Arthur Tristan FAVREL

acceptée sur proposition du jury:

Prof. D. Pioletti, président du jury  
Prof. F. Avellan, directeur de thèse  
Dr J. Koutnik, rapporteur  
Prof. Y. Tsujimoto, rapporteur  
Prof. F. Gallaire, rapporteur



ÉCOLE POLYTECHNIQUE  
FÉDÉRALE DE LAUSANNE

Suisse  
2016



I have not failed. I have just found 10,000 ways that won't work  
— Thomas A. Edison



# Acknowledgements

I would first like to thank the members of the jury, Prof. Dominique Pioletti, Prof. François Avellan, Prof. François Gallaire, Dr Jiri Koutnik and Prof. Yoshinobu Tsujimoto for their valuable time, their relevant questions and their inspiring comments during the private defense. This thesis was realized thanks to the financial support of the European Commission (HYPERBOLE research project, ERC/FP7-ENERGY-2013-1-Grant 608532). I would like also to acknowledge all the partners of the HYPERBOLE research project for the discussions during the different meetings and their support during the experimental campaigns.

Pour la suite des remerciements, je me permets de continuer en français. J'aimerais tout d'abord remercier sincèrement mon directeur de thèse, Prof. François Avellan, pour m'avoir donné l'opportunité de réaliser cette thèse au sein de son laboratoire et d'intégrer l'EPFL. Je souhaite le remercier pour son encadrement tout au long de ma recherche, ainsi que pour m'avoir donné la chance de participer à un projet européen de grande envergure qui m'a permis de rencontrer différents partenaires industriels et académiques. Enfin, je le remercie pour m'avoir offert l'opportunité de présenter mes travaux de recherche lors de nombreux congrès internationaux.

Je souhaiterais exprimer ma gratitude à tout le personnel du laboratoire sans qui cette thèse n'aura pas pu voir le jour. Je souhaite tout d'abord remercier Isabelle Stoudmann-Schmutz pour son travail administratif et son support avec les notes de frais relatives aux différentes conférences auxquelles j'ai pu participer. Je remercie très sincèrement toute l'équipe de l'atelier mécanique, dirigée successivement par Louis Besançon et Maxime Raton: Victor Rivas, David Buzzi, Raymond Fazan, Christian Sierro, Louis Vina et le nouveau venu, Pierre-André Peloux. Sans leur super travail et leur soutien technique avant et pendant les différentes campagnes expérimentales, la réalisation de cette thèse n'aura pas pu être possible. Au-delà de leur professionnalisme, je souhaiterais les remercier pour leur bonne humeur ainsi que pour les parties de beach-volley et barbecue que l'on a pu faire ensemble. Je souhaite enfin bonne chance à Maxime Raton et Victor Rivas pour leurs futurs projets professionnels qui se réaliseront malheureusement en-dehors du laboratoire, mais je ne doute pas que l'on se retrouvera pour quelques verres.

Ensuite, je souhaiterais remercier sincèrement les membres du bureau d'étude du laboratoire, dirigé par Dr Philippe Cerrutti. Merci beaucoup à ce dernier pour son support informatique

## Acknowledgements

---

tout au long de ma thèse. Je remercie aussi Alain Renaud, Philippe Faucherre et Vincent Berruex pour leur soutien technique, ainsi que pour l'élaboration des dessins techniques nécessaires à la description des différentes mesures expérimentales.

Un grand merci également à l'équipe d'ingénieurs d'essai dirigée par Henri-Pascal Mombelli, qui est composée d'Ambrosio Acal, d'Alberto Bullani, de Lillie Croft et de Monica Suarez. Un merci particulier à Georges Crittin pour son aide si précieuse lors des campagnes expérimentales et à Ambrosio et Alberto pour leur aide lors de la réalisation des mesures.

Je souhaiterais également remercier tous les anciens doctorants du laboratoire que j'ai pu côtoyer au cours de ma thèse et qui ont contribué à l'ambiance remarquable qui règne au laboratoire. Merci notamment aux docteurs Christophe Nicolet et Sébastien Alligné pour les très nombreuses discussions relatives à ma thèse, ainsi que les différents apéros mémorables qu'on a pu faire ensemble. Merci à Vlad Hasmatuchi pour son enthousiasme lors des discussions professionnelles pendant la pause-café. Merci à Cécile Münch pour sa bonne humeur constante. Merci également à Olivier Pacot, que je n'ai pas eu la chance de côtoyer très longtemps au laboratoire avant son départ pour le Japon. Ce fut toujours un grand plaisir de te revoir, que ce soit en Suisse ou de l'autre côté de l'Atlantique, à Montréal. Ta désinvolture la veille de ta soutenance privée restera un modèle du genre. Merci à Steven Roth, notamment pour la visite du laboratoire lors de mon arrivée, ainsi que pour cette mémorable séance de strangulation lors de sa défense publique de thèse qui restera finalement comme un grand souvenir. Je remercie également le (très) calme docteur Marc Tinguely, notamment pour sa ténacité lors de la noce suivant ma défense privée alors qu'il devait être chairman le lendemain pour la conférence CAV2015. Enfin, je remercie Martino Reclari pour l'ambiance musicale qu'il a su instaurer dans le bureau d'à côté. Les enceintes sont malheureusement un peu moins utilisées depuis ton départ.

Je souhaiterais maintenant passer à mes très chers collègues doctorants avec qui j'ai passé le plus de temps lors de ces quatre dernières années. Ce fut un plaisir de vous voir rester (ou même revenir après une petite pause) après la fin de vos doctorats respectifs. Je souhaiterais tout d'abord remercier Christian Vessaz, pour sa science culinaire, son enthousiasme pour l'organisation des repas du midi et pour nous avoir fait découvrir les spécialités vaudoises, malgré quelques dysfonctionnements concernant l'appellation de certains produits. Un grand merci à Christian Landry également. Bien que nos sujets fussent très similaires au début de nos thèses respectives, nous avons su trouver nos voies respectives, tout en s'aidant remarquablement pour l'organisation des campagnes expérimentales, particulièrement celle de 2013. Enfin, notre voyage en Chine après la conférence à Pékin me restera en mémoire. Il faudrait cependant penser à faire un peu plus honneur à ton côté valaisan... Un grand merci à Andres Müller, que ce soit pour ton soutien dans la sphère professionnelle ou personnelle, même si je n'ai pas toujours suivi tes conseils avisés pour cette dernière. Ton aide fut précieuse, que ce soit pour la réalisation de cette thèse, l'organisation de nos différents voyages via le tour opérateur HMTS ou encore lors de nos innombrables apéros. Je souhaite aussi remercier

notre musicien et scientifique de grand talent, Matthieu Dreyer. J'ai enfin rencontré quelqu'un d'aussi maladroit que moi. Notre entente lors de certaines soirées nous a joué parfois de mauvais tours mais l'escapade en taxi à Montréal me restera en mémoire. Enfin, merci à vous quatre pour avoir préservé l'esprit du laboratoire ces derniers mois, et pour nos différentes escapades lors de la conférence à Montréal, que ce soit à Québec ou New-York.

Merci à Loïc Andolfatto pour sa très bonne connaissance des répliques de Dikkenek et son humour toujours très fin. Ton engagement physique, viril mais correct, lors des matches de football reste un exemple à montrer dans les écoles de football. J'en profite pour remercier également tous les membres de l'équipe de foot du laboratoire. Je suis persuadé que le titre nous reviendra un jour ou l'autre. Merci également à Audrey et je te souhaite bon courage pour la suite de ton travail au sein de l'équipe SPHEROS. Un grand merci aussi à Keita Yamamoto pour avoir organisé la campagne expérimentale 2015. Je te souhaite bonne chance pour la rédaction de ta thèse. Merci aussi à Ebrahim pour avoir supporté le bruit dans le bureau et les discussions plus que limites qui pouvaient s'y dérouler durant toutes ces années. Merci à Elena, l'italienne buveuse de Spritz du labo, et bonne chance pour ta thèse. Enfin, je souhaite également bonne chance à tous les doctorants restant au labo pour vos thèses respectives: Simon, Joao, Outi, Sebastian et Siamak.

Je souhaite enfin remercier toutes les personnes que j'ai pu rencontrer sur Lausanne, notamment James, Pierre-Alain, Axel et Lucas. Merci pour ces Jeudredi mémorables et ces voyages courts mais intenses, que ce soit à Budapest ou à Vienne. Enfin, merci à mes amis français de Lyon et Bourg-en-Bresse, et à ceux de Haute-Savoie, pour votre présence et votre amitié continues depuis maintenant de nombreuses années. Je remercie aussi Kate pour son soutien lors de l'écriture de ma thèse et ces deux dernières années. Je remercie enfin ma famille, et plus particulièrement mon frère Emilien et ma belle-sœur Sara, ainsi que mes parents Sylvie et Philippe, sans qui rien n'aurait été possible. Merci pour votre soutien inconditionnel et pour avoir toujours accepté mes choix.

*Lausanne, 21 Décembre 2015*

Arthur Favrel





# Abstract

The latest European energy policies promote a massive penetration of the existing electrical grid by renewable energy sources. Their importance for the electrical energy supply has rapidly grown in the past decades and is expected to increase further in the future. However, the intermittent nature of these energy sources directly impacts the balance between electrical energy consumption and production, threatening the stability of the power system. Typical examples are wind and solar energy, which strongly depend on the weather conditions. It is crucial to guarantee a smooth integration of the renewable energy sources by ensuring a sufficient storage capacity as well as primary and secondary grid control capability to enable the energy balancing process. Hydroelectric powerplants play a decisive role in this development. They are characterized by their flexible operation capability and they represent a renewable energy source with little emissions of greenhouse gas. This however requires a continuous extension of their operating range, which can lead to cavitation flow instabilities inducing undesirable mechanical vibrations and large fluctuations of pressure and output power, putting at risk the structural integrity of the machine and ultimately the grid stability.

A typical example is the development of a cavitation precessing vortex rope at the outlet of a Francis turbine runner operating at part load conditions. It acts as an excitation source for the hydraulic system, leading to the propagation of pressure fluctuations in the hydraulic circuit which are greatly amplified in case of resonance. Therefore, the assessment of the stability of hydropower plants operating at part load is crucial in order to ensure the safe extension of their operating range. The accurate prediction and transposition of pressure fluctuations from the model scale to the prototype scale by means of one-dimensional hydro-acoustic models represents a major challenge, as the physical mechanisms driving the excitation source and its interaction with the hydraulic system remain partially unclear.

The main objective of this research work is to experimentally investigate the influence of the operating conditions on the dynamics of the cavitation precessing vortex rope and the excitation source it induces, as well as the interaction with the system. The test-case is a reduced scale physical model of a Francis turbine, accurately reproducing the behaviour of a real size machine. Experimental investigations include study of the flow field in the draft tube cone by means of Particle Image Velocimetry (PIV) and Laser Doppler Velocimetry (LDV), high-speed visualizations of the cavitation vortex and pressure measurements performed at various part load operating conditions, including cavitation-free and cavitation conditions.

## Acknowledgements

---

PIV measurements of the tangential flow field in the draft tube cone in cavitation-free conditions highlight the influence of the flow discharge on the vortex characteristics in terms of trajectory, circulation and structure, as well as the link between the vortex dynamics and the intensity of the excitation source. The effect of cavitation on the vortex rope dynamics and its interaction with the surrounding system is also studied, with a particular focus on resonance conditions. Flow velocity measurements performed for different values of the Thoma number reveal that the axial and tangential velocity fields in the draft tube cone are not impacted by the propagation of large synchronous pressure fluctuations. Among the other observations is a phenomenon of frequency lock-in between the excitation source and the system's oscillations occurring for low values of the Froude number. This phenomenon is assumed to be a consequence of the non-linear coupling taking place in resonance conditions between the excitation source and the oscillation of the cavitation volume. Finally, it is shown that the convective component of the pressure fluctuations at the precession frequency represents the main source of mechanical excitation for the runner.

**Key words:** Francis turbine, part load, precessing vortex cope, cavitation, pressure fluctuations, LDV/PIV measurements, excitation source, resonance, frequency lock-in, mechanical excitation

## Résumé

Les politiques énergétiques européenne actuelles conduisent à une pénétration massive des sources d'énergie renouvelable dans le réseau électrique existant. Leur importance dans l'approvisionnement en énergie électrique s'est largement accrue lors de la décennie passée et il est attendu qu'elle continue de croître dans le futur. Cependant, la nature intermittente de ce type de source d'énergie a un impact direct sur l'équilibre entre la production et la consommation d'énergie électrique. Des exemples typiques sont les sources d'énergie solaire et éolienne dont la production dépend fortement de conditions météorologiques difficilement prévisibles. Par conséquent, il est important de garantir l'intégration des sources d'énergie renouvelable en assurant au réseau existant d'avoir suffisamment de capacité de stockage ainsi que des capacités de contrôle primaire et secondaire afin d'assurer l'équilibre énergétique. Les centrales hydro-électriques sont caractérisées par leur flexibilité et ont l'avantage d'utiliser une énergie propre en émettant que très peu de gaz à effet de serre. Elles jouent ainsi un rôle crucial dans l'intégration des énergies renouvelables en réalisant l'équilibre énergétique ainsi que le contrôle primaire et secondaire du réseau. Cependant, cela mène à une extension constante de leur domaine de fonctionnement, ce qui conduit au développement d'écoulements instables et cavitant causant des vibrations mécaniques indésirables et des fluctuations de pressions et de puissance capable de menacer la stabilité du système et l'intégrité structurelle de la machine.

Un exemple typique est le développement d'un vortex de cavitation animé d'un mouvement de précession, appelé communément torche de cavitation, à la sortie de la roue des turbines Francis opérant à charge partielle. Celui-ci représente une source d'excitation pour le circuit hydraulique, conduisant à la propagation de fluctuations de pression qui sont fortement amplifiées en cas de résonance avec le système. Ainsi, l'évaluation de la stabilité des centrales hydrauliques opérant à charge partielle est cruciale afin d'assurer une extension sans danger de leur domaine de fonctionnement. La prédiction précise et la transposition des fluctuations de pression de l'échelle modèle à l'échelle prototype via des modèles hydroacoustiques restent pour le moment difficiles étant donné la complexité des phénomènes hydrodynamiques mis en jeu.

Ce travail de thèse a pour objectif principal l'évaluation expérimentale de l'influence des conditions de fonctionnement de la machine sur la dynamique du vortex de précession et sur la source d'excitation induite, ainsi que sur l'interaction entre cette dernière et le

## Acknowledgements

---

système hydraulique. Le cas d'étude est un modèle réduit d'une turbine Francis reproduisant parfaitement le comportement de la machine réelle. L'investigation expérimentale inclut des mesures de champs de vitesse dans le cône du diffuseur par PIV et LDV, des visualisations rapides de la torche de cavitation et des mesures de fluctuations de pressions réalisées pour un grand nombre de conditions d'opération différentes. Les mesures PIV des champs de vitesse tangentielle dans le cône réalisées hors-cavitation mettent en lumière l'influence du débit sur les caractéristiques du vortex en termes de trajectoire, circulation et structure, ainsi que le lien existant entre l'intensité de la source d'excitation et la dynamique du vortex. L'effet de la cavitation sur la dynamique du vortex et son interaction avec le système est également étudié, avec une attention particulière sur les conditions de résonance. Des mesures de vitesses d'écoulement réalisées dans le cône par LDV pour différentes valeurs de nombre de cavitation ont révélé que les champs de vitesse axiale et tangentielle ne sont pas affectés par la propagation d'ondes de pression synchrones dans le diffuseur. Parmi les autres observations, un phénomène de "lock-in" de fréquence a été mis en évidence pour de faibles valeurs du nombre de Froude. Ce phénomène est supposé être une conséquence du couplage se mettant en place entre la source d'excitation et les oscillations du volume de cavitation en conditions de résonance. Enfin, il est démontré que la composante convective des fluctuations de pression induites par le vortex représente la principale source d'excitation mécanique pour la roue, alors que cette composante ne représente pas une source d'excitation hydroacoustique pour le système.

**Mots clefs** : turbine Francis, charge partielle, vortex de précession, cavitation, fluctuations de pression, mesures LDV/PIV, source d'excitation, résonance, lock-in, excitation mécanique.

# Contents

<b>Acknowledgements</b>	<b>v</b>
<b>Abstract (English/Français)</b>	<b>ix</b>
<b>List of figures</b>	<b>xvii</b>
<b>List of tables</b>	<b>xxv</b>
<b>Nomenclature</b>	<b>xxvii</b>
<b>1 Introduction</b>	<b>1</b>
1.1 Energy context . . . . .	1
1.2 Francis turbines . . . . .	2
1.3 Off-design conditions . . . . .	4
1.4 State of the art . . . . .	7
1.5 Thesis Objective . . . . .	9
1.6 Document Structure . . . . .	10
<b>2 Test-case and Experimental set-up</b>	<b>11</b>
2.1 Reduced scale physical model . . . . .	11
2.2 Pressure measurement on the test rig . . . . .	12
2.3 Draft tube flow field investigation . . . . .	13
2.3.1 Laser Doppler Velocimetry . . . . .	13
2.3.2 Particle Image Velocimetry . . . . .	16
2.4 Flow visualization . . . . .	20
<b>3 Precessing vortex core in cavitation-free conditions</b>	<b>23</b>
3.1 Introduction . . . . .	23
3.2 Definition of the excitation source . . . . .	24
3.3 Identification of flow regimes by pressure measurements . . . . .	24
3.3.1 Pressure fluctuations in the headwater connecting pipe . . . . .	25
3.3.2 Pressure fluctuations in the draft tube cone . . . . .	27
3.3.3 Cavitation influence on the flow regimes . . . . .	29
3.4 Methodology for PIV measurements . . . . .	30
3.4.1 Flow parameters . . . . .	30

## Contents

---

3.4.2	Mean phase averaging . . . . .	32
3.4.3	Vortex parameters . . . . .	38
3.5	Draft tube flow . . . . .	43
3.5.1	Vortex structure . . . . .	43
3.5.2	Vortex trajectory . . . . .	46
3.5.3	Axial flow recirculation zone . . . . .	53
3.5.4	Swirl number . . . . .	54
3.6	Summary and Discussion . . . . .	56
<b>4</b>	<b>Effect of cavitation on the precessing vortex core and system interaction</b>	<b>59</b>
4.1	Introduction . . . . .	59
4.2	Methodology . . . . .	60
4.2.1	Investigated operating conditions . . . . .	60
4.2.2	Frequency domain analysis in cavitation conditions . . . . .	61
4.2.3	Time domain analysis in cavitation conditions . . . . .	64
4.2.4	Radial positions for LDV measurements . . . . .	67
4.3	Cavitation influence on pressure fluctuations . . . . .	71
4.3.1	Resonance identification . . . . .	71
4.3.2	Pressure fluctuations decomposition in the cone . . . . .	72
4.4	Flow fields in cavitation-free conditions . . . . .	75
4.4.1	Mean phase averaged velocity profiles . . . . .	75
4.4.2	Vortex centre passage . . . . .	77
4.4.3	Amplitude and phase shift of velocity fluctuations . . . . .	79
4.5	Flow fields in cavitation conditions . . . . .	83
4.5.1	Mean phase averaged velocity field . . . . .	83
4.5.2	Time delay and RMS value . . . . .	85
4.6	Summary and discussion . . . . .	89
<b>5</b>	<b>Influence of the Froude number on the resonance conditions</b>	<b>91</b>
5.1	Non-linear effects in resonance conditions . . . . .	91
5.1.1	Pressure pulsations in resonance conditions . . . . .	91
5.1.2	Cavitation volume pulsations in resonance conditions . . . . .	92
5.2	Effect of the Froude number on the test rig hydro-acoustic response . . . . .	95
5.2.1	Definition of the Froude number . . . . .	95
5.2.2	Resonance identification for different values of Froude number . . . . .	96
5.2.3	Lock-in effect at low Froude number . . . . .	97
5.2.4	Effect on the pressure fluctuations components . . . . .	99
5.3	Effect of the Froude number on the cavitation volume . . . . .	101
5.4	Summary and Discussion . . . . .	102

<b>6 Impact on the runner mechanical behavior</b>	<b>105</b>
6.1 Motivation . . . . .	105
6.2 Instrumented runner . . . . .	106
6.3 Pressure and strain fluctuations on the runner blades . . . . .	107
6.3.1 Pressure fluctuations in the rotating frame . . . . .	107
6.3.2 Strain fluctuations on the runner blades . . . . .	110
6.4 Impact of resonance conditions on the mechanical behavior . . . . .	111
6.4.1 Pressure and strain fluctuations . . . . .	111
6.4.2 Torque fluctuations . . . . .	112
6.5 Summary . . . . .	113
<b>7 Conclusions and Perspectives</b>	<b>115</b>
7.1 Conclusions . . . . .	115
7.2 Perspectives . . . . .	117
<b>A Hill chart of the reduced scale model</b>	<b>119</b>
<b>B List of operating points investigated by PIV and LDV</b>	<b>121</b>
<b>C Mean phase averaged velocity profiles</b>	<b>123</b>
C.1 Cavitation-free conditions . . . . .	123
C.2 Non-resonance conditions . . . . .	124
<b>D Decomposition of the pressure fluctuations</b>	<b>127</b>
D.0.1 Description of the problem . . . . .	127
D.0.2 Mathematical demonstration . . . . .	128
<b>Bibliography</b>	<b>137</b>
<b>Curriculum Vitae</b>	<b>139</b>





# List of Figures

1.1	Worldwide electricity generation in 2012 [68]. . . . .	1
1.2	Components of a Francis turbine. . . . .	3
1.3	Layout of a Francis turbine hydropower plant. . . . .	4
1.4	Definition of the velocity triangles at the outlet of a Francis turbine [59]. . . . .	5
1.5	Velocity triangles at the runner outlet at off-design conditions (part load and full load conditions) and at the Best Efficiency Point. . . . .	5
1.6	Visualization of the cavitation vortex rope in the draft tube cone during reduced scale model tests at part load and full load conditions. . . . .	6
2.1	Reduced scale physical model of a Francis turbine installed on EPFL test rig PF3 [59]. . . . .	11
2.2	Cut-view of the upper section of the draft tube cone with the location of the wall pressure sensors and the diffuser. . . . .	12
2.3	Vertical cut-view of the reduced scale model, with the streamwise position of the LDV measurement sections. . . . .	14
2.4	Experimental setup for the LDV measurements with the data acquisition flow chart. The LDV probe is set up in two different configurations, parallel and perpendicular to the feeding pipe of the machine. . . . .	15
2.5	Experimental setup for the PIV measurements in horizontal cross-sections of the draft tube cone together with a cut-view of the optical access. . . . .	16
2.6	Side-view of the draft tube cone with the streamwise positions of the PIV measurement sections. . . . .	17
2.7	Upstream view of the reduced scale physical model, together with both PIV setup and PIV data acquisition flow chart. . . . .	19
2.8	Wall pressure coefficient $C_p$ measured in the draft tube cone (black solid line), together with the Q-switch voltage signal from the PIV Laser (red solid line). . . . .	19
2.9	Setup for the high-speed visualizations of the cavitation vortex rope, together with the data flow between the high-speed camera and the PXI device. . . . .	20
2.10	Snapshots of the cavitation vortex rope at different instants of the same precession cycle, together with the corresponding time history of two wall pressure coefficients measured in the same cross-section of the draft tube cone (positions C1N and C1S) - $Q_{ED} = 0.128$ , $\sigma = 0.17$ (resonance conditions). . . . .	21

## List of Figures

---

3.1	Auto-spectral density function of a pressure signal measured in the feeding pipe of the machine (position P1) for $Q_{ED}/Q_{ED}^* = 0.9$ (left) and $Q_{ED}/Q_{ED}^* = 0.83$ (right).	25
3.2	(a) Precession frequency made dimensionless by the runner frequency and (b) auto-spectral amplitude at the precession frequency as a function of the discharge factor. The pressure signal is measured in the feeding pipe (location P1).	26
3.3	Auto-spectral density function of a pressure signal measured in the upstream pipe (position P1) for $Q_{ED}/Q_{ED}^* = 0.65$ (left) and $Q_{ED}/Q_{ED}^* = 0.58$ (right).	27
3.4	Coherence at the precession frequency between two pressure signals measured in the same cone cross-section as a function of the discharge factor.	28
3.5	Amplitude of the auto-spectral density function at the precession frequency of both convective and synchronous pressure components (upper section of the cone) as a function of the discharge factor.	29
3.6	Influence of the discharge factor on both the coherence at the precession frequency between two pressure signals and the precession frequency. The pressure signals are measured in the draft tube cone (locations C1S-C1E) - $\sigma = \sigma_{plant} = 0.11$ .	30
3.7	Visualizations of the cavitation vortex rope for different values of the discharge factor - $\sigma = \sigma_{plant} = 0.11$ .	30
3.8	Mean phase averaging of a wall pressure signal measured in the draft tube cone (location C1N). A total number of 4400 precession cycles was used for the calculation.	33
3.9	Reference pressure signal (black solid line) and voltage signal from Q-switch laser (red solid line). The limits of the successive precession cycles are indicated by the dashed black line in the right-handed figure.	34
3.10	Influence of the number of instantaneous velocity fields used for the mean phase averaging on the value of the velocity components $C_x$ and $C_y$ at the spatial position $(x, y) = (R/4, -R/2)$ (section 3).	35
3.11	Influence of the number of instantaneous velocity fields used for the mean phase averaging on the value of the velocity components $C_x$ and $C_y$ at the spatial position $(x, y) = (-R/8, 3R/8)$ (section 3).	35
3.12	Example of one instantaneous velocity field, together with the corresponding phase averaged velocity field for the relative phase $\theta = 10\pi/6$ of the precession period.	36
3.13	Comparison between the direct experimental results and those obtained by applying a truncated Fourier series decomposition for the velocity component $C_y$ .	37
3.14	Instantaneous velocity field centered on the vortex centre, together with the corresponding $\gamma_1$ values computed with the definition given by Graftieaux et al. [36]	39
3.15	Mean phase averaged velocity field centered on the vortex centre, together with the corresponding $\gamma_1$ values computed with the definition given by Graftieaux et al. [36]. The corresponding phase is equal to $\theta = 8\pi/5$ .	39

3.16 Average trajectory of the vortex centre (red o-markers), together with the distribution of the instantaneous vortex centres (black point markers), in the PIV measurement section 1 ( $Q_{ED} = 0.128$ ). . . . .	40
3.17 Scalar $\gamma_2$ computed with the definition of Graftieaux et al. [36] for one instantaneous velocity field and the corresponding phase averaged velocity field at the phase $\theta = \pi/10$ . ( $Q_{ED} = 0.128$ , PIV measurement section 3). . . . .	42
3.18 (a) Velocity magnitude and (b) vorticity for a given phase ( $\theta = \pi/10$ ) of the precession cycle in the PIV measurement section 3. The limits of the vortex core are indicated by the solid black contour ( $Q_{ED} = 0.128$ ). . . . .	42
3.19 Influence of the discharge factor on the magnitude of the velocity fields in the section 3. The black solid line corresponds to the limits of the vortex core. The value of the phase is different from one discharge factor value to another. . . .	44
3.20 Influence of the discharge factor on the normal component of the vorticity $\omega_z$ in the section 3. The black solid line corresponds to the limits of the vortex core. The value of the phase is different from one discharge factor value to another. . .	44
3.21 Influence of the discharge factor on the magnitude of the velocity fields in the section 1. The black solid line corresponds to the limits of the vortex core. The value of the phase is different from one discharge factor value to another. . . .	45
3.22 Average circulation of the vortex as a function of the discharge factor in each measurement section for the flow regimes 1 and 2. . . . .	46
3.23 (a) Dispersion of the instantaneous vortex centres for a given phase ( $\theta = 8\pi/5$ ) of the precession cycle and (b) comparison between the trajectory obtained by averaging the position of the instantaneous vortex centres and the one obtained by determining the vortex centre position in the phase averaged velocity fields ( $Q_{ED} = 0.64 \times Q_{ED}^*$ , section 1). . . . .	47
3.24 Vortex centre trajectory during one precession period for different values of discharge factor. . . . .	48
3.25 Vortex trajectory length as a function of the discharge factor in each measurement section. The length of the vortex trajectory is made dimensionless by the perimeter of the corresponding measurement section. . . . .	49
3.26 Phase averaged convective pressure components in the draft tube cone ( $Q_{ED} = 0.81 \times Q_{ED}^*$ ) . . . . .	50
3.27 Phase averaged convective pressure components in the draft tube cone ( $Q_{ED} = 0.64 \times Q_{ED}^*$ ) . . . . .	50
3.28 Average trajectory of the vortex centre (red dots), together with the instantaneous vortex centres (black dots) for different values of the discharge factor in the section 3. . . . .	51
3.29 Standard deviation of the vortex centre coordinates ( $x_c, y_c$ ) as a function of the discharge factor in the measurement section 3. . . . .	52

## List of Figures

---

3.30	Time-averaged axial velocity field in the meridional cross-section of the draft tube cone for different values of the discharge factor. The diagonal black solid line represents the outer cone wall. The axes $x$ and $z$ are made dimensionless by the runner diameter $D_1$ . . . . .	53
3.31	Recirculation zone radius as a function of the discharge factor for three different cross-sections of the cone. The radius of the recirculation zone is made dimensionless by the radius of the corresponding section $R_{sec}$ . . . . .	54
3.32	Time-averaged axial and tangential velocity profiles for different values of discharge factor, $1.02 \times D_1$ downstream the runner outlet. . . . .	55
3.33	Swirl number $S$ as a function of the discharge factor. The swirl number is computed with the time-averaged velocity profiles obtained in the cone cross-section located $1.02 \times D_1$ downstream the runner outlet. . . . .	56
3.34	Fluctuations of the flow separation zone induced by the precession of the vortex in the draft tube elbow [33] . . . . .	58
4.1	Cross-Spectral analysis between two pressure signals measured in the upper section of the cone in cavitation conditions at OP#1 ( $Q_{ED} = 0.161, \sigma = 0.11$ ). . .	62
4.2	Cross-Spectral analysis between two pressure signals measured in the cone in cavitation conditions at OP#2 ( $Q_{ED} = 0.128, \sigma = 0.11$ ). . . . .	63
4.3	Axial and tangential velocity signals and the corresponding auto-spectral density functions at OP#2 in cavitation conditions ( $Q_{ED} = 0.128, \sigma = 0.13$ ) at $(x, y) = (-0.84R, 0)$ . . . . .	64
4.4	Comparison between a pressure signal (position C1E) measured in the draft tube cone at OP#2 in cavitation conditions and the corresponding convective pressure component, together with the corresponding auto-spectral density functions ( $Q_{ED} = 0.128, \sigma = 0.11$ ). . . . .	65
4.5	Example of a convective pressure signal and an axial velocity signal, together with the resulting phase averaged signals ( $Q_{ED} = 0.128, \sigma = 0.13$ ). . . . .	66
4.6	Visualization of the cavitation vortex rope at two different instants of the precession period, corresponding to the passages of the vortex rope across the measurement diameter $x$ ( $Q_{ED} = 0.128, \sigma = 0.17$ ). . . . .	67
4.7	Mean phase averaged tangential velocity computed at 3 different radial positions along the $x$ -axis of the measurement section 2 ( $Q_{ED} = 0.128, \sigma = 0.17$ ) . . . . .	68
4.8	Mean phase averaged tangential velocity computed at 3 different radial positions along the $x$ -axis of the LDV measurement section 1 ( $Q_{ED} = 0.128, \sigma = 0.17$ ). . .	69
4.9	(a) Frequencies of interest (precession and natural frequencies) and (b) auto-spectra amplitude at the precession frequency as a function of the Thoma number at OP#1. The pressure signal is measured in the feeding pipe (location P1). . . . .	71
4.10	(a) Frequencies of interest (precession and natural frequencies) and (b) auto-spectra amplitude at the precession frequency as a function of the Thoma number at OP#2. The pressure signal is measured in the feeding pipe (location P1). . . . .	71

4.11	RMS value of the convective and synchronous pressure components as a function of the Thoma number in the upper section of the cone at OP#1. . . . .	73
4.12	RMS value of both convective and synchronous pressure components as a function of the Thoma number in the upper section of the cone at OP#2. . . . .	73
4.13	Evolution of the axial velocity profile over one precession cycle in the measurement section 2 at OP#1 ( $Q_{ED} = 0.161, \sigma = \sigma_{atm} = 0.31$ ). . . . .	75
4.14	Evolution of the tangential velocity profile over one precession cycle in the measurement section 2 at OP#1 ( $Q_{ED} = 0.161, \sigma = \sigma_{atm} = 0.31$ ). . . . .	75
4.15	Evolution of the axial velocity profile over one precession cycle in the measurement section 2 at OP#2 ( $Q_{ED} = 0.128, \sigma = \sigma_{atm} = 0.38$ ). . . . .	76
4.16	Evolution of the tangential velocity profile over one precession cycle in the measurement section 2 at OP#2 ( $Q_{ED} = 0.128, \sigma = \sigma_{atm} = 0.38$ ). . . . .	76
4.17	Sketch of axi-symmetric and asymmetric vortices with one corresponding horizontal flow streamline tangent to the $x$ -axis. . . . .	77
4.18	Evolution of the radial position for which $Cu = 0$ during one precession period at OP#1 ( $Q_{ED} = 0.161, \sigma_{atm} = 0.31$ ). . . . .	78
4.19	Evolution of the radial position for which $Cu = 0$ during one precession period at OP#2 ( $Q_{ED} = 0.128, \sigma_{atm} = 0.38$ ). . . . .	79
4.20	RMS value of the axial and tangential velocity fluctuations along the axes $x$ and $y$ at OP#1 in the measurement section 2 ( $Q_{ED} = 0.161, \sigma_{atm} = 0.31$ ). . . . .	80
4.21	RMS value of the axial and tangential velocity fluctuations along the axes $x$ and $y$ at OP#2 in the measurement section 2 ( $Q_{ED} = 0.128, \sigma_{atm} = 0.38$ ). . . . .	80
4.22	Different angular positions for a given radial position of the measurement volume.	81
4.23	Time delay as a function of the the radial position for the axial and tangential velocity fluctuations at OP#1 in the measurement section 2 ( $Q_{ED} = 0.161, \sigma_{atm} = 0.31$ ). . . . .	82
4.24	Time delay as a function of the radial position for the axial and tangential velocity fluctuations at OP#2 in the measurement section 2 ( $Q_{ED} = 0.128, \sigma_{atm} = 0.38$ ). . . . .	82
4.25	Evolution of the axial velocity profile over one precession period in the measurement section 2 at OP#1 in resonance conditions ( $Q_{ED} = 0.161, \sigma = \sigma_{res} = 0.10$ ). . . . .	84
4.26	Evolution of the tangential velocity profile over one precession period in the measurement section 2 at OP#1 in resonance conditions ( $Q_{ED} = 0.161, \sigma = \sigma_{res} = 0.10$ ). . . . .	84
4.27	Evolution of the axial velocity profile over one precession period in the measurement section 2 at OP#2 in resonance conditions ( $Q_{ED} = 0.128, \sigma = \sigma_{res} = 0.1625$ ). . . . .	85
4.28	Evolution of the tangential velocity profile over one precession period in the measurement section 2 at #OP2 in resonance conditions ( $Q_{ED} = 0.128, \sigma = \sigma_{res} = 0.1625$ ). . . . .	85
4.29	Time delay as a function of the radial position for the axial and tangential velocity fluctuations in resonance conditions ((a) $Q_{ED} = 0.161, \sigma_{res} = 0.10$ - (b) $Q_{ED} = 0.128, \sigma_{res} = 0.1625$ ). . . . .	86

## List of Figures

---

4.30	Time delay as a function of the radial position for the axial and tangential velocity fluctuations in non-resonance conditions ((a) $Q_{ED} = 0.161$ , $\sigma_{out} = 0.13$ - (b) $Q_{ED} = 0.128$ , $\sigma_{out} = 0.13$ ). . . . .	86
4.31	RMS value of the axial and tangential velocity fluctuations along the axes $x$ and $y$ at OP#1 in resonance conditions in the measurement section 2 ( $Q_{ED} = 0.161$ , $\sigma_{res} = 0.10$ ). . . . .	87
4.32	RMS value of the axial and tangential velocity fluctuations along the axes $x$ and $y$ at OP#2 in resonance conditions in the measurement section 2 ( $Q_{ED} = 0.128$ , $\sigma_{res} = 0.1625$ ). . . . .	87
4.33	RMS value of both axial and tangential velocity fluctuations along the axes $x$ and $y$ at OP#1 in non-resonance conditions in the measurement section 2 ( $Q_{ED} = 0.161$ , $\sigma_{out} = 0.13$ ). . . . .	88
4.34	RMS value of both axial and tangential velocity fluctuations along the axes $x$ and $y$ at OP#2 in non-resonance conditions in the measurement section 2 ( $Q_{ED} = 0.128$ , $\sigma_{out} = 0.13$ ). . . . .	88
5.1	Fluctuations of the wall pressure coefficients measured in the upper section of the draft tube cone at OP#2 ( $Q_{ED} = 0.128$ ) in non-resonance and resonance conditions. . . . .	91
5.2	Example of one single raw image and the corresponding binary image used for the detection of the cavitation vortex rope edges. . . . .	92
5.3	Time history of the fluctuating component $\Delta\beta$ of the void fraction for two values of Thoma number, together with the corresponding auto-spectral density functions ( $Q_{ED} = 0.128$ ). . . . .	94
5.4	Auto-spectra amplitude at $f_{rope}$ as a function of the Thoma number for different values of Froude number. The pressure signal is measured in the feeding pipe (location P1). . . . .	97
5.5	Cross-spectra phase at $f_{rope}$ as a function of the Thoma number for two pairs of pressure signals measured in the upstream section of the cone for different values of Froude number. . . . .	98
5.6	Precession frequency and associated auto-spectra amplitude as a function of the Thoma number ( $Fr = 6.56$ ). . . . .	99
5.7	RMS value of the convective pressure components as a function of the Thoma number for different values of Froude number. . . . .	100
5.8	RMS value of the synchronous pressure component as a function of the Thoma number for different values of Froude number. . . . .	101
5.9	Mean void fraction as a function of the Thoma number for two different values of the Froude number. . . . .	101
5.10	Mean pressure as a function of the Thoma number in two different cross-sections of the cone for different values of Froude number. . . . .	102

6.1	3D side and bottom views of the instrumented runner with on-board pressure sensors and strain gauges. The initials PS and SS mean Pressure Side and Suction Side, respectively. . . . .	106
6.2	Suction side of the blades 1 and 5 with the location of the pressure sensors and strain gauges. The initials PS and SS mean Pressure Side and Suction Side, respectively. . . . .	107
6.3	Pressure signals measured in the draft tube cone (location C1S) and on the runner blade 1 (location PS-TE2), together with the corresponding auto-spectral density functions ( $Q_{ED} = 0.128, \sigma = 0.11$ ). . . . .	108
6.4	Relative position between the runner (represented by the rotating frame $(O, \vec{x}, \vec{y})$ ) and the precessing vortex rope (symbol V) from Duparchy et al. [24]. . . . .	109
6.5	Auto-spectra amplitude at $f_{syn}$ and $f_{conv}$ as a function of the discharge factor for three pressure signals measured on the runner blade 1 in cavitation-free conditions. . . . .	109
6.6	Auto-spectral density function of signals measured on the runner blade 5 by two different strain gauges ( $Q_{ED} = 0.128, \sigma = 0.11$ ). . . . .	110
6.7	Auto-spectra amplitude at $f_{syn}$ and $f_{conv}$ as a function of the discharge factor for two strain gauges located on the runner blade 5 in cavitation-free conditions. . . . .	111
6.8	Amplitude of the auto-spectral density function at the frequencies $f_{rope}$ and $f_{conv} = n - f_{rope}$ as a function of $\sigma$ for pressure signals measured in the cone and on the blade 1 (a) and for fluctuating strain measured on the blade 5 (b). . . . .	112
6.9	Time-history of the torque measured on the runner shaft, together with the corresponding auto-spectral density function, for two values of Thoma number ( $Q_{ED} = 0.128$ ). . . . .	113
A.1	Hill chart of the reduced scale physical model on the EPFL test rig PF3 as a function of the speed factor $n_{ED}$ and the discharge factor $Q_{ED}$ . . . . .	119
C.1	Evolution of the axial velocity profile over one precession cycle in the measurement section 1 at OP#1 - $Q_{ED} = 0.161, \sigma = \sigma_{atm} = 0.31$ . . . . .	123
C.2	Evolution of the tangential velocity profile over one precession cycle in the measurement section 1 at OP#1 - $Q_{ED} = 0.161, \sigma = \sigma_{atm} = 0.31$ . . . . .	123
C.3	Evolution of the axial velocity profile over one precession cycle in the measurement section 1 at OP#2 - $Q_{ED} = 0.128, \sigma = \sigma_{atm} = 0.38$ . . . . .	124
C.4	Evolution of the tangential velocity profile over one precession cycle in the measurement section 1 at OP#2 - $Q_{ED} = 0.128, \sigma = \sigma_{atm} = 0.38$ . . . . .	124
C.5	Evolution of the axial velocity profile over one precession cycle in the measurement section 2 at OP#1 - $Q_{ED} = 0.161, \sigma = \sigma_{out} = 0.13$ . . . . .	124
C.6	Evolution of the tangential velocity profile over one precession cycle in the measurement section 2 at OP#1 - $Q_{ED} = 0.161, \sigma = \sigma_{out} = 0.13$ . . . . .	125
C.7	Evolution of the axial velocity profile over one precession cycle in the measurement section 2 at OP#2 - $Q_{ED} = 0.128, \sigma = \sigma_{out} = 0.13$ . . . . .	125

## List of Figures

---

- C.8 Evolution of the tangential velocity profile over one precession cycle in the measurement section 2 at OP#2 -  $Q_{ED} = 0.128$ ,  $\sigma = \sigma_{out} = 0.13$ . . . . . 125
- D.1 Illustration of the spatial decomposition of the pressure field  $p(\theta)$  into synchronous component  $p_{syn}(\theta)$  and convective component  $p_{conv}(\theta)$  for a given time  $t$ .  $\theta$  corresponds to the angular position along the perimeter of the cone section. . . . . 128



# List of Tables

1.1	Electric energy production in 2002 and 2012 for different types of energy source.	2
2.1	Technical specifications of the LDV system.	14
2.2	Technical specifications of the PIV system.	17
2.3	Specifications for the visualization equipment.	20
3.1	List of the operating points investigated by PIV.	31
4.1	List of the investigated operating points.	61
4.2	Radial positions of the control volume for each investigated operating conditions	70
5.1	List of the investigated operating points.	96
6.1	List of pressure sensors and strain gauges on the instrumented runner	106
B.1	List of the operating points investigated by PIV (Chapter 3).	121
B.2	List of the operating points investigated by LDV (Chapter 4).	121



# Nomenclature

## Acronyms

BEP	<b>B</b> est <b>E</b> fficiency <b>P</b> oint
BSA	<b>B</b> urst <b>S</b> pectrum <b>A</b> nalyzer
EPFL	<b>É</b> cole <b>P</b> olytechnique <b>F</b> édérale de <b>L</b> ausanne
fps	<b>f</b> rames <b>p</b> er <b>s</b> econd
LED	<b>L</b> ight- <b>E</b> mitting <b>D</b> iode
LDV	<b>L</b> aser <b>D</b> oppler <b>V</b> elocimetry
NRE	<b>N</b> ew <b>R</b> enewable <b>E</b> nergy
OP	<b>O</b> perating <b>P</b> oint
PIV	<b>P</b> article <b>I</b> mage <b>V</b> elocimetry
PXI	<b>P</b> CI <b>e</b> Xtensions for <b>I</b> nstrumentation
RMS	<b>R</b> oot <b>M</b> ean <b>S</b> quare
rpm	<b>r</b> evolutions <b>p</b> er <b>m</b> inute
std	<b>s</b> tandard <b>d</b> eviation

## Subscripts

1	runner high pressure reference section
$\bar{1}$	runner low pressure reference section
<i>c</i>	cavitation vortex rope
<i>I</i>	power unit high pressure reference section
$\bar{I}$	power unit low pressure reference section
$\bar{B}$	tailwater reservoir reference section
<i>B</i>	headwater reservoir reference section
atm	atmosphere
cav	cavitation
plant	power plant
rope	precessing vortex rope
sec	section

## List of Tables

---

### Superscripts

conv	convective component
syn	synchronous component

### Latin letters

$x, y, z$	cartesian coordinates	(m)
$x_c, y_c$	vortex centre coordinates	(m)
$C$	absolute flow velocity	(m s <sup>-1</sup> )
$W$	relative flow velocity	(m s <sup>-1</sup> )
$U$	peripheral runner velocity	(m s <sup>-1</sup> )
$C_m$	axial (meridional) velocity component	(m s <sup>-1</sup> )
$C_u$	tangential velocity component	(m s <sup>-1</sup> )
$C_r$	radial velocity component	(m s <sup>-1</sup> )
$C_x$	velocity component along the $x$ -axis	(m s <sup>-1</sup> )
$C_y$	velocity component along the $y$ -axis	(m s <sup>-1</sup> )
$C_Q$	discharge velocity; $C_Q = Q/A$	(m s <sup>-1</sup> )
$g$	gravitational acceleration	(m s <sup>-2</sup> )
$n$	runner rotational frequency	(Hz)
$Z$	elevation	(m)
$Z_{\text{ref}}$	power unit reference level (horizontal spiral case symmetry plane)	
$D$	diameter	(m)
$H$	head; $H = p/(\rho \cdot g) + Z + C^2/(2 \cdot g)$	(m)
$E$	specific energy; $E = g \cdot (H_I - H_{\bar{I}})$	(J kg <sup>-1</sup> )
$f$	frequency	(Hz)
$H_s$	$Z_{\text{ref}} - Z_{\bar{B}}$	(m)
$N$	runner speed	(min <sup>-1</sup> )
NPSE	net Positive Suction Energy; $\text{NPSE} = (p_b - p_v)/\rho - gH_s + \frac{1}{2}C_{\bar{I}}^2$	(J kg <sup>-1</sup> )
$p_v$	vapor pressure	(Pa)
$Q$	discharge	(m <sup>3</sup> s <sup>-1</sup> )
$R$	radius	(m)
$S$	swirl number	(-)
$T$	torque	(Nm)
$T$	period	(s)
$V$	volume	(m <sup>3</sup> )

## Greek letters

$\beta$	relative flow angle	(-)
$\Gamma$	circulation	(m <sup>2</sup> s <sup>-1</sup> )
$\theta$	phase	(-)
$\theta$	angular position	(-)
$\nu$	kinematic viscosity	(m <sup>2</sup> s <sup>-1</sup> )
$\rho$	density	(kg m <sup>-3</sup> )
$\tau$	time delay	(s)
$\omega$	angular velocity	(rad s <sup>-1</sup> )
$\omega$	vorticity	(s <sup>-1</sup> )

## Non-dimensional variables

$C_p$	pressure factor; $C_p = (p - \bar{p})/(\rho E)$	(-)
$Fr$	Froude number; $Fr = \sqrt{H/D_1}$	(-)
$n_{ED}$	speed factor; $n_{ED} = (n \cdot D)/\sqrt{E}$	(-)
$Q_{ED}$	discharge factor; $Q_{ED} = Q/(D^2 \cdot \sqrt{E})$	(-)
$Re$	Reynolds number; $Q_{ED} = C \cdot D_{ref}/\nu$	(-)
$\nu$	specific speed; $\nu = \omega \cdot \sqrt{Q}/(\sqrt{\pi} \cdot (2 \cdot E)^{3/4})$	(-)
$\sigma$	Thoma number or cavitation number; $\sigma = NPSE/E$	(-)



# 1 Introduction

## 1.1 Energy context

In 2012, hydraulic powerplants provided approximately 16 % of the total worldwide electricity production, whereas the share of the other New Renewable Energy (NRE) sources represented less than 5%. With a contribution equal to 68 %, fossil energy sources remained the baseload of the total electric energy production, as illustrated in Figure 1.1, with consequences in terms of environmental impacts and greenhouse gas emissions. However, in recent years, environmental and geopolitical concerns have led to the establishment of energy policies promoting the development of alternative renewable energy sources, such as wind and solar power, in order to reduce drastically the greenhouse gas emissions and the dependance on fossil energy producers. As a consequence, the global electric energy production from renewable energy sources has been on a constant rise from 2002 and 2012, as illustrated in Table 1.1. It is particularly remarkable for solar and wind power, whose total output production has been multiplied respectively by 57 and 10 during the last decade.

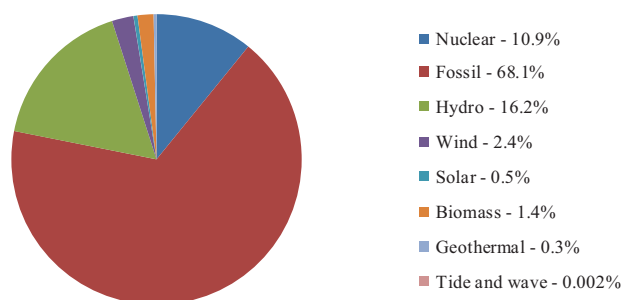


Figure 1.1: Worldwide electricity generation in 2012 [68].

In Europe, the recent decision taken by the European Union (EU) to adopt an energy policy promoting the massive integration of new renewable energy sources will lead to a dramatic electric energy system transition. A set of objectives has been defined under the name of the *2020 climate and energy package*. It includes the raise of the share of the EU energy

Table 1.1: Electric energy production in 2002 and 2012 for different types of energy source.

	2002 (TWh)	2012 (TWh)	Ratio (-)
Hydro	2606	3646	1.4
Wind	52.8	520	9.9
Solar	1.7	96.4	56.3
Other NRE	240	453	1.9
Nuclear	2546	2345	0.92
Fossil	9979	14498	1.5
Total	15393	21532	1.4

consumption produced by NRE to 20 %, a reduction of EU greenhouse gas emissions of 20 % from the level in 1990 and an improvement of the EU energy efficiency of 20 % [26].

However, the intermittent nature of the NRE production seriously impacts the energy balance between production and consumption, as well as the stability of the electrical grid. Typical examples are wind and solar energy sources, which strongly depend to the weather conditions. In order to guarantee the smooth integration of NRE into the existing power system, it is therefore necessary to ensure the electrical grid has enough storage capacity as well as primary and secondary grid control capability to enable the energy balancing process. Pumped storage and hydraulic powerplants provide the necessary storage capacities and feature the ability of flexible generation to address these issues. However, it requires the constant extension of the operating range of hydraulic powerplants, for which the turbine components experience the development of unstable two-phase flows. Under certain conditions, these latter can cause severe pressure and power pulsations, as well as mechanical vibrations, which can jeopardize the structural integrity of the powerplant and the system stability in the worst case.

The present research work focuses on the investigation of flow instabilities occurring in the draft tube of Francis turbines at part load conditions and their interaction with the surrounding system. This range of operating conditions is defined by a flow discharge lower than the value at the Best Efficiency Point (BEP) of the turbine.

## 1.2 Francis turbines

Among the different types of hydraulic turbines, Francis turbines are the most widespread worldwide in terms of power capacity, representing about 60 % of the installed hydropower capacity in the world and 42 % in Europe. They are reaction turbines used for medium head values, typically from about 50 m to 500 m. The different components of a Francis turbine are presented in Figure 1.2. An angular momentum is created at the runner inlet by the spiral casing, stay vanes and guide vanes. The opening angle of the guide vanes controls the value of the flow rate through the runner. The angular momentum of the flow is recovered



by the runner blades and converted into mechanical momentum on the shaft. The flow is then released into the draft tube, which recovers the residual kinetic energy of the flow by converting it into static pressure.

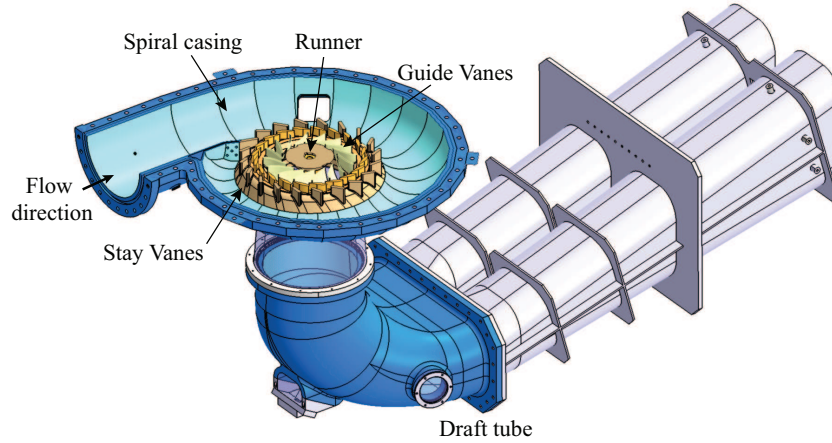


Figure 1.2: Components of a Francis turbine.

The operating conditions of a Francis turbine, with an outer runner diameter  $D_1$  and a rotation frequency  $n$ , are expressed by means of two dimensionless factors, the speed and discharge factors  $n_{ED}$  and  $Q_{ED}$ , defined according to the IEC Standards [42] as follows:

$$n_{ED} = \frac{nD_1}{\sqrt{E}} \quad (1.1)$$

$$Q_{ED} = \frac{Q}{D_1^2 \sqrt{E}} \quad (1.2)$$

with  $Q$  the flow discharge and  $E$  the available specific energy of the turbine. The latter corresponds to the specific energy available for the machine and is given by the difference of specific energy of the fluid at the inlet and outlet of the machine,  $E = gH_I - gH_f$ . It can be expressed as a function of the altitudes of the headwater and tailwater reservoirs and the energies losses in the hydraulic circuit, as following:

$$E = gH = gH_I - gH_f = g(Z_B - Z_{\bar{B}}) - gH_r \quad (1.3)$$

with  $Z_B$  and  $Z_{\bar{B}}$  the altitudes of the upstream and downstream reservoirs and  $gH_r$  the energy losses in the hydraulic circuit. A complete layout of a Francis turbine powerplant, including

one single power unit connected to the upstream and downstream reservoirs, is presented in Figure 1.3.

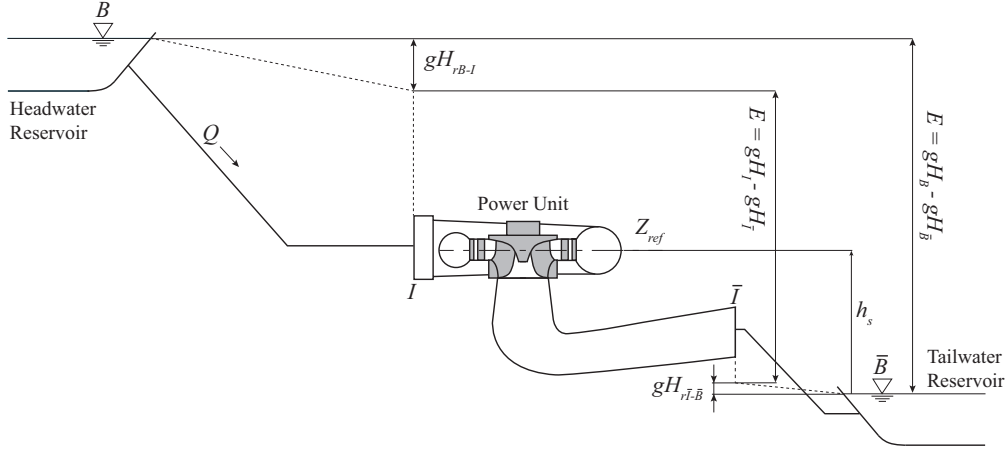


Figure 1.3: Layout of a Francis turbine hydropower plant.

Generally, the machine is designed for a rated operating point defined by rated discharge  $Q_n$  and head  $H_n$  values, which are chosen as a function of the hydrology of the site and the strategy of operation. The Best Efficiency Point (BEP) of the machine is defined as the operating point featuring the maximum energetic efficiency  $\eta$ , defined as the ratio between the hydraulic specific energy  $E$  and the transformed specific energy  $E_t$ . The operating range of the machine can be extended according to the electricity demand variations by adjusting the discharge  $Q$  via the guide vanes opening. However, such operations at off-design conditions are characterized by a loss of efficiency and the development of complex two-phase flows in the draft tube.

### 1.3 Off-design conditions

Operating at off-design conditions, Francis turbines experience the development of a swirling flow in the draft tube. This is illustrated by the velocity triangles at the runner outlet in Figures 1.4 and 1.5. The absolute flow velocity  $\vec{C}_1$  can be written as the sum of the runner circumferential speed  $\vec{U}_1$  and the relative flow velocity  $\vec{W}_1$  as follows:

$$\vec{C}_1 = \vec{U}_1 + \vec{W}_1 \quad (1.4)$$

As the direction of the relative flow velocity is imposed by the blades orientation, defined by the relative flow angle  $\beta_1$ , a modification of the flow rate induces the apparition of a tangential component of the absolute velocity  $\vec{C}u_1$  in addition to the axial component  $\vec{C}m_1$  in the main flow direction. The resulting swirling flow rotates in the same direction than the runner at part

load conditions ( $Q < Q_{BEP}$ ) and in the opposite direction at full load conditions ( $Q > Q_{BEP}$ ).

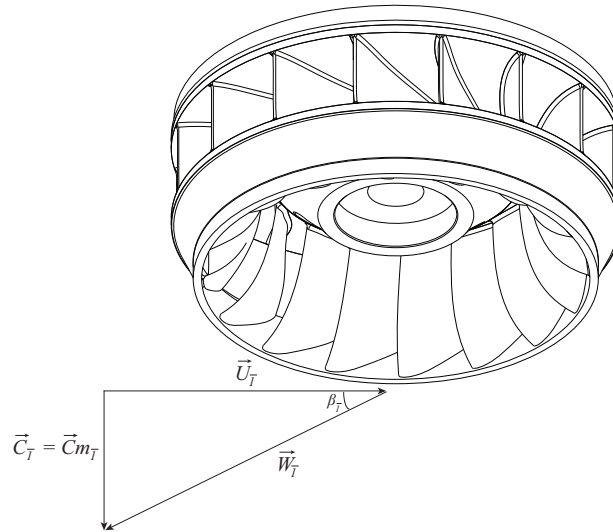


Figure 1.4: Definition of the velocity triangles at the outlet of a Francis turbine [59].

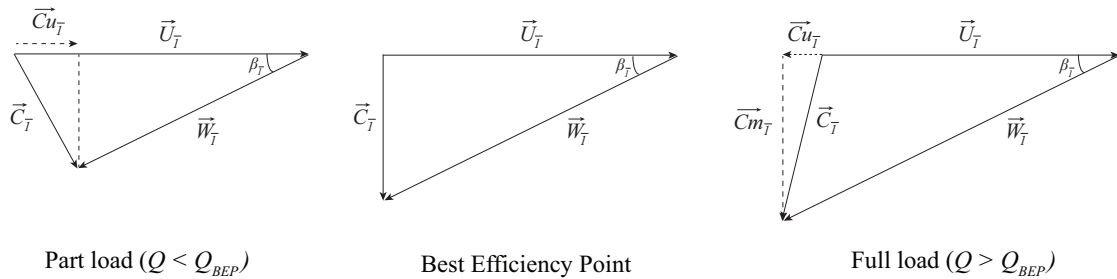


Figure 1.5: Velocity triangles at the runner outlet at off-design conditions (part load and full load conditions) and at the Best Efficiency Point.

At part load conditions, the development of a swirling flow at the runner outlet gives rise an helical precessing vortex core in the draft tube wrapped around a zone of recirculating flow which is identified as a manifestation of the vortex breakdown phenomenon [38]. The precessing vortex core rotates with a frequency comprised between 0.2 and 0.4 times the runner frequency, depending on the flow parameters. If the static pressure in the draft tube is sufficiently low, the pressure in the vortex core can decrease below the value of the vapor pressure which makes the vortex core visible under the form of a cavity of vapour. This phenomenon, called cavitation, corresponds to the vaporization of the water at constant temperature when the local static pressure is lower than the vapor pressure [35]. At full load conditions, the development of cavitation in the draft tube cone gives rise to a nearly axisymmetric cavitation vortex rope along the draft tube cone centerline. Examples of cavitation vortex ropes observed at both part load and full load conditions are presented in Figure 1.6.

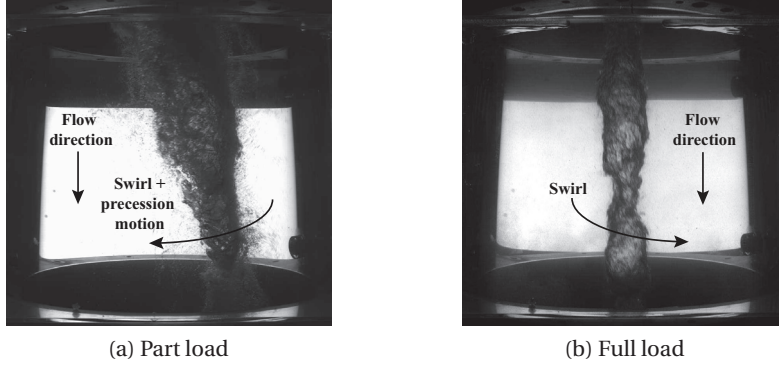


Figure 1.6: Visualization of the cavitation vortex rope in the draft tube cone during reduced scale model tests at part load and full load conditions.

The level setting  $h_s$  (see Figure 1.3) of the runner is a decisive parameter for the inception of cavitation in Francis turbine draft tube. In order to characterize the absolute level of pressure at the turbine level, the Net Positive Suction Energy (NPSE) is introduced, corresponding to the difference between the specific energy  $gH_{\bar{I}}$  at the suction section relative to the reference machine level and the specific energy corresponding to the vapor pressure:

$$NPSE = (gH_{\bar{I}} - gZ_{ref}) - \frac{p_v}{\rho} \quad (1.5)$$

with  $Z_{ref}$  the reference altitude of the turbine runner. Expressing  $gH_{\bar{I}}$  as a function of the specific energy at the free surface of the tailwater reservoir yields [35]:

$$NPSE = \frac{p_{\bar{B}}}{\rho} - \frac{p_v}{\rho} - gh_s + \frac{C_{\bar{I}}^2}{2} \quad (1.6)$$

The last term corresponds to the energy losses at the tailwater reservoir inlet. The Thoma number  $\sigma$  of the machine is defined by IEC Standards [42] as the dimensionless ratio between the NPSE and the specific energy  $E$  of the machine:

$$\sigma = \frac{NPSE}{E} \quad (1.7)$$

A low Thoma number indicates a high risk of cavitation development. Generally, the machine is set up the highest possible level above the free surface of the tailwater reservoir to minimize

the civil engineering costs, although it promotes the development of cavitation in the draft tube at off-design conditions.

The cavitation vortex rope arising at part load and full load conditions represents an excitation source for the hydraulic system to which the machine is connected. It leads to the propagation of pressure waves in the system, which can be amplified under certain conditions, causing pressure surge and output power swings able to compromise the system stability. At full load conditions, the propagation of pressure fluctuations is induced by the self-oscillation of the cavitation vortex rope at the natural frequency of the system [59]. At part load conditions, on the other hand, the periodical precession motion of the vortex rope acts as an external excitation source at the precession frequency for the system. It can lead to the occurrence of hydro-acoustic resonances in case of a match between the natural frequency of the hydraulic system and the precession frequency. The present research work focuses on the investigation of the part load vortex rope and proposes a study of the influence of different parameters on its dynamics and its interaction with the hydro-mechanical system.

### 1.4 State of the art

The precessing vortex core (PVC) has been extensively studied for a wide range of engineering applications involving swirling flows, from combustor systems and delta wings to hydraulic machines (see Escudier [25] or Syred [75] for a review).

Increasing the swirl number, defined by Gupta et al. [38] as the ratio between the axial flux of angular momentum and the axial flux of axial momentum, rotating flows experience an abrupt change in their structure, with the apparition of a stagnant point and an axial recirculation zone under the action of an adverse axial pressure gradient. Even though this phenomenon, commonly called vortex breakdown, has been widely investigated, the underlying physical mechanisms are still only partially understood (see Lucca-Negro and O'Doherty [57] for an extensive review). Harvey [39] was one of the first to experimentally observe the vortex breakdown. He defined it as the critical state between the existence or not of an axial recirculation zone. At the same time, Benjamin [10] suggested that the vortex breakdown is a finite transition between two dynamically conjugate states of axisymmetric flow. Later, Sarpkaya [73] and Faler and Leibovich [27] pointed out different forms of vortex breakdowns, including the axisymmetric, the double helix and the spiral vortex breakdowns. The precessing vortex core was identified as a manifestation of the vortex breakdown phenomenon. Chanaud [15] was among the first to report the observation of oscillatory motions in swirling flows as an evidence of the PVC occurrence. Later, Cassidy and Falvey [14] focused on the investigation of the PVC and showed the linear dependence between the precession frequency and the flow discharge.

In the case of Francis turbines operating at part load conditions, the precession of the cavitation vortex rope acts as an excitation source for the system. This can cause a system resonance and consequently lead to draft tube pressure surge and power swings of the hydro-electric in-

stallation, as reported by Rheingans [71] in the early 1940s. The pressure fluctuations induced by the precessing vortex rope in Francis turbines draft tube cones can be decomposed into two different components: the convective or asynchronous component, caused by the local rotation of the flow, and the synchronous one, which features equal phase and amplitudes in a given horizontal cross-section of the cone. Nishi et al. [66] highlighted this decomposition and developed an analytical method to identify both components by using the Fourier series decomposition of pressure signals measured in the same cross-section of the cone. Angelico et al. [5] confirmed this decomposition by using three pressure sensors located in the same cross-section of the cone. They performed a vector analysis in the frequency domain of the pressure signals in order to identify both components. Dörfler [19] assumed that the synchronous pressure component results from the excitation source and the hydro-acoustic response of the system. Thus, the accurate decomposition of the pressure fluctuations in the cone is of major importance as it permits to extract the hydro-acoustic response of the system. Recent works have presented novel methods for the computation of both components, for instance by Dörfler and Ruchonnet [20] and Duparchy et al. [23].

In the past decades, many experimental investigations focused on the precessing vortex rope in an effort to understand and characterize the hydrodynamic of the Francis turbine draft tube at part load conditions (the reader may refer to Nishi and Liu [64] for an extensive review). In the 1980s, Nishi et al. [65, 66, 67] identified different flow regimes with respect to the swirl number by using a set of stationary guide vanes instead of a real turbine. They investigated the flow pattern in the draft tube cone and elbow, and also carried out pressure fluctuations measurements for different values of the swirl number and the cavitation number. Later, in the framework of the FLINDT project [8], Iliescu et al. [44] performed 2D-PIV measurements in a meridional cross-section of the draft tube cone of a Francis turbine reduced scale model, in presence of a cavitation precessing vortex rope. By synchronizing the PIV measurements with pressure measurements, the evolution of the velocity field during one precession cycle was reconstructed and the influence of the cavitation on the vortex rope centerline was investigated. These results were used to validate CFD simulations of the draft tube unsteady flow performed by Ciocan et al. [16]. Kirschner et al. [49] characterized the periodical fluctuations of the axial velocity field in the draft tube cone and estimated the vortex core motion by means of 2D-PIV measurements. Arpe [6] performed unsteady wall pressure measurements by using a total of 104 pressure transducers installed throughout the draft tube, including the cone, the elbow and the diffuser. He highlighted the propagation of a synchronous pressure component for different values of Thoma number, as well as a wave front travelling in the diagonal direction which is induced by the precession of the vortex core.

From an analytical point of view, Fanelli [28] derived a model of the excitation source by describing the swirling flow as the superposition of two potential flow motions. He found out that the synchronous pressure component is not created in the case of a perfectly rectilinear draft tube. This theoretical result is in agreement with the observations from Nishi et al. [66], who experimentally demonstrated that the synchronous pressure surge is not observed in the case of a conical diffuser. They suggested that the excitation source is the result of an

oscillation of the pressure recovery in the elbow, induced by the rotation of the vortex rope. Later, Susan-Resiga et al. [74] modeled the swirling flow at the runner outlet by a combination of three elementary vortices and identified their parameters on the basis of time-averaged velocity profiles measured experimentally. Kuibin et al. [52] derived an analytical model for recovering the time-averaged velocity profiles at the runner outlet, as well as the precession frequency and the amplitude of the pressure fluctuations.

Another part of the research dealing with part load conditions focused on the investigation of hydropower plants stability in order to predict and simulate the part load resonance induced by the cavitation vortex rope. For this purpose, transfer matrices are extensively used to evaluate the risk of resonance and to identify the parameters modelling the cavitation draft tube flow [46, 47]. The latter is generally modeled by the cavitation compliance, according to the definition introduced by Brennen and Acosta [12], which represents the variation of cavitation volume with respect to the pressure, while the excitation source induced by the vortex precession is modeled by a source term. Dörfler [19] was one of the first to determine experimentally the cavitation compliance for different values of the Thoma number by using a transfer matrix model based on pressure measurements performed on a reduced scale model of a Francis turbine. With this method, he also determined the excitation source in cavitation-free conditions and assumed that it is independent of the Thoma number. Later, Couston and Philibert [17] proposed a new transfer matrix model taking into account the wave speed along the draft tube, which is considered as a constant, and the vortex rope length. Lately, one-dimensional time analysis approaches based on T-shaped equivalent electrical circuits were introduced [63]. Alligné [2] determined the hydro-acoustic parameters of the cavitation draft tube flow by means of CFD simulations. He finally simulated the part load resonance by injecting the resulting parameters into an one-dimensional model of the hydraulic circuit. He also introduced an additional hydro-acoustic parameter related to the thermodynamic dissipation occurring during phase changes. Recently, Landry [53] developed a novel experimental methodology to identify the hydro-acoustic parameters of the cavitation vortex rope at part load conditions.

## 1.5 Thesis Objective

The primary aim of this research work is to gain a better understanding of the underlying physical mechanisms for the formation of an excitation source induced by the cavitation vortex rope and the interaction of the latter with the hydraulic system. This is achieved by experimentally investigating the influence of the flow parameters on the cavitation vortex rope dynamics and the hydro-acoustic response of the system with a series of measurements performed on a reduced scale physical model of a Francis turbine.

In particular, the influence of the flow discharge on the vortex dynamics is investigated by performing flow and pressure measurements in the Francis turbine draft tube in cavitation-free conditions. The flow properties are obtained for a wide range of discharge value by means

of PIV measurements. Furthermore, the effect of cavitation on the draft tube flow velocity fields and the interaction between the excitation source and the hydraulic system is also investigated by LDV and pressure measurements performed in the draft tube for different values of the Thoma number.

Another important aspect is to quantify the impact of the propagation of pressure fluctuations induced by the cavitation vortex rope on the mechanical behaviour of the runner by measuring the pressure and strain on the runner blades.

Finally, the resulting data forms an extensive database for the validation of CFD simulations and analytical flow models in the framework of the HYPERBOLE research project (ERC/FP7-ENERGY-2013-1-Grant 608532).

### 1.6 Document Structure

Chapter 2 details the experimental apparatus and techniques used on a 1:16 reduced scale physical model of a Francis turbine installed on the EPFL test rig PF3. A detailed description of the test rig is provided, as well as the location of the pressure transducers. The experimental methods used for the draft tube flow field investigation and the corresponding set-up, including Laser Doppler Velocimetry (LDV), Particle Image Velocimetry (PIV) and high speed visualization, are presented.

Chapter 3 focuses on the influence of the flow discharge on the precessing vortex rope dynamics. It includes a detailed description of both tangential and axial velocity fields in the draft tube cone for a wide range of discharge factor in cavitation-free conditions, as well as a distinction between three different flow regimes based on pressure fluctuation measurements.

Chapter 4 is dedicated to the study of the influence of the Thoma number on the velocity flow fields in the draft tube cone. The velocity flow fields measured in cavitation conditions, including resonance conditions, are compared with those obtained in cavitation-free conditions for two particular operating points.

Chapter 5 investigates the influence of the Froude number on the interaction between the cavitation vortex rope and the system. A phenomenon of frequency lock-in occurring at low values of Froude number is notably highlighted.

Finally, Chapter 6 contains the study of the pressure fluctuations propagation through the runner and its impact on the runner mechanical behavior, with a particular focus on cavitation and resonance conditions.



## 2 Test-case and Experimental set-up

### 2.1 Reduced scale physical model

The test case is a 1:16 reduced scale physical model of a  $v = 0.27$  specific speed Francis turbine featuring 16 runner blades and 20 guide vanes. The hill chart of the runner is given in Appendix A. The real generating unit is installed on a hydropower plant located in British Columbia (Canada) and features a rated output power of 444 MW. It experiences severe pressure surges at full load conditions, which led to previous experimental studies, including flow fields investigation in the draft tube cone in cavitation conditions [59]. The reduced scale physical model is installed on the EPFL test rig PF3 of the Laboratory for Hydraulic Machines. It allows for accurate performance tests of reduced scale models of hydraulic machines within an accuracy better than 0.3 % according to the IEC Standards [42]. The facility is operated in close-looped configuration and includes two axial double-volute pumps of 400 kW connected in series permitting to generate the specified head by adjusting the pumps speed, with a maximum head of 100 m. The upper part of the hydraulic circuit is displayed in Figure 2.1, with the reservoir, the diffuser, the spiral casing and the headwater connecting pipes.

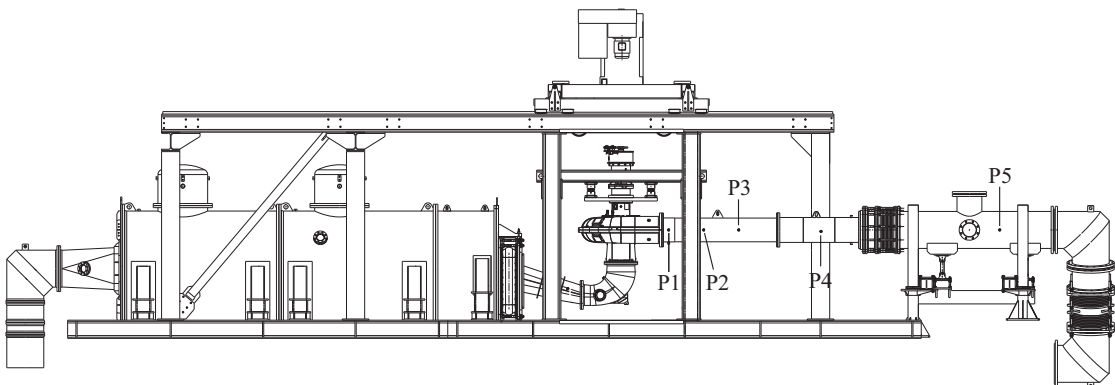


Figure 2.1: Reduced scale physical model of a Francis turbine installed on EPFL test rig PF3 [59].

The flow discharge is adjusted by the guide vane opening of the machine. The Thoma number  $\sigma$  is set by changing the pressure over the free surface of the reservoir with a vacuum pump. The turbine speed is regulated by the drive controller of the DC generator. The draft tube cone is made of Plexiglas, providing an optical access for high speed visualizations of the vortex rope in cavitation conditions and flow fields investigation by means of PIV.

### 2.2 Pressure measurement on the test rig

The dynamic wall pressure is measured by flush-mounted piezo-resistive pressure sensors installed at different locations of the test rig. They allow for pressure measurements in the range of  $0 \div 5$  bar with a maximum measurement uncertainty of  $0.7 \text{ ‰}$ . In the draft tube cone, the dynamic wall pressure is measured at two different streamwise positions, respectively  $0.39 \times D_1$  (upper section) and  $1.02 \times D_1$  (lower section) downstream the runner outlet (see Figure 2.3). For each cross-section, 4 pressure sensors are installed, regularly spaced by  $90^\circ$  (upper section: sensors C1N, C1W, C1S, C1E - lower section: sensors C2N, C2W, C2S, C2E) in order to decompose the pressure fluctuations at the precession frequency into convective and synchronous components. A second cone is used for PIV measurements and high-speed visualizations (see Section 2.3.2). 11 pressure sensors are also regularly distributed in the headwater connecting pipes of the test rig (sensors P1  $\rightarrow$  P11) in order to capture its hydro-acoustic response and the shape of its eigenmodes. Three sensors are arranged in the same cross-section at the inlet of the diffuser (sensors D2, D3 and D4) and two others sensors are placed between this section and the downstream reservoir (sensors D0 and D1).

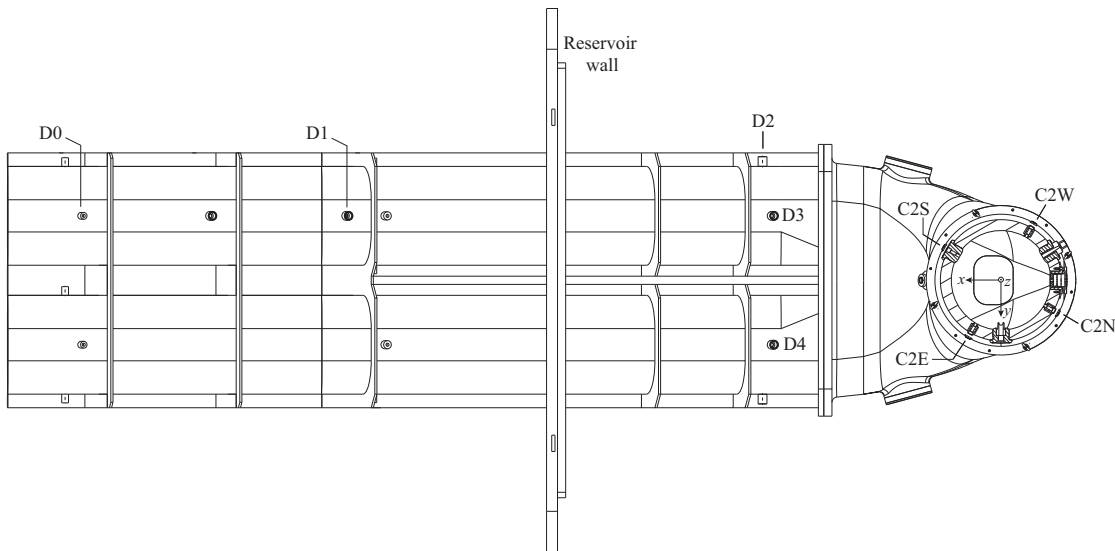


Figure 2.2: Cut-view of the upper section of the draft tube cone with the location of the wall pressure sensors and the diffuser.

Dynamic wall pressure signals are acquired via an amplifier and a NI-PXI device, mostly with a sampling frequency of 1'000 Hz and an acquisition time of 180 s, synchronously with the measurement of the test rig parameters, e.g. the shaft torque  $T$ , the flow discharge  $Q$ , the hydraulic specific energy  $E$  and the Thoma number  $\sigma$ . According to IEC 60193 Standards requirements, the flow discharge is measured by means of an electromagnetic flow meter installed in the headwater connecting pipes of the test rig between the pumps and the model. The hydraulic specific energy  $E$  is measured by using a differential pressure transducer between the turbine inlet and the turbine draft tube outlet, which is also used to compute the instantaneous value of the Thoma number.

## 2.3 Draft tube flow field investigation

The complex and unsteady flow field at the runner outlet is investigated in the draft tube cone by means of non-intrusive optical techniques, such as Laser Doppler Velocimetry (LDV) and 2D-Particle Image Velocimetry (PIV), each one being used depending on the flow conditions and the presence of cavitation or not in the vortex core. For each type of measurements, the parameters of the investigated operating conditions are summarized in Appendix B. The following section describes both optical techniques and the corresponding experimental setups.

### 2.3.1 Laser Doppler Velocimetry

#### Measurement principle

Laser Doppler Velocimetry (LDV) is a non-intrusive optical technique for instantaneous flow velocity measurements at the position of a control volume formed by the intersection of two frequency-shifted Laser beams. It is based on the analysis of the light reflected by seeding particles passing through said measurement volume. A detailed overview of the LDV technique is given in [82]. The intersection of two coherent Laser beams forms an interference fringe pattern, whose spacing depends of the laser wavelength and the intersection angle of the beams. By analysing the light scattered by the seeding particles, the velocity component normal to the fringe direction can be determined, as it only depends of the Doppler frequency of the scattered signal and the fringe spacing. Different velocity components can be measured simultaneously by combining several pairs of Laser beams with different wavelengths and orientation.

#### Laser Doppler Velocimetry set-up

For the present test case, a two-components Dantec FlowExplorer LDV system is used with a focal lens of 500 mm, allowing for measurements of simultaneous axial and tangential velocity components  $C_m$  and  $C_u$ , respectively. The specifications of the LDV system are given in

Table 2.1: Technical specifications of the LDV system.

<b>Laser</b>	
Wavelength Channel 1	660 nm
Wavelength Channel 2	785 nm
Focal length	500 mm
Energy	35 mW / Channel
Model	Dantec FlowExplorer
Measurement volume (in air)	2.806 mm × 0.1684 mm × 0.1681 mm (Channel 1) 3.338 mm × 0.2003 mm × 0.1999 mm (Channel 2)
<b>Burst Spectrum Analyzer</b>	
Model	Dantec BSA F60

Table 2.1. LDV measurements are performed at two different streamwise positions of the draft tube cone, respectively  $0.39 \times D_1$  and  $1.02 \times D_1$  downstream the runner outlet, see Figure 2.3. For each streamwise position, the LDV probe is set up in two different configurations, as illustrated in Figure 2.4, in order to measure the axial and tangential velocity components along two different diameters of the section, respectively parallel and perpendicular to the upstream pipe. The LDV probe is mounted on a remotely controlled traversing system for accurate radial and vertical displacements of the measurement volume to perform a complete survey of the measurement diameter. For the optical access, Laser-grade parallel windows with anti-reflection coating for wavelengths between 650 and 1000 nm are used. Hollow glass spheres of  $10 \mu\text{m}$  with a density of  $1100 \text{ kg} \cdot \text{m}^{-3}$  are used as seeding particles.

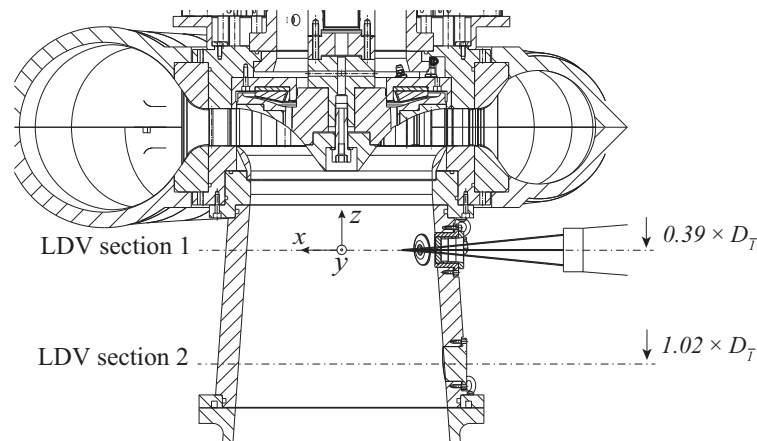


Figure 2.3: Vertical cut-view of the reduced scale model, with the streamwise position of the LDV measurement sections.

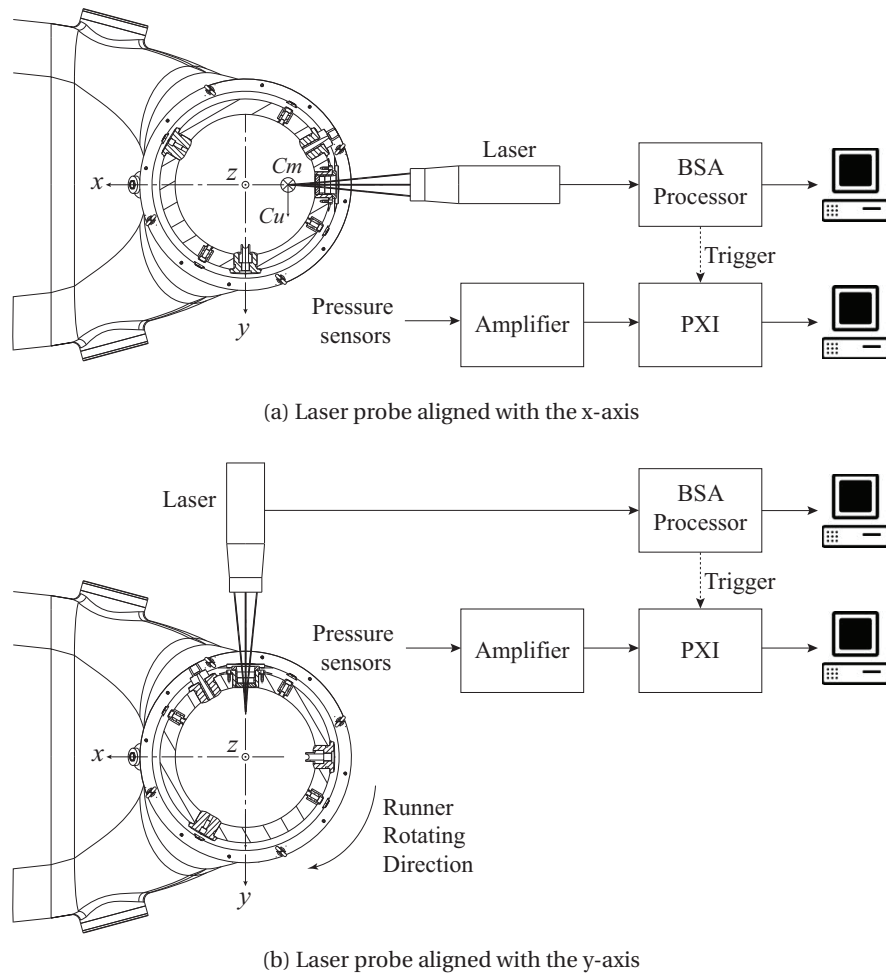


Figure 2.4: Experimental setup for the LDV measurements with the data acquisition flow chart. The LDV probe is set up in two different configurations, parallel and perpendicular to the feeding pipe of the machine.

### Measurement procedure

The flow velocity components  $C_m$  and  $C_u$  are measured along the axes  $x$  and  $y$  for both sections 1 and 2 by varying the radial position of the measurement volume with the traversing system. In the vicinity of the cone wall, the measurement volume is moved by steps of 1 mm and the LDV measurements are not synchronized with the wall pressure measurements. Beyond 10 mm from the cone wall, the flow velocity components are measured synchronously with the wall pressure measurements each 10 mm with an acquisition time of 180 s. An external trigger is provided by the BSA processor to ensure the synchronization between the LDV system and the wall pressure measurements. The setup and the acquisition chain for the LDV measurements are presented in Figure 2.4.

### 2.3.2 Particle Image Velocimetry

#### Measurement principle

Particle Image Velocimetry (PIV) is another type of non-intrusive optical technique for flow velocity measurements. It is based on the comparison between two consecutive images of the flow seeded with particles and illuminated by a double pulsed Laser sheet. An overview of the PIV technique is available in Raffel et al. [69]. The images are divided into a certain number of windows, called Interrogation Areas (IA). The average particle displacement vector is computed for each IA by a cross-correlation between the two consecutive images. As the time lag between the two consecutive images is known, the corresponding average particle velocity vector (in pixels/s) can be determined for each IA. By using a calibration image, the correspondence between the displacement in pixels and the displacement in meters can be determined, yielding finally a velocity vector map in the 2D-plane of the Laser sheet.

#### Particle Image Velocimetry set-up

In the present test-case, the 2D-velocity fields are measured in three different horizontal cross-sections of the draft tube cone. The reduced scale physical model installed on the PF3 test rig is presented in Figure 2.5, together with the setup for the PIV measurements. The measurement sections are situated respectively  $0.39 \times D_1$ ,  $0.75 \times D_1$  and  $1.02 \times D_1$  downstream the runner outlet, as illustrated in Figure 2.6. Their diameters are equal to  $1.05 \times D_1$ ,  $1.1 \times D_1$  and  $1.19 \times D_1$ , respectively. A second cone is used, featuring a flat waterbox and 4 pressure sensors distributed in two different cross-sections,  $0.39 \times D_1$  and  $1.02 \times D_1$  downstream the runner outlet.

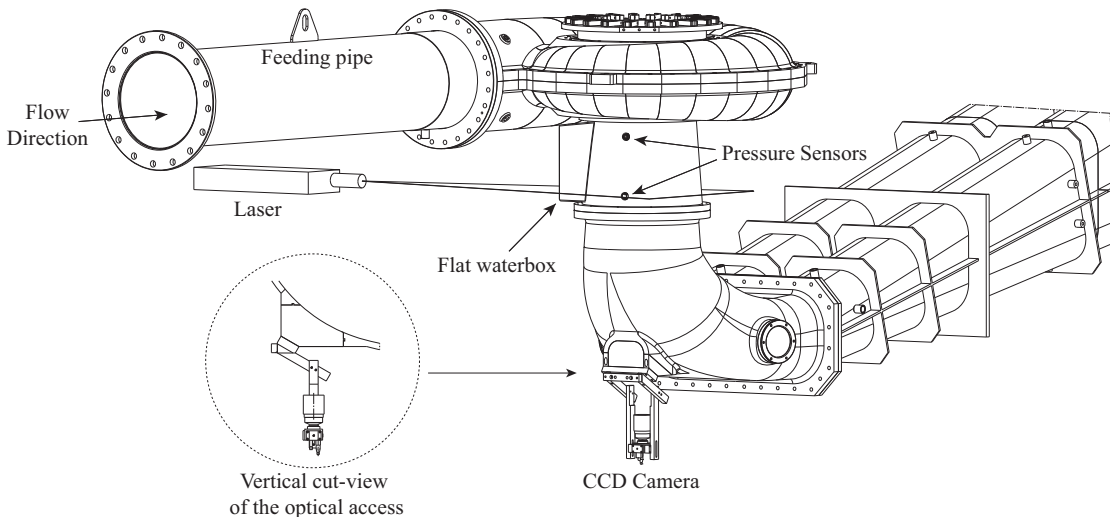


Figure 2.5: Experimental setup for the PIV measurements in horizontal cross-sections of the draft tube cone together with a cut-view of the optical access.

Table 2.2: Technical specifications of the PIV system.

<b>Laser</b>		
Wavelength		532 nm
Energy		200 mJ
Type		double-pulsed Nd:YAG laser
Model		Litron DualPower
<b>Camera</b>		
Resolution		2048 × 2048 pixels
Lens		60 mm
Filter		none
Model		Dantec FlowSense EO 4M

The Laser sheet of roughly 2 mm-thickness is generated by a double-pulsed Nd:YAG Laser and a cylindrical lens. The time interval between two consecutive pulses is adjusted according to the average axial velocity of the flow to limit the out of plane particle displacement to 1/10 of the laser sheet thickness (for instance,  $\Delta t = 75 \mu\text{s}$  for a discharge equal to  $Q = 0.320 \text{ m}^3 \cdot \text{s}^{-1}$  in measurement section 3). A flat waterbox is used to minimize the optical deformation of the laser sheet induced by the conical shape of the cone. The images are recorded by a CCD camera placed perpendicularly to the laser sheet at the bottom of the draft tube elbow. A curved Plexiglas window fitting the shape of the draft tube elbow is installed to provide an optical access for the camera. The latter is aligned with the coordinate system of the test rig to measure directly the velocity components  $C_x$  and  $C_y$  corresponding to this system. For the seeding particles, standard  $20 \mu\text{m}$  polyamide particles are used as the PIV measurements are performed in cavitation-free conditions. The specifications for the PIV system, including camera and Laser, are given in Table 2.2.

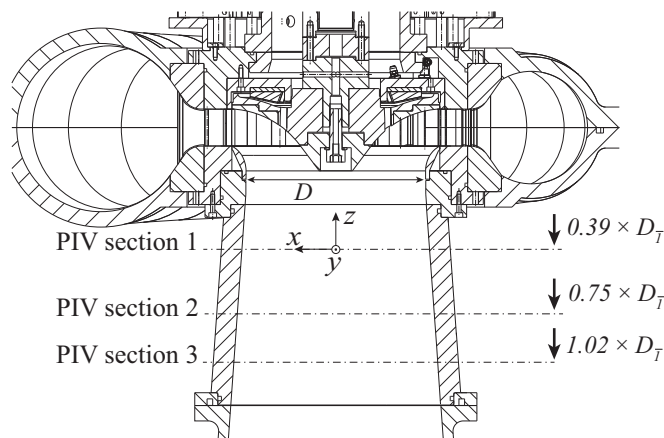


Figure 2.6: Side-view of the draft tube cone with the streamwise positions of the PIV measurement sections.

## Chapter 2. Test-case and Experimental set-up

---

The PIV system is set up in a second configuration to measure the axial velocity fields at the runner outlet in the meridional section of the draft tube cone. The Laser is mounted parallel to the upstream pipe, the Laser sheet intersecting vertically the draft tube cone. For this configuration, the optical access for the camera is provided by the flat waterbox.

### Calibration

The curved Plexiglass window used for the optical access during horizontal PIV measurements induces a very strong non-linear optical distortion. Consequently, particular attention must be paid to the calibration procedure. For each measurement section, a calibration image is taken with a circular dotted target, which covers exactly the measurement section. Moreover, the camera is placed on a support fixed on the draft tube elbow in order to preserve the position of the camera when the draft tube elbow is uninstalled for removing the calibration target. For the vertical PIV measurements, a trapezoidal dotted target is used, covering completely the meridional vertical section of the cone from  $0.39 \times D_1$  to  $1.02 \times D_1$  downstream the runner outlet.

### Measurement procedure

The primary objective of the PIV measurements is to recover properly the periodical behaviour of the velocity field over one precession period. For this purpose, a phase averaging procedure is performed by using a pressure signal measured in the cone as a reference (see Section 3.4.2). For the present test-case, the relative irregularity of the pressure signals does not permit to perform phase-locked PIV measurements. To overcome this problem, the possibility for the PIV system to deliver a continuous output voltage signal during the measurements is used. This signal, referred as the Q-switch voltage, features a peak each time the Laser releases a pair of pulses. Each peak corresponds therefore to the acquisition of one pair of images by the PIV system. For a given operating point, the PIV data are acquired continuously with a sampling frequency of 10 Hz, while the Q-switch voltage and the wall pressure signals are recorded synchronously with a sampling frequency of 1'000 Hz. For each operating point, a total of 10'000 pairs of images are acquired, corresponding to an acquisition time of 1'000 s for the pressure signal and the Q-switch voltage. An example of signals is shown in Figure 2.8 for a shortened sample.

### Image post-processing

Each image from the camera is first dewarped using a third order polynomial imaging model fit, based on the calibration described above. Instantaneous velocities are then obtained by applying an adaptative cross-correlation method to each dewarped image pair. It adapts the size and the shape of the interrogation areas (IA) to local seeding densities and flow gradients. The minimum size for the IA is set to  $16 \times 16$  pixels. Moreover, an universal outlier detection



### 2.3. Draft tube flow field investigation

algorithm is used in order to suppress the eventual outlier vectors produced by undesirable effects such as reflection or passage of gas bubbles through the Laser sheet. The algorithm replaces the outlier vectors by the the average of the neighboring vectors within a window of  $5 \times 5$  velocity vectors. Finally, it results in instantaneous velocity fields containing  $272 \times 241$  velocity vectors for the horizontal PIV measurements. The corresponding spatial resolution is equal to  $\Delta x = \Delta y = 1.54$  mm, 1.62 mm and 1.68 mm for the sections 1, 2 and 3 respectively.

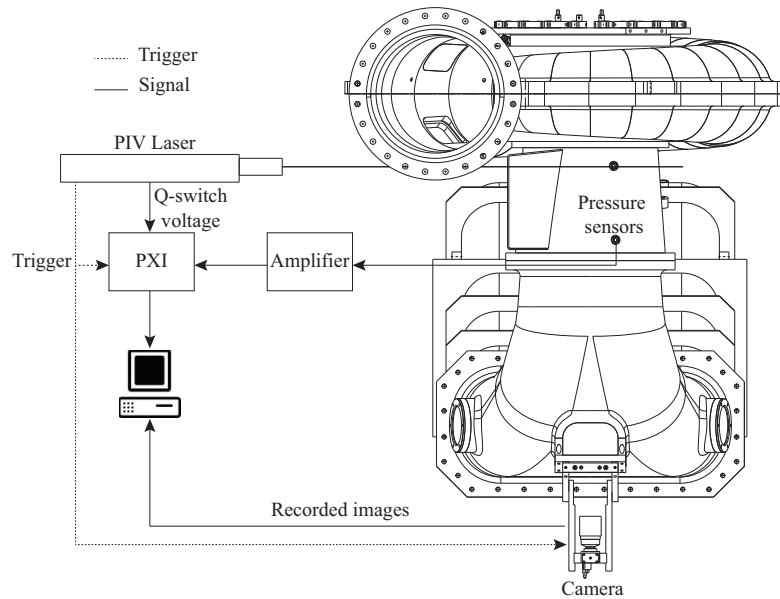


Figure 2.7: Upstream view of the reduced scale physical model, together with both PIV setup and PIV data acquisition flow chart.

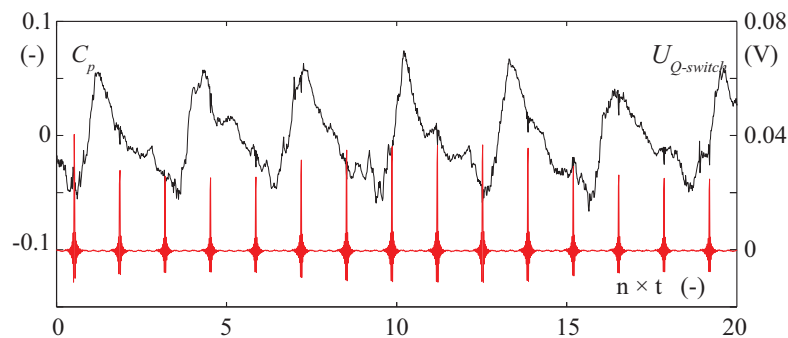


Figure 2.8: Wall pressure coefficient  $C_p$  measured in the draft tube cone (black solid line), together with the Q-switch voltage signal from the PIV Laser (red solid line).

## 2.4 Flow visualization

The cavitation precessing vortex rope is visualized in the draft tube cone by means of a high-speed camera. To limit the optical deformations induced by the conical surface of the cone wall, a flat waterbox is installed on the draft tube cone. An uniform LED screen is installed as a back light to provide a good contrast between the gaseous and the liquid phases. The technical specifications of the visualization equipment are given in Table 2.3. The images are acquired by the camera with a sampling frequency set at 1'000 Hz, which corresponds to the sampling frequency for the pressure signals acquisition. A trigger is provided by the camera to the NI-PXI device to synchronize the high-speed visualization and the dynamic wall pressure measurements. The setup for the high-speed visualization is presented in Figure 2.9, together with the acquisition chain. Examples of individual images of the cavitation vortex rope extracted from the same visualization are provided in Figure 2.10. The corresponding time history of two wall pressure coefficients  $C_p$  measured in the draft tube cone (positions C1N and C1S) is also given.

Table 2.3: Specifications for the visualization equipment.

<b>Camera</b>	
Model	Photron FastCam SA1.1
Maximum resolution	1024 × 1024 pixels
Maximum frame rate	675'000 fps
<b>LED screen</b>	
Model	PHLOX LEDW-BL-550X400-MSLLUB-Q-1R-24V
Dimension	550 × 400 mm

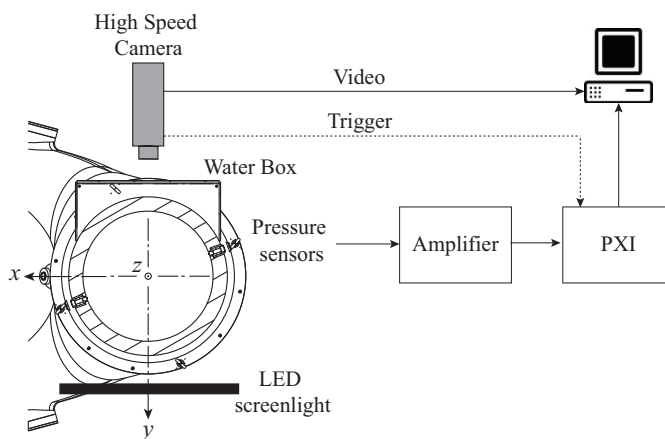
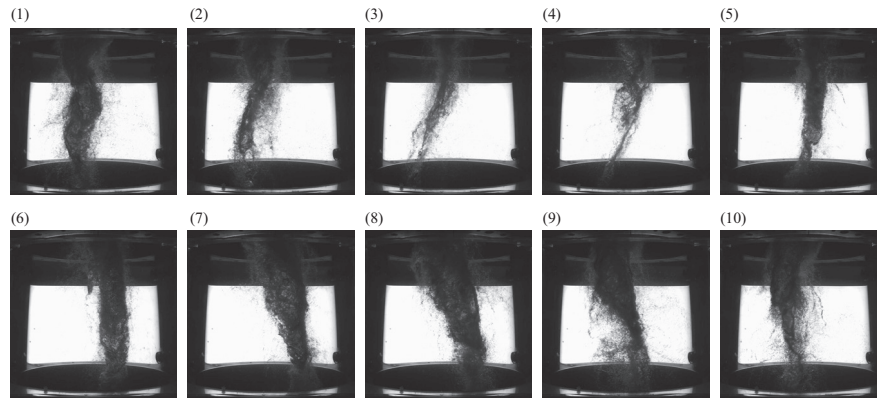
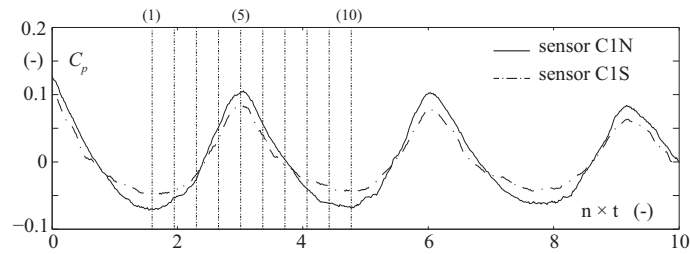


Figure 2.9: Setup for the high-speed visualizations of the cavitation vortex rope, together with the data flow between the high-speed camera and the PXI device.



(a) Snapshots of the cavitation vortex rope



(b) Corresponding wall pressure coefficients

Figure 2.10: Snapshots of the cavitation vortex rope at different instants of the same precession cycle, together with the corresponding time history of two wall pressure coefficients measured in the same cross-section of the draft tube cone (positions C1N and C1S) -  $Q_{ED} = 0.128$ ,  $\sigma = 0.17$  (resonance conditions).



# 3 Precessing vortex core in cavitation-free conditions

## 3.1 Introduction

At part load conditions, the flow at the runner outlet is characterized by its complex, turbulent and unsteady nature due to the development of the precessing vortex core wrapped around a recirculation zone in the draft tube [38]. The dynamics of the precessing vortex core in terms of precession frequency and structure strongly depend on the flow parameters, such as the Reynolds number and the swirl number, as shown in different engineering applications involving swirling flows [34, 45]. In the case of Francis turbines, a decrease of the flow discharge below the value at the BEP involves an increase of the tangential velocity component at the runner outlet, combined with a decrease of the axial velocity component, resulting in an increase of the swirl intensity. The influence of the flow discharge on the vortex core dynamics and the induced excitation source is not very well-documented and this chapter attempts to fill this gap.

For this purpose, the dynamics of the precessing vortex core are investigated in a wide range of part load operating conditions and a link between the intensity of the excitation source and the vortex dynamics is highlighted. The influence of the discharge factor on the vortex structure and the vortex parameters, such as the trajectory and the circulation, is studied by means of PIV. The measurements are carried out in cavitation-free conditions in order to suppress the influence of additional parameters linked to the two-phase flow. Indeed, cavitation development in the draft tube decreases the eigenfrequency values of the hydraulic system [54], leading to the risk of resonance [32]. Moreover, the onset of cavitation in the vortex core is inclined to influence the vortex dynamics and therefore the resulting excitation source.

Preliminary pressure fluctuation measurements are performed in the entire test rig in order to investigate the influence of the discharge factor on both the precession frequency and the amplitude of the pressure fluctuations. Based on these results, a distinction between three different flow regimes is made. The tangential flow field at the runner outlet is then investigated by means of PIV in three horizontal cross-sections of the draft tube cone for

different values of the discharge factor, for which a periodical pressure oscillation is observed. Based on the mean phase averaged velocity fields, the vortex parameters are determined for each value of the discharge factor. The axial flow field is also investigated at the runner outlet by PIV in a meridional cross-section section of the draft tube cone, in order to quantify the influence of the discharge factor on the axial recirculation zone and the swirl number of the flow.

## 3.2 Definition of the excitation source

The precession of the vortex core in the draft tube at part load conditions acts as an excitation source for the hydraulic circuit by inducing the propagation of synchronous pressure pulsations at the precession frequency. In one-dimensional hydro-acoustic models, the excitation is commonly modeled as a pressure source term in the axial momentum equation, which is defined by its amplitude, frequency and position in the draft tube [2, 53].

The exact physical mechanisms driving the excitation source remain unclear. However, Nishi et al. [65] showed that the presence of the elbow is the main cause for the establishment of synchronous pressure pulsations by comparing the pressure fluctuations induced by the precessing vortex core in elbowed and rectilinear draft tubes. Later, Fanelli [28] analytically confirmed these results. Two different mechanisms of excitation are highlighted, which only depend on the presence of the elbow. First, it is shown that the precession of the vortex core creates a periodical pressure difference between the inlet and outlet sections of the elbow. Finally, the flow is subject to flow separation at the intrados of the draft tube elbow, as observed in simple applications with elbowed pipe [76]. The precession of the vortex core in the elbow periodically distorts the flow separation zone area, giving rise to a periodical fluctuation of the pressure recovery  $\tilde{p}_{recov}(t)$  at the precession frequency in the diffuser.

The amplitude (or intensity) of the excitation source can therefore be defined as the amplitude of the pressure source term which is induced by the two effects described above.

## 3.3 Identification of flow regimes by pressure measurements

The discharge factor is first modified by steps of  $\Delta Q_{ED} = 0.05$  in cavitation-free conditions from 100 % to 50 % of the value  $Q_{ED}^*$  at the BEP. The speed factor  $n_{ED}$  is kept constant at the rated value of  $n_{ED} = 0.288$ . The runner frequency  $n$  and the hydraulic specific energy  $E$  are equal to  $n = 13.33$  Hz and  $E = 263$  J·kg<sup>-1</sup>, respectively. For each value of the discharge factor, pressure measurements are carried out in order to highlight the behaviour of both the precession frequency and the amplitude of the synchronous and convective pressure components. Oscillations at a distinct frequency equal to about  $0.25 \times n$  are observed in the pressure signals for  $Q_{ED} < 0.85 \times Q_{ED}^*$ . It indicates the development of a coherent precessing vortex core in the draft tube cone, inducing pressure fluctuations in the hydraulic system at the precession frequency. The time history of a wall pressure coefficient  $C_p$  measured in

### 3.3. Identification of flow regimes by pressure measurements

the upstream pipe (location P1) is given in Figure 3.1 for two different values of discharge factor,  $Q_{ED}/Q_{ED}^* = 0.9$  and  $Q_{ED}/Q_{ED}^* = 0.83$ , together with the corresponding auto-spectral density functions. The frequency is made dimensionless by the runner frequency  $n$  and the auto-spectral density functions are only represented in the range of frequency  $f/n = [0 - 0.8]$ , as the phenomenon of interest for the present test-case occurs at low frequencies.

For values of the discharge factor  $Q_{ED}/Q_{ED}^* > 0.85$ , the pressure signals are mainly dominated by random fluctuations, with no distinct periodical behavior. For values of the discharge factor  $Q_{ED}/Q_{ED}^* < 0.85$ , a distinct peak appears in the auto-spectrum at a low frequency equal to about  $0.25 \times n$ . In the following, the investigation will be focused on discharge factors between  $0.50 \times Q_{ED}^*$  and  $0.85 \times Q_{ED}^*$ , as the precessing vortex core does not occur beyond this range or it is not intense enough to induce clear periodical fluctuations in the pressure signal and thereby in the flow velocity signals.

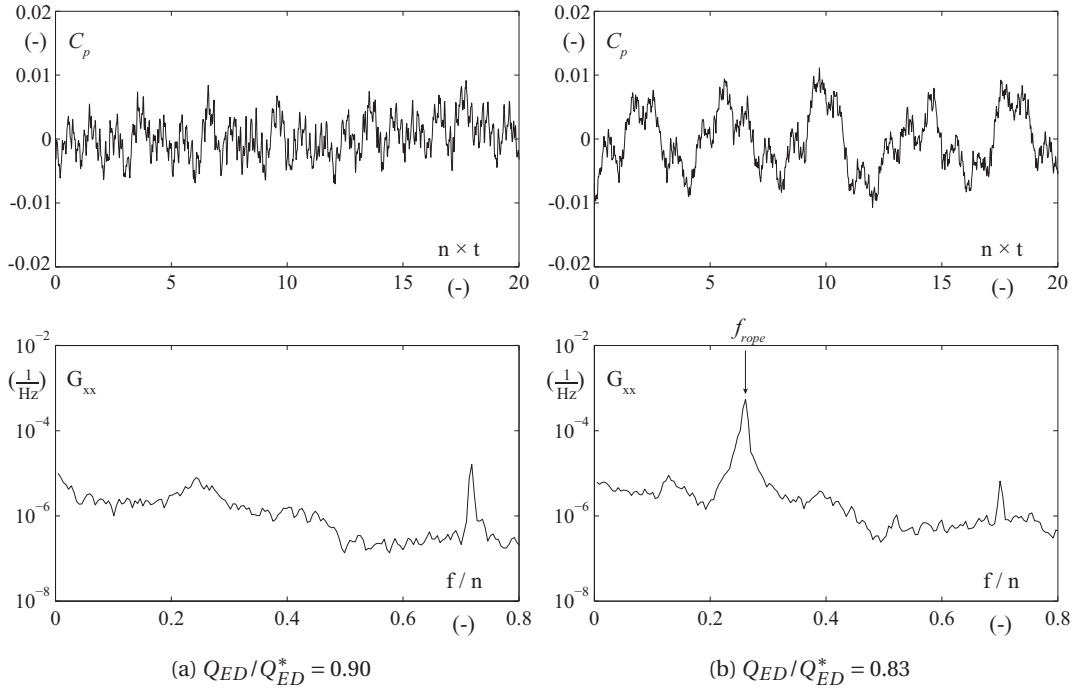


Figure 3.1: Auto-spectral density function of a pressure signal measured in the feeding pipe of the machine (position P1) for  $Q_{ED}/Q_{ED}^* = 0.9$  (left) and  $Q_{ED}/Q_{ED}^* = 0.83$  (right).

#### 3.3.1 Pressure fluctuations in the headwater connecting pipe

As the measurements are performed in cavitation-free conditions, it is assumed that the eigenfrequencies of the system are sufficiently high to avoid any amplification of the synchronous pressure component, which is identified as the hydro-acoustic response of the system, through resonance. Therefore, the influence of the discharge factor on the excitation intensity can

### Chapter 3. Precessing vortex core in cavitation-free conditions

be quantified by measuring pressure fluctuations directly in the headwater connecting pipe, where they are purely synchronous.

For values of the discharge factor between 85 % and 50 % of the value at the BEP, the precession frequency is determined by computing the auto-spectral density function of the pressure signal measured in the feeding pipe (location P1). The influence of the discharge factor on its value is given in Figure 3.2-a. The precession frequency is made dimensionless by the runner frequency  $n$ . The precession frequency is observed at the same value at the other locations of the test rig, including the diffuser. The amplitude at the precession frequency of the synchronous pressure fluctuations corresponds to the auto-spectral amplitude of the pressure signal measured in the upstream pipe. The influence of the discharge factor on its value is given in Figure 3.2-b. For both figures, the discharge factor is expressed as a fraction of the value at the BEP.

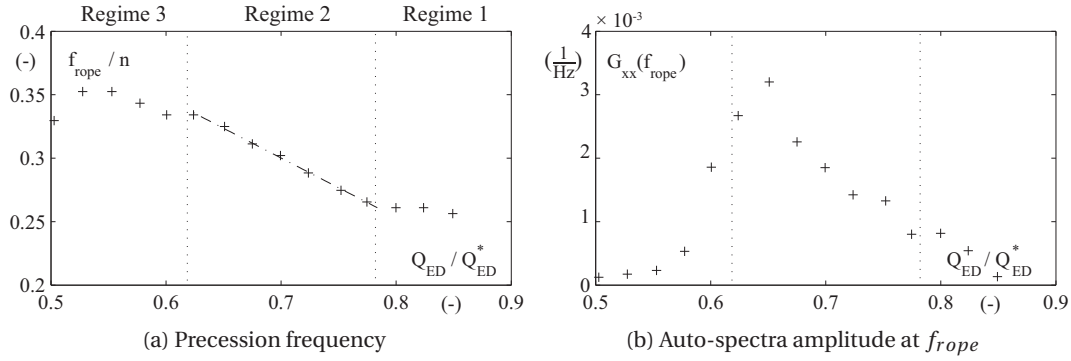


Figure 3.2: (a) Precession frequency made dimensionless by the runner frequency and (b) auto-spectral amplitude at the precession frequency as a function of the discharge factor. The pressure signal is measured in the feeding pipe (location P1).

According to the results presented in Figure 3.2, three different flow regimes are identified, characterized by different types of evolution for both the precession frequency and the pressure fluctuations amplitude. Within the first regime, i.e. for  $Q_{ED}$  values between 78 % and 85 % of the value at the BEP, the precession frequency remains quasi-constant and is equal to about  $0.26 \times n$ . The amplitude of the synchronous pressure fluctuations at this frequency increases when the discharge decreases. It remains however relatively low, indicating a weak excitation source. From 62 % to 78 % of the value at the BEP, the precession frequency increases linearly from  $0.26 \times n$  to  $0.34 \times n$  as the discharge decreases. In parallel, the amplitude of the pressure fluctuations increases and reaches its maximum at  $Q_{ED} = 0.65 \times Q_{ED}^*$ , which indicates a significant increase of the excitation source strength in this segment. Below the value  $Q_{ED} = 0.62 \times Q_{ED}^*$ , the results suggest that the dynamics of the precessing vortex rope is drastically modified. The precession frequency does not follow a particular law anymore and the amplitude of the pressure fluctuations swiftly decreases, indicating that the strength of the excitation source is significantly reduced.



### 3.3. Identification of flow regimes by pressure measurements

The time history of the pressure coefficient  $C_p$  measured in the feeding pipe (location P1) is given in Figure 3.3 for two different values of discharge factor,  $Q_{ED}/Q_{ED}^* = 0.65$  (Regime 2) and  $Q_{ED}/Q_{ED}^* = 0.58$  (Regime 3), together with the corresponding auto-spectral density functions. The pressure signal measured at  $Q_{ED}/Q_{ED}^* = 0.65$  features a well-defined periodical fluctuation at a distinct frequency equal to  $0.33 \times n$ , visible in the auto-spectral density function of the signal. This type of spectra is obtained for all the values of discharge factor between 62 % and 85 % of the value at the BEP. However, at  $Q_{ED} = 0.58 \times Q_{ED}^*$ , the energy at the precession frequency, equal to  $0.35 \times n$ , is spread over a broader range of frequencies, indicating a loss of periodicity in the pressure signal, and thereby in the flow structure.

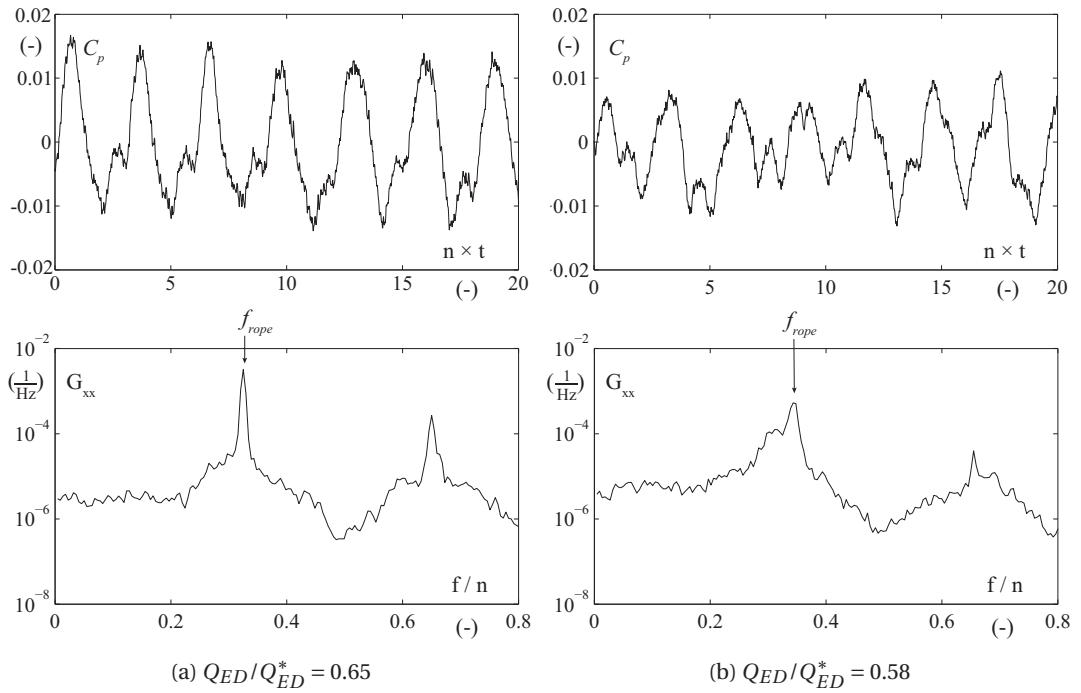


Figure 3.3: Auto-spectral density function of a pressure signal measured in the upstream pipe (position P1) for  $Q_{ED}/Q_{ED}^* = 0.65$  (left) and  $Q_{ED}/Q_{ED}^* = 0.58$  (right).

#### 3.3.2 Pressure fluctuations in the draft tube cone

The coherence between two pressure signals measured in the same cross-section of the draft tube cone is computed for each value of discharge factor [9]. The influence of the discharge factor on its value at the precession frequency is presented in Figure 3.4 for two pairs of pressure signals. It must be noticed that the precession frequency observed in the draft tube cone and in the headwater connecting pipes are identical. The coherence is almost equal to 1 in Regime 2 and suddenly falls when the value of the discharge factor is decreased below the value  $Q_{ED} = 0.62 \times Q_{ED}^*$ , confirming the transition of the unsteady behavior of the flow from a periodical nature to an increasingly stochastic nature.

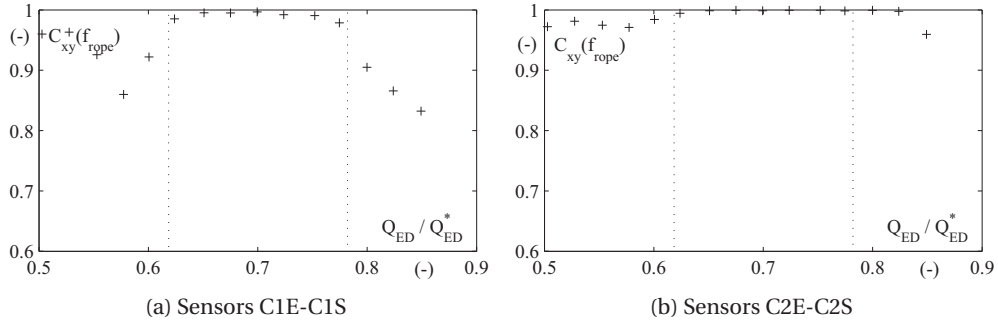


Figure 3.4: Coherence at the precession frequency between two pressure signals measured in the same cone cross-section as a function of the discharge factor.

Pressure fluctuations at the precession frequency in the draft tube cone can be decomposed into the convective and the synchronous components, respectively [20]. Four sensors located in the same cross-section of the draft tube cone and regularly spaced allow determining both components in the time domain, as demonstrated in Appendix D. Here, the decomposition is performed by using the pressure sensors located in the upper section of the draft tube cone (locations C1N, C1E, C1S, C1W),  $0.39 \times D_1$  downstream the runner outlet. For each value of the discharge factor, the synchronous component  $C_p^{syn}(t)$  is computed in the time domain by averaging the 4 pressure coefficients  $C_p^i(t)$  at each instant  $t$ :

$$C_p^{syn}(t) = \frac{1}{4} \sum_{i=1}^4 C_p^i(t) \quad (3.1)$$

with  $i = 1 \dots 4$  the index of the pressure sensors. For each pressure sensor  $i$ , the convective component  $C_p^{conv,i}(t)$  is then determined as following:

$$C_p^{conv,i}(t) = C_p^i(t) - C_p^{syn}(t) \quad (3.2)$$

The auto-spectral density function of both synchronous and convective components is computed. The influence of the discharge factor on its amplitude at the precession frequency is given for each component in Figure 3.5. The influence of the discharge factor on the amplitude of the synchronous component in the draft tube cone is similar to that observed for the amplitude of the pressure fluctuations measured in the feeding pipe. It is at its maximum for a discharge factor equal to  $Q_{ED} = 0.65 \times Q_{ED}^*$  and it quickly decreases after the transition between the regimes 2 and 3. The amplitude of the convective component follows a similar evolution, with a rise from  $Q_{ED} = 0.85 \times Q_{ED}^*$  to  $Q_{ED} = 0.65 \times Q_{ED}^*$  and a decrease below this

### 3.3. Identification of flow regimes by pressure measurements

point. It indicates a possible enlargement of the vortex rope trajectory when the value of the discharge factor is decreased within the regime 2.

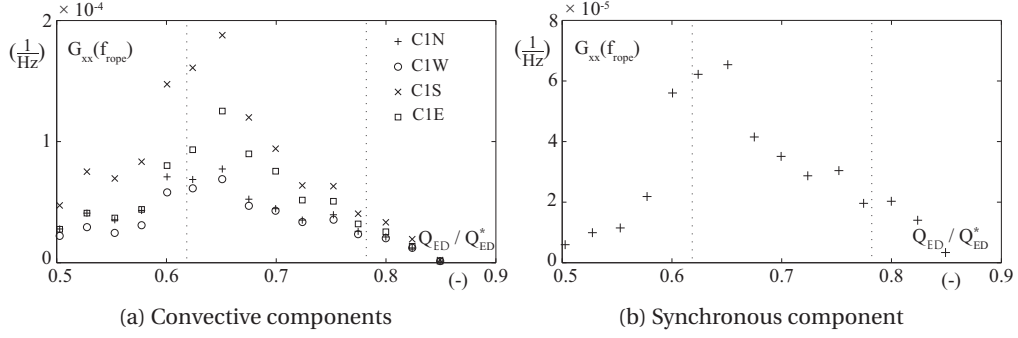


Figure 3.5: Amplitude of the auto-spectral density function at the precession frequency of both convective and synchronous pressure components (upper section of the cone) as a function of the discharge factor.

#### 3.3.3 Cavitation influence on the flow regimes

The pressure in the draft tube is now decreased by reducing the pressure over the free surface in the reservoir to promote the cavitation development and make the vortex core visible. The Thoma number is set to the value  $\sigma = 0.11$ , which corresponds to the prototype value for the present test-case. As previously, the value of the discharge factor is modified step by step from 100 % to 50 % of the value at the BEP. The influence of the discharge factor on the precession frequency and the coherence at the precession frequency between two pressure signals measured in the draft tube cone (C1S-C1E) is presented in Figure 3.6. The red points correspond to the operating points for which a visualization is provided in Figure 3.7. Similar flow regimes are observed in cavitation conditions, with however a slight shift. The regime 1, which is characterized by a constant precession frequency, continues to the point  $Q_{ED} = 0.75 \times Q_{ED}^*$  whereas the regime 2, for which the precession frequency evolves linearly with the discharge factor, is comprised between  $Q_{ED} = 0.85 \times Q_{ED}^*$  and  $Q_{ED} = 0.60 \times Q_{ED}^*$ . A sudden decrease in the coherence between the pressure signals is observed beyond the transition from regimes 2 to 3, similarly to what is observed in cavitation-free conditions.

Visualizations of the cavitation vortex rope are presented in Figure 3.7 for different values of the discharge factor, each one corresponding to a given flow regime. The cavitation volume observed in the regime 1 ( $Q_{ED} = 0.81 \times Q_{ED}^*$ ) is not very well-developed and its limits are poorly defined, while the precession motion of the vortex rope is weak. In the regime 2, represented by the visualization at  $Q_{ED} = 0.64 \times Q_{ED}^*$ , the limits of the cavitation vortex are well-defined and stable while the precession motion of the vortex rope is more important. After the transition from regimes 2 to 3, illustrated by the visualization at  $Q_{ED} = 0.55 \times Q_{ED}^*$ , the large cavity initially present within the limits of the vortex core has almost disappeared,

### Chapter 3. Precessing vortex core in cavitation-free conditions

confirming the loss of coherence in the flow structure and a strong decrease of the vortex strength.

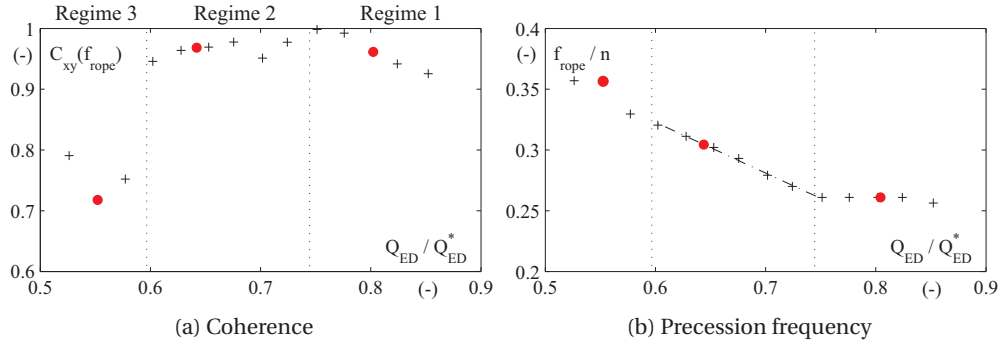


Figure 3.6: Influence of the discharge factor on both the coherence at the precession frequency between two pressure signals and the precession frequency. The pressure signals are measured in the draft tube cone (locations C1S-C1E) -  $\sigma = \sigma_{plant} = 0.11$ .

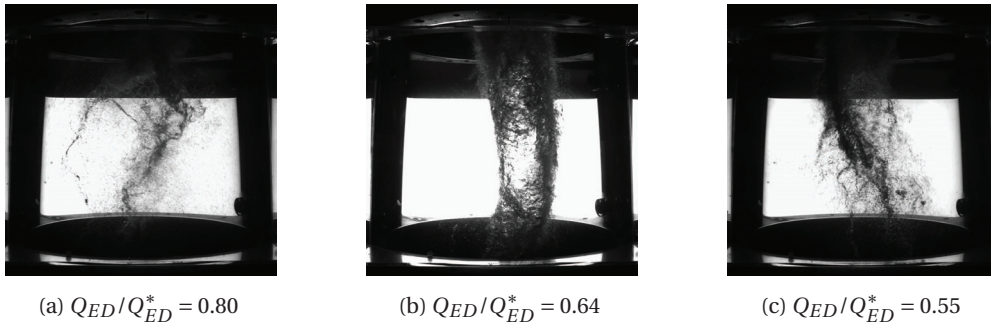


Figure 3.7: Visualizations of the cavitation vortex rope for different values of the discharge factor -  $\sigma = \sigma_{plant} = 0.11$ .

## 3.4 Methodology for PIV measurements

In this section, the methodology used for the post-processing of the PIV measurements is described, as well as a description of the investigated operating conditions.

### 3.4.1 Flow parameters

PIV measurements are performed in the draft tube cone to measure both tangential and axial velocity fields at different values of the discharge factor for which an oscillation is observed in the pressure signals, confirming the development of a precessing vortex core in the draft tube cone. The parameters of the investigated operating conditions are summarized in Table

### 3.4. Methodology for PIV measurements

3.1. The point 1 corresponds to the flow regime 1, the points from 2 to 5 correspond to the regime 2 and the points 6 and 7 correspond to the regime 3. As mentioned previously, the precessing vortex core tends to lose its coherence after the transition from flow regimes 2 to 3 ( $Q_{ED}/Q_{ED}^* < 0.62$ ), resulting in a loss of periodicity in the flow structure and thereby in the pressure signals. This effect is particularly important for the operating point  $Q_{ED}/Q_{ED}^* = 0.55$ , making the achievement of a reliable phase averaging for the velocity fields impossible.

Table 3.1: List of the operating points investigated by PIV.

Point	$Q_{ED}$ (-)	$Q$ ( $m^3 \cdot s^{-1}$ )	$Q_{ED}/Q_{ED}^*$ (-)	$Re$ (-)	Regime
1	0.161	0.320	0.81	$1.11 \times 10^6$	1
2	0.155	0.308	0.78	$1.07 \times 10^6$	2
3	0.145	0.288	0.74	$1.00 \times 10^6$	2
4	0.135	0.268	0.68	$0.93 \times 10^6$	2
5	0.128	0.255	0.64	$0.89 \times 10^6$	2
6	0.12	0.239	0.60	$0.83 \times 10^6$	3
7	0.11	0.219	0.55	$0.76 \times 10^6$	3

The only parameter modified during this investigation is the flow discharge. However, it is expected that a change of the discharge value strongly influences the dynamics of the precessing vortex core. Indeed, a decrease of the flow discharge at a fixed speed factor  $n_{ED}$  leads to a decrease of the axial velocity  $Cm_{\bar{1}}$  and an increase of the tangential velocity  $Cu_{\bar{1}}$  at the runner outlet. It results in an increase of the swirl intensity, which is the main driving parameter for the development of the precessing vortex rope. The swirl intensity is commonly characterized by a dimensionless number, the swirl number  $S$ , which is defined by Gupta et al. [38] as the ratio between the axial flux of angular momentum  $G_{\theta}$  and the axial flux of axial momentum  $G_z$ :

$$S = \frac{G_{\theta}}{G_z R} = \frac{\int_0^R \rho \cdot Cm \cdot Cu \cdot r^2 dr}{R \int_0^R \rho \cdot Cm^2 \cdot r \cdot dr} \quad (3.3)$$

In the previous expression, the turbulent stress and pressure terms have been omitted, as they are difficult to obtain. The swirl number will be evaluated by using the time-averaged axial and tangential velocity profiles obtained by PIV measurements. In terms of turbulence, a modification of the discharge value alters also the Reynolds number, which is defined in the present test-case by:

$$Re = \frac{Cq_{\bar{1}} D_{\bar{1}}}{\mu} = \frac{4Q}{\pi D_{\bar{1}} v} \quad (3.4)$$

with  $\nu$  the kinematic viscosity and  $Cq_1$  the average axial velocity computed at the runner outlet. For the investigated operating conditions, the Reynolds number is in the order of  $10^6$  (Table 3.1), indicating a fully developed turbulent flow in the draft tube cone. Therefore, it is assumed that the precession frequency and the pressure fluctuations amplitude are independent of viscous effects, as reported by Cassidy and Falvey [14]. More recently, Ingvorsen et al. [45] confirmed this in the case of a model of a two-stroke engine.

#### 3.4.2 Mean phase averaging

##### Phase averaging for the pressure signals

At part load conditions, the velocity fields in the draft tube cone and the pressures feature a well-defined periodical behaviour at the precession frequency. Therefore, the corresponding velocity and pressure signals can be decomposed as [70]:

$$C(\mathbf{x}, t) = \bar{C}(\mathbf{x}) + \tilde{C}(\mathbf{x}, t) + C'(\mathbf{x}, t) \quad (3.5)$$

$$p(\mathbf{x}, t) = \bar{p}(\mathbf{x}) + \tilde{p}(\mathbf{x}, t) + p'(\mathbf{x}, t) \quad (3.6)$$

where  $\bar{C}(\mathbf{x})$  and  $\bar{p}(\mathbf{x})$  are the time-average values of the velocity and pressure at a given spatial position  $\mathbf{x}$ ,  $\tilde{C}(\mathbf{x}, t)$  and  $\tilde{p}(\mathbf{x}, t)$  the pure periodical components and  $C'(\mathbf{x}, t)$  and  $p'(\mathbf{x}, t)$  the incoherent fluctuations due to the turbulent background noise. Small variations of the period and the fluctuations amplitude are observed from one precession cycle to another, as the vortex rope precession does not have a purely deterministic nature and can experience variations between cycles. The possible reasons are the random flow component induced by the fully-developed turbulence and the potential fluctuations generated by the test rig control (runner and pump speeds). However, the periodical component of both pressure and velocity signals can be extracted by using a mean phase averaging. For this purpose, the different individual precession cycles are identified in a reference pressure signal. The latter is first low-pass filtered and the individual precession cycles are identified through their minimum values, corresponding to the passage of the vortex rope in the vicinity of the pressure sensor. The different precession cycles are then superimposed in the same period  $[0, 2\pi]$ , which is divided into a certain number of windows. Typically, a number of windows equal to 90 is used, each one corresponding to  $4^\circ$  of the precession cycle. All the pressure samples corresponding to the same phase window are averaged together to obtain the mean pressure value for this phase window. The different steps of the mean phase averaging procedure are presented in Figure 3.8, which includes the raw reference pressure signal, the corresponding filtered pressure signal and finally the mean phase averaged signal. The large phase difference observed between the

signals in Figures 3.8-a and 3.8-b is induced by the filtering but it does not affect the mean phase averaging.

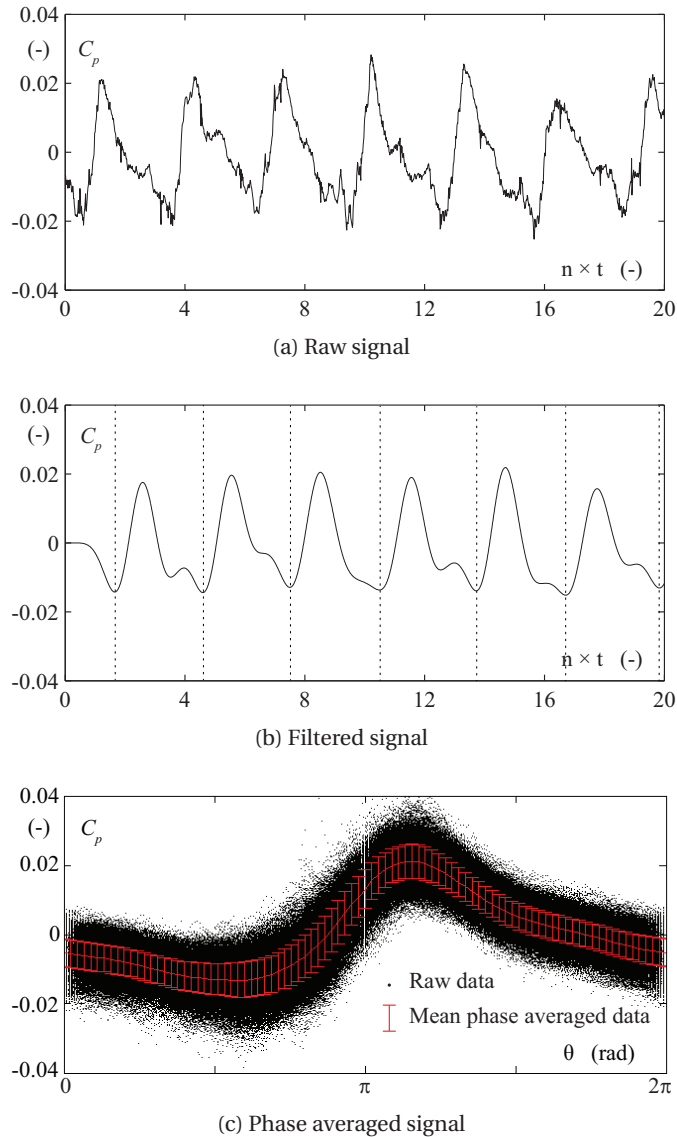


Figure 3.8: Mean phase averaging of a wall pressure signal measured in the draft tube cone (location C1N). A total number of 4400 precession cycles was used for the calculation.

The mean phase averaging of pressure signals was applied in a case of a self-excited cavitation vortex rope observed at full load conditions [60, 62]. In this research work, the different pressure cycles are isolated by defining an analytical signal  $z(t)$  whose argument is interpreted as the instantaneous phase of the pressure signal [9]. It permits to identify the passage from one cycle to another. In the present study, this method provides similar results to those obtained with the method based on the minimum pressure level.

Phase averaging for the velocity fields

Contrary to LDV, the PIV technique does not allow for continuous measurements of the flow velocity components with a sampling frequency sufficiently high to capture the periodical fluctuations, as the maximum sampling frequency is equal to 10 Hz for the used system. To overcome this problem, different authors [61, 58] performed phase-locked PIV measurements by triggering directly the PIV acquisition with the level of a reference pressure signal. In this configuration, the PIV system acquires a pair of images at each moment for which the reference pressure signal is at a given level. The instantaneous velocity fields corresponding to the same pressure level are then averaged together. However, this methodology does not permit to take into account the variations of the period length and the pressure fluctuations amplitude from one cycle to another.

In the present study, the voltage of the internal trigger of the PIV system (Q-switch) is used to determine a unique time stamp for each recorded pair of images, which later enables the phase averaging. Hence, each voltage peak in Figure 3.9 corresponds to a PIV acquisition. For a given operating point, the PIV data are acquired continuously with a sampling frequency of 10 Hz, while the Q-switch voltage and the pressure signals are recorded synchronously with a sampling frequency of 1'000 Hz. For each operating point, a total of 10'000 pairs of images are acquired. An example of signals is shown in Figure 3.9 for a shortened sample.

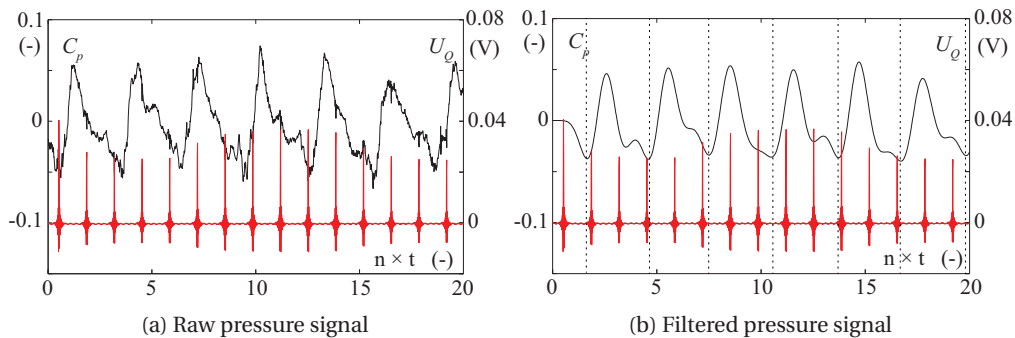


Figure 3.9: Reference pressure signal (black solid line) and voltage signal from Q-switch laser (red solid line). The limits of the successive precession cycles are indicated by the dashed black line in the right-handed figure.

To compute the mean phase averaged velocity fields, a reference pressure signal measured in the draft tube cone  $0.39 \times D$  downstream the runner outlet is used. After applying a low-pass filter to the pressure signal, the different precession cycles are easily defined by the position of the local pressure minima. Each cycle, corresponding to a period of  $2\pi$ , is then divided into 90 phase windows of  $2\pi/90$  ( $4^\circ$ ) width. The velocity fields measured inside a given phase window over the entire acquisition time, identified by the corresponding Q-switch voltage peaks, are then averaged together. This results in 90 mean phase averaged velocity fields, representing the flow behaviour over one typical precession period. As the distribution of



### 3.4. Methodology for PIV measurements

the pairs of images in the different phase windows is random, the number of instantaneous velocity fields averaged for a given phase window typically varies from 90 to 120.

The statistical convergence of the final velocity fields is checked by investigating the influence of the number of averaged instantaneous velocity fields  $N_f$  on the value of the velocity components  $C_x$  and  $C_y$ . Two examples are presented in Figures 3.10 and 3.11 for two given spatial positions situated in the PIV measurement section 3,  $(x_1, y_1) = (R/4, -R/2)$  and  $(x_2, y_2) = (-R/8, 3R/8)$ , where  $R$  is the section radius. The point  $(x_1, y_1)$  is situated within the boundaries of the vortex core whereas the point  $(x_2, y_2)$  corresponds to the zone of irrotational flow. It is checked that 90 instantaneous velocity fields are sufficient to reach a satisfactory statistical convergence of the velocity components.

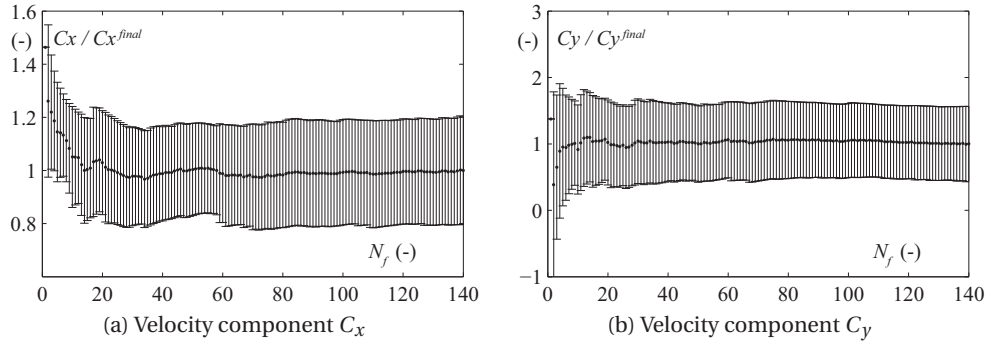


Figure 3.10: Influence of the number of instantaneous velocity fields used for the mean phase averaging on the value of the velocity components  $C_x$  and  $C_y$  at the spatial position  $(x, y) = (R/4, -R/2)$  (section 3).

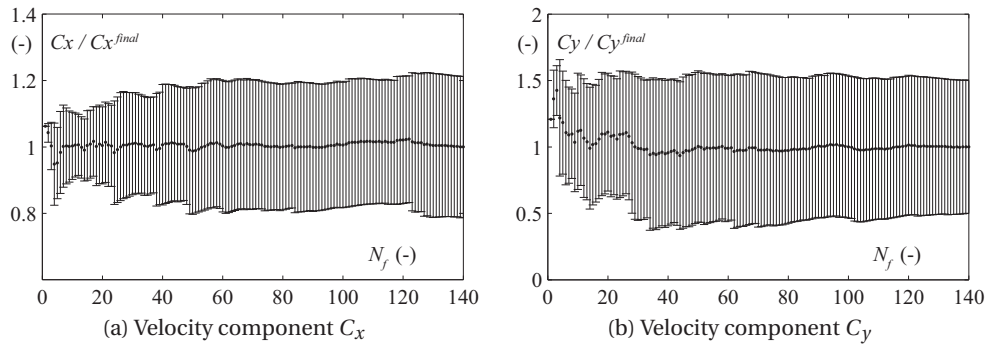


Figure 3.11: Influence of the number of instantaneous velocity fields used for the mean phase averaging on the value of the velocity components  $C_x$  and  $C_y$  at the spatial position  $(x, y) = (-R/8, 3R/8)$  (section 3).

An example of one instantaneous velocity field is given in Figure 3.12, together with the corresponding phase averaged velocity field. Here, only a small fraction of the measurement

### Chapter 3. Precessing vortex core in cavitation-free conditions

section is represented in order to visualize the centre of the vortex. It can be noticed that the position of the vortex centre in the instantaneous velocity field does not exactly correspond to the one in the mean phase averaged velocity field. The dispersion of the vortex centre position due to the irregularity of the vortex precession will be discussed in Section 3.5.

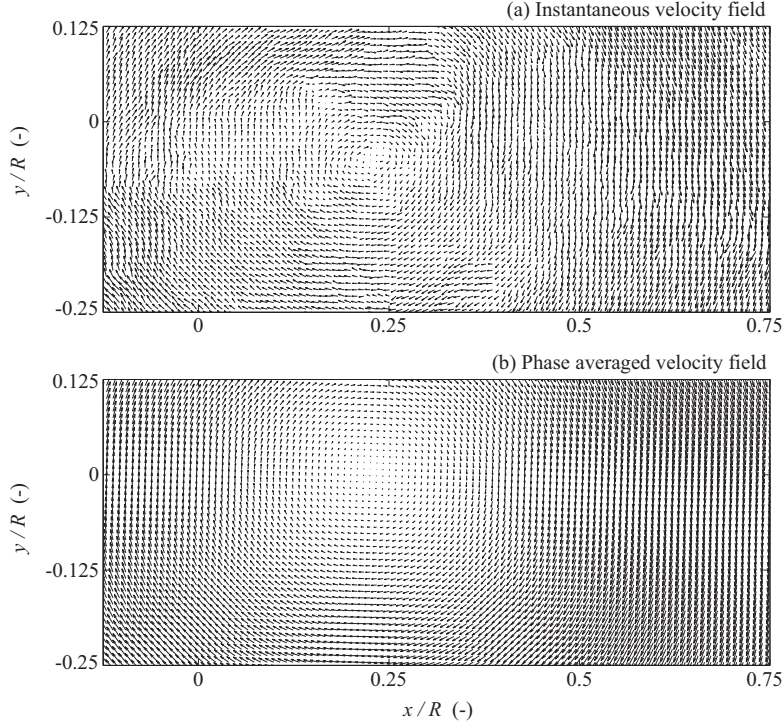


Figure 3.12: Example of one instantaneous velocity field, together with the corresponding phase averaged velocity field for the relative phase  $\theta = 10\pi/6$  of the precession period.

#### Fourier series decomposition

The procedure of mean phase averaging is supposed to extract the periodical component of the velocity fields. However, a residue of noise remains in the final velocity fields. Therefore, a pure filter is applied to the evolution of each phase averaged velocity component with the phase by using a Fourier series decomposition. For a given spatial position  $\mathbf{x}$ , the Fourier series decomposition of the velocity component  $Cy$  (or  $Cx$ ) can be expressed as:

$$Cy(\mathbf{x}, t) = \sum_{n=1}^N A_n \cos(2\pi \cdot f_{\text{rope}} \cdot n \cdot t + \theta_n) \quad (3.7)$$

with  $A_n$  and  $\theta_n$  the amplitude and the phase of the  $n^{\text{th}}$  harmonics, respectively. They can be

computed as following [9]:

$$\begin{aligned} A_n &= \sqrt{a_n^2 + b_n^2} \\ \theta_n &= \arctan(b_n / a_n) \end{aligned} \quad (3.8)$$

where the coefficient  $a_n$  and  $b_n$  are given by:

$$\begin{aligned} a_n &= \frac{2}{T_{rope}} \int_0^{T_{rope}} Cy(t) \cdot \cos(2\pi \cdot n \cdot f_{rope} t) \cdot dt \\ b_n &= \frac{2}{T_{rope}} \int_0^{T_{rope}} Cy(t) \cdot \sin(2\pi \cdot n \cdot f_{rope} t) \cdot dt \end{aligned} \quad (3.9)$$

$T_{rope}$  and  $f_{rope}$  correspond to the mean precession period and frequency, respectively. They are obtained by averaging the length of all the different precession cycles identified during the procedure of phase averaging. The evolution of the mean phase averaged velocity components with respect to the phase of the precession cycle is replaced by their Fourier series decomposition by computing the coefficients  $a_n$  and  $b_n$  for a given number of harmonics. The number of harmonics is limited to  $N = 3$ , as it is sufficient to neglect the contribution of the higher-order harmonics. A comparison between the direct experimental results and those obtained after applying the truncated Fourier series decomposition is presented in Figure 3.13 for the profile of the velocity component  $Cy$  along the axis  $x$  and its evolution with the phase at the spatial position  $(x, y) = (0, 0)$ .

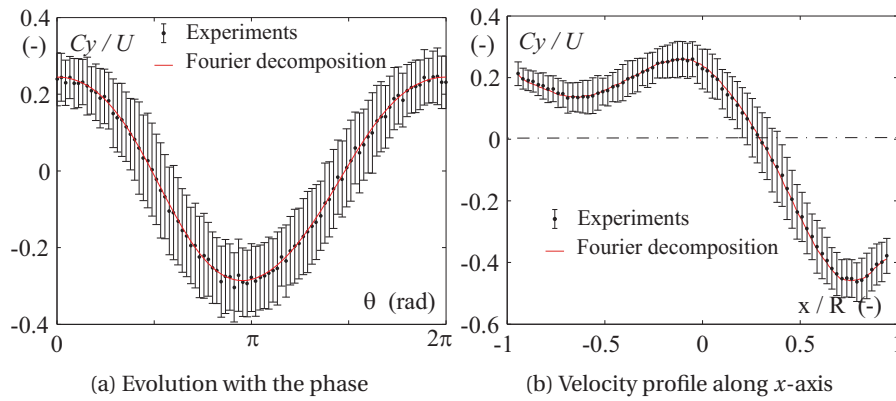


Figure 3.13: Comparison between the direct experimental results and those obtained by applying a truncated Fourier series decomposition for the velocity component  $Cy$ .

Martinelli et al. [58] similarly found that the contribution of the higher-order harmonics are negligible, by fitting the power density function of velocity components measured by means of LDV survey with an analytical expression. In the following, the velocity fields obtained after applying the Fourier series decomposition are used to describe the dynamics of the precessing vortex core and to determine its parameters, such as the vortex circulation and vortex trajectory.

#### 3.4.3 Vortex parameters

This section described the different post-processing methods used for the extraction of the main vortex characteristics, such as the vortex centre, the vortex core limits and the circulation.

##### Determination of the vortex centre

Large-scale vortical structures can be identified by different techniques. For instance, the vorticity is a good and common indicator for the presence of vortices. However, in complex flows, a region of high vorticity does not necessary feature a swirling motion, as a region of strong shear can also exhibit a high vorticity. Alternatively, Jeong and Hussain [48] gave a definition of a vortex by introducing the  $\lambda_2$ -criterion, which is based on the computation of velocity gradients. The scalar  $\lambda_2$  corresponds to the second largest eigenvalues of the tensor  $S^2 + \Omega^2$ , with  $S$  the strain tensor and  $\Omega$  the vorticity tensor. The vortex core is identified as the region featuring negative values of the scalar  $\lambda_2$ . The  $\lambda_2$ -criterion has been used by several researchers for the detection of the precessing vortex core, as Martinelli et al. [58] and Cala et al. [13].

However, in the case of a highly turbulent flow, the techniques based on velocity gradients computation are not really well-adapted for the detection of the vortex centre in the case of an instantaneous velocity field. Graftieaux et al. [36] proposed an algorithm to identify the vortex centre without computing any velocity gradients. They introduced a dimensionless scalar  $\gamma_1$  which is defined at a position  $P$  for a velocity field sampled at discrete spatial locations by:

$$\gamma_1(P) = \frac{1}{N} \sum_S \frac{(\vec{P}\vec{M} \wedge \vec{C}(M)) \cdot z}{\|\vec{P}\vec{M}\| \cdot \|\vec{C}(M)\|} \quad (3.10)$$

where  $S$  is an arbitrary rectangular domain of fixed size surrounding the point  $P$ ,  $M$  a point inside the domain  $S$  and  $N$  the number of points inside  $S$ .  $\vec{C}(M)$  is the velocity vector in the  $(x, y)$ -plane and  $z$  the unit vector normal to the  $(x, y)$ -plane. The symbols  $\wedge$  and  $\cdot$  correspond to the cross product and the scalar product, respectively. The authors showed that in the case of an ideal axi-symmetrical vortex, the scalar  $\gamma_1$  reaches its maximum equal to 1 at the vortex centre. In the general case, the vortex centre lies at the location where the scalar  $\gamma_1$  is at its

maximum, which is typically comprised between 0.9 and 1. As the vortex centre does not necessary lie on a measurement grid node, the spatial resolution is first increased by a cubic spline interpolation applied for both velocity components  $C_x$  and  $C_y$ . The criterion proposed by Graftieaux et al. [36] is a robust way to detect the swirl centre and has been successfully applied by Dreyer et al. [22] for the detection of the tip leakage vortex centre and the correction of the vortex axis wandering.

An example of one instantaneous velocity field is given in Figure 3.14, together with the corresponding values of the scalar  $\gamma_1$ . Here, a window of  $20 \times 20$  velocity vectors centered on a given point  $P$  is used to computed the value of  $\gamma_1$  at this point. It has been checked that increasing the window size does not change the results. The same type of results are given for the corresponding phase averaged velocity field in Figure 3.15. Only a limited part of the measurement section, centered on the vortex centre, is plotted in these figures.

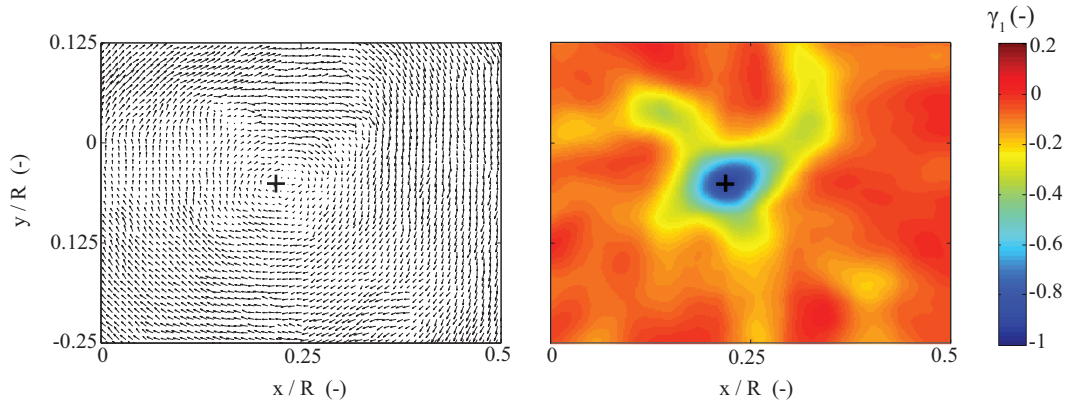


Figure 3.14: Instantaneous velocity field centered on the vortex centre, together with the corresponding  $\gamma_1$  values computed with the definition given by Graftieaux et al. [36]

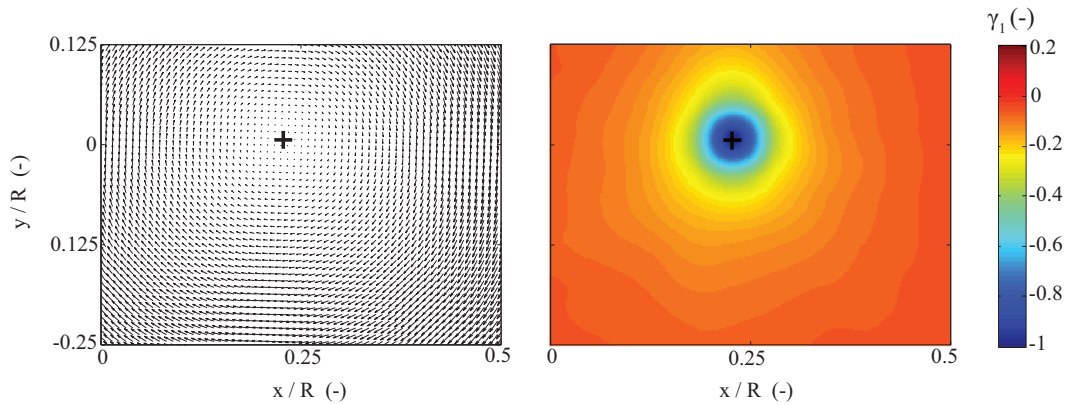


Figure 3.15: Mean phase averaged velocity field centered on the vortex centre, together with the corresponding  $\gamma_1$  values computed with the definition given by Graftieaux et al. [36]. The corresponding phase is equal to  $\theta = 8\pi/5$ .

### Chapter 3. Precessing vortex core in cavitation-free conditions

The  $\gamma_1$ -criterion identifies the swirling centre fairly well in both cases. The vortex centre is determined for all the instantaneous velocity fields by applying the  $\gamma_1$ -criterion, as well as for the mean phase averaged velocity fields, in order to determine the average trajectory of the vortex centre during one precession cycle and its corresponding dispersion. An example of distribution of the vortex centre position in the  $(x, y)$ -plane is given in Figure 3.16, together with the corresponding average trajectory.

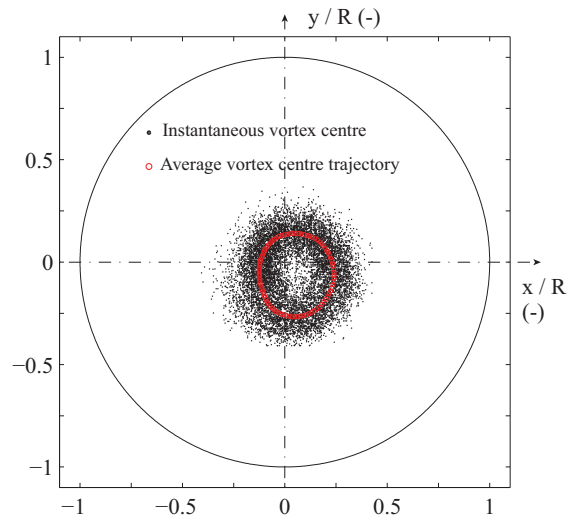


Figure 3.16: Average trajectory of the vortex centre (red o-markers), together with the distribution of the instantaneous vortex centres (black point markers), in the PIV measurement section 1 ( $Q_{ED} = 0.128$ ).

#### Determination of the vortex circulation

The precessing vortex core is composed of two different zones: the vortex core, surrounding the vortex centre and characterized by a strong vorticity, and the surrounding zone in which the flow is quasi-irrotational. In the case of an axi-symmetric vortex, the experimental velocity profiles of the vortex can be fitted with simple vortex models, permitting to extract the vortex characteristics such as the vortex intensity. Dreyer [21] gave a small review of the different vortex models available in the literature and used the vortex model proposed by Vatistas et al. [78], which is able to reproduce a wide range of velocity profiles by changing a shape parameter. In the case of a precessing vortex core in Francis turbine draft tubes, Susan-Resiga et al. [74] modeled the mean swirling flow at the runner outlet by three elementary vortices, whose parameters are identified on the basis of time-averaged velocity profiles measured experimentally. However, the unsteady effects caused by the precession of the vortex are not taken into account and the resulting parameters of the vortices do not represent the instantaneous characteristics of the precessing vortex core.

For the present study, the structure of the vortex features a strong asymmetry, making the use of simple analytical vortex models impossible for the identification of the vortex characteristics, such as the vortex core radius and the vortex circulation. However, the vortex circulation can be computed via the normal component of the vorticity  $\omega_z = \frac{\partial C_y}{\partial x} - \frac{\partial C_x}{\partial y}$ . The latter is computed by direct derivation of the velocity components ( $C_x, C_y$ ) by using a 5-point stencil numerical scheme. The vorticity at a given spatial measurement node  $(x_i, y_j)$  is given by [69]:

$$\omega_z(x_i, y_j) = \frac{1}{12\Delta x}(-Cy(x_{i+2}, y_j) + 8Cy(x_{i+1}, y_j) - 8Cy(x_{i-1}, y_j) + Cy(x_{i-2}, y_j)) - \frac{1}{12\Delta y}(-Cx(x_i, y_{j+2}) + 8Cx(x_i, y_{j+1}) - 8Cx(x_i, y_{j-1}) + Cx(x_i, y_{j-2})) \quad (3.11)$$

where  $\Delta x$  and  $\Delta y$  are the spatial resolutions for the coordinates  $x$  and  $y$ , respectively. Spline cubic interpolation is first applied to the velocity field and the vortex circulation is then computed by integrating the normal component of the vorticity within the limits of the vortex core:

$$\Gamma = \oint_{\mathcal{C}} \vec{C} \cdot d\vec{l} = \int_S \vec{\omega} \cdot z dS = \int_S \omega_z \cdot dS \quad (3.12)$$

where  $\mathcal{C}$  and  $S$  represent the contour and the surface of the vortex core, respectively. Accordingly, the limits of the vortex core must be defined properly. Graftieaux et al. [36] proposed a second algorithm for the detection of the boundaries of large-scale vortices, which considers only the topology of the velocity field. They introduced another scalar  $\gamma_2$  defined as:

$$\gamma_2(P) = \frac{1}{N} \sum_S \frac{(\vec{P}\vec{M} \wedge (\vec{C}(M) - \vec{C}(P))) \cdot z}{\|\vec{P}\vec{M}\| \cdot \|\vec{C}(M) - \vec{C}(P)\|} \quad (3.13)$$

where  $\vec{C}(P)$  is the average velocity vector within the domain  $S$ . Graftieaux et al. [36] showed that when the scalar  $|\gamma_2|$  is greater than  $2/\pi$ , the flow is locally dominated by the rotating motion, corresponding to the vortex core zone. An example of results for the computation of the scalar  $\gamma_2$  is given in Figure 3.17 for one instantaneous velocity field and the corresponding phase averaged velocity field. The scalar  $\gamma_2$  is not defined in the entire measurement section as it is computed at a given spatial position  $P$  by using a window of  $50 \times 50$  velocity vectors surrounding the point  $P$ . The limits of the vortex core are not well defined in the case of the instantaneous velocity field because of the presence of a turbulent background noise, unlike the phase averaged velocity field for which the vortex core limits can be properly determined. The magnitude of one phase averaged velocity field is given in Figure 3.18, together with the

### Chapter 3. Precessing vortex core in cavitation-free conditions

corresponding vorticity values and the limits of the vortex core (indicated by the black solid contour). To verify the accuracy of the vortex circulation computation by surface integration of the vorticity, the curvilinear integration of the tangential velocity along the vortex core limits is also implemented. Without further proof, the difference between both results does not exceed 0.15 % of the value obtained by surface integration in the measurement section 1 and 0.2 % in the measurement section 2.

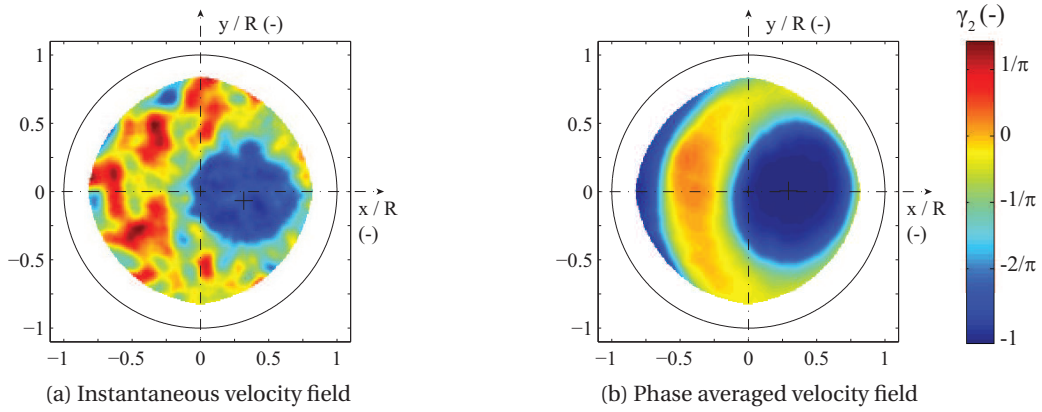


Figure 3.17: Scalar  $\gamma_2$  computed with the definition of Graftieaux et al. [36] for one instantaneous velocity field and the corresponding phase averaged velocity field at the phase  $\theta = \pi/10$ . ( $Q_{ED} = 0.128$ , PIV measurement section 3).

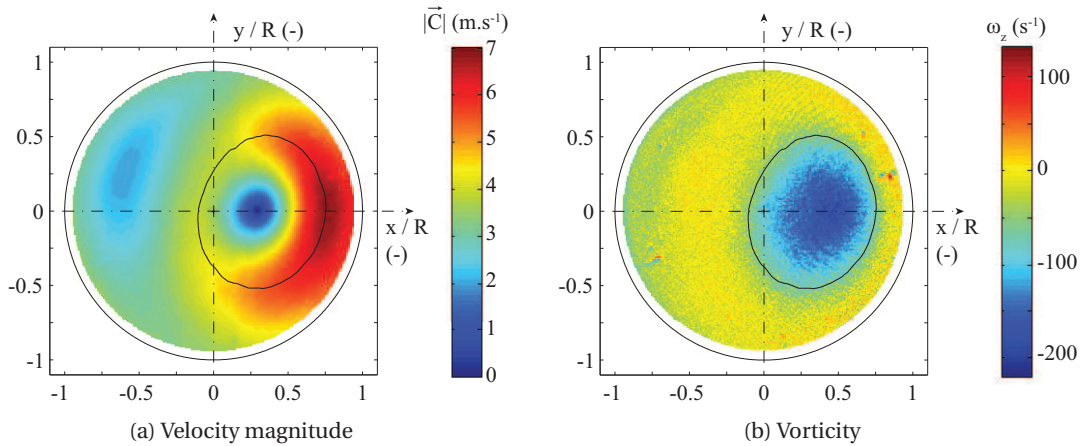


Figure 3.18: (a) Velocity magnitude and (b) vorticity for a given phase ( $\theta = \pi/10$ ) of the precession cycle in the PIV measurement section 3. The limits of the vortex core are indicated by the solid black contour ( $Q_{ED} = 0.128$ ).



### 3.5 Draft tube flow

In this section, the influence of the discharge factor on the vortex parameters is presented and linked with that on the precession frequency and the synchronous pressure pulsations amplitude presented in Section 3.3. For each operating point, the determination of the vortex parameters, such as vortex centre and circulation, is based on the mean phase averaged velocity fields obtained in the horizontal draft tube cone cross-sections. The effect of the discharge factor on the recirculation zone is also investigated by using the time-averaged axial velocity fields measured in the meridional section of the cone for each operating point. Finally, based on the presented results, a discussion about the excitation mechanisms is proposed.

#### 3.5.1 Vortex structure

The phase averaged velocity fields obtained in the different horizontal cross-sections of the cone are presented to investigate the structure of the precessing vortex core within the different flow regimes introduced in Section 3.3. The magnitude  $\|\vec{C}\| = \sqrt{Cx^2 + Cy^2}$  of the velocity fields obtained in the measurement section 3 at a given phase of the precession cycle is reported in Figure 3.19 for each investigated value of discharge factor. The phase of the precession cycle corresponds to the instant for which the vortex centre (identifiable by the black crosses in Figure 3.19) is situated exactly on the positive  $x$ -axis. The limits of the vortex core, computed with the  $\gamma_2$ -criterion, are made visible by the solid black contour. Additionally, the corresponding distribution of vorticity  $\omega_z$  is reported in Figure 3.20 for each value of discharge factor.

For all the values of the discharge factor between 81 % and 60 % of the value at the BEP, a wide vortical structure is identifiable, which corresponds to the precessing vortex core. It is characterized by a region of high vorticity near the vortex centre, corresponding to the vortex core, which is surrounded by a zone of quasi-irrotational flow. The surface delimited by the contour of the vortex core is greater than 19 % of the total surface of the measurement section for all the operating points.

However, varying the value of the discharge factor changes the flow structure through the swirl number, which is the main driving parameter of the precessing vortex core [38]. At a low value of the swirl number, i.e. with a discharge factor equal to  $Q_{ED} = 0.81 \times Q_{ED}^*$ , the vortex core is quasi-circular and the distribution of tangential velocity around the vortex centre is nearly axisymmetric, although a slight acceleration of the tangential flow between the vortex centre and the cone wall starts to appear at this operating point. Decreasing the value of the discharge factor, the vortex core is deformed and takes an elliptical shape, as illustrated by the results obtained at the operating point  $Q_{ED} = 0.64 \times Q_{ED}^*$ , while the vorticity within the limits of the vortex core strongly increases, as documented in Figure 3.20. Moreover, the distribution of tangential velocity around the vortex core is increasingly asymmetric and features an important rise of the tangential velocity between the vortex centre and the cone wall.

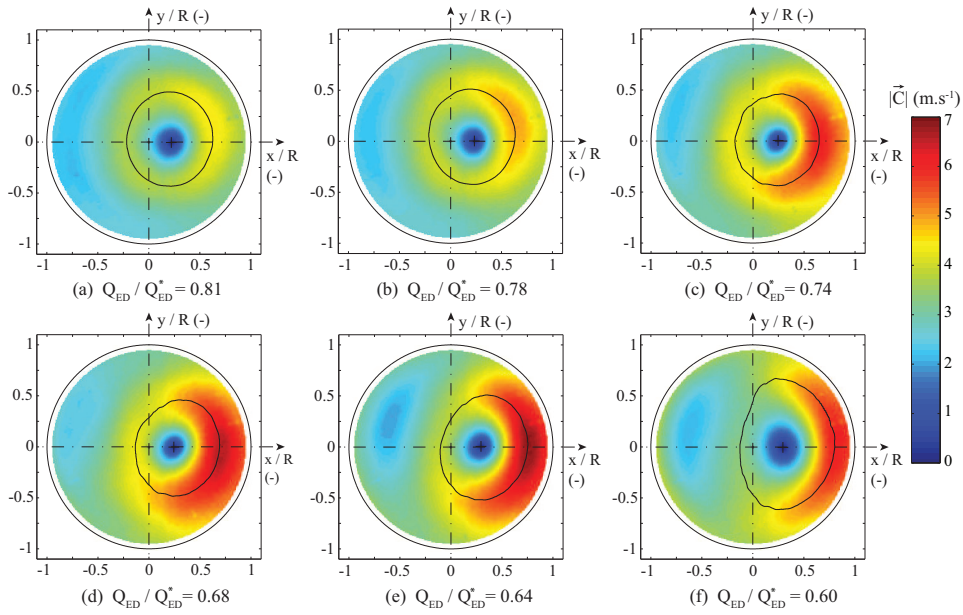


Figure 3.19: Influence of the discharge factor on the magnitude of the velocity fields in the section 3. The black solid line corresponds to the limits of the vortex core. The value of the phase is different from one discharge factor value to another.

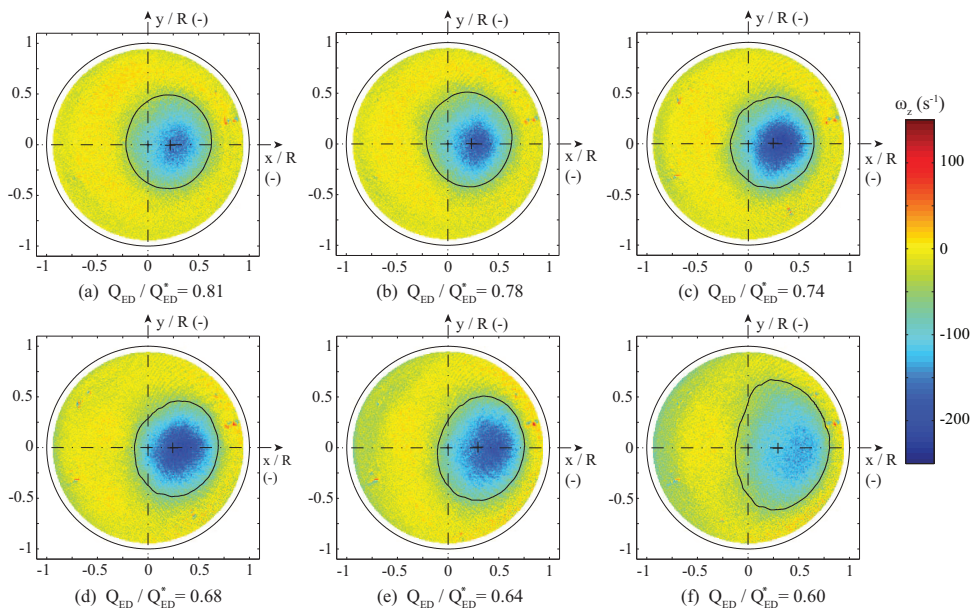


Figure 3.20: Influence of the discharge factor on the normal component of the vorticity  $\omega_z$  in the section 3. The black solid line corresponds to the limits of the vortex core. The value of the phase is different from one discharge factor value to another.

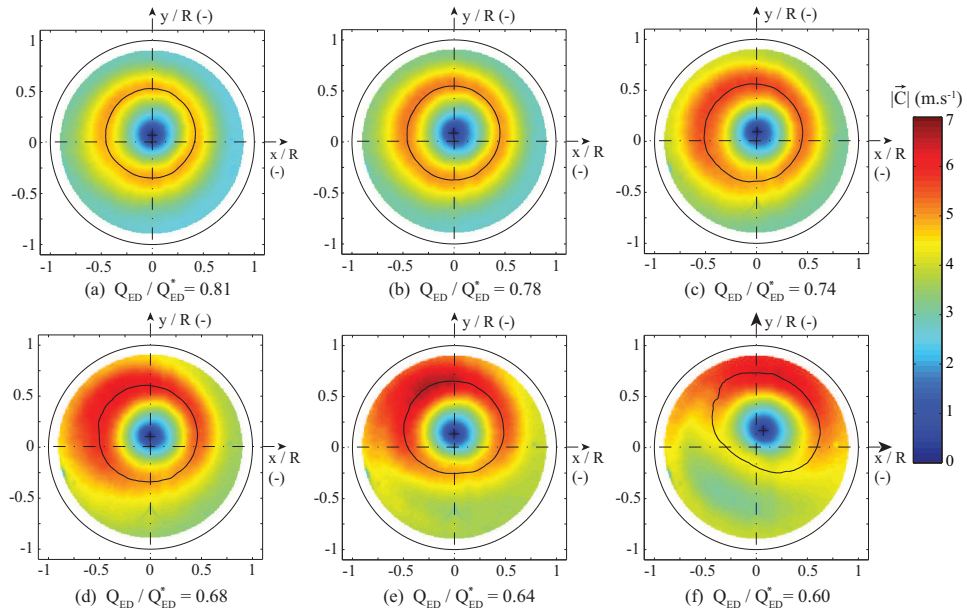


Figure 3.21: Influence of the discharge factor on the magnitude of the velocity fields in the section 1. The black solid line corresponds to the limits of the vortex core. The value of the phase is different from one discharge factor value to another.

This phenomenon has already been reported by different authors (for instance Cala et al. [13]) and it was suggested that this effect is produced by the squeezing of the swirling flow between the vortex centre and the wall, as the angular momentum flux is conserved [37]. For the present case, it is shown that when the discharge factor is decreased, the vortex centre moves closer to the cone wall (see the following section), inducing a more important squeezing of the flow between the vortex centre and the cone wall and consequently a more important acceleration of the flow in this zone.

The results obtained in the measurement section 1 (Figure 3.21) are similar to those obtained in the section 3. The vortex core is however much more symmetric for low values of swirl number ( $Q_{ED} = 0.81 \times Q_{ED}^*$  and  $Q_{ED} = 0.78 \times Q_{ED}^*$ ) as the the vortex centre almost lies on the geometrical centre of the section, mitigating therefore the squeezing effect of the tangential flow field.

### Vortex circulation

The vortex circulation  $\Gamma$  is computed at each phase of the precession cycle by integrating the vorticity within the vortex core. Its mean value is, then, obtained for all the investigated operating points by averaging over the complete precession cycle. Its evolution with the discharge factor is reported in Figure 3.22 for each measurement section. A decrease of the vortex circulation away from the runner outlet in the direction of the flow is observed, which illustrates the gradual decay of the vortex strength due to viscous effects [58, 13]. As it could be

expected, the circulation of the vortex increases quasi-linearly with a decrease of the discharge factor, as the latter induces an increase of the swirl number of the flow feeding the draft tube.

For low values of the discharge factor (typically  $Q_{ED} = 0.64 \times Q_{ED}^*$  and  $Q_{ED} = 0.60 \times Q_{ED}^*$ ), a second zone with a vorticity different to 0 appears (see Figure 3.20-f), which is located in the vicinity of the cone wall at  $180^\circ$  of the zone featuring a high tangential velocity. However, this second structure is not associated with a global swirling motion of the flow and may correspond to a flow region of high shear. At the operating point  $Q_{ED} = 0.60 \times Q_{ED}^*$ , the presence of this second structure and its occasional merge with the main vortical structure at certain phases of the precession cycle does not permit to identify clearly the boundaries of the precessing vortex core by applying the algorithm of Graftieaux et al. [36]. Even though it is possible to plot the vortex core in Figures 3.19 and 3.20 for this operating point, its limits are not well defined for certain phase values, and the algorithm for the calculation of the vortex circulation fails.

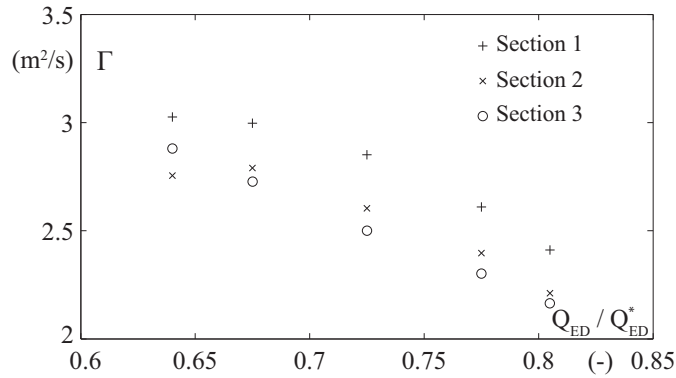


Figure 3.22: Average circulation of the vortex as a function of the discharge factor in each measurement section for the flow regimes 1 and 2.

### 3.5.2 Vortex trajectory

#### Determination of the average trajectory of the vortex centre

For each operating point, the average trajectory of the vortex centre is recovered by determining the position of the vortex centre at each phase of the precession cycle. For a given phase of the precession cycle, the vortex centre is identified directly in the corresponding phase averaged velocity field by using the  $\gamma_1$ -criterion. A comparison between the average trajectory obtained by applying this procedure and the one obtained by averaging the positions of the instantaneous vortex centres identified for the same phase window is presented in Figure 3.23, as well as an example for a given phase of the precession cycle. The red dots represent the position of the instantaneous vortex centres whereas the green and blue circles represent the vortex centre position in the phase averaged velocity field and the average position of the instantaneous vortex centres, respectively.

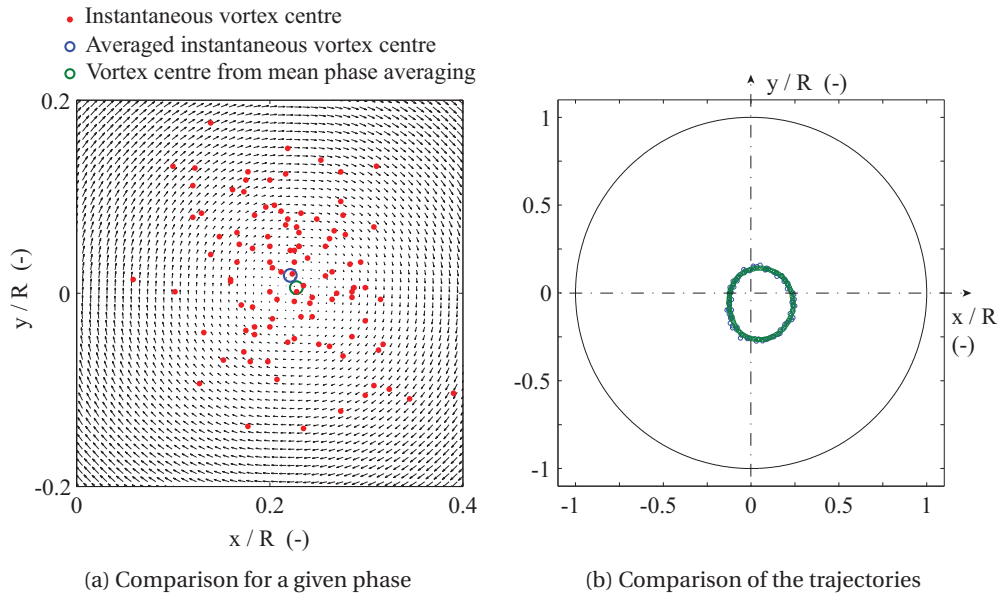


Figure 3.23: (a) Dispersion of the instantaneous vortex centres for a given phase ( $\theta = 8\pi/5$ ) of the precession cycle and (b) comparison between the trajectory obtained by averaging the position of the instantaneous vortex centres and the one obtained by determining the vortex centre position in the phase averaged velocity fields ( $Q_{ED} = 0.64 \times Q_{ED}^*$ , section 1).

The average position of the instantaneous centres, which are globally situated within a circle of radius  $3R/16$  centered on the mean vortex centre, differs slightly from the vortex centre determined in the mean phase averaged velocity field. The distance between both positions is however less than 1.5 % of the measurement section radius. The difference between both trajectories is almost insignificant, although the trajectory of the vortex centre obtained by using directly the mean phase averaged velocity fields is more continuous, as a Fourier series decomposition has first been applied. The following analysis is based on the mean vortex centre identified directly in the phase averaged velocity fields.

### Asymmetry and widening of the vortex trajectory

The average trajectories of the vortex centre obtained in all the measurement sections are presented in Figure 3.24. Each sub-figure corresponds to a given value of discharge factor. The trajectory of the vortex centre features a strong asymmetry which is increasingly pronounced as the value of the discharge factor is decreased. The vortex centre precesses around an axis which slightly differs from the cone centerline. More precisely, the vortex trajectories at the operating points  $Q_{ED} = 0.81 \times Q_{ED}^*$  and  $Q_{ED} = 0.78 \times Q_{ED}^*$ , which correspond respectively to the regime 1 and the first operating point investigated in the regime 2, are quasi-circular and very similar, aside from a slight difference in their radius. This indicates that the vortex characteristics do not experience significant changes within the regime 1 and are altered only

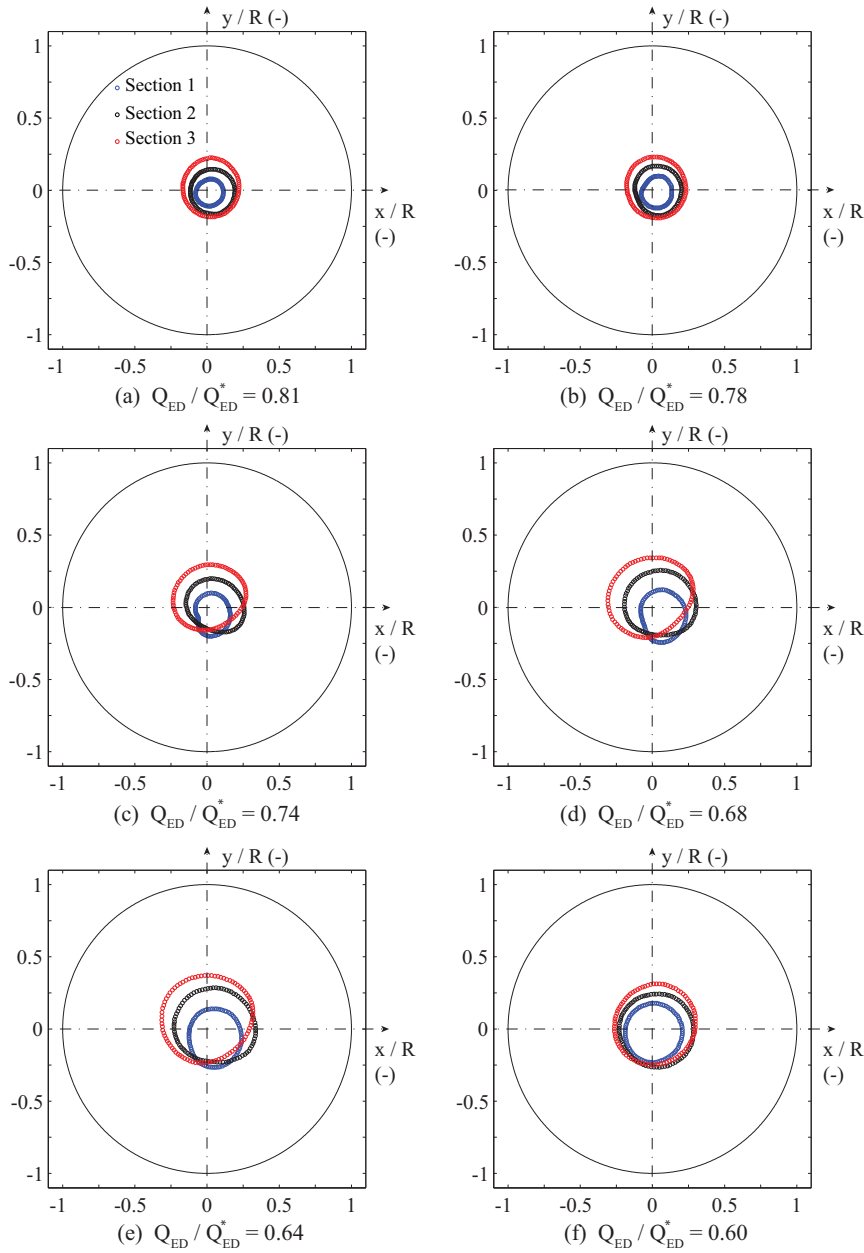


Figure 3.24: Vortex centre trajectory during one precession period for different values of discharge factor.

below a value of the discharge factor equal to  $Q_{ED} = 0.78 \times Q_{ED}^*$ , e.g. beyond the transition from regime 1 to regime 2. In flow regime 2, with a discharge factor between 78 % to 62 % of the value at the BEP, the trajectory of the vortex significantly widens as the discharge factor is decreased. Below the value  $Q_{ED} = 0.62 \times Q_{ED}^*$ , the diameter of the vortex centre trajectory is however reduced and its asymmetry is less pronounced. This results is an additional evidence of a change in the flow structure occurring in the flow regime 3.

The widening of the vortex centre trajectory is illustrated in Figure 3.25 by the distance  $d$  covered by the vortex centre over one precession period, as function of the discharge factor. The distance  $d$  covered by the vortex centre is obtained by computing the length of the vortex trajectory via a curvilinear integral along the vortex trajectory (defined as  $T_v$ ):

$$d = \oint_{T_v} dl \quad (3.14)$$

The vortex trajectory length evolves linearly with the value of the discharge factor in all the measurement sections. For a given discharge factor, the length of the vortex trajectory progressively increases far away from the runner outlet, illustrating the widening of the vortex trajectory in the direction of the flow. It reaches its maximum at a discharge factor equal to  $Q_{ED} = 0.64 \times Q_{ED}^*$  in the measurement sections 2 and 3, i.e. when the excitation source is also at its maximum. Below this value, although the precession frequency does not diminish, the length of the vortex trajectory drastically decreases in the sections 2 and 3 whereas its value remains stable in the section 1. The retraction of the vortex trajectory is accompanied by a modification of the trajectory shape, which becomes again nearly circular and centred on the cone centerline.

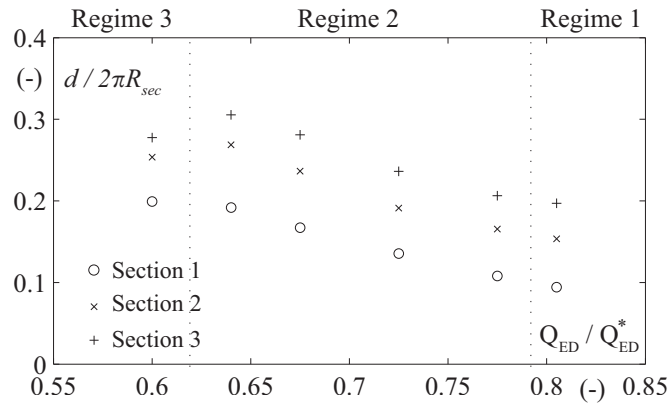


Figure 3.25: Vortex trajectory length as a function of the discharge factor in each measurement section. The length of the vortex trajectory is made dimensionless by the perimeter of the corresponding measurement section.

The strong asymmetry of the vortex trajectory observed in the flow regime 2 is also illustrated by the convective component of the pressure fluctuations in the draft tube cone, which presents singular differences in terms of amplitude and phase from one sensor to another. The phase averaged convective pressure components are given in Figures 3.26 and 3.27 for two different values of discharge factor, respectively  $Q_{ED} = 0.64 \times Q_{ED}^*$  and  $Q_{ED} = 0.81 \times Q_{ED}^*$ .

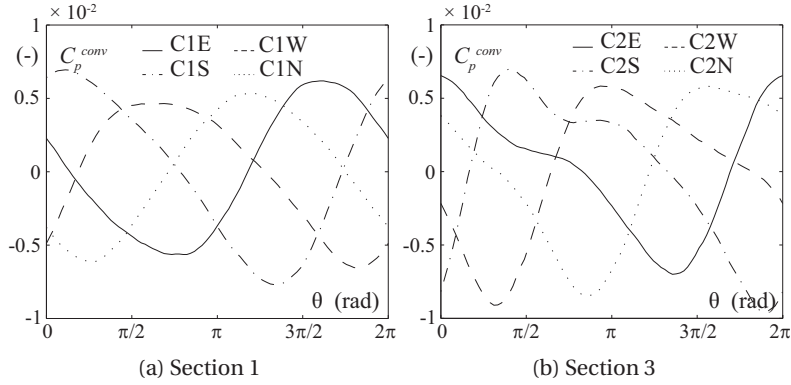


Figure 3.26: Phase averaged convective pressure components in the draft tube cone ( $Q_{ED} = 0.81 \times Q_{ED}^*$ )

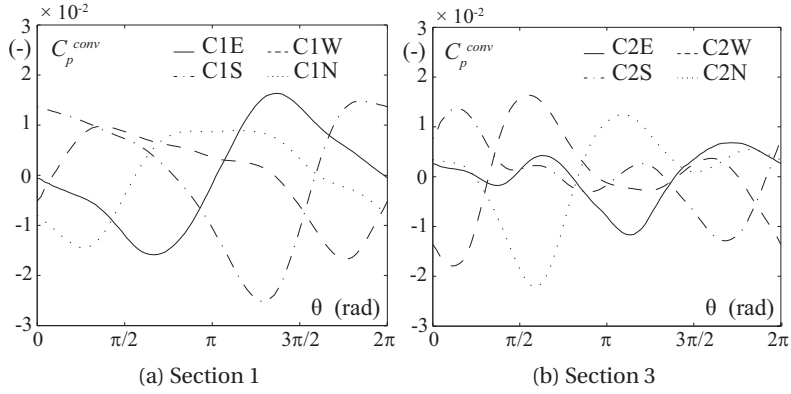


Figure 3.27: Phase averaged convective pressure components in the draft tube cone ( $Q_{ED} = 0.64 \times Q_{ED}^*$ )

The convective pressure components are not only composed of pressure fluctuations at the fundamental precession frequency as their shape is deformed, particularly in the measurement section 3 for  $Q_{ED} = 0.64 \times Q_{ED}^*$ . This is explained by the increasing asymmetry of the vortex structure and trajectory as the discharge factor decreases. The instant for which the convective pressure component is at its minimum corresponds to the passage of the vortex core in the vicinity of the pressure sensor. Fernandes et al. [34] used this property to determine the evolution of the axial wavelength of the precessing vortex core with the swirl number in the case of a model vortex combustor by using a microphone situated at various positions. In the present test case, the phase shift between the passages of the vortex centre in the vicinity of two consecutive sensors is not exactly equal to  $\pi/2$  and is not constant all around the circumference of the section. Moreover, the pressure level at the passage of the vortex core differs from one sensor to another as the distance between the vortex centre and the cone wall is not constant during the precession cycle.



### Dispersion of the vortex centre

As discussed in Section 3.4.3, the instantaneous positions of the vortex centre present a dispersion around the average trajectory of the vortex. The latter is plotted in Figure 3.28 for 4 different values of discharge factor together with the instantaneous position of the vortex centre determined for each instantaneous velocity fields. To quantify more precisely the dispersion of the vortex position, the evolution of the standard deviation of the vortex centre coordinates  $(x_c, y_c)$  with the discharge factor is plotted in Figure 3.29. For a given value of the discharge factor, the standard deviation is computed for each phase of the precession cycle and is then averaged over the complete precession cycle. The standard deviation for both coordinates  $x_c$  and  $y_c$  remains quite constant within the flow regimes 1 and 2 and is comprised between 6 and 7 % of the section radius. Below the value  $Q_{ED}/Q_{ED}^* = 0.6$ , it drastically increases compared with the others operating point. The wider dispersion of the vortex centre position observed at this operating point is another evidence of the loss of periodicity and coherence in the vortex structure occurring beyond the transition from regime 2 to regime 3.

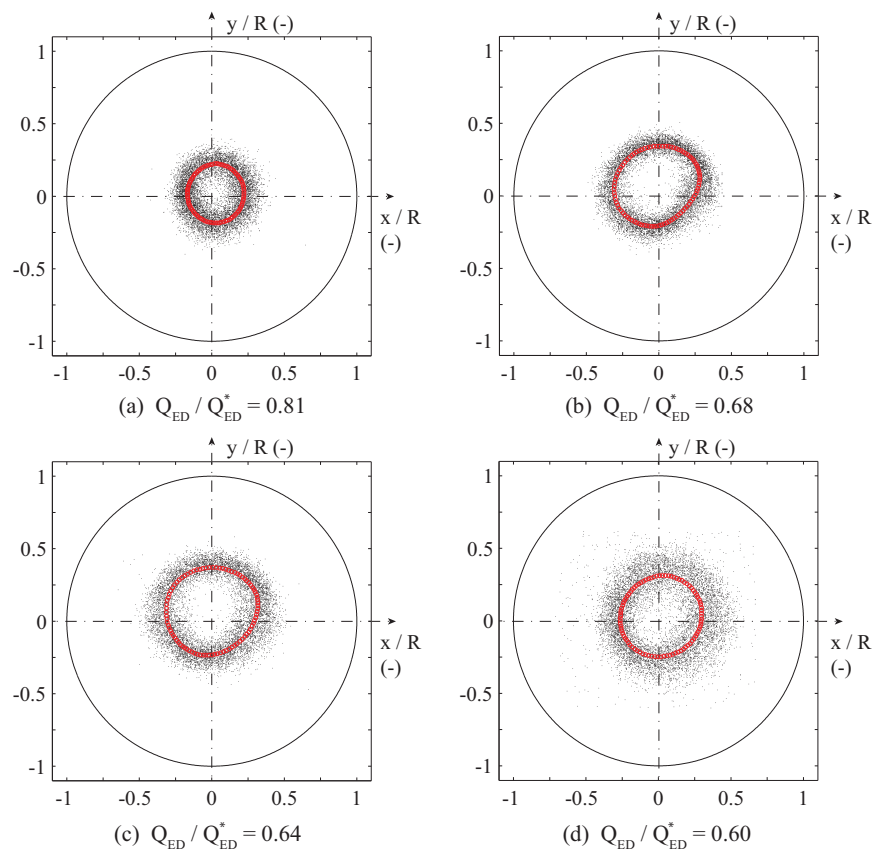


Figure 3.28: Average trajectory of the vortex centre (red dots), together with the instantaneous vortex centres (black dots) for different values of the discharge factor in the section 3.

### Chapter 3. Precessing vortex core in cavitation-free conditions

The dispersion of the vortex centre for a given phase of the precession cycle is able to introduce an artificial diffusion of the phase averaged velocity fields and, consequently, an overestimation of the vortex core size yielding a biased estimation of the vortex circulation. For instance, in the case of steady vortices such as tip leakage vortex, a random fluctuation of the vortex axis position is observed, referred to the wandering phenomenon. The induced undesirable effects may be corrected by different techniques in order to avoid an overestimation of the vortex core size (Dreyer et al. [22], Bhagwat and Ramasamy [11]). In the case of a precessing vortex core, Ingvorsen et al. [45] also observed a dispersion of the instantaneous vortex centre by performing stereoscopic PIV in different cross-sections of a scale model of a simplified uniflow-scavenged cylinder. In the case of a swirling flow featuring a fluctuation of the vortex centre around the mean swirl centre, they estimated the radial profile of the velocity components by averaging in the  $\theta$ -direction the instantaneous velocity fields centered on the instantaneous vortex centres. However, in the present test-case, the use of this method does not produce reliable results because of the strong asymmetry of the tangential velocity around the vortex centre, which is highlighted in Figure 3.19. Nevertheless, the average distance between the instantaneous vortex centres and the mean vortex centre for a given phase is estimated to less than 15 % of the vortex core size in the flow regimes 1 and 2. Therefore, it is assumed that the phase averaging of velocity fields mitigates the artificial diffusion of the velocity fields for the operating points in the flow regimes 1 and 2.

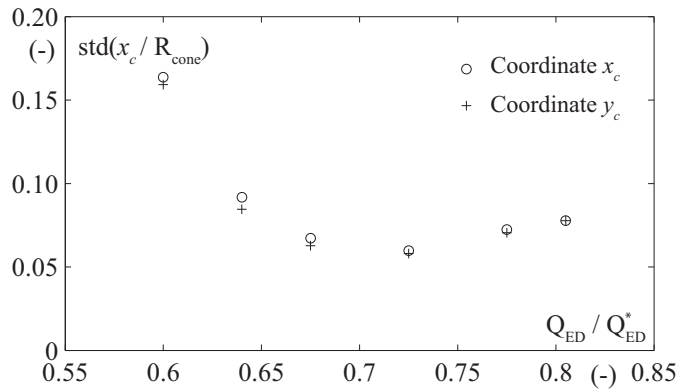


Figure 3.29: Standard deviation of the vortex centre coordinates ( $x_c, y_c$ ) as a function of the discharge factor in the measurement section 3.

### 3.5.3 Axial flow recirculation zone

For each value of discharge factor, the time-averaged axial velocity field in the meridional cross-section of the draft tube cone is obtained by averaging the complete set of instantaneous velocity fields recorded by the PIV system. The resulting velocity fields are given in Figure 3.30 and are limited to the axis  $x < 0$  and the streamwise positions from  $-0.36 \times D_1$  to  $-1.05 \times D_1$  downstream the runner outlet. A negative value of axial velocity represents a direction opposite to that of the main flow. The zone of reverse flow corresponds therefore to the region featuring a negative value of axial velocity.

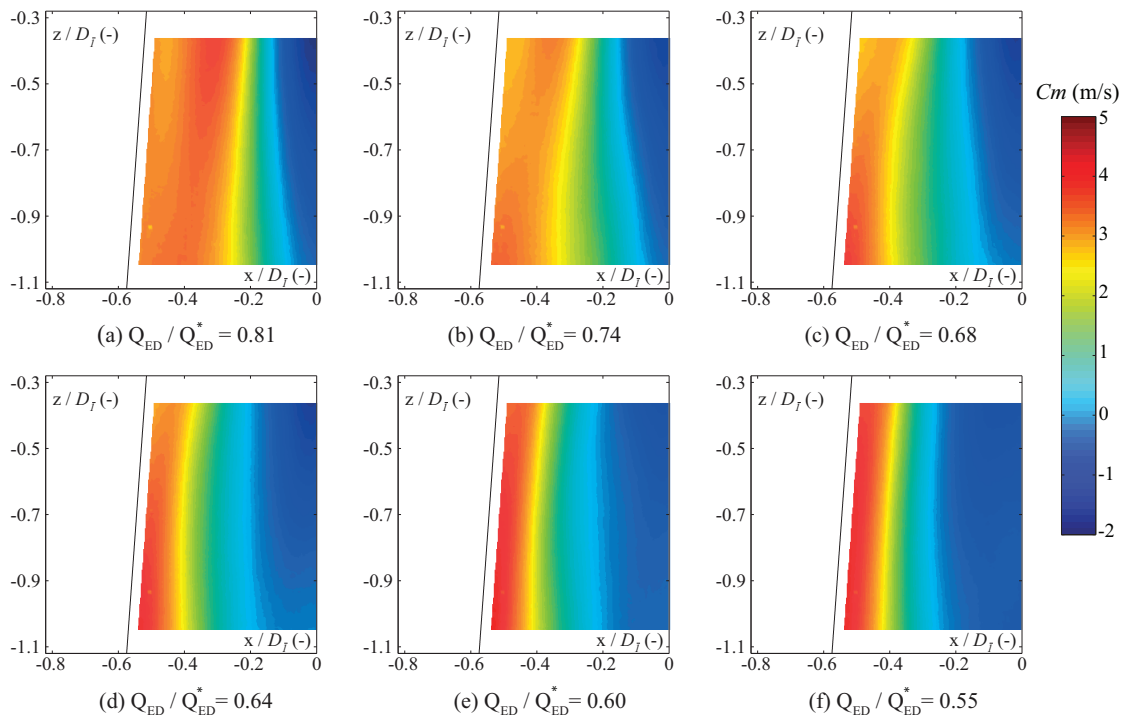


Figure 3.30: Time-averaged axial velocity field in the meridional cross-section of the draft tube cone for different values of the discharge factor. The diagonal black solid line represents the outer cone wall. The axes  $x$  and  $z$  are made dimensionless by the runner diameter  $D_1$ .

The radial pressure gradient induced by the swirling motion and the decay of swirl velocity in the flow direction give rise to an axial adverse pressure gradient, which causes an axial flow recirculation zone if the swirl number is high enough [38]. For the present test case, the emergence of a recirculation zone is also observed for the largest value of discharge factor in Figure 3.30-a. However, a decrease in the value of the discharge factor leads to an increase in the value of the swirl number, as illustrated in the following section, which results in an important growth of the size of the recirculation zone. At low values of the discharge factor, it gives rise to a very high positive axial velocities near the cone wall, as the totality of the flow is discharged through a small fraction of the cone.

### Chapter 3. Precessing vortex core in cavitation-free conditions

The radius of the recirculation zone is estimated for each value of the discharge factor at the three measurement sections. Its evolution with the discharge factor is reported in Figure 3.31. For each section, the radius of the recirculation zone is made dimensionless by the radius of the cone  $R_{sec}$ .

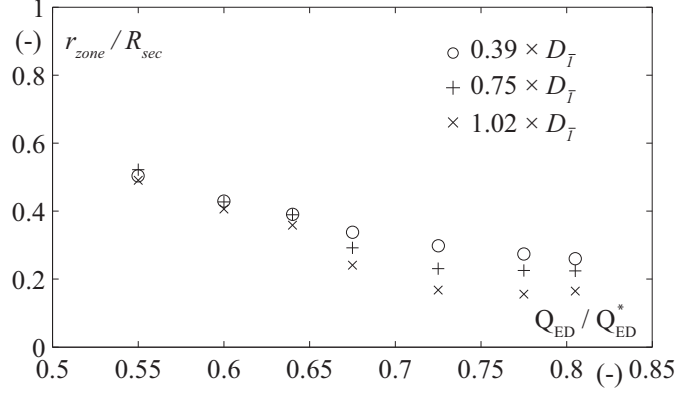


Figure 3.31: Recirculation zone radius as a function of the discharge factor for three different cross-sections of the cone. The radius of the recirculation zone is made dimensionless by the radius of the corresponding section  $R_{sec}$ .

A decrease of the discharge factor induces a growth of the recirculation zone. However, the evolution features several interesting characteristics which are worth being pointed out. For the highest values of the discharge factor (from 81 % to 68 % of the value at the BEP), the ratio  $r_{zone}/R_{section}$  progressively decreases far away from the runner outlet. However, below  $Q_{ED}/Q_{ED}^* = 0.64$ , the ratio is almost constant with the distance  $z/D_1$ , indicating that the growth of the recirculation zone in the main flow direction follows the expansion of the cone section. Moreover, in the cross-sections located  $0.75 \times D_1$  and  $1.02 \times D_1$  downstream the runner outlet, the size of the recirculation zone remains almost constant for  $Q_{ED}$  between 81 % and 68 % of the value at the BEP and only starts increasing when the discharge factor is less than 68 % of the value at the BEP, whereas it continuously increases in the cross-section located  $0.39 \times D_1$  downstream the runner outlet.

#### 3.5.4 Swirl number

For each value of discharge factor, the swirl number of the flow is estimated by using the definition given by Gupta et al. [38] (see Equation 3.3). In its expression, the pressure and turbulence terms are omitted. PIV measurements performed in the horizontal and meridional sections of the cone are used. The computation of the swirl number is based on the time-averaged axial and tangential velocity half-profiles obtained  $1.02 \times D_1$  downstream the runner outlet, which corresponds to the horizontal section 3. The results obtained in the other cross-sections, i.e.  $0.39 \times D_1$  and  $0.75 \times D_1$  downstream the runner outlet, are not used for the present analysis as the time-averaged velocity profiles in these sections are strongly asymmetric and

not centered on the radial position  $x/R = 0$ .

It has been emphasized that different time-averaged velocity profiles can lead to the same value of the swirl number (Farokhi et al. [30], Toh et al. [77]). Thus, the minimum swirl number necessary for the occurrence of the vortex breakdown can be different depending on the initial conditions of the swirling flow. It is therefore important to present the value of the swirl number together with the corresponding time-averaged velocity profiles. They are plotted in Figure 3.32 for each value of discharge factor. The axial and tangential velocity components are made dimensionless by the discharge velocity  $C_Q = Q/A$  and the runner velocity  $U = \omega R_1$ , respectively. The evolution of the axial velocity profiles highlights the growth of the recirculation zone and the increase of the maximum axial velocity near the cone wall, as reported previously. Moreover, when the discharge factor decreases, the location featuring the maximum tangential velocity moves closer towards the cone wall, and the corresponding maximum value increases. As a result, the time-averaged tangential velocity profile features the shape of a solid body rotation for the lowest values of the discharge factor.

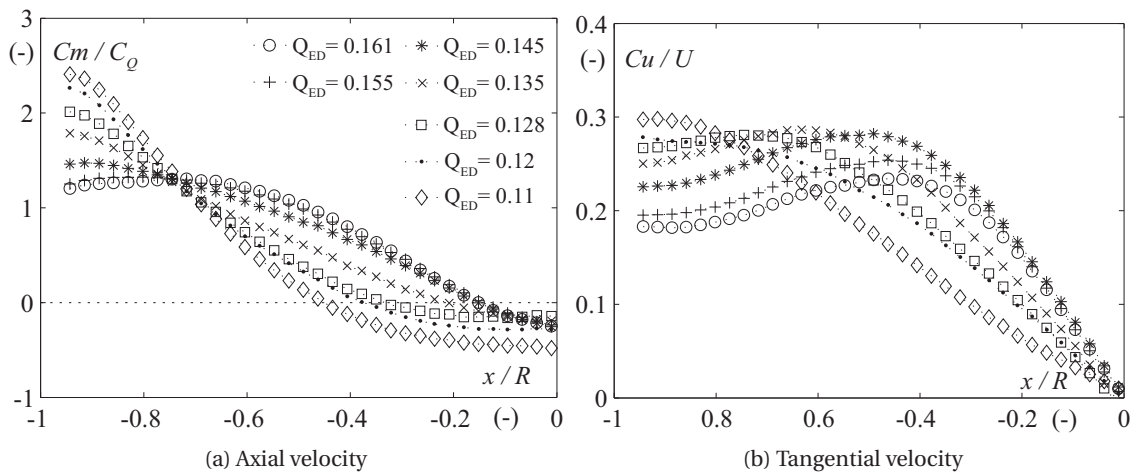


Figure 3.32: Time-averaged axial and tangential velocity profiles for different values of discharge factor,  $1.02 \times D_1$  downstream the runner outlet.

The influence of the discharge factor on the swirl number  $S$  is reported in Figure 3.33. It linearly increases as the discharge factor is decreased from 81 % to 68 % of the value at the BEP. Below the value  $Q_{ED}/Q_{ED}^* = 0.64$ , the swirl number remains almost constant and approximately equal to 1. It has been shown in Section 3.3 that pressure fluctuations at a well-defined frequency, identified as the precession frequency, are highlighted in the auto-spectrum of the pressure signals when the value of the discharge factor is less than 85 % of the value at the BEP. Thus, it can be assumed that the precessing vortex core is established for values of the discharge factor  $Q_{ED} < 0.85 \times Q_{ED}^*$ .

A linear fitting of the swirl number obtained experimentally in the range  $Q_{ED}/Q_{ED}^* = [0.68 - 0.81]$  is realized. By extrapolating it, the swirl number at the operating point  $Q_{ED}/Q_{ED}^* = 0.85$

can be computed. The corresponding value is equal to  $S_{critical} = 0.54$ . This value corresponds to the minimum value of the swirl number for which the development of a precessing vortex core is observed in the draft tube cone.

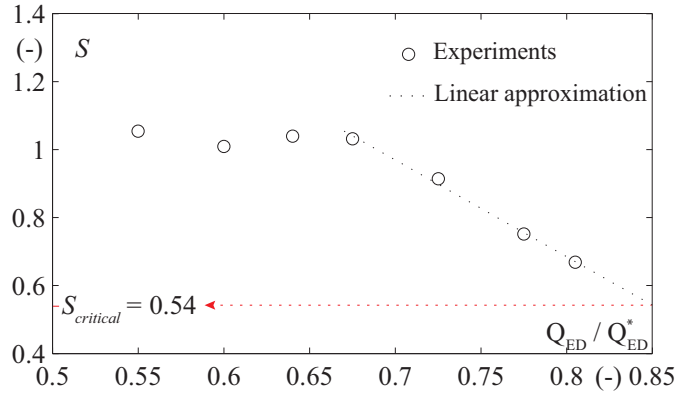


Figure 3.33: Swirl number  $S$  as a function of the discharge factor. The swirl number is computed with the time-averaged velocity profiles obtained in the cone cross-section located  $1.02 \times D_1$  downstream the runner outlet.

These results have to be linked with the results reporting the evolution of the recirculation zone, the precession frequency and the vortex parameters. The results suggest the occurrence of a global change in the flow structure beyond the transition from the regime 2 to the regime 3, affecting the coherence of the precessing vortex rope. However, the mechanisms driving this transition remain to be established. This may be done by performing for instance a stability analysis of the draft tube flow or an accurate investigation of the structure of the flow leaving the runner blades.

### 3.6 Summary and Discussion

This chapter reports the investigation of the influence of the discharge factor on the precessing vortex core dynamics and the intensity of the induced excitation source. The tangential velocity fields at the runner outlet are measured in cavitation-free conditions by means of PIV performed in three different cross-sections of the draft tube cone for 7 different values of the discharge factor between 81 % and 55 % of the value at the BEP. At these operating conditions, the wall pressure signals feature well-defined periodical oscillations, indicating the development of a precessing vortex core. Pressure measurements are carried out throughout the test rig to characterize the precession frequency and the amplitude of the synchronous pressure pulsations. Additionally, PIV measurements are performed in the meridional cross-section of the draft tube cone to investigate the influence of the discharge factor on the axial flow recirculation zone and the swirl number of the draft tube flow. For each investigated flow condition, the periodical evolution of the velocity field over one precession cycle is recovered in the horizontal cone cross-sections by performing an appropriate phase averaging based on

a reference pressure signal measured in the draft tube. Based on the phase averaged velocity fields, the vortex centre position and the vortex core boundaries are identified, yielding the vortex trajectory and the circulation within the vortex core.

The results suggest the occurrence of 3 different flow regimes depending on the discharge value. From 78 % to 85 % of the value at the BEP, the precession frequency remains constant and, then, linearly increases as the discharge is decreased from 62 % to 78 % of the BEP. It is accompanied by a linear increase of the vortex circulation and a broadening of the vortex trajectory which are observed in all the measurement sections. The modification of the vortex parameters induces an important increase of the amplitude of the synchronous pressure pulsations at the precession frequency, which highlights an increase of the excitation source intensity. The latter reaches its maximum when the vortex circulation and the vortex trajectory are also at their maximum. However, below a certain value of the discharge factor, the vortex trajectory retracts, along with a sudden decrease of the synchronous pressure fluctuations amplitude. The precessing vortex core loses its coherence, which is illustrated by the important increase of the dispersion of the instantaneous vortex centres and the loss of periodicity in the pressure signals. As a result, the excitation source is weakened. This drastic change in the flow structure is also illustrated by the evolution of the recirculation zone size and the swirl number. The latter linearly increases as the discharge factor is decreased within the flow regime 2, whereas it remains approximately constant beyond the transition from flow regimes 2 to 3. Finally, a critical swirl number is estimated at the value  $S_{critical} = 0.54$ . It corresponds to the minimum value of the swirl number necessary for the establishment of the precessing vortex core in the draft tube for the present test-case.

#### **Excitation mechanisms**

It is assumed that the intensity of the excitation source is directly related to the amplitude of the synchronous pressure pulsations measured in cavitation-free conditions. As shown in this chapter, the latter is directly related to the vortex strength and the diameter of the vortex trajectory. More precisely, the broader the vortex trajectory is, the higher is the excitation source intensity and the amplitude of the resulting synchronous pressure pulsations. As explained in Section 3.2, the flow is subject to flow separation at the intrados of the elbow, as observed in simple applications with elbowed pipe [76]. This flow separation zone, illustrated in Figure 3.34, impacts the pressure recovery in the diffuser and is altered by the presence of the vortex rope. The precession movement of the vortex core therefore periodically distorts the flow separation zone area, giving rise to a periodical fluctuation of the pressure recovery  $\tilde{p}_{recov}(t)$  at the precession frequency, whose amplitude is a function of the vortex circulation and trajectory according to Fanelli [28]. This gives rise to the propagation of synchronous pressure pulsations exciting the system at the precession frequency. Thus, a wider vortex trajectory in the elbow, together with a greater value of the vortex circulation, yields a more significant variation in the separation zone and the pressure recovery, and as a consequence in an increase in the excitation source intensity. However, the exact interaction of the precessing

**Chapter 3. Precessing vortex core in cavitation-free conditions**

vortex core with the secondary flows produced by the arising of a flow separation zone remains to be established. This could be achieved by performing an accurate investigation of the three-dimensional flow in the draft tube elbow by means of stereo-PIV. Currently, such experiments are however made difficult by the complex geometry of the reduced scale physical model of the Francis turbine.

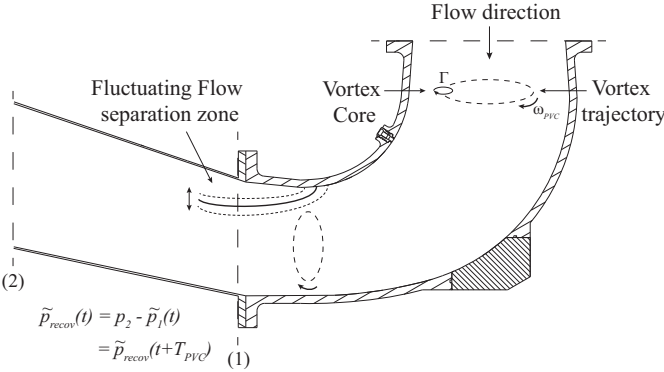


Figure 3.34: Fluctuations of the flow separation zone induced by the precession of the vortex in the draft tube elbow [33]



## 4 Effect of cavitation on the precessing vortex core and system interaction

### 4.1 Introduction

In hydraulic machines, cavitation occurs under different forms, from inlet edge cavitation to inter-blade cavitation vortices [80, 81], with consequences ranging from generation of noise and vibration to blade erosion [35]. At part load operating conditions in Francis turbines, the low pressure region prevailing in the precessing vortex can lead to the vaporization of its core if the static pressure in the draft tube cone is sufficiently low. This is generally the case on the prototype scale, for which the turbine level is sufficiently high to allow cavitation development in the case of part load or full load operations. The major issue caused by the cavitation development in the draft tube at part load is related to the risk of resonance inducing pressure surge and power swings [71]. The development of cavitation is susceptible to modify the vortex characteristics and the excitation source induced by the precession of the vortex rope. Therefore, it is crucial to determine the influence of the cavitation on the precessing vortex rope dynamics and on the hydro-acoustic response of the system. The resulting physical understanding is used in the hydro-acoustic 1D modeling of the complex two-phase flow in the draft tube [53, 3] for the accurate assessment of the plant stability.

In the literature, different contributions have already reported the experimental investigation of the two-phase flow in the draft tube of hydraulic machines. At full load conditions, the axial velocity field in the draft tube cone has been investigated recently by Müller et al. [61] by means of fluorescent 2D-PIV performed in cavitation conditions to investigate the discharge pulsations occurring in the draft tube. A global characterization of the hydro-acoustic response in case of a self-oscillating vortex rope was performed on a simplified test-case by the same authors [62]. At part load conditions, the flow velocity fields in the case of a cavitation precessing vortex rope have been investigated by Iliescu et al. [44] by means of 2D-PIV performed in a vertical section of the draft tube cone for different values of Thoma number. It has been shown that the cavitation development modifies the vortex rope diameter and the vortex centerline. However, the latter was reconstructed by assuming a solid body rotation of the vortex, which does not hold true for the observed asymmetry of the vortex rope

## Chapter 4. Effect of cavitation on the precessing vortex core and system interaction

---

trajectory shown in Section 3.5. More recently, stereoscopic PIV measurements have been reported in Iliescu et al. [43] for the investigation of the cavitation precessing vortex rope at the outlet of an axial hydraulic turbine. However, to the author's knowledge, no contribution reports the exact influence of cavitation on both axial and tangential velocity fluctuations induced by the precession of the vortex rope. Moreover, the impact of resonance occurrence on the flow velocity field is not documented presently.

The present chapter aims at providing a first contribution to the investigation of the flow velocity fluctuations observed in the draft tube cone in resonance conditions. For this purpose, the instantaneous axial and tangential velocity components are locally measured along two different axis of the cone by means of LDV at different  $\sigma$ -values for two operating points. The methodology is first presented with a particular focus on the spectral analysis of both pressure and velocity signals. The effect of cavitation on the frequencies of interest and the amplitude of the pressure fluctuations is then highlighted in order to identify the resonance conditions for each operating point. Finally, the velocity fields obtained in cavitation-free conditions are presented and analysed in terms of amplitude and time delay before being compared with those measured in cavitation conditions.

## 4.2 Methodology

### 4.2.1 Investigated operating conditions

The investigation is focused on two particular part load operating points for which the discharge factor is equal to 81 % (OP#1) and 64 % (OP#2) of the value at the Best Efficiency Point. The speed factor  $n_{ED}$  is kept constant at the rated value  $n_{ED} = 0.288$ , with the runner speed and the hydraulic specific energy equal to  $n = 13.33 \text{ Hz}^{-1}$  and  $E = 262 \text{ J} \cdot \text{kg}^{-1}$ , respectively. These two operating points corresponds respectively to the flow regimes 1 and 2, for which the precessing vortex rope features a well-defined periodical behavior (see Section 3.3).

The cavitation development in the vortex core is promoted by decreasing the pressure in the draft tube. Visualizations of the cavitation vortex rope observed in the draft tube cone at these operating conditions for a value of Thoma number equal to the prototype value  $\sigma_{plant} = 0.11$  are already presented in Section 3.3.3. The Thoma number is increased step by step from  $\sigma = 0.06$  to  $\sigma = 0.15$  for OP#1 and from  $\sigma = 0.11$  to  $\sigma = 0.21$  for OP#2. The last value of  $\sigma$  corresponds to the value for which cavitation has almost disappeared in the draft tube cone. The pressure over the free surface of the downstream reservoir is finally set to the atmospheric pressure, for which no cavitation is observed in the draft tube cone. The parameters of the operating conditions are summarized in Table 4.1, together with the range of investigated  $\sigma$  values.

Table 4.1: List of the investigated operating points.

Point	$n_{ED}$ (-)	$Q_{ED}$ (-)	$Q$ ( $m^3 \cdot s^{-1}$ )	$Q_{ED}/Q_{ED}^*$ (-)	$\sigma_{cav}$ (-)	$\sigma_{atm}$ (-)
1	0.288	0.161	0.320	0.81	0.06 → 0.15	0.31
2	0.288	0.128	0.255	0.64	0.11 → 0.21	0.38

For each value of  $\sigma$ , wall pressure measurements are carried out in order to highlight the evolution of the hydro-acoustic response of the system and the influence of cavitation on both synchronous and convective pressure components. Based on these results, resonance conditions are finally identified for both operating points. It corresponds to the value of  $\sigma$  for which the precession frequency, seen as an excitation frequency for the system, matches with one of the eigenfrequencies of the system [31], typically the first one. For each operating point, the flow field at the runner outlet is then investigated by means of LDV surveys for three different values of the Thoma number, corresponding respectively to:

1. Resonance in cavitation conditions
2. Out of resonance in cavitation conditions
3. Cavitation-free conditions

#### 4.2.2 Frequency domain analysis in cavitation conditions

##### Wall pressure signals

In this section, an example of cross-spectral analysis of two pressure signals measured in cavitation conditions is presented in order to highlight the different types of pressure fluctuations, as well as their nature (synchronous or convective). The Thoma number  $\sigma$  is equal to the prototype value  $\sigma_{plant} = 0.11$  for both operating points. The pressure signals are measured in the same cross-section of the cone at two locations spaced by  $90^\circ$  (locations C1E and C1S). The cross-spectral density function  $G_{xy}$  is computed for each operating point. Its phase and its amplitude are plotted as a function of the frequency made dimensionless by the runner frequency in Figure 4.1 for OP#1 and in Figure 4.2 for OP#2. The coherence between the pressure signals is also given for both cases.

Two types of pressure fluctuations with a coherence level above 0.95 are highlighted for both operating points. The first one corresponds to the pressure fluctuations at the vortex rope precession frequency  $f_{rope}$ . At this frequency, the phase shift between the two pressure signals is different to  $-\pi/4$ , which results from the superimposition of two pressure components at the same frequency, the synchronous and the convective one. The second type of pressure fluctuations features a broadband spectra centered on the frequency  $f_0$ . At this frequency, the phase shift is equal to 0, indicating the synchronous nature of these pressure fluctuations. The

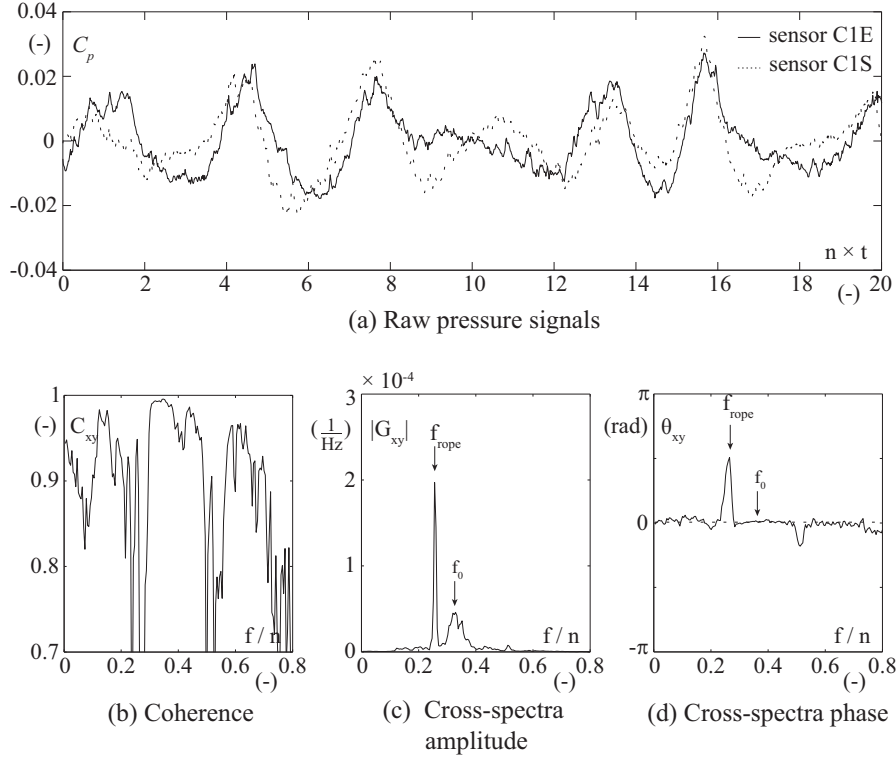


Figure 4.1: Cross-Spectral analysis between two pressure signals measured in the upper section of the cone in cavitation conditions at OP#1 ( $Q_{ED} = 0.161$ ,  $\sigma = 0.11$ ).

frequency  $f_0$  can be identified as the first eigenfrequency of the system [32]. Its value at OP#1 is different than that at OP#2, as the eigenfrequencies of the system are strongly dependent on the wave speed in the draft tube and therefore on the amount of cavitation in the vortex core. The frequency  $f_0$  is greater at OP#1, indicating a lower cavitation volume at this point.

### Axial and tangential velocity components

The LDV system is recording the axial and tangential flow velocity components synchronously at a given position. The measurement is based on the random passage of seeding particles through the measurement volume formed by the intersection of two Laser beams. Therefore, the time interval between two consecutive passages of seeding particle through the measurement volume is arbitrary and the resulting velocity signals are randomly sampled, contrary to the wall pressure signals. For the present test-case, the average sampling frequency for a given velocity signal is typically between 500 Hz and 10'000 Hz, depending on the operating point and on the position of the measurement volume. It is large enough to capture the velocity fluctuations occurring at the precession frequency  $f_{rope}$  and the natural frequency  $f_0$ .

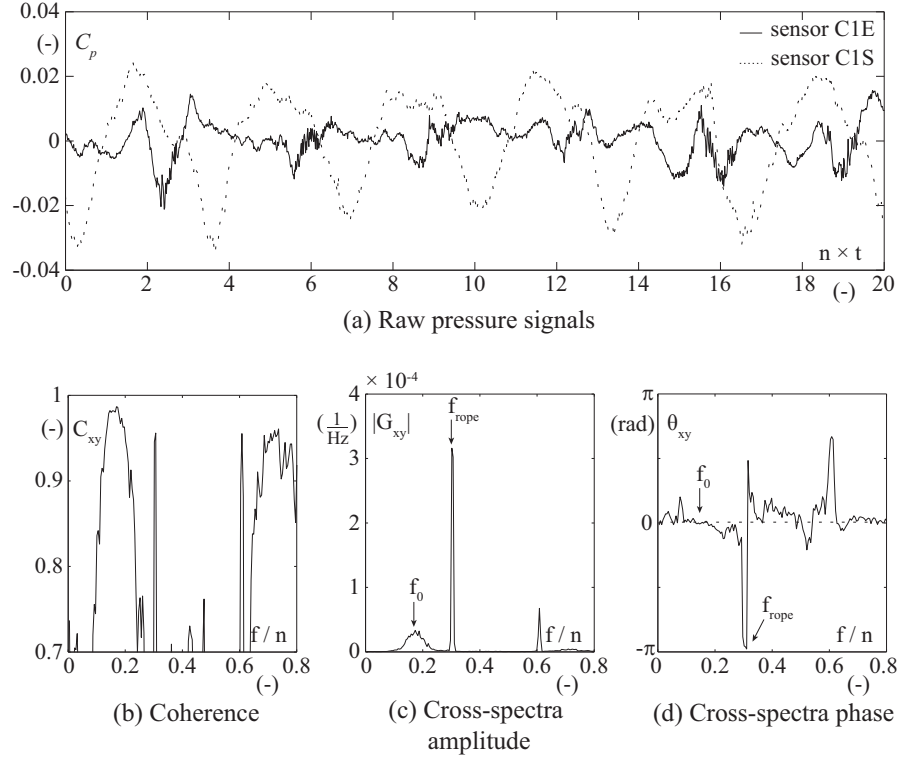


Figure 4.2: Cross-Spectral analysis between two pressure signals measured in the cone in cavitation conditions at OP#2 ( $Q_{ED} = 0.128$ ,  $\sigma = 0.11$ ).

The spectral analysis of the LDV data requires the transformation of the randomly sampled data into regularly sampled data to enable the use of standard tools for the computation of the auto-spectral density function, such as Fast Fourier Transforms (FFT). One option is the *sample and hold* technique, consisting in holding the last measured velocity value until the arrival of the next one (Adrian and Yao [1]). Other types of interpolation can also be used, such as classic cubic piecewise polynomial interpolation for instance. It has been verified that these two types of interpolation provide similar results. The latter is used in the present study, as its computational time is relatively low compared to the *sample and hold* interpolation. An example of axial and tangential velocity signals measured at OP#2 in cavitation conditions ( $\sigma = 0.13$ ) is presented in Figure 4.3, together with the corresponding auto-spectral density functions. The measurement volume is located on the  $x$ -axis of the LDV measurement section 1 at the radial position  $r = -0.84 \times R$ . Both axial and tangential velocity signals feature a well-defined periodicity at a given frequency, which corresponds to the precession frequency  $f_{rope} = 0.31 \times n$ . However, contrary to the pressure signals, no velocity fluctuation is observed at the natural frequency  $f_0$ , suggesting that the flow field is not influenced by the propagation of synchronous pressure pulsations in the system. This needs to be confirmed in the following.

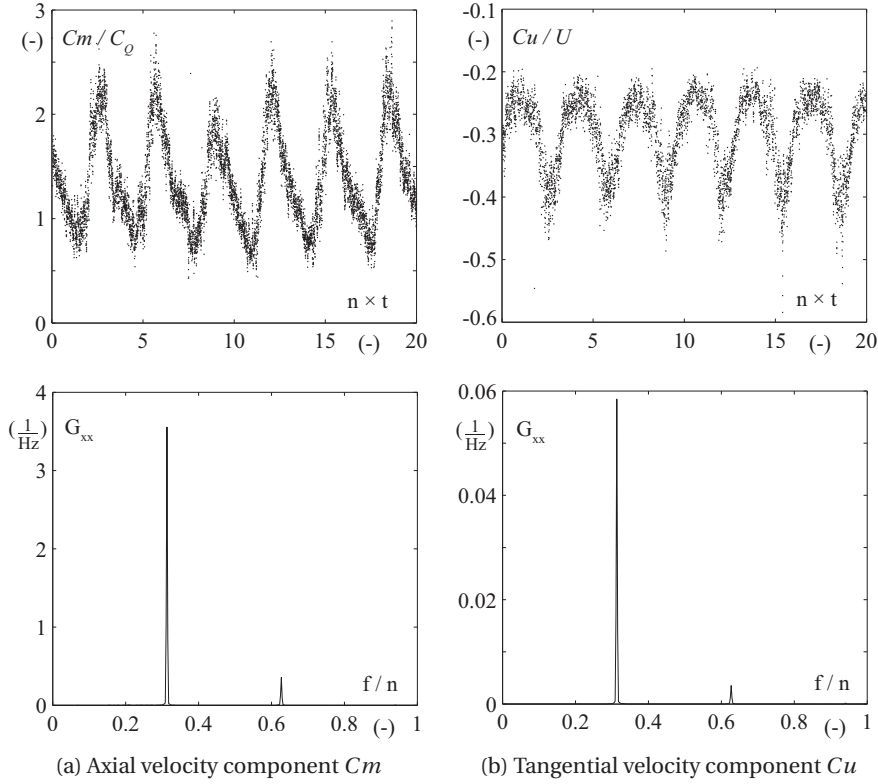


Figure 4.3: Axial and tangential velocity signals and the corresponding auto-spectral density functions at OP#2 in cavitation conditions ( $Q_{ED} = 0.128$ ,  $\sigma = 0.13$ ) at  $(x, y) = (-0.84R, 0)$ .

### 4.2.3 Time domain analysis in cavitation conditions

The mean phase averaging of the flow velocity components  $Cm$  and  $Cu$  measured by means of LDV at a given radial position can be realized by using a wall pressure signal as a reference [60]. In cavitation-free conditions, the successive precession cycles can be easily identified in the reference wall pressure signal (location C1S) by using the method already described in Section 3.4.2. However, in cavitation conditions, the presence of an additional synchronous pressure pulsation at the frequency  $f_0$  generally lower than the precession frequency makes the identification of the precession cycles in the raw pressure signal difficult. An additional post-processing is necessary to clearly identify them. The idea is to suppress the synchronous pressure pulsations from the original pressure signals. For this purpose, the synchronous component of the pressure fluctuations is computed in the time domain by averaging the wall pressure signals measured at 4 different locations in the upstream section of the cone. The convective component experienced by each wall pressure sensor is, then, deduced according to Equation 3.2.

The synchronous pressure pulsations occurring at the frequency  $f_0$  are completely suppressed in the convective pressure component, giving rise to a periodical pressure signal. The procedure is illustrated in Figure 4.4, in which an example of a raw pressure signal and the corresponding convective pressure component is shown, together with the auto-spectral density functions.

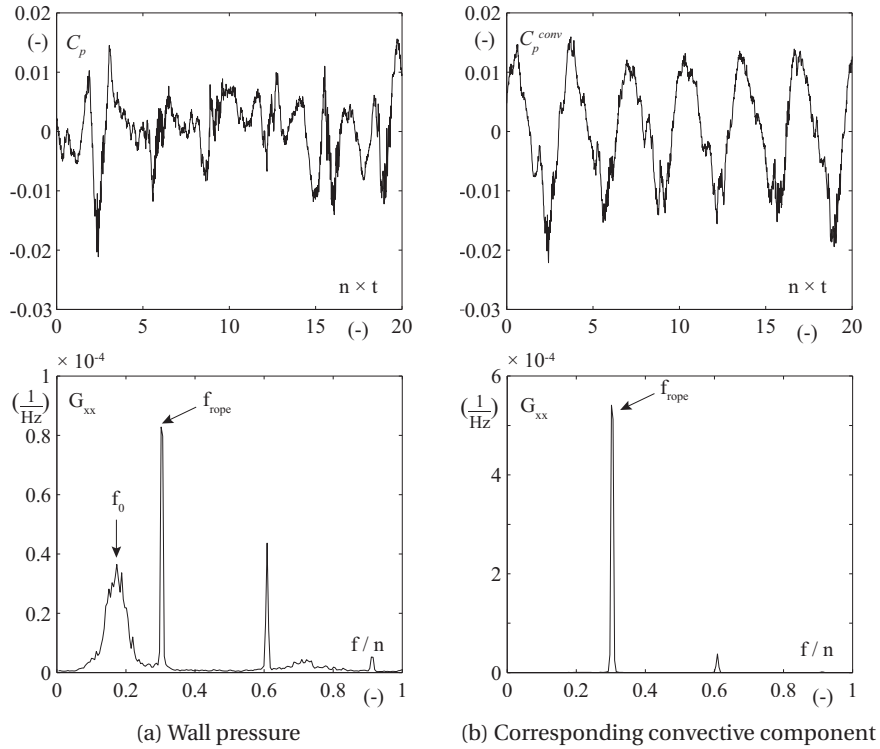
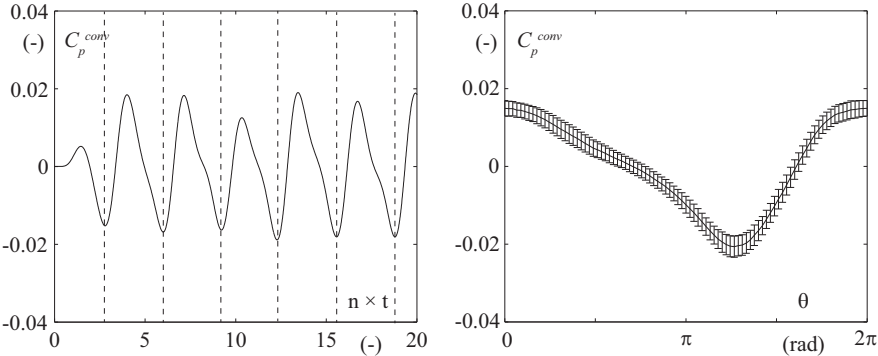


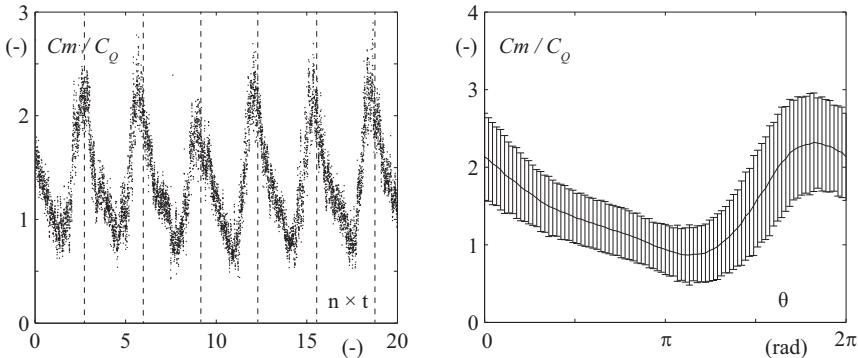
Figure 4.4: Comparison between a pressure signal (position C1E) measured in the draft tube cone at OP#2 in cavitation conditions and the corresponding convective pressure component, together with the corresponding auto-spectral density functions ( $Q_{ED} = 0.128$ ,  $\sigma = 0.11$ ).

In the following, the phase averaging of the velocity signals is based on the convective component of a pressure signal measured in the draft tube cone (location C1S). The successive precession cycles are identified in the convective pressure signal through their minimum pressure value and their limits are reported in the velocity signals. The different precession cycles are then superimposed and split into 180 phase windows. The velocity data corresponding to the same phase window are averaged together, allowing for the reconstruction of the evolution of both axial and tangential velocity components over a single precession period at each given radial position. An example of a convective pressure signal and an axial velocity signal is presented in Figure 4.5, together with the resulting mean phase averaged signals. The limits of the precession cycles are marked by the dashed lines. The convective pressure signal is low-pass filtered with a cut-off frequency of 15 Hz to clearly determine the pressure minimum but the raw convective pressure signal is used for the phase averaging.

**Chapter 4. Effect of cavitation on the precessing vortex core and system interaction**



(a) Convective pressure component (filtered) and the resulting phase averaged signal



(b) Axial velocity signal and the resulting phase averaged signal

Figure 4.5: Example of a convective pressure signal and an axial velocity signal, together with the resulting phase averaged signals ( $Q_{ED} = 0.128$ ,  $\sigma = 0.13$ ).



#### 4.2.4 Radial positions for LDV measurements

LDV measurements are performed along two different axes ( $x$ -axis and  $y$ -axis) in two different horizontal cross-sections of the draft tube cone, referred to LDV measurement sections 1 and 2 (see Section 2.3.1). The focal length of the lens is equal to 500 mm to survey the complete diameters for both measurement sections. In cavitation-free conditions, the flow velocity components are measured synchronously with the wall pressure measurement with a step of 10 mm across the entire  $x$  and  $y$  axes. A visualization of the cavitation vortex rope is given in 4.6. Each snapshot corresponds to a given phase of the precession cycle. The discharge factor and the Thoma number are equal to  $Q_{ED} = 0.128$  and  $\sigma = 0.17$ , respectively. As illustrated by this visualization, the periodical passage of the cavitation vortex rope across the measurement axis prevents the measurement of reliable data at certain radial positions, due to the reflection of the Laser beams at the cavity surface. In Figure 4.6, the optical access is located on the left side of the image. Three radial positions are marked in the measurement section 2 by black crosses at  $x_1 = -3R/4$ ,  $x_2 = 0$  and  $x_3 = 3R/4$  and three other radial positions are marked in the section 1 by white crosses at  $x_4 = -3R/4$ ,  $x_5 = -3R/8$  and  $x_6 = 0$ . For each radial position, the mean phase averaged velocity signals are computed by using the methodology previously described. The results for the tangential velocity components  $Cu$  are given in Figure 4.7 for the measurement section 2 and in Figure 4.8 for the measurement section 1.

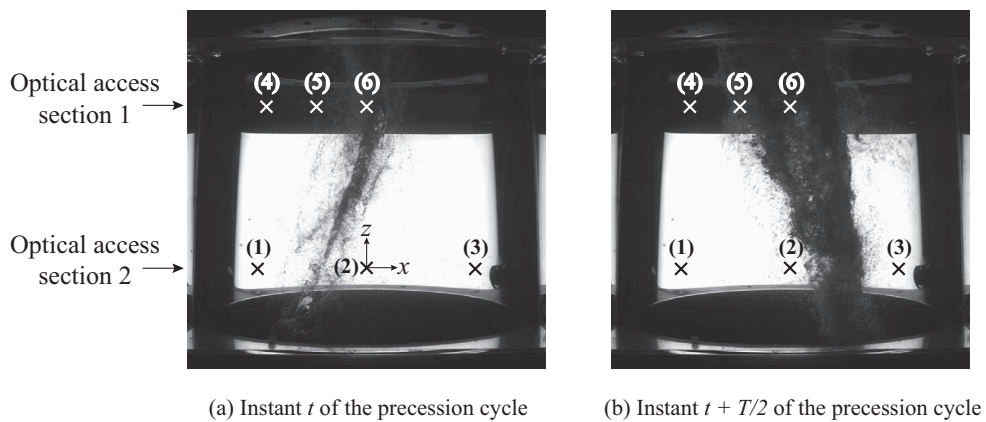


Figure 4.6: Visualization of the cavitation vortex rope at two different instants of the precession period, corresponding to the passages of the vortex rope across the measurement diameter  $x$  ( $Q_{ED} = 0.128$ ,  $\sigma = 0.17$ ).

#### LDV measurement section 2

In the section 2, the LDV measurements performed at the radial position (1) are not affected by the cavitation as the vortex rope does not interfere with the measurement volume at any instant of the precession period. In Figure 4.7-a, it can also be noticed that the LDV seems to produce valid velocities even when the vortex rope passes across the measurement diameter,

## Chapter 4. Effect of cavitation on the precessing vortex core and system interaction

despite potential problems due to the Laser beam reflections. This can be explained by the low vapor fraction within the vortex core at this particular phase of the period, for which the amplitude of the synchronous pressure pulsations is at its highest level.

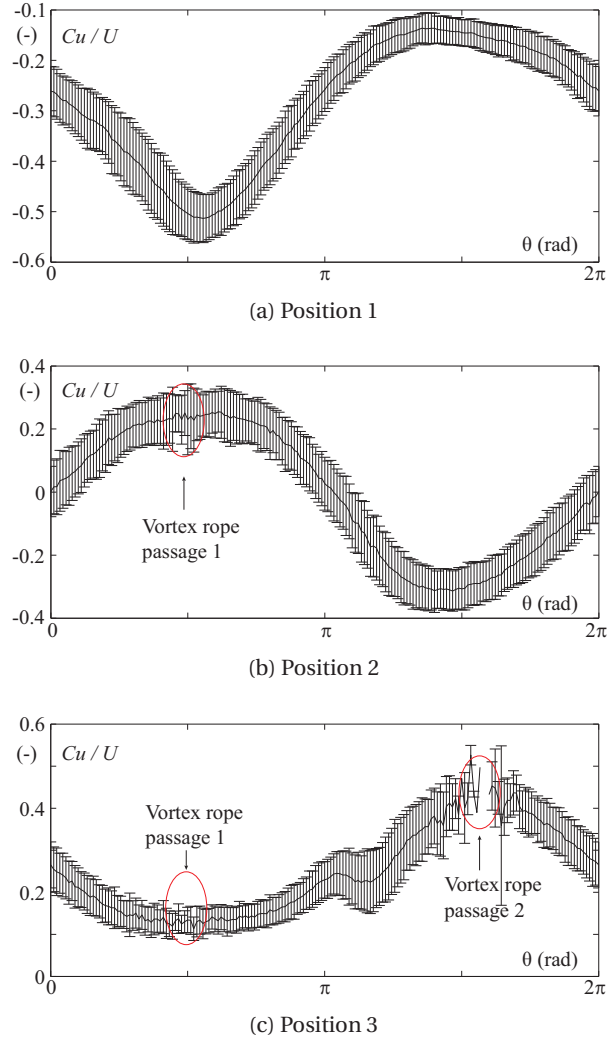


Figure 4.7: Mean phase averaged tangential velocity computed at 3 different radial positions along the  $x$ -axis of the measurement section 2 ( $Q_{ED} = 0.128$ ,  $\sigma = 0.17$ )

At the radial position (2), the cavitation vortex rope passes periodically between the measurement volume and the optical access. It results in a slightly noisy mean phase averaged signal when the relative phase of the precession period is nearly equal to  $\theta = \pi/2$ , as shown in Figure 4.7-b. However, as mentioned previously, the cavitation volume at this instant is low, enabling the reconstruction of a reliable mean phase averaged signal at this phase of the precession cycle. The LDV measurements are disturbed twice during one single precession cycle when the measurement volume is located at the radial position (3). The first passage produces a slight noise in the mean phase averaged signal. The vortex rope passes a second time between

the LDV probe and the measurement volume, resulting in a complete loss of information for the phases of the precession cycle between  $\theta = 3\pi/2$  and  $\theta = 5\pi/3$  because of the large size of the cavity at this instant.

### LDV measurement section 1

In the section 1, the size of the cavitation volume is greater than that observed in section 2 and the trajectory of the vortex rope is less wide, as shown in the previous chapter.

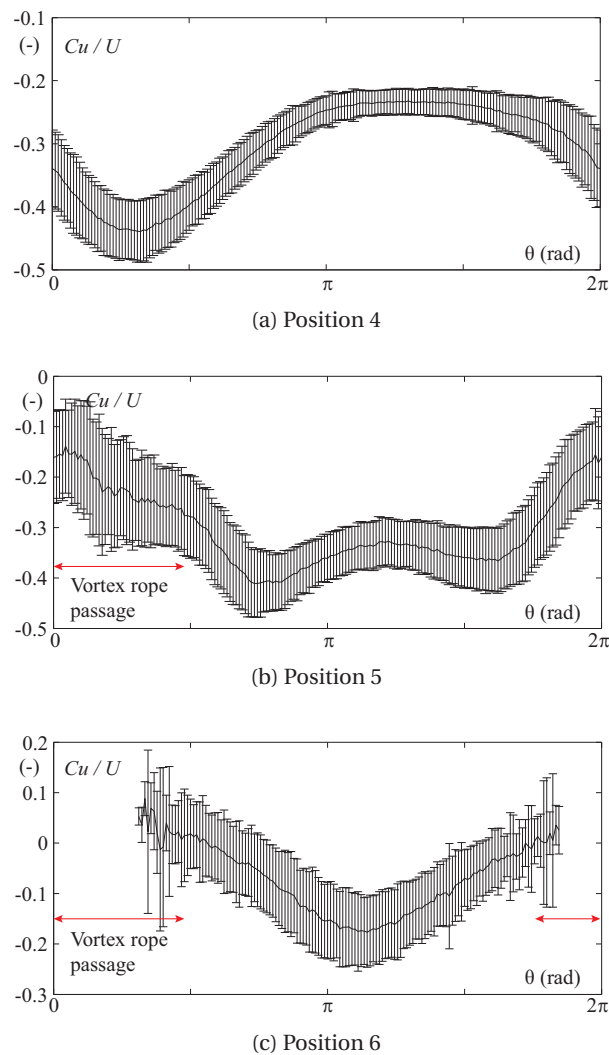


Figure 4.8: Mean phase averaged tangential velocity computed at 3 different radial positions along the  $x$ -axis of the LDV measurement section 1 ( $Q_{ED} = 0.128$ ,  $\sigma = 0.17$ ).

## Chapter 4. Effect of cavitation on the precessing vortex core and system interaction

Consequently, the LDV measurements are strongly disturbed by the presence of the cavitation volume beyond the radial position (5). At this radial position, the mean phase averaged velocity signals are disturbed during the corresponding phases of the precession period between  $\theta = 0$  to  $\theta = \pi/2$ . At the radial position (6), which corresponds to the centre of the section, the information is completely lost during a large segment of the precession period, from about  $\theta = 0$  to  $\theta = \pi/2$ , as well as from  $\theta = 7\pi/4$  to  $\theta = 2\pi$ .

Regarding these preliminary observations, the range of investigated radial positions must be adapted for each LDV survey depending on the size of the cavity and the measurement section. Table 4.2 summarizes the radial positions for which LDV measurements have been performed at the different investigated flow conditions.

Table 4.2: Radial positions of the control volume for each investigated operating conditions

OP#	$\sigma$ (-)	Measurement section	Radial position
1	0.10	1	$-R \rightarrow -R/4$
		2	$-R \rightarrow 0$
	0.13	1	$-R \rightarrow 0$
		2	$-R \rightarrow 0$
	0.31	1	$-R \rightarrow R$
		2	$-R \rightarrow R$
2	0.13	1	$-R \rightarrow -R/4$
		2	$-R \rightarrow 0$
	0.1625	1	$-R \rightarrow -R/4$
		2	$-R \rightarrow 0$
	0.38	1	$-R \rightarrow R$
		2	$-R \rightarrow R$

### 4.3 Cavitation influence on pressure fluctuations

#### 4.3.1 Resonance identification

The influence of the Thoma number on the frequencies of interest, i.e the precession and the natural frequencies, as well on the amplitude of the pressure fluctuations, is investigated by computing the auto-spectral density function of a wall pressure signal measured in the feeding pipe for each value of  $\sigma$ . The evolution of both natural and precession frequencies with the Thoma number at OP#1 is reported in Figure 4.9, together with the evolution of the auto-spectra amplitude at  $f_{rope}$ . Similar results are also presented in Figure 4.10 for OP#2.

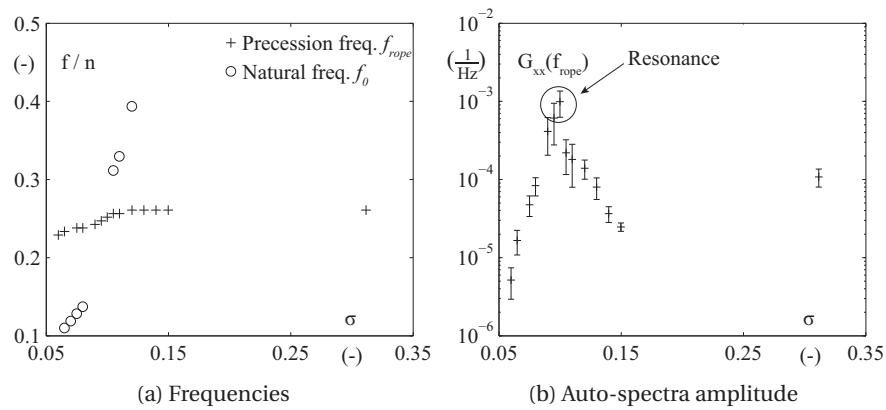


Figure 4.9: (a) Frequencies of interest (precession and natural frequencies) and (b) auto-spectra amplitude at the precession frequency as a function of the Thoma number at OP#1. The pressure signal is measured in the feeding pipe (location P1).

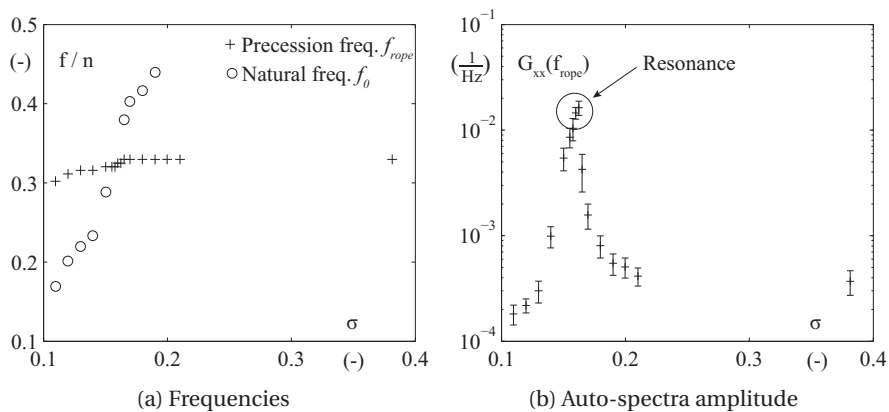


Figure 4.10: (a) Frequencies of interest (precession and natural frequencies) and (b) auto-spectra amplitude at the precession frequency as a function of the Thoma number at OP#2. The pressure signal is measured in the feeding pipe (location P1).

## Chapter 4. Effect of cavitation on the precessing vortex core and system interaction

---

The development of cavitation has little impact on the precession frequency. The latter increases slightly with the Thoma number, from  $0.23 \times n$  to  $0.26 \times n$  at OP#1 and from  $0.30 \times n$  to  $0.33 \times n$  at OP#2. Beyond a certain value of  $\sigma$  ( $\sigma = 0.12$  for OP#1 and  $\sigma = 0.17$  for OP#2), the precession frequency remains constant although the Thoma number increases, as the cavitation volume has already almost disappeared beyond this threshold. These results are however contrary to those obtained by Arpe [6], who reported a decrease of the precession frequency as  $\sigma$  increases. Concerning the frequency  $f_0$ , it increases strongly as the Thoma number increases, from  $0.11 \times n$  to  $0.39 \times n$  at OP#1 in the range of  $\sigma = [0.06 - 0.12]$  and from  $0.17 \times n$  to  $0.44 \times n$  at OP#2 in the range of  $\sigma = [0.11 - 0.19]$ . Beyond the value  $\sigma = 0.12$  at OP#1 and  $\sigma = 0.19$  at OP#2, the identification of the frequency  $f_0$  in the spectra of the pressure signals is not possible anymore, as the cavitation volume has almost disappeared, inducing a strong decrease of the pressure fluctuations at this frequency.

The evolution of  $f_0$  with the Thoma number, as well as the synchronous nature of the pressure fluctuations occurring at this frequency, suggests that  $f_0$  can be identified as the natural frequency of the hydro-acoustic system, which strongly depends on the wave speed and therefore of the cavitation volume [46]. However, the exact physical mechanisms driving the propagation of pressure fluctuations at the frequency  $f_0$  remain unclear, as no excitation source can be identified in the system at this frequency. It may be a result of a self-oscillation of the cavitation volume at the natural frequency.

Increasing the value of the Thoma number, the difference between the precession frequency, seen as an excitation frequency for the system, and the natural frequency is reduced, resulting in an important increase of the amplitude of the synchronous pressure fluctuations propagating in the system. It reaches its maximum when the frequency  $f_0$  matches the excitation frequency  $f_{rope}$ , which corresponds to the resonance conditions. It occurs when the Thoma number is equal to  $\sigma = 0.10$  for OP#1 and  $\sigma = 0.1625$  for OP#2. Beyond the resonance conditions, the frequency  $f_0$  again increases as the value of the Thoma number is increased, resulting in a drop of the amplitude of the pressure fluctuations.

### 4.3.2 Pressure fluctuations decomposition in the cone

For each operating condition, the pressure fluctuations in the draft tube cone are decomposed into convective and synchronous components in order to highlight the effect of cavitation on each of them. Both pressure components are computed in the time domain by applying Equations 3.1 and 3.2 to the wall pressure signals measured in the same cross-section of the draft tube cone. The mean phase averaged signal is then computed for each pressure component by using the convective pressure component recorded by the pressure sensor C1S for the identification of the successive precession cycles. In order to highlight the effect of cavitation on the amplitude of each pressure component, the RMS value of the mean phase averaged signals is computed for each value of  $\sigma$  by integrating directly the square of the the

### 4.3. Cavitation influence on pressure fluctuations

mean phase averaged signals over one precession period, as following:

$$\text{RMS} = \sqrt{\frac{1}{T} \int_0^T \tilde{C}_p^2(t) dt} \quad (4.1)$$

The evolution of the RMS value with the value of  $\sigma$  for each of the 4 convective components and the synchronous component computed in the upper section of the cone is presented in Figure 4.11 for OP#1 and in Figure 4.12 for OP#2.

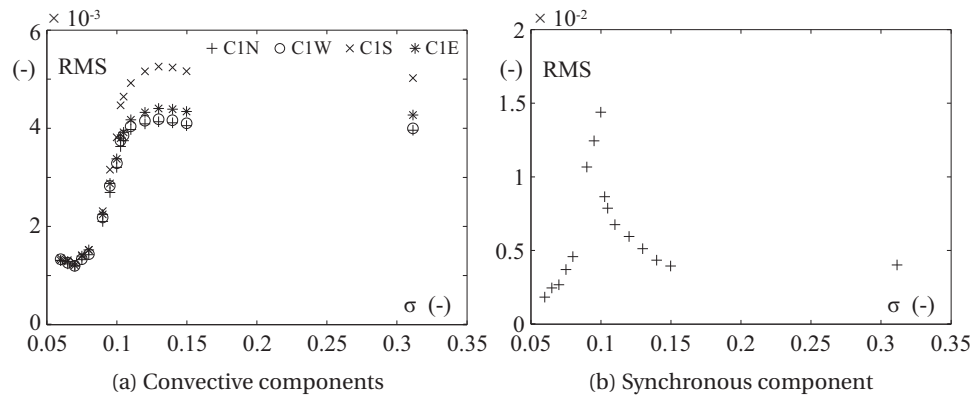


Figure 4.11: RMS value of the convective and synchronous pressure components as a function of the Thoma number in the upper section of the cone at OP#1.

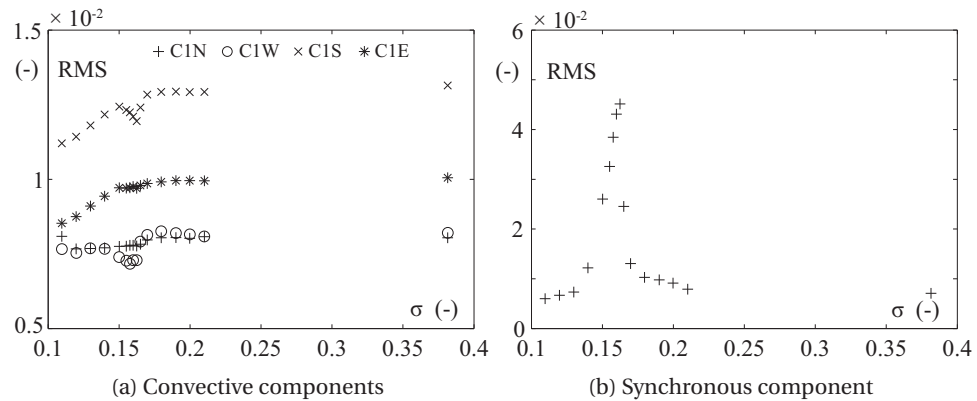


Figure 4.12: RMS value of both convective and synchronous pressure components as a function of the Thoma number in the upper section of the cone at OP#2.

The synchronous pressure component is strongly amplified approaching the resonance conditions for both operating conditions. This was expected, as the synchronous pressure compo-

#### **Chapter 4. Effect of cavitation on the precessing vortex core and system interaction**

---

ment corresponds to the response of the hydraulic system to the excitation source. However, the amplitude of the synchronous pressure fluctuations is greatly higher at OP#2, which can be explained by the higher intensity of the excitation source at this point, as shown in the previous chapter.

More interesting is the effect of cavitation on the convective pressure components for both operating points. Figures 4.11-a and 4.12-a show that a decrease of the pressure level in the draft tube induces a decrease of the convective pressure components amplitude. It indicates that the development of cavitation in the vortex core modifies the vortex dynamics by inducing a contraction of its trajectory. Above a given value of  $\sigma$ , a modification of the pressure level does not affect the RMS value of the convective components, as the cavitation volume has almost disappeared. At OP#2, it can be noticed that the RMS value of the convective components locally decreases when the resonance conditions are reached. The reason might be that the synchronous pressure fluctuations of high amplitude occurring in resonance conditions induce a periodical fluctuation of the cavitation volume at the precession frequency. As it is shown that the amount of cavitation affects the dynamics of the precessing vortex rope via the amplitude of the convective components, a periodical fluctuation of the cavitation volume is able to modify instantaneously the vortex rope dynamics during one precession cycle. The drop of the RMS value may be a result of these non-linear effects, which will be investigated more precisely in the next chapter.



## 4.4 Flow fields in cavitation-free conditions

### 4.4.1 Mean phase averaged velocity profiles

The flow velocity fields along both  $x$  and  $y$  axes are first measured in cavitation-free conditions at OP#1 and OP#2 and the mean phase averaged velocity signals are computed for both velocity components  $C_m$  and  $C_u$  at each radial position. The resulting evolution of the velocity profiles over one precession cycle is presented in Figures 4.13 and 4.14 for both axial and tangential velocity components in the measurement section 2 at OP#1. Similar results at OP#2 are presented in Figures 4.15 and 4.16. The results are interpolated via a cubic spline interpolation for a better visualization. The results obtained in the measurement section 1 are presented in Appendix C for both operating points.

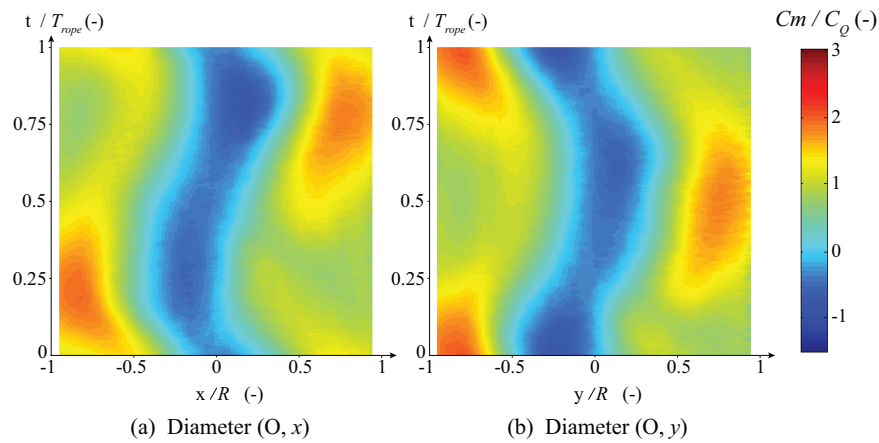


Figure 4.13: Evolution of the axial velocity profile over one precession cycle in the measurement section 2 at OP#1 ( $Q_{ED} = 0.161$ ,  $\sigma = \sigma_{atm} = 0.31$ ).

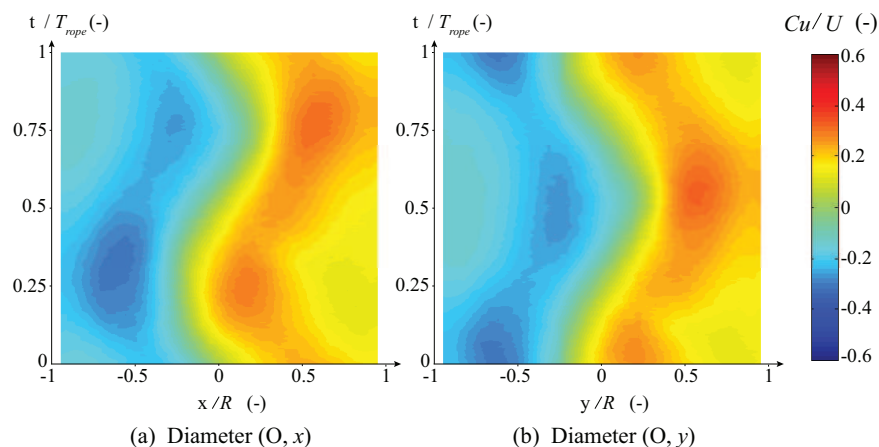


Figure 4.14: Evolution of the tangential velocity profile over one precession cycle in the measurement section 2 at OP#1 ( $Q_{ED} = 0.161$ ,  $\sigma = \sigma_{atm} = 0.31$ ).

## Chapter 4. Effect of cavitation on the precessing vortex core and system interaction

For each operating point, the velocity profiles feature a periodical oscillation at the precession frequency. The phase shift between the velocity fluctuations measured along the two different axes is equal to about  $T/4$ , corresponding to the spatial shift between the two axes.

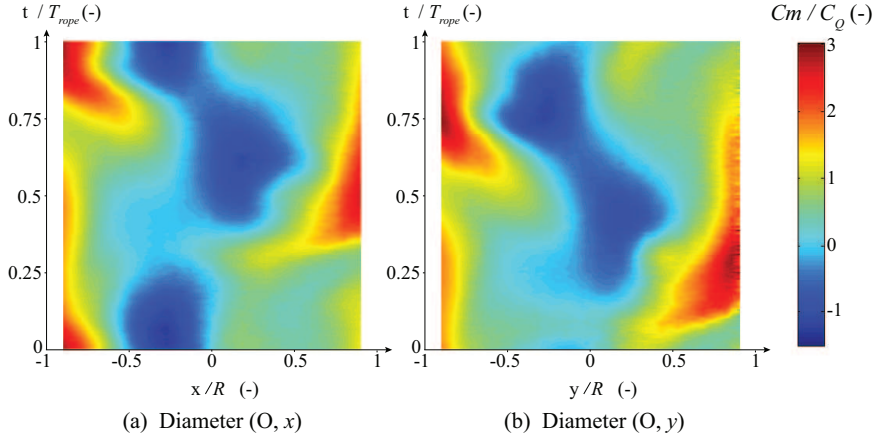


Figure 4.15: Evolution of the axial velocity profile over one precession cycle in the measurement section 2 at OP#2 ( $Q_{ED} = 0.128$ ,  $\sigma = \sigma_{atm} = 0.38$ ).

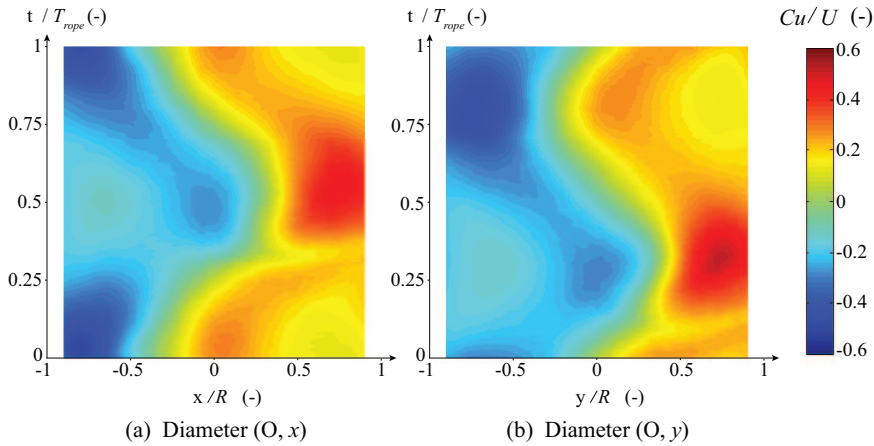


Figure 4.16: Evolution of the tangential velocity profile over one precession cycle in the measurement section 2 at OP#2 ( $Q_{ED} = 0.128$ ,  $\sigma = \sigma_{atm} = 0.38$ ).

For each phase value, there is a radial position for which the tangential velocity component is zero ( $Cu = 0$ ). This position moves periodically around the centre of the section, which illustrates the rotation of the vortex centre around the section centre. The amplitude of this motion is larger at OP#2 and is accompanied by a higher maximum tangential velocity between the point  $Cu = 0$  and the cone wall, in accordance with the observations regarding the vortex trajectory in Section 3.5.

Concerning the axial velocity profiles, a zone of recirculating flow, i.e. with an axial velocity  $Cm < 0$ , is highlighted at both operating points. The position of the recirculation zone is

clearly unsteady and moves periodically with the precession of the vortex core. This behavior has already been reported by different authors investigating highly swirling flows, for instance Griffiths et al. [37] or more recently Martinelli et al. [58]. The fluctuation of the recirculation zone position is much more important at OP#2 than at OP#1, which is a result of the larger vortex trajectory observed at this point, as highlighted in Section 3.5.2. When the recirculation zone is at its position closer to the wall, both axial and tangential velocity components reach their maximum value, as shown in Figures 4.15 and 4.16. It corresponds to the passage of the vortex core across the measurement diameter. These results indicate that the recirculation zone precesses with the vortex centre, the latter being located at the boundaries of the recirculation zone [37].

#### 4.4.2 Vortex centre passage

As mentioned previously, the tangential velocity profiles are characterized at each phase of the precession period by a radial position for which the value of  $Cu$  is equal to 0. This position moves periodically on either side of the section centre. Its evolution over one precession period is given in Figure 4.18 for OP#1 and in Figure 4.18 for OP#2. This position corresponds to the one for which the horizontal flow streamlines in the  $(x, y)$ -plane are tangent to the measurement axis, as illustrated in Figure 4.17 with the drawings of an axis-symmetric vortex with circular streamlines (Figure 4.17-a) and an asymmetric vortex with deformed streamlines (Figure 4.17-b).

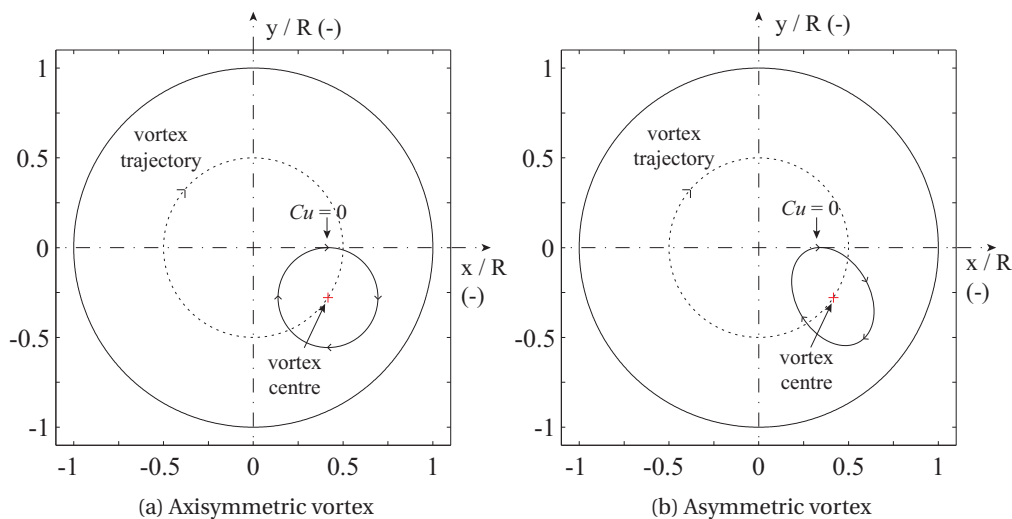


Figure 4.17: Sketch of axis-symmetric and asymmetric vortices with one corresponding horizontal flow streamline tangent to the  $x$ -axis.

In both sketches, the vortex centre is represented when it is not located on one of the measurement axes. However, the tangential velocity component  $Cu$  is equal to 0 at a given radial position on both measurement axes. It corresponds to the position for which the horizontal

## Chapter 4. Effect of cavitation on the precessing vortex core and system interaction

flow streamline is tangent to the axis. This is illustrated in Figure 4.17 for the  $x$ -axis. In this case, the point where  $Cu = 0$  moves periodically along each axis from the radial positions  $r = R_t = 0.5 \times R$  to  $r = -R_t = -0.5 \times R$ , with  $R_t$  the radius of the circular vortex trajectory. The extremum positions of this point correspond to the passage of the vortex centre across the axis  $x$  or  $y$ . Additionally, in the case of an axisymmetric vortex, the point  $Cu = 0$  lies exactly on the section centre on a given measurement axis when the vortex core passes across the second measurement axis. It is not the case for an asymmetric vortex because of the deformation of the flow streamlines. Therefore, the evolution of the radial position where  $Cu = 0$  over one precession period can provide additional information about the vortex trajectory, whether in cavitation-free conditions or in cavitation conditions.

For the present test-case, the vortex core passage across the measurement axes is marked by the vertical black solid lines in Figure 4.18 for OP#1 and in Figure 4.18 for OP#2.

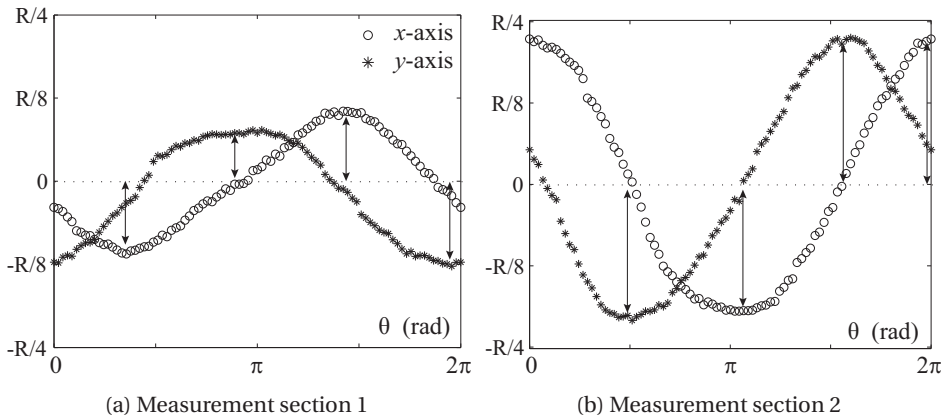


Figure 4.18: Evolution of the radial position for which  $Cu = 0$  during one precession period at OP#1 ( $Q_{ED} = 0.161$ ,  $\sigma_{atm} = 0.31$ ).

At OP#1, the position for which  $Cu = 0$  evolves approximately from  $-R/8$  to  $R/8$  along the  $x$ -axis and from  $-R/8$  to  $R/16$  along the  $y$ -axis in the measurement section 1. In the measurement section 2, the extremum positions are approximately equal to  $-3R/16$  and  $R/4$  for the  $x$ -axis,  $-3R/16$  and  $R/4$  for the  $y$ -axis. This difference between both measurement sections indicates a widening of the vortex trajectory away from the runner outlet, confirming the results obtained in Chapter 3. Moreover, when the vortex passes across a given measurement axis, the point for which  $Cu = 0$  approximately lies on the centre of the second measurement axis, highlighting the relative symmetry of the vortex for high values of discharge factor. At OP#2, the trajectory of the vortex centre is larger than the one at OP#1, as demonstrated in the previous chapter. Moreover, during the passage of the vortex across a given measurement axis, the point  $Cu = 0$  does not lie on the centre of the second measurement axis (Figure 4.19), which illustrates the deformation of the flow streamlines due to the asymmetry of the vortex core. The increasing asymmetry of the vortex as the discharge factor is decreased has

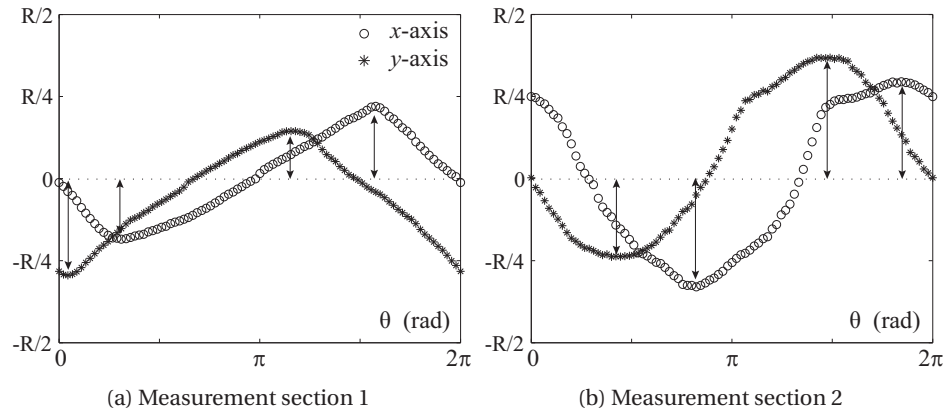


Figure 4.19: Evolution of the radial position for which  $Cu = 0$  during one precession period at OP#2 ( $Q_{ED} = 0.128$ ,  $\sigma_{atm} = 0.38$ ).

already been observed in the previous chapter and can be explained by the widening of the vortex trajectory, making the vortex centre position closer to the cone wall. It induces a more important squeezing of the flow between the vortex centre and the cone wall, resulting in an increasing dissymmetry of the vortex core.

### 4.4.3 Amplitude and phase shift of velocity fluctuations

#### RMS value

In order to evaluate the amplitude of the axial and tangential velocity fluctuations, their RMS value is computed similarly to the pressure fluctuations. It is performed at each radial position by directly integrating the square of the mean phase averaged velocity fluctuations over one precession period (Equation 4.1). The evolution of the RMS value for both velocity components with the radial position is presented in Figure 4.20 for OP#1 and in Figure 4.21 for OP#2. Only the results obtained in the measurement section 2 are presented there.

Globally, the evolution of the RMS value of both velocity components features the same characteristics whatever the operating point. For the axial velocity component in Figures 4.20-a and 4.21-a, the evolution of the RMS value presents two maxima. The first one is located near the cone wall at the radial position for which the axial velocity reaches its maximum value during the passage of the vortex core across the measurement axis. The second one is located at a radial position which is successively inside and outside the recirculation zone according to the periodical motion of the latter with the precession of the vortex rope. The minimum RMS value is observed at the section centre, i.e. at the average position of the recirculation zone centre, for which the flow is mainly turbulent. However, the minimum value is much more important at OP#2 as the vortex centre trajectory is larger, which induces a more important variation of the recirculation zone position and consequently a more important axial velocity

fluctuation at the section centre.

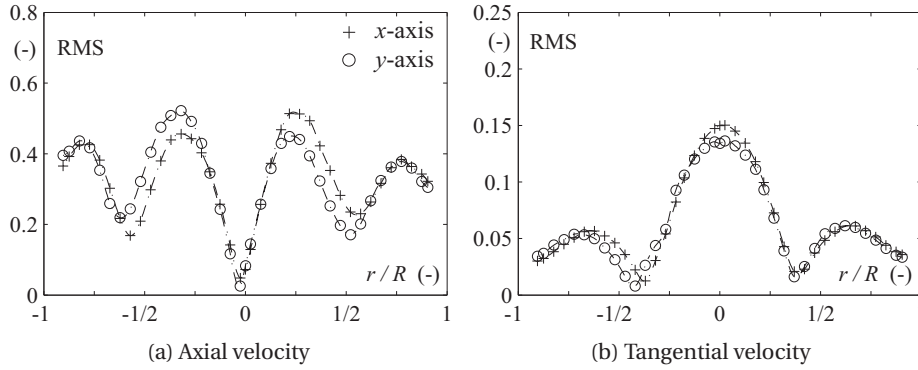


Figure 4.20: RMS value of the axial and tangential velocity fluctuations along the axes  $x$  and  $y$  at OP#1 in the measurement section 2 ( $Q_{ED} = 0.161$ ,  $\sigma_{atm} = 0.31$ ).

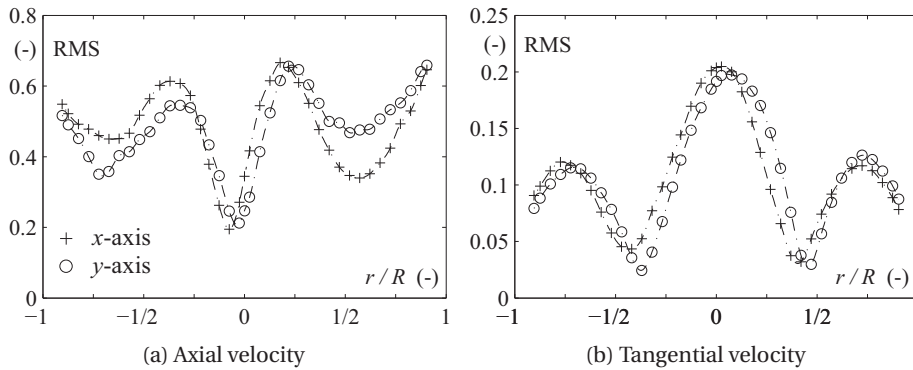


Figure 4.21: RMS value of the axial and tangential velocity fluctuations along the axes  $x$  and  $y$  at OP#2 in the measurement section 2 ( $Q_{ED} = 0.128$ ,  $\sigma_{atm} = 0.38$ ).

For the tangential velocity component, the evolution of the RMS value with the radial position also presents two distinct maxima. The first one is also located between the vortex centre and the cone wall at a radial position corresponding to the position for which the tangential flow is squeezed and accelerated during the passage of the vortex centre in the vicinity of the cone wall. The second position is located at the centre of the measurement axis. It is induced by the rotation of the vortex centre around this point which causes tangential velocity fluctuations of high amplitude because of the continuous change of the orientation of the velocity vectors. This type of profile for the RMS value of the tangential velocity component has already been reported by Heitor and Whitelaw [40] or more recently Fernandes et al. [34] in the case of swirling flows in combustor device. The maximum RMS value observed at the centre section is much more important at OP#2 as the trajectory of the precession vortex is larger for low values of discharge factor.

**Cross-correlation for time delay**

For a given radial position  $r$  between the cone wall ( $r = -R$ ) and the section centre ( $r = 0$ ), the mean phase averaged velocity signals are available at 4 different angular positions:  $\theta_1 = 0$ ,  $\theta_2 = -\pi/2$ ,  $\theta_3 = -\pi$  and  $\theta_4 = -3\pi/2$ . It corresponds respectively to the semi-axes  $x > 0$ ,  $y < 0$ ,  $x < 0$  and  $y > 0$ . These angular positions are illustrated in Figure 4.22. The vortex core rotates in the clockwise direction.

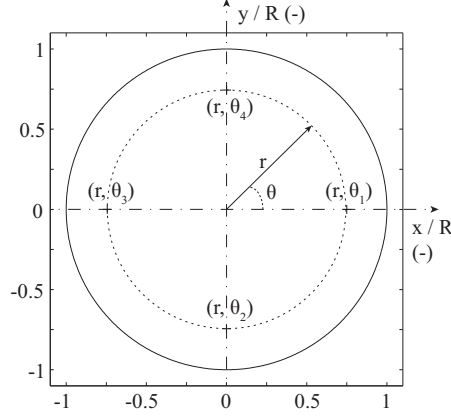


Figure 4.22: Different angular positions for a given radial position of the measurement volume.

For each radial position, the cross-correlation function is computed between the mean phase averaged velocity signals obtained at two consecutive angular positions [9]:

$$R_{12}(\tau) = E[Cm_1(t) \times Cm_2(t + \tau)] \tag{4.2}$$

with  $Cm_1$  and  $Cm_2$  the phase averaged axial velocity signals at the positions  $(r, \theta_1)$  and  $(r, \theta_2)$ , respectively. For two correlated signals, the cross-correlation function features a maximum peak at the value  $\tau$  which corresponds to the time delay between both signals [9]. The evolution of the time delay with the radial position for both axial and tangential velocity components is reported in Figure 4.23 for OP#1 and in Figure 4.24 for 2. The radial position and the time delay  $\tau$  are made dimensionless by the section radius and the precession period, respectively. The mean precession period is equal to  $T = 0.2875$  s at OP#1 and  $T = 0.2275$  s at OP#2. It is obtained by averaging the length of the individual precession periods identified during the phase averaging procedure.

At OP#1, the time delay remains approximately equal to  $\tau = T/4$  from  $r = -R$  to  $r = 0$  for all the pairs of angular positions, which corresponds to the spatial difference between two consecutive angular positions. It highlights the symmetry of the vortex trajectory for high values of discharge factor (flow regime 1). It can be noticed that the time delay for the tangential velocity components breaks down for the radial positions between  $r/R = -1/2$  and  $r/R = -1/4$

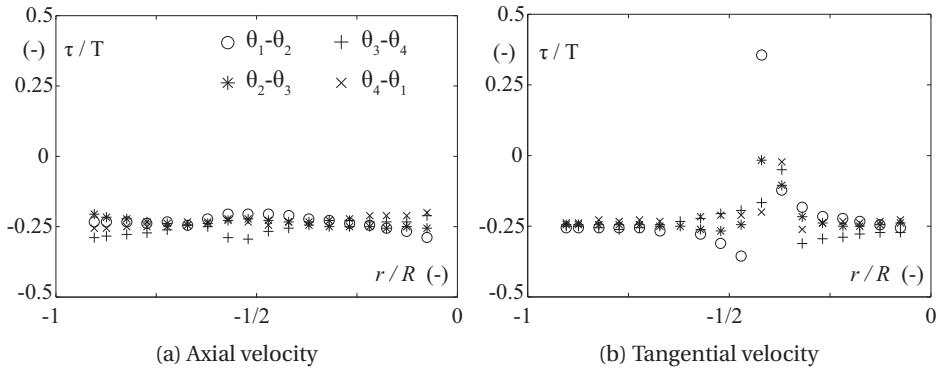


Figure 4.23: Time delay as a function of the the radial position for the axial and tangential velocity fluctuations at OP#1 in the measurement section 2 ( $Q_{ED} = 0.161$ ,  $\sigma_{atm} = 0.31$ ).

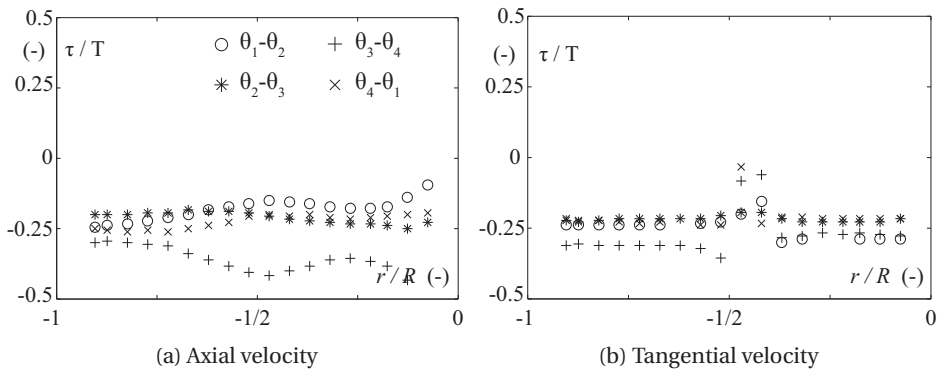


Figure 4.24: Time delay as a function of the radial position for the axial and tangential velocity fluctuations at OP#2 in the measurement section 2 ( $Q_{ED} = 0.128$ ,  $\sigma_{atm} = 0.38$ ).

in Figure 4.23-b, as the phase averaged tangential velocity signals change phase in this zone. This change does not occur exactly at the same radial position for both measurement axes. It results in a zone of finite length for which the value of the time delay is not reliable.

At OP#2, the results are slightly different, although the time delay is also approximately equal to  $T/4$  for both velocity components. The differences observed between the different pairs of angular position highlight the dissymmetry of the vortex rope precession which is observed for low values of discharge factor. In the light of these analyses, it can be concluded that the flow velocity fluctuations seem to be entirely driven by the convection of the vortex rope whereas the propagation of synchronous pressure fluctuations does not impact the flow field in the draft tube in cavitation-free conditions.



## 4.5 Flow fields in cavitation conditions

In this section, the flow velocity fields measured in cavitation conditions at OP#1 and OP#2 are analysed. For each operating point, LDV measurements are performed for two values of the Thoma number, which are chosen according to the resonance identification presented in Section 4.3.1:  $\sigma = 0.10$  (resonance) and  $\sigma = 0.13$  (out of resonance) at OP#1,  $\sigma = 0.13$  (out of resonance) and  $\sigma = 0.1625$  (resonance) at OP#2. At OP#1, the value of  $\sigma$  chosen for the investigation of the flow field in non-resonance conditions is higher than the one in resonance conditions as a decrease of the Thoma number below the value of  $\sigma = 0.09$  leads to the formation of a significant cavitation volume at this operating point, which does not permit a proper flow investigation.

LDV measurements are performed from the cone wall (position  $r = -R$ ) to the section centre (position  $r = 0$ ), as discussed in Section 4.2.4. In the following, only the results obtained in the measurement section 2 are presented and compared with the results obtained in cavitation-free conditions. In this measurement section, the size of cavitation vortex rope is less important than the one in the measurement 1, which is due to the positive pressure gradient in the main direction of the flow induced by the divergent shape of the cone and the decrease of the elevation  $Z$ .

### 4.5.1 Mean phase averaged velocity field

The evolution of the velocity profiles with the relative phase of the precession at OP#1 in resonance conditions is presented in Figure 4.25 for the axial velocity component and in Figure 4.26 for the tangential velocity component. Similarly, the results obtained in resonance conditions at OP#2 are presented in Figures 4.27 and 4.28. The velocity components  $Cm$  and  $Cu$  are made dimensionless with the discharge velocity  $C_Q$  and the circumferential runner speed  $U_{\bar{1}}$ , respectively. The mean phase averaged velocity signal is obtained after averaging between 600 and 780 precession periods, depending on the flow parameters and the corresponding precession frequency.

In a first approach, the velocity profiles display similar characteristics to those observed in cavitation-free conditions. The passage of the vortex rope across the measurement axes, which is given by the moment for which the radial position of the point  $Cu = 0$  is at its minimum (for the semi-axes  $x < 0$  and  $y < 0$ ), corresponds to the moment for which both tangential and axial velocity components reach their maximum values between the cone wall and the vortex centre. The recirculation zone is also closer to the cone wall. The maximum values of the axial and tangential velocity components are relatively similar to those observed in cavitation-free conditions for both operating points OP#1 and OP#2.

The periodical passage of the cavitation vortex rope across the measurement axes does almost not affect the quality of the LDV measurements at OP#1. At OP#2, the results are disrupted by the passage of the cavitation volume for the measurement axis  $y$ , which induces noisy mean

## Chapter 4. Effect of cavitation on the precessing vortex core and system interaction

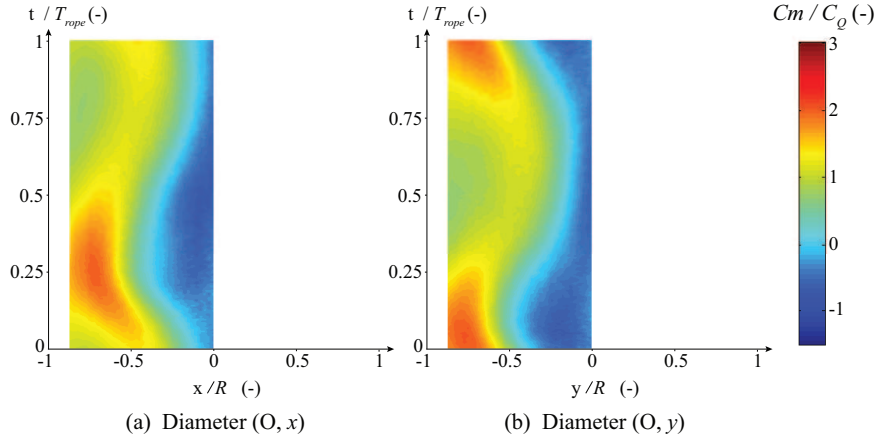


Figure 4.25: Evolution of the axial velocity profile over one precession period in the measurement section 2 at OP#1 in resonance conditions ( $Q_{ED} = 0.161$ ,  $\sigma = \sigma_{res} = 0.10$ ).

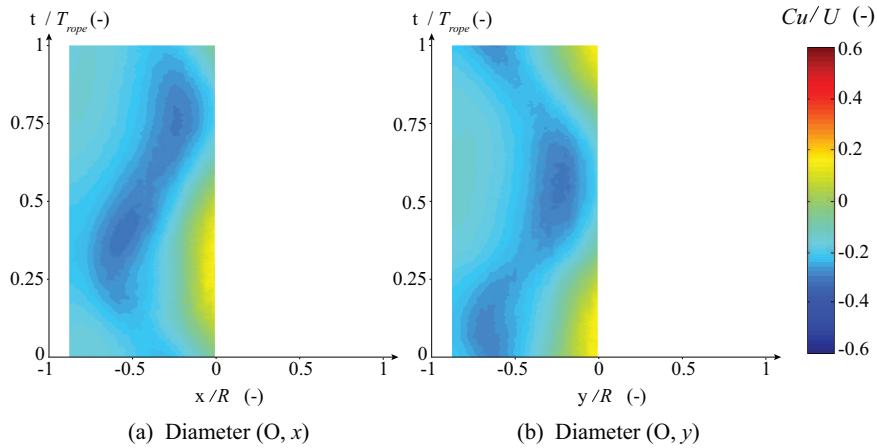


Figure 4.26: Evolution of the tangential velocity profile over one precession period in the measurement section 2 at OP#1 in resonance conditions ( $Q_{ED} = 0.161$ ,  $\sigma = \sigma_{res} = 0.10$ ).

phase averaged velocity signals at the instant  $t = 0.75 \times T_{rope}$  in Figures 4.27-b and 4.28-b. However, the passage of the cavitation vortex rope does not affect the measurements along the  $x$ -axis as the cavitation volume is at its minimum at this moment of the precession period.

For the non-resonance conditions at OP#1 and OP#2, the results are presented in Appendix C. The same preliminary conclusions can be drawn regarding the mean phase averaged velocity signals obtained in non-resonance conditions. However, at OP#2, the measurements are strongly disrupted by the cavitation vortex passage for both measurement axes, as the low pressure level in the draft tube promotes the development of an important cavity in the vortex core. Moreover, the cavity volume is relatively stable as the amplitude of the synchronous pressure pulsations in the cone is relatively low compared to that in resonance conditions.

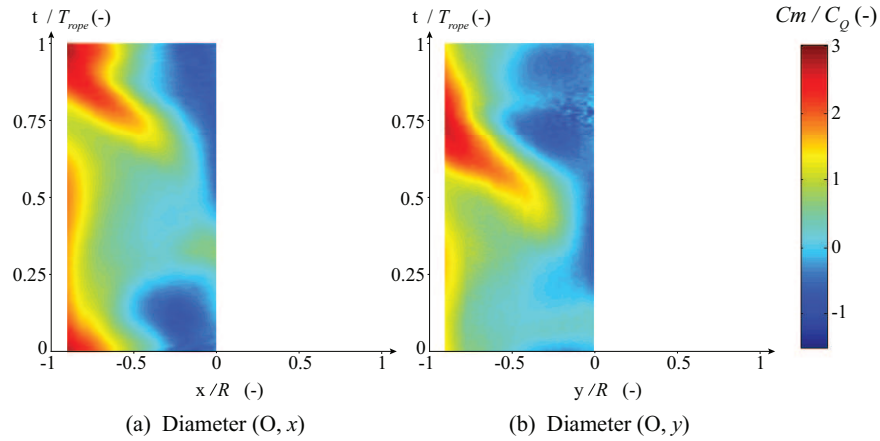


Figure 4.27: Evolution of the axial velocity profile over one precession period in the measurement section 2 at OP#2 in resonance conditions ( $Q_{ED} = 0.128$ ,  $\sigma = \sigma_{res} = 0.1625$ ).

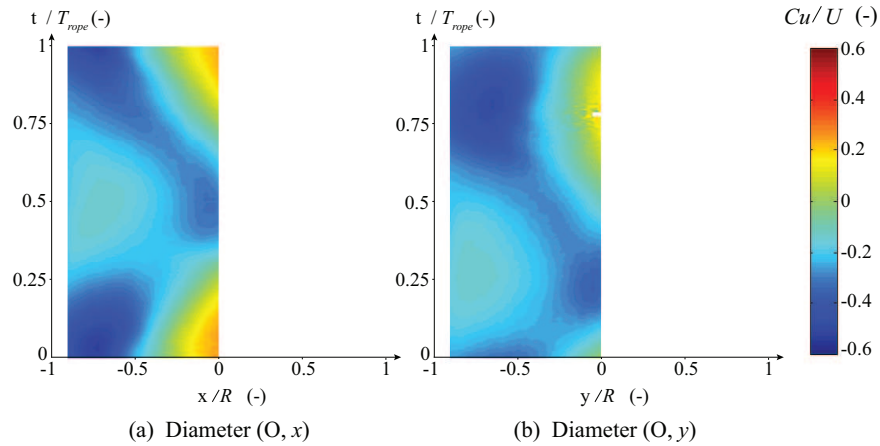


Figure 4.28: Evolution of the tangential velocity profile over one precession period in the measurement section 2 at #OP2 in resonance conditions ( $Q_{ED} = 0.128$ ,  $\sigma = \sigma_{res} = 0.1625$ ).

#### 4.5.2 Time delay and RMS value

Similarly to the analysis made for the results obtained in cavitation-free conditions, the time delay  $\tau$  between the phase averaged velocity signals obtained at two successive angular positions is computed in cavitation conditions for each radial position. However, the flow velocity components are only measured from  $r = -R$  to  $r = 0$ , making the computation of the time delay possible only for the angular positions  $\theta_2$  and  $\theta_3$ . The time delay as a function of the radial position for both operating points is presented in Figure 4.29 for the resonance conditions and in Figure 4.30 for the non-resonance conditions.

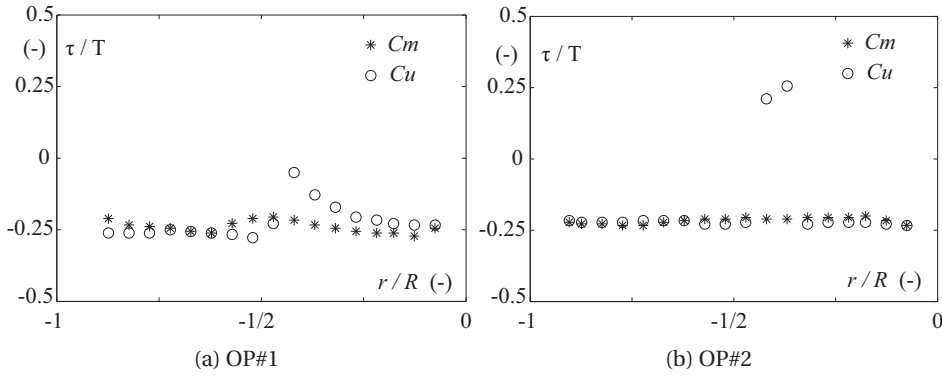


Figure 4.29: Time delay as a function of the radial position for the axial and tangential velocity fluctuations in resonance conditions ((a)  $Q_{ED} = 0.161$ ,  $\sigma_{res} = 0.10$  - (b)  $Q_{ED} = 0.128$ ,  $\sigma_{res} = 0.1625$ ).

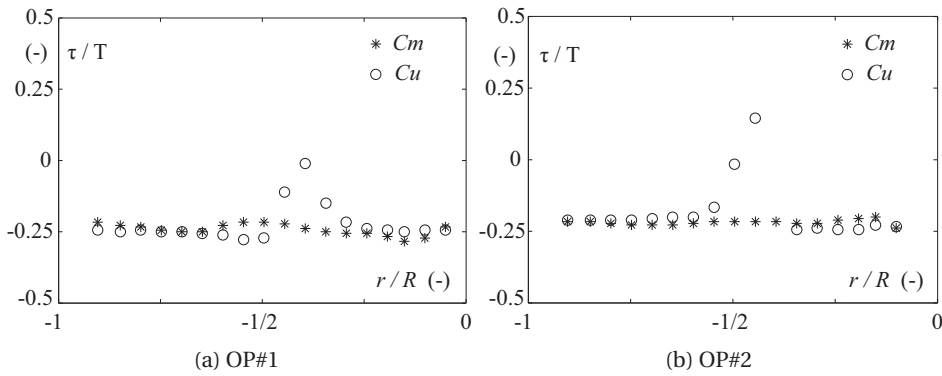


Figure 4.30: Time delay as a function of the radial position for the axial and tangential velocity fluctuations in non-resonance conditions ((a)  $Q_{ED} = 0.161$ ,  $\sigma_{out} = 0.13$  - (b)  $Q_{ED} = 0.128$ ,  $\sigma_{out} = 0.13$ ).

For both operating points, the results in terms of time delay are very similar to those obtained in cavitation-free conditions. The phase shift between two consecutive angular positions is equal to about  $T/4$  for both velocity components, whether in resonance conditions or in non-resonance conditions. The computation of the time delay for the tangential component again breaks down for the radial positions comprised between  $r/R = -1/2$  and  $r/R = -1/4$ .

These results confirm that the periodical fluctuations observed in both axial and tangential velocity signals are mainly induced by the vortex rope precession. Although the propagation of synchronous pressure fluctuations is able to induce a periodical fluctuation of the cavitation volume at the same frequency, particularly in resonance conditions as it will be discussed in the next chapter, the periodical axial and tangential velocity fields in the draft tube cone do not seem to be affected by the propagation of high synchronous pressure pulsations in

resonance conditions. It suggests that the discharge axial fluctuations induced by hydro-acoustic resonances are much smaller than the axial velocity disturbances caused by the precession of the vortex rope in the draft tube.

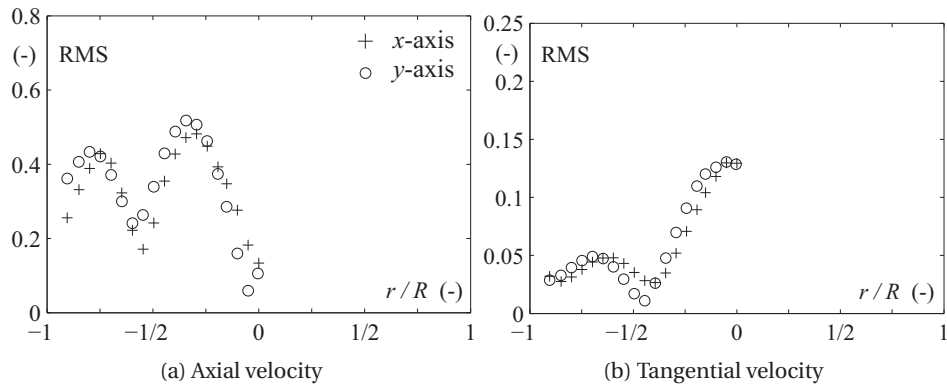


Figure 4.31: RMS value of the axial and tangential velocity fluctuations along the axes  $x$  and  $y$  at OP#1 in resonance conditions in the measurement section 2 ( $Q_{ED} = 0.161$ ,  $\sigma_{res} = 0.10$ ).

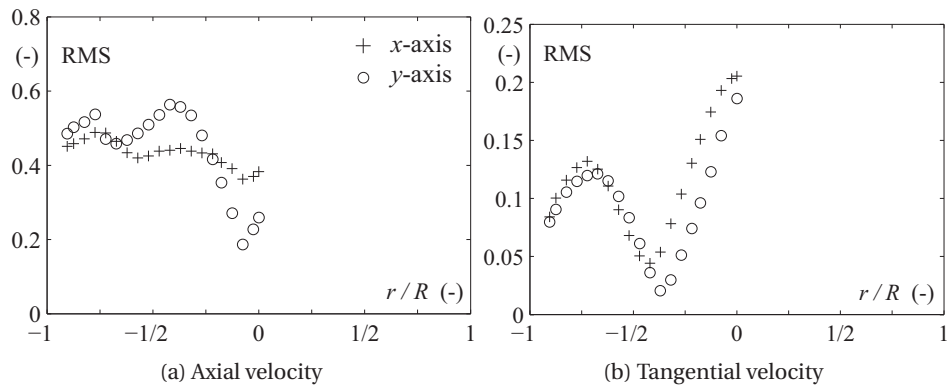


Figure 4.32: RMS value of the axial and tangential velocity fluctuations along the axes  $x$  and  $y$  at OP#2 in resonance conditions in the measurement section 2 ( $Q_{ED} = 0.128$ ,  $\sigma_{res} = 0.1625$ ).

The evolution of the RMS value with the radial position for both axial and tangential velocity components is presented in Figures 4.31 (resonance conditions) and 4.33 (non-resonance conditions) for OP#1, as well as in Figures 4.32 (resonance conditions) and 4.34 (non-resonance conditions) for OP#2. The profiles are plotted from  $r = -R$  to  $r = 0$  for most of the cases, except for the non-resonance case at OP#2 as the cavitation volume does not permit to obtain reliable results in the vicinity of the section centre of the measurement axis  $x$ .

For both operating points, the evolution of the RMS value along the measurement axes in cavitation conditions features similar characteristics to those observed in cavitation-free conditions. Some small differences are however worth being mentioned. At OP#1, the RMS

## Chapter 4. Effect of cavitation on the precessing vortex core and system interaction

values obtained in non-resonance conditions are very similar to those obtained in cavitation-free conditions for both velocity components, as the cavitation volume has almost disappeared for this value of  $\sigma$ . However, in resonance conditions, the maximum RMS values for the tangential component are slightly lower than those in cavitation-free conditions. It indicates the effect of the cavitation on the vortex rope dynamics, which is to contract the vortex trajectory and reduce therefore the precession frequency. This results is in agreement with the decrease of the RMS value of the convective pressure components observed when the value of the Thoma number is decreased (Section 4.3.2). At OP#2, the maximum RMS values for the tangential component is also slightly lower than those in cavitation-free conditions, specially for the measurement axis  $y$ .

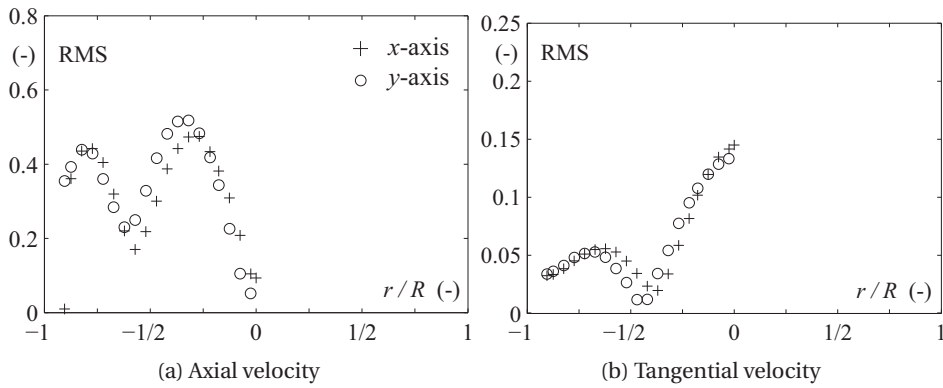


Figure 4.33: RMS value of both axial and tangential velocity fluctuations along the axes  $x$  and  $y$  at OP#1 in non-resonance conditions in the measurement section 2 ( $Q_{ED} = 0.161$ ,  $\sigma_{out} = 0.13$ ).

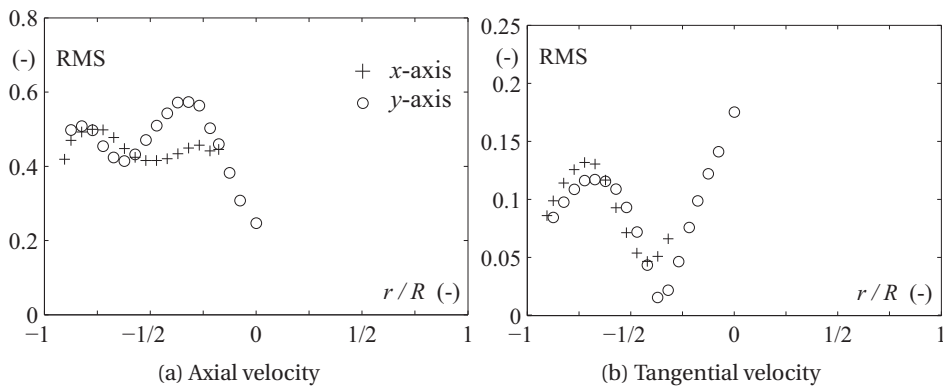


Figure 4.34: RMS value of both axial and tangential velocity fluctuations along the axes  $x$  and  $y$  at OP#2 in non-resonance conditions in the measurement section 2 ( $Q_{ED} = 0.128$ ,  $\sigma_{out} = 0.13$ ).

## 4.6 Summary and discussion

The effect of cavitation on the pressure fluctuations and the flow velocity fields in the draft tube is investigated, with a particular focus on the effect of the occurrence of resonance conditions. Pressure fluctuations measurements are first performed in the draft tube and the feeding pipes of the machine in a wide range of  $\sigma$ -values for two distinct operating points. A preliminary spectral analysis of pressure signals measured in cavitation condition reveals the propagation of synchronous pressure pulsations at a low frequency  $f_0$  in addition to the pressure fluctuations occurring at the precession frequency. The frequency  $f_0$  is identified as the first eigenfrequency of the system. The evolutions of the precession and natural frequencies and the amplitude of the pressure fluctuations with the Thoma number reveals the occurrence of a hydro-acoustic resonance at a given  $\sigma$ -value, for which the precession frequency matches with the first natural frequency of the system. The resonance conditions are characterized by an abrupt rise of the amplitude of the synchronous pressure component at the precession frequency.

Moreover, the effect of cavitation on the convective pressure components is revealed by computing their RMS value for each value of the Thoma number. It is shown that an increase of the amount of cavitation within the precessing vortex core leads to a decrease of the RMS value of the convective components, which is accompanied by a simultaneous slight decrease of the precession frequency. The development of cavitation in the vortex core alters therefore the dynamics of the precessing vortex rope, via a contraction of its trajectory and a reduction of its frequency, and therefore the excitation source intensity.

LDV measurements are performed in cavitation-free and cavitation conditions, including resonance, along two different axes of the draft tube cone for two operating points. A preliminary spectral analysis of the velocity signals measured in cavitation conditions reveals the absence of velocity fluctuations at the natural frequency  $f_0$ , contrary to the pressure signals. The mean phase averaged velocity signals are computed by using the convective pressure component of a pressure signal measured in the cone as a reference. For each investigated  $\sigma$ -value, the RMS value of the velocity fluctuations is computed, as well as the time delay between the velocity fluctuations measured at two different angular positions. The results suggest that the velocity fluctuations at the precession frequency are mainly induced by the convection of the precessing vortex rope in the draft tube. The periodical axial velocity field is not altered by the propagation of synchronous pressure fluctuations of high amplitude in resonance conditions. These results suggest that the discharge velocity fluctuations caused by the occurrence of hydro-acoustic resonances are much smaller than the axial velocity disturbances induced by the precession of the vortex rope. It might be confirmed by estimating the magnitude of discharge fluctuations in resonance conditions from the application of the unsteady Bernoulli equation at the runner exit and the cavitation volume fluctuations. A one-dimensional hydro-acoustic model can also be used with the hydro-acoustic parameters of the cavitation vortex rope identified in [53].





# 5 Influence of the Froude number on the resonance conditions

## 5.1 Non-linear effects in resonance conditions

### 5.1.1 Pressure pulsations in resonance conditions

In the previous chapter, it has been shown that resonance conditions are met when the precession frequency, acting as an excitation frequency for the system, matches with the first natural frequency of the hydraulic system. It induces a significant increase of the amplitude of the pressure fluctuations at the precession frequency in the entire system. A comparison between the wall pressure signals measured in the upper section of the draft tube cone at #OP2 in non-resonance and resonance conditions is presented in Figure 5.1.

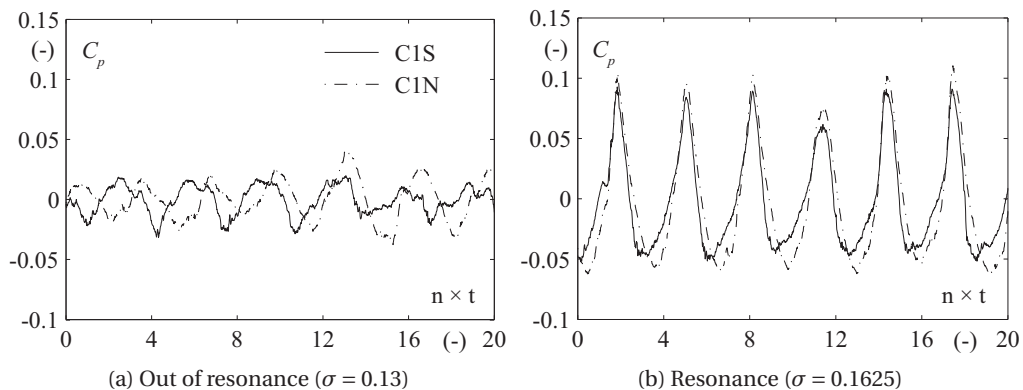


Figure 5.1: Fluctuations of the wall pressure coefficients measured in the upper section of the draft tube cone at OP#2 ( $Q_{ED} = 0.128$ ) in non-resonance and resonance conditions.

The peak-to-peak value of the pressure fluctuations in cavitation conditions corresponds to 15 % of the turbine head  $H$ , which is comparable with the amplitude observed during violent self-oscillations of the cavitation rope at full load conditions [59]. In resonance conditions, the pressure fluctuations in the same cross-section of the cone are almost synchronous contrary

to the non-resonance case, which is due to the amplification of the synchronous pressure component. It is expected these large pressure fluctuations to have an important effect on the cavitation volume as its size depends on the conditions of pressure in the draft tube.

### 5.1.2 Cavitation volume pulsations in resonance conditions

#### Methodology for the estimation of the vortex rope volume

The effect of resonance conditions on the cavitation volume is investigated by estimating the fluctuations and the average value of the cavity size in the draft tube cone by means of high speed visualizations. The corresponding setup is detailed in Section 2.4. The total number of frames is limited to 5'500 and the acquisition rate is equal to 1'000 fps. The visualizations of the vortex rope are recorded synchronously with pressure measurements.

The cavitation vortex rope size is determined by identifying the edges of the cavitation rope for each image. This is made possible by the good contrast between the gaseous and liquid phases of the flow provided by the LED backlight. For each single image of the vortex rope, a region of interest is defined, corresponding to the zone for which the LED lightening provides a sharp contrast between the different flow phases. The vortex rope edges are detected after conversion of the original image into a binary picture obtained by applying an ideal threshold value [59, 53]. The procedure of image post-processing is illustrated in Figure 5.2 by the example of one single raw snapshot of the vortex rope and the corresponding binary image.

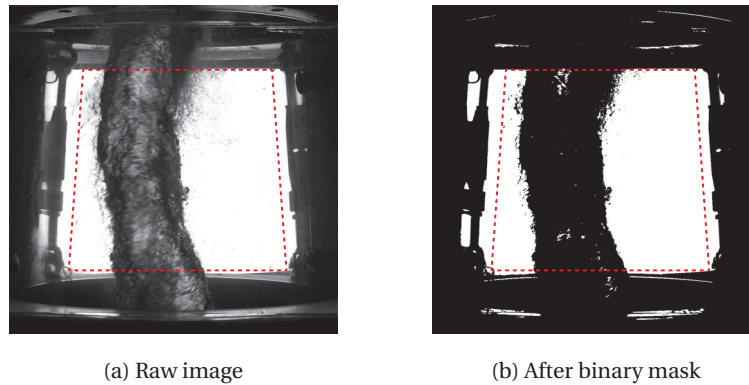


Figure 5.2: Example of one single raw image and the corresponding binary image used for the detection of the cavitation vortex rope edges.

For each vertical position  $z$  along the draft tube cone, the position of the vortex rope edges permits to obtain the corresponding vortex rope radius  $R_{pixel}(z)$  in pixels. To convert the pixels indices into spatial coordinates, a calibration image is taken with a dotted target located in the meridional cross-section of the draft tube cone and attached to the runner cone.

For the calculation of the vortex rope volume, the shape of the cavity is considered as circular for each vertical position. The section of the cavitation vortex rope is then integrated from the vertical positions  $z_1$  to  $z_2$ , corresponding to the upper and lower limits of the region of interest:

$$V_c = \int_{z_1}^{z_2} A_c dz = \int_{z_1}^{z_2} \pi R(z)^2 dz \quad (5.1)$$

The cavitation volume is determined for each image of the visualization for computing mean value  $\bar{V}_c$  and fluctuating component  $\tilde{V}_c(t)$ , respectively.

### Limits of the methodology

The procedure of estimation of the cavitation volume in the draft tube cone presents several disadvantages. On the one hand, it only takes into account a small fraction of the cavitation vortex rope as this one extends beyond the cone in the draft tube elbow and the diffuser. The cavitation volume is therefore underestimated. To overcome this problem, a local void fraction  $\beta$  is defined, corresponding to the ratio between the cavitation volume estimated in the region of interest and the total volume of the region of interest. However, the local void fraction does not represent a global void fraction as the size of the cavitation vortex rope progressively decreases beyond the cone due to the increase of the static pressure combined with the decrease of the swirl intensity.

On the other hand, the objective of the camera is focused on the meridional cross-section of the draft tube cone and the computation of the cavitation volume is based on the calibration image taken in this cross-section. Therefore, the periodical precession of the vortex rope leads to an overestimation of the cavitation volume when this one is situated between the camera and the calibration section whereas it leads to an underestimation of the volume when the vortex rope is situated beyond the calibration section. This effect introduces an artificial fluctuation of the vortex rope volume at the precession frequency which does not correspond to any real physical behavior. However, it is assumed that it does not affect the mean value of the cavitation volume.

Finally, the cross-section of the cavitation vortex rope is assumed to be circular whereas it has been shown in Chapter 3 that the core of the precessing vortex features a nearly elliptical shape for low values of discharge factor. Others authors have pointed out this elliptical shape by performing high-speed visualizations of the vortex rope, as well as stability analysis of the vortex rope [50, 51, 72].

**Cavitation volume fluctuation in non-resonance and resonance conditions**

The evolution of the cavitation volume is estimated at OP#2 ( $Q_{ED} = 0.128$ ) for two values of Thoma number,  $\sigma = 0.12$  and  $\sigma = 0.16$ , corresponding to the non-resonance and resonance conditions, respectively. The time history of the fluctuating component  $\Delta\beta$  of the local void fraction  $\beta$  is plotted in Figure 5.3 for both values of Thoma number, together with the corresponding auto-spectral density functions. The fluctuating component  $\Delta\beta$  of the void fraction is made dimensionless by the mean value  $\beta_{mean}$ .

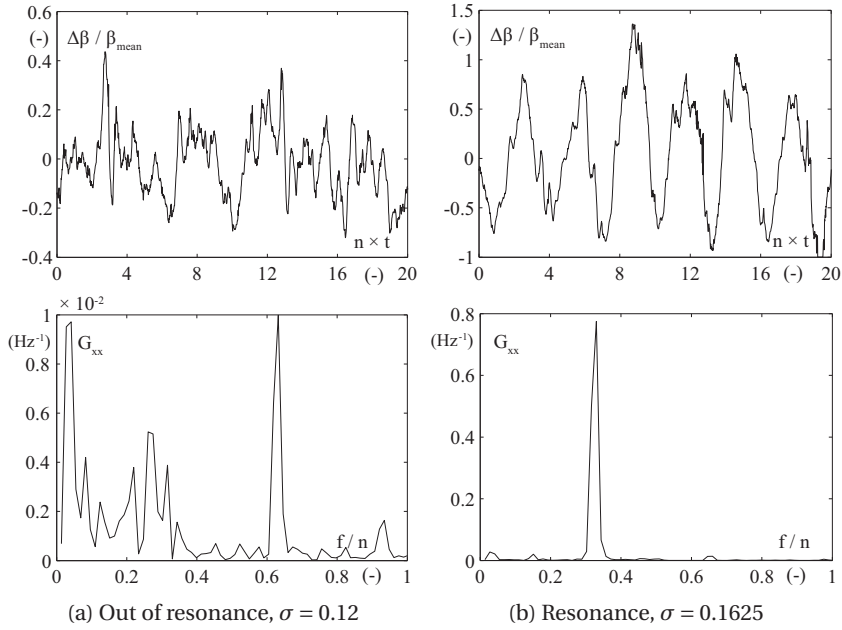


Figure 5.3: Time history of the fluctuating component  $\Delta\beta$  of the void fraction for two values of Thoma number, together with the corresponding auto-spectral density functions ( $Q_{ED} = 0.128$ ).

The mean value of the void fraction is equal to  $\beta_{mean} = 0.084$  for  $\sigma = 0.12$  and  $\beta_{mean} = 0.044$  for  $\sigma = 0.1625$ . Out of resonance, the fluctuations of the cavitation volume do not present a well-defined periodicity at a given frequency. They mainly occurs in a wide range of low frequencies and can be related to the pressure fluctuations at the natural frequency of the system, which is equal to  $f_0 = 0.2 \times n$  for this value of  $\sigma$ . The precession frequency  $f_{rope}$  is not dominant although a peak at its first harmonic  $2 \times f_{rope}$  is visible and dominant in the auto-spectra. In resonance conditions, the amplitude of the cavitation volume fluctuations at the precession frequency greatly increases and becomes dominant, giving rise a well-periodical signal. As the eigenfrequencies of the system strongly depend on the cavitation volume, the occurrence of resonance forces the system eigenfrequencies to periodically fluctuate at the precession frequency. As a result, the system becomes strongly non-linear and it yields a coupling between the excitation source, whose frequency slightly depends on the cavitation

volume, and the system's oscillations. Non-linearities of the system in resonance conditions have already been taken into account for the simulation of pressure fluctuations at part load resonance conditions [2, 53]. By considering a periodical fluctuation of the wave speed and the bulk viscosity in a 1D hydro-acoustic model, Landry [53] obtained numerical results in perfect agreement with the experimental measurements in terms of amplitude and shape of the pressure fluctuations.

## 5.2 Effect of the Froude number on the test rig hydro-acoustic response

### 5.2.1 Definition of the Froude number

The Froude number is of major importance for the investigation of cavitation in Francis turbines as it affects the distribution of cavitation in the draft tube by changing the pressure gradient relatively to the size of the machine. The Froude number of the machine is defined by:

$$Fr = \sqrt{\frac{E}{gD_{ref}}} = \sqrt{\frac{H}{D_{ref}}} \quad (5.2)$$

with  $D_{ref}$  the reference diameter. A relation between the elevation of the vapor pressure at two different values of Froude number is derived in [35]:

$$\frac{Z_{ref} - Z_1}{Z_{ref} - Z_2} = \frac{Fr_1^2}{Fr_2^2} \quad (5.3)$$

Usually, the Froude similitude between the model and the prototype is not fulfilled during reduced scale physical model tests as it can require very low values of head or, on the contrary, very high values of head exceeding the test rig capacity. The Froude number is usually higher during the reduced scale model tests, inducing a lower elevation of the cavitation onset and a more important development of cavitation. Thus, the cavitation vortex rope is generally narrower and longer at the model scale than at the prototype scale [35].

As the development of cavitation crucially changes the natural frequencies of the hydraulic system and the interaction between the excitation source and the system, it is important to understand the influence of the Froude number on the cavitation development in the draft tube and the corresponding hydro-acoustic response of the system.

For this purpose, the influence of the Froude number on the occurrence of resonance and

Table 5.1: List of the investigated operating points.

# OP	$n_{ED}$ (-)	$Q_{ED}$ (-)	$Q$ (m <sup>3</sup> .s <sup>-1</sup> )	$H$ (m)	$Fr$ (-)	$\sigma$ (-)
2	0.288	0.128	0.286	33.9	9.84	0.11 → 0.21
			0.254	26.8	8.75	
			0.222	20.5	7.66	
			0.191	15.1	6.56	

the evolution of the hydro-acoustic response of the system is investigated for a given value of discharge factor,  $Q_{ED} = 0.128$ . The value of the Froude number is modified by changing both turbine runner speed and pump speed so that the speed factor  $n_{ED}$  is kept constant at the rated value  $n_{ED} = 0.288$ . Finally, 4 values of Froude number are investigated. For each value, the pressure level in the draft tube is modified step by step to cover a wide range of Thoma number. The parameters of the investigated operating points are given in Table 5.1.

### 5.2.2 Resonance identification for different values of Froude number

For each Froude number, the resonance conditions are identified by increasing step by step the value of the Thoma number from the prototype value  $\sigma_{plant} = 0.11$  to the value corresponding to the cavitation-free conditions  $\sigma_{atm}$ . Pressure fluctuations measurements are carried out for each value of  $\sigma$  in the draft tube and the upstream pipes of the test rig. The evolution of the auto-spectra amplitude at the precession frequency with the Thoma number is reported in Figure 5.4 for each value of Froude number.

For all values of Froude number, resonance conditions occur at a value of Thoma number equal to approximately  $\sigma = 0.16$ . However, some important differences can be noticed between the different cases. First, the maximum amplitude reached in resonance conditions is greater for low values of Froude number, indicating that the hydro-acoustic response of the system is more important in resonance conditions for low values of Froude number. Moreover, the evolution of the auto-spectra amplitude at the precession frequency presents differences between the different values of Froude number. For high values of Froude number, the decrease of the auto-spectra amplitude beyond the resonance conditions is continuous and regular. Furthermore, the overall curve presents a symmetry with respect to the point of resonance, which is easily identified as the point featuring the maximum value. Decreasing the Froude number, the curve features an increasing dissymmetry about the point of resonance, with a sudden transition between the resonance conditions and the cavitation-free conditions. This phenomenon is particularly important for the lowest value of Froude number  $Fr = 6.56$ .

## 5.2. Effect of the Froude number on the test rig hydro-acoustic response

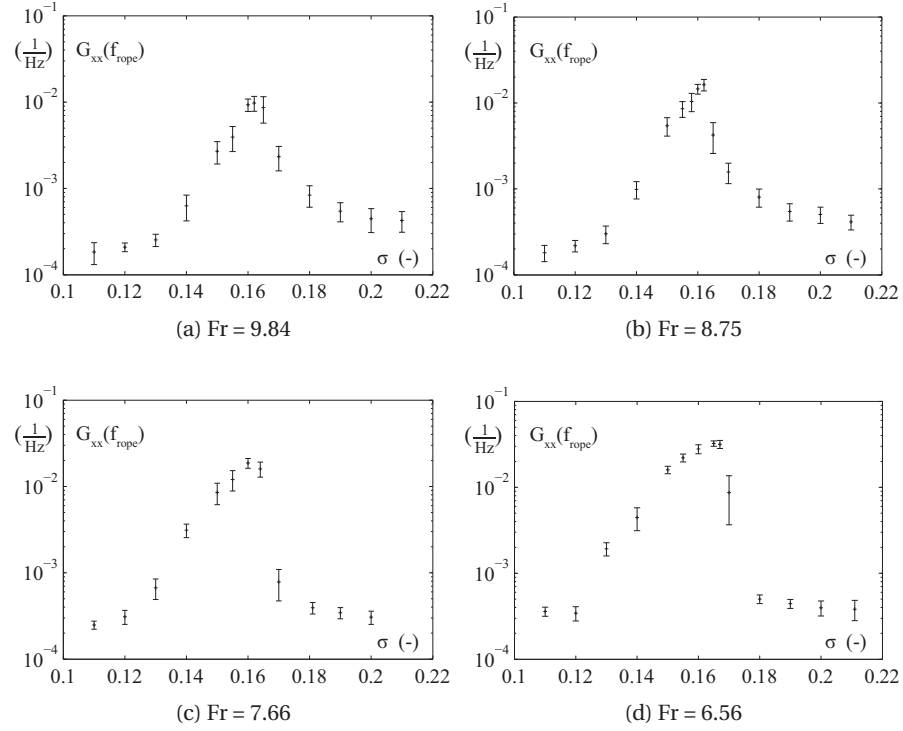


Figure 5.4: Auto-spectra amplitude at  $f_{ropre}$  as a function of the Thoma number for different values of Froude number. The pressure signal is measured in the feeding pipe (location P1).

This phenomenon can also be highlighted by the influence of the Thoma number on the phase shift at the precession frequency between two pressure signals. The results for two pairs of sensors located in the upper cross-section of the cone are presented in Figure 5.5. For all the values of Froude number, the phase shift tends to 0 when the system get closer to the resonance conditions. This reflects the amplification of the synchronous pressure component which becomes dominant compared to the convective one. However, for the lowest values of Froude number, the evolution of the phase shift features a sudden jump beyond the resonance conditions, passing directly from 0 to  $\pi$  for the couple of sensors C1N-C1E and from 0 to  $-\pi/2$  for the couple of sensors C1E-C1S.

### 5.2.3 Lock-in effect at low Froude number

This section is focused on the lowest value of Froude number, i.e.  $Fr = 6.56$ . Two additional series of pressure measurements are performed to confirm the behavior observed for this value of Froude number. For the first series, the Thoma number is increased step by step from  $\sigma_{plant} = 0.11$  to  $\sigma_{atm}$  whereas its value is decreased in the same range for the second measurement series. The evolution of the precession frequency and the associated auto-spectra amplitude with the Thoma number is presented in Figure 5.6 for both series of measurement.

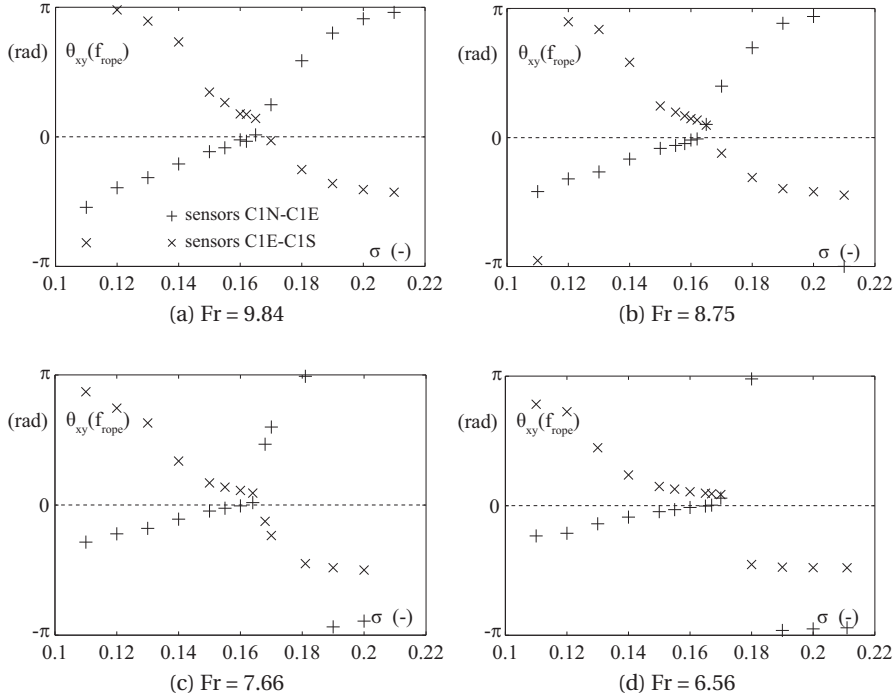


Figure 5.5: Cross-spectra phase at  $f_{rope}$  as a function of the Thoma number for two pairs of pressure signals measured in the upstream section of the cone for different values of Froude number.

Similar results are obtained with both measurement series. The evolution of the amplitude suggests that the system remains in resonance conditions over a wide range of  $\sigma$ -value, approximately from  $\sigma = 0.16$  to  $\sigma = 0.175$ . Beyond  $\sigma = 0.175$ , the amplitude of the pressure fluctuations abruptly decreases. In terms of precession frequency, the latter increases as the Thoma number is increased in the range of values  $\sigma = [0.11 - 0.14]$  and, then, remains constant over the range  $\sigma = [0.14 - 0.175]$ , which corresponds to the resonance conditions. These results suggest the occurrence of a frequency lock-in phenomenon between the precession frequency, seen as an excitation frequency for the system, and the first natural frequency of the system for low values of Froude number. It is followed by an abrupt jump of the system from the resonance conditions to the non-resonance conditions.

Frequency lock-in is a widely spread phenomenon mainly observed in the case of flow-induced vibrations, such as vortex shedding in the wake of a bluff body (the reader can find a review in Williamson and Govardhan [79]) or an hydrofoil [7]. For these particular cases, the vortex shedding frequency linearly increases with the flow velocity in absence of motion of the body. If the latter is able to vibrate, a strong coupling between the vortex shedding frequency and the vibration frequency takes place as the resonance conditions are approached by increasing the flow velocity. It results in a lock-in between the shedding frequency and the natural



## 5.2. Effect of the Froude number on the test rig hydro-acoustic response

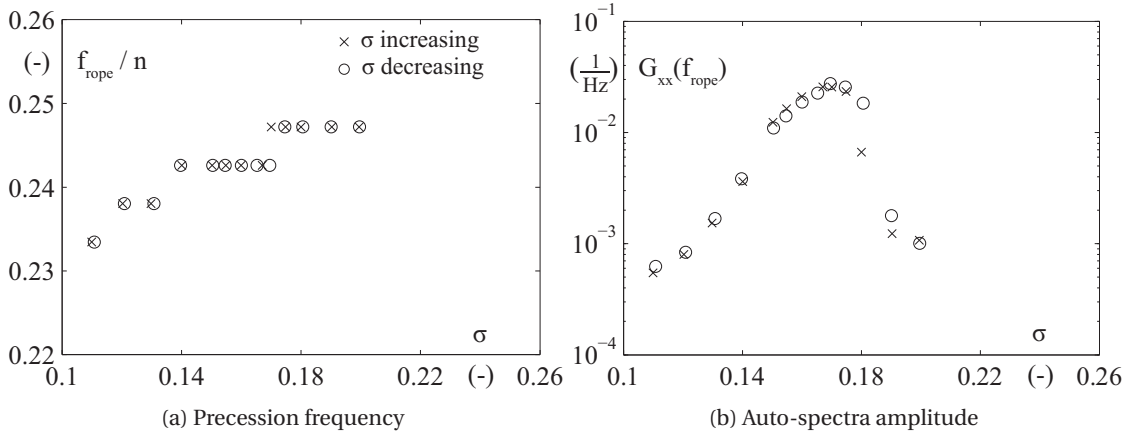


Figure 5.6: Precession frequency and associated auto-spectra amplitude as a function of the Thoma number ( $Fr = 6.56$ ).

frequency of the bluff body: the shedding frequency is controlled by the body vibrations. Its value deviates from the expected value and remains equal to the natural frequency of the body in a range of flow velocity values whom limits depend on the system parameters. The frequency lock-in appears generally in the case of a coupling between an oscillating system and an oscillating instability [18]. It is caused by a non-linear feedback mechanism between the oscillations of the system and the instability occurring in resonance conditions.

The present case does not exactly correspond to the frequency lock-in observed in the case of vortex-induced vibrations. Here, the eigenfrequencies of the system are changed by increasing (or decreasing) the static pressure in the draft tube while the excitation frequency is only slightly altered. Approaching the resonance conditions, a coupling between the excitation source and the system's oscillations takes place, resulting in a lock-in between the excitation frequency and the natural frequency of the system in a given range of Thoma number. Both excitation and natural frequencies deviate from their normal evolution without interaction and remain constant at an equal value. However, the reasons for which this phenomenon is considerable for low values of Froude number remain to be established.

### 5.2.4 Effect on the pressure fluctuations components

In the following, the effect of the Froude number on the evolution of both synchronous and convective pressure components with the Thoma number is investigated. The evolution of the RMS value of the convective pressure components with the Thoma number is presented in Figure 5.7 for each value of Froude number. As shown in Chapter 4, the RMS value of the convective pressure components slightly increases as the Thoma number is increased, indicating that the development of cavitation in the vortex core has a little impact on the precession of the vortex rope.

## Chapter 5. Influence of the Froude number on the resonance conditions

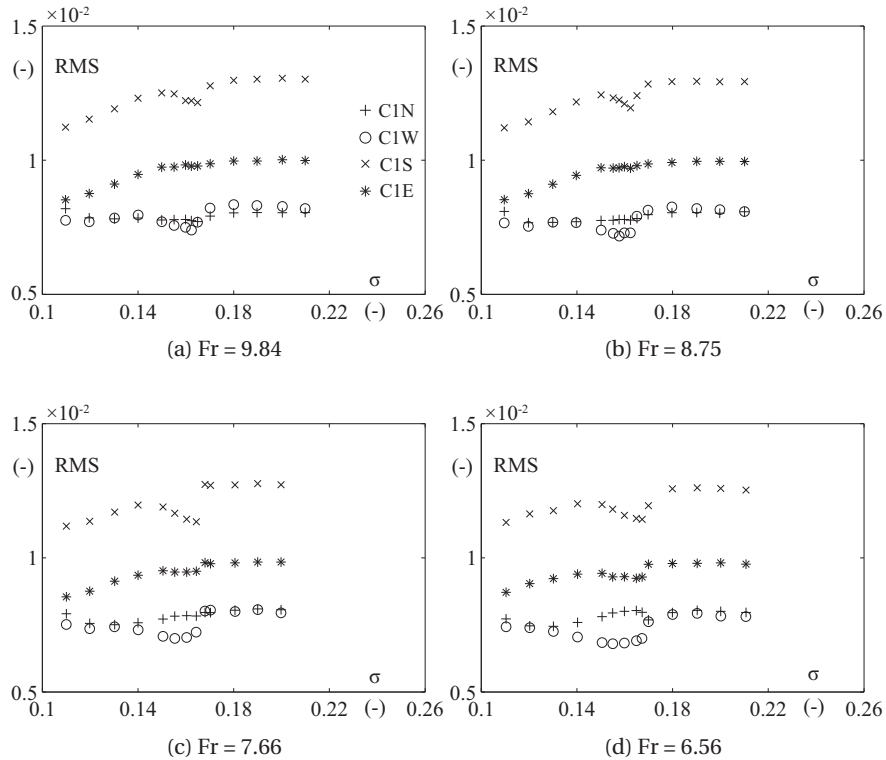


Figure 5.7: RMS value of the convective pressure components as a function of the Thoma number for different values of Froude number.

However, the evolution of the RMS value is disturbed approaching the resonance conditions and deviated from its expected values. It has been assumed that this effect is a result of the system non-linearities in resonance conditions which impact in real time the precession of the vortex rope. During frequency lock-in observed for low values of Froude number, this effect is much more important and occurs in a wider range of  $\sigma$ -value. However, this effect is not observed for high values of discharge factor, as shown in Chapter 4 with a value of discharge factor equal to 81 % of the value at the BEP. At this operating point, the intensity of the excitation source is too low (Chapter 3) to engender great oscillations of the system in resonance conditions and a coupling between the system's oscillations and the excitation source.

The evolution of the RMS value of the synchronous pressure component with the Thoma number is presented in Figure 5.8 for each value of Froude number. For all the values of Froude number, the maximum RMS value is reached for a value of  $\sigma$  comprised between [0.16 – 0.17]. However, the maximum RMS value observed in resonance conditions increases as the Froude number decreases, indicating that the amplification of the hydro-acoustic response of the system engendered by the occurrence of resonance conditions is more important for low values of Froude number.

### 5.3. Effect of the Froude number on the cavitation volume

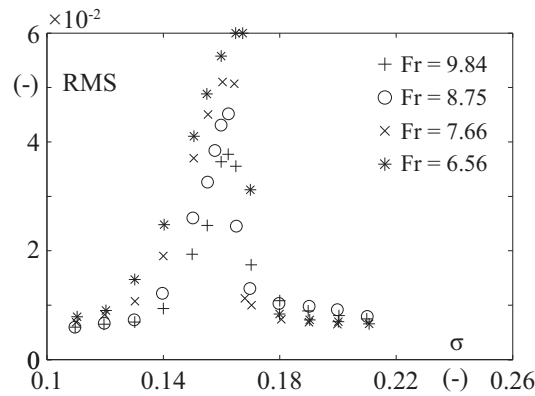


Figure 5.8: RMS value of the synchronous pressure component as a function of the Thoma number for different values of Froude number.

### 5.3 Effect of the Froude number on the cavitation volume

The mean value of the void fraction  $\beta_{mean}$  is estimated by using the methodology described in Section 5.1.2 at three different values of the Thoma number for two values of the Froude number,  $Fr = 8.75$  and  $Fr = 6.56$ . Two values of Thoma number correspond to non-resonance conditions ( $\sigma = 0.12$  and  $\sigma = 0.14$ ) whereas the last value corresponds to the resonance conditions ( $\sigma = 0.165$ ). The results are given in Figure 5.9 for both values of the Froude number.

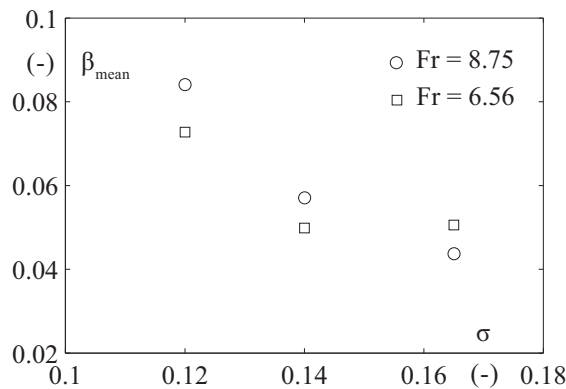


Figure 5.9: Mean void fraction as a function of the Thoma number for two different values of the Froude number.

As expected, the mean void fraction decreases as the value of the Thoma number is increased. For a Froude number of  $Fr = 8.75$ , the mean void fraction regularly decreases in the range of investigated  $\sigma$ -value. For a Froude number of  $Fr = 6.56$ , the decrease of the mean void fraction in the range  $\sigma = [0.12 - 0.14]$  is less important. Above the value  $\sigma = 0.14$ , the mean void fraction seems to remain almost constant. These results suggest that the cavitation volume

## Chapter 5. Influence of the Froude number on the resonance conditions

decreases more slowly with an increase of the Thoma number for low values of the Froude number. It is confirmed by the mean pressure in two cross-sections of the draft tube cone, represented in Figure 5.10 as a function of the Thoma number for all the investigated values of the Froude number.

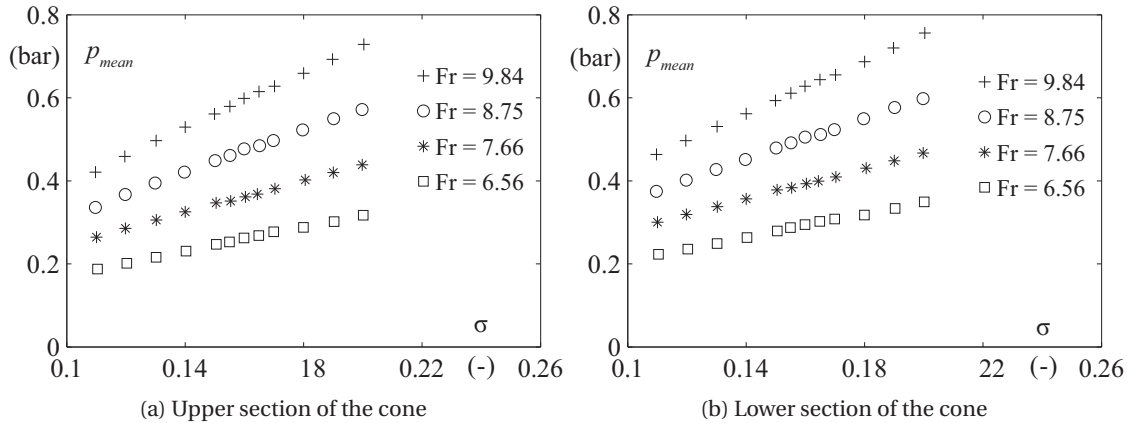


Figure 5.10: Mean pressure as a function of the Thoma number in two different cross-sections of the cone for different values of Froude number.

As the eigenfrequencies of the system strongly depend on the cavitation volume in the draft tube, these results suggest that the system eigenfrequencies increase more slowly with an increase of the Thoma number for low values of the Froude number. However, the cavitation volume is only estimated in the draft tube cone in the present investigation and for a limited number of  $\sigma$ -values and Froude numbers. This behaviour must be confirmed by further investigations of the cavitation volume in a wider range of  $\sigma$ -value and for different Froude numbers.

### 5.4 Summary and Discussion

At part load conditions, the occurrence of resonance conditions forces the system to be non-linear as the amplification of the synchronous pressure component imposes the cavitation volume to fluctuate. As the cavitation volume in the vortex core has an effect on the vortex precession, a coupling between the excitation source and the system's oscillations is set-up. For low values of Froude number, this coupling gives rise a frequency lock-in phenomenon between the excitation frequency and the natural frequency of the system. Resonance conditions occur in a wide range of  $\sigma$ -value, for which the precession frequency remains constant. It is followed by an abrupt jump of the system from resonance conditions to non-resonance conditions.

Given the evolution of the mean static pressure in the draft tube and the resulting mean cavitation volume, it is assumed that the eigenfrequencies of the system, which are directly

related to the size of the cavitation vortex rope, increase more slowly as the value of the Thoma number is decreased for low values of Froude number. Therefore, it permits the coupling between the excitation source and the system's oscillations to occur in a wider range of  $\sigma$ -value when the system passes through the resonance conditions by increasing or decreasing the value of  $\sigma$ .

The coupling between the excitation source and the oscillations of the cavitation volume can be modelled by including a feedback between the excitation source and the cavitation compliance  $C_c$  in the 1D hydro-acoustic models. Further investigations should focus on the quantitative study of such a feedback. Taking into account such a phenomenon is however important for an accurate assessment of the hydropower plant stability and a correct prediction of the operating points for which the hydraulic system is supposed to experience the occurrence of resonance conditions.



# 6 Impact on the runner mechanical behavior

## 6.1 Motivation

The vortex rope precession induces the propagation of synchronous pressure pulsations at the precession frequency in the hydraulic test rig and therefore through the blade channels of the runner. Amplitude of these pressure fluctuations depends on both the discharge factor, which drives the development of the precessing vortex rope in the draft tube by impacting directly the swirl number of the flow, and the Thoma number, which characterizes the pressure level and the size of the cavitation volume in the draft tube. It is expected that the pressure fluctuations caused by the precessing vortex rope impact directly the mechanical behavior of the runner, as well as the torque applied to the shaft. This impact is expected to be very important in case of resonance between the excitation source and the system as it leads to an important amplification of the pressure fluctuations amplitude.

In addition to a risk for the stability of the electrical system, the occurrence of hydro-acoustic resonance and the repetition of operating hours at part load conditions may lead to mechanical fatigue problem, endangering the mechanical integrity of the runner. It is therefore necessary to assess more precisely the impact of the pressure fluctuations propagation on the mechanical behavior of the runner with respect to the operating conditions.

The improvement of the instrumentation and data acquisition systems in the past decades offers the possibility to measure strain and pressure on the runner blades by using on-board sensors without alteration of the runner geometry (Farhat et al. [29]). Few contributions have already reported on-board measurements on reduced scale physical models of Francis and propeller turbines (Lowys et al. [56], Houde et al. [41]), as well as on the prototype of a Francis turbine (Lowys et al. [55]). Here, on-board measurements are performed by using a special instrumented runner reproducing exactly the geometry of the original Francis turbine runner. The impact of both synchronous and convective pressure fluctuations on the strain of the runner blades is highlighted with respect to the operating conditions.

## 6.2 Instrumented runner

An instrumented runner equipped with on-board pressure sensors and strain gauges is designed and manufactured to measure dynamic pressure and strain fluctuations on the runner blades during part load operating conditions. 3D views of the instrumented runner are presented in Figure 6.1, including side and bottom views. 4 distinct runner blades are equipped with on-board sensors. More precisely, the runner blade referred as blade n°1 (see Figure 6.1) is equipped with 6 pressure sensors, three of them being located on the pressure side of the runner blade and the other three on the suction side. 4 strain gauges are installed on each side of the blade n°5. Finally, the blades 9 and 13 are equipped with 8 strain gauges on the suction side and the pressure side, respectively (see Table 6.1). The location of the sensors on the blades 1 and 5 are detailed in Figure 6.2. Only the suction side is represented in this figure. For a given location on the suction side, a second sensor is placed on the pressure side of the blade. The data are acquired by using a telemetric system with 8 different acquisition channels, allowing for simultaneous acquisition of only 8 different signals. Therefore, on-board measurements for each runner blade are realized separately.

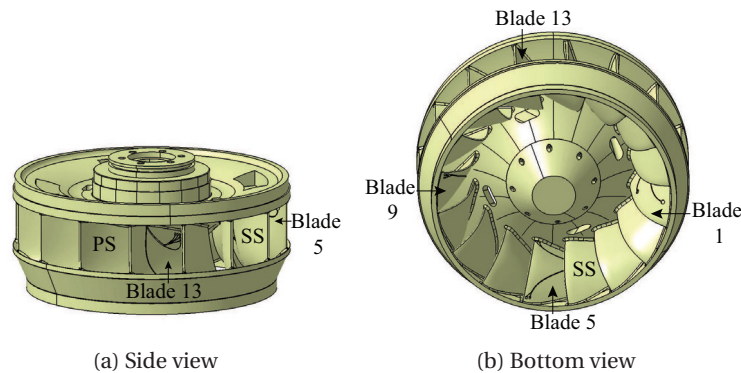


Figure 6.1: 3D side and bottom views of the instrumented runner with on-board pressure sensors and strain gauges. The initials PS and SS mean Pressure Side and Suction Side, respectively.

Table 6.1: List of pressure sensors and strain gauges on the instrumented runner

Blade	Type	Pressure side	Suction side
1	pressure sensor	3	3
5	strain gauge	4	4
9	strain gauge	-	8
13	strain gauge	8	-



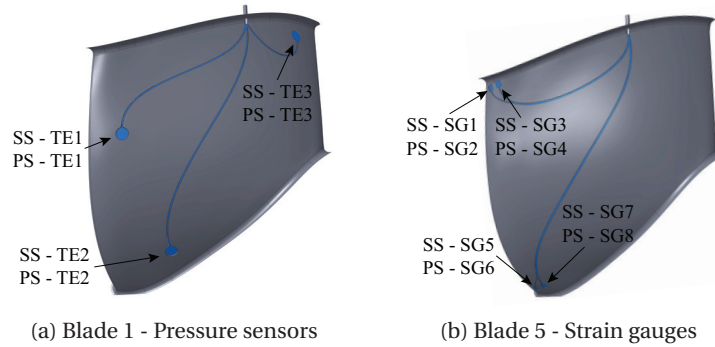


Figure 6.2: Suction side of the blades 1 and 5 with the location of the pressure sensors and strain gauges. The initials PS and SS mean Pressure Side and Suction Side, respectively.

## 6.3 Pressure and strain fluctuations on the runner blades

### 6.3.1 Pressure fluctuations in the rotating frame

Pressure fluctuations are measured on the runner blades and in the draft tube cone at a given operating point in cavitation conditions. The discharge factor is equal to  $Q_{ED} = 0.128$ , corresponding to 64 % of the value at the BEP. The auto-spectral density function of each pressure signal is computed to highlight the frequencies of interest. Examples are presented in Figure 6.3 for one pressure signal measured in the draft tube cone and another measured on the runner blade 1.

In the draft tube cone (e.g. in the fixed frame), the auto-spectral density function of the pressure signal features two peaks at two distinct frequencies. The first one corresponds to the synchronous pressure fluctuations occurring at the low frequency  $f_0 = .17 \times n$ , which is identified as the natural frequency of the system. The second one is related to the pressure fluctuations at the vortex precession  $f_{rope} = 0.31 \times n$ , which result of the superposition of two distinct components, the convective and the synchronous one.

In the rotating frame, e.g. on the runner blades, both peaks at  $f_0$  and  $f_{rope}$  are also present in the auto-spectral density function of the pressure signal. However, another peak appears at a frequency equal to exactly  $n - f_{rope}$ . This frequency corresponds to the convective pressure fluctuations induced by the vortex rotation seen in the rotating frame. As this pressure component rotates at a frequency different from the runner frequency, it is seen by on-board pressure sensors at a frequency corresponding to the difference between the runner rotating frequency and the pressure fluctuations frequency. It is illustrated by the scheme presented in Figure 6.4. In the latter, the scheme (a) depicts the initial time  $t = 0$  for which the  $x$ -axis of the rotating frame and the vortex rope are aligned. At  $t = T_{runner} = 1/n$  (scheme (b)), e.g. after a complete rotation of the rotating frame, the vortex rope has made only  $T_{runner}/T_{rope}$  revolution. The rotating frame and the vortex rope are again aligned (scheme (c)) when their

## Chapter 6. Impact on the runner mechanical behavior

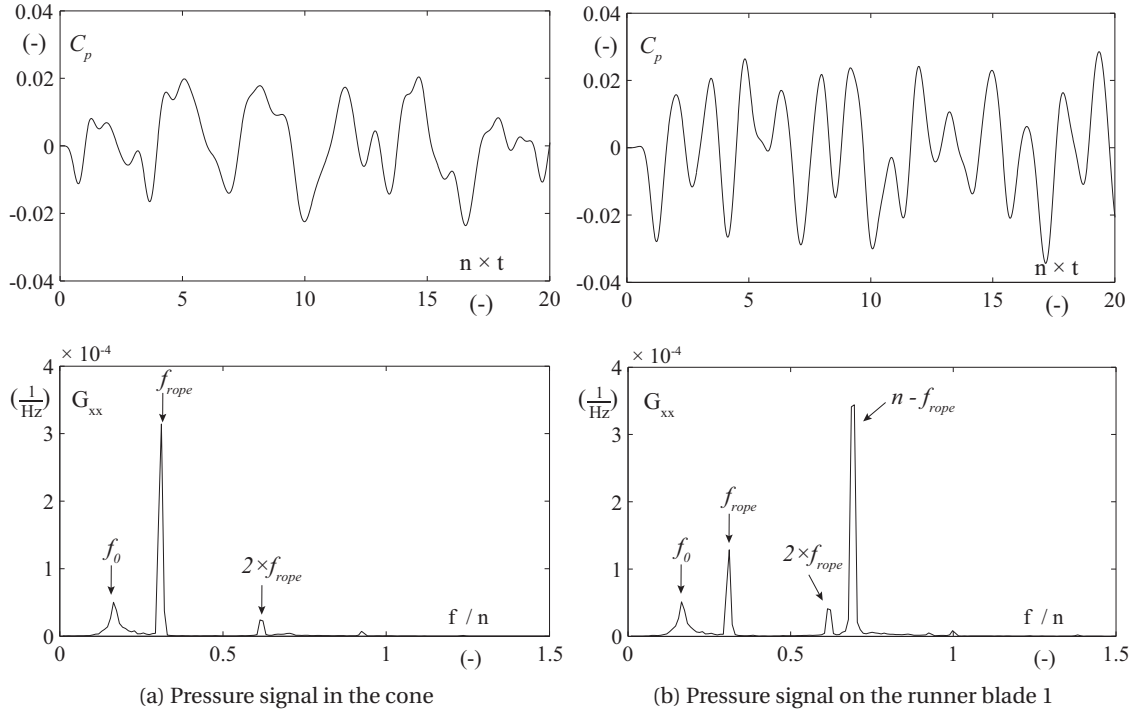


Figure 6.3: Pressure signals measured in the draft tube cone (location C1S) and on the runner blade 1 (location PS-TE2), together with the corresponding auto-spectral density functions ( $Q_{ED} = 0.128$ ,  $\sigma = 0.11$ ).

angular positions  $\theta_x$  and  $\theta_{rop}$  are equal:

$$\theta_x = \theta_{rop} + 2\pi \quad (6.1)$$

By expressing the angular positions as a function of the angular speeds, it gives:

$$2\pi nT = 2\pi f_{rop}T + 2\pi \quad (6.2)$$

Finally, the rotating frame and the vortex rope are aligned again at a time equal to  $T = 1/(n - f_{rop})$ , which corresponds to the period of the convective pressure components seen in the rotating frame.

On the contrary, the synchronous pressure fluctuations at both frequencies  $f_0$  and  $f_{rop}$  are seen in the rotating frame with the same frequency, as they have equal phase and amplitude in

### 6.3. Pressure and strain fluctuations on the runner blades

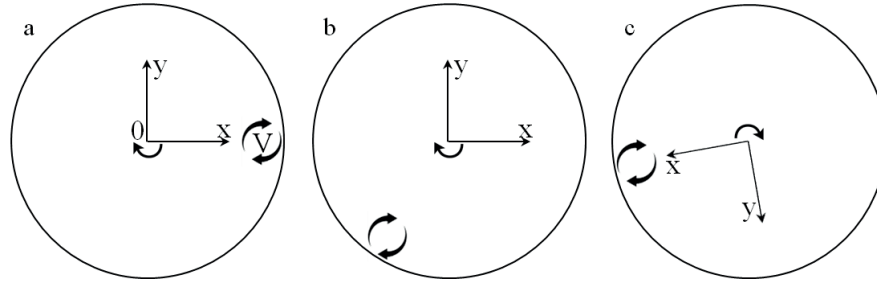


Figure 6.4: Relative position between the runner (represented by the rotating frame  $(O, \vec{x}, \vec{y})$ ) and the precessing vortex rope (symbol V) from Duparchy et al. [24].

the same cross-section. Such a decomposition of the pressure fluctuations at the precession frequency in the rotating frame has already been reported by Amiri et al. [4] and Houde et al. [41] in the case of low-head axial turbines operating at part load conditions. In the latter research work, two pressure sensors located on two different runner blades are used to compute the phase shift at both frequencies, permitting to highlight the synchronous nature of the pressure fluctuations at  $f_{rope}$  and the convective nature of those at  $f_{conv} = n - f_{rope}$ .

The use of on-board pressure sensor enables therefore to naturally decompose the pressure fluctuations at the precession frequency into convective and synchronous components and to analyse each of them individually without performing any post-processing. For instance, the influence of the discharge factor on each components can be directly analysed. The evolution of the auto-spectra amplitude at both frequencies ( $f_{syn} = f_{rope}$  and  $f_{conv} = n - f_{rope}$ ) with the discharge factor is presented in Figure 6.5 for three different pressure signals measured on the runner blade 1.

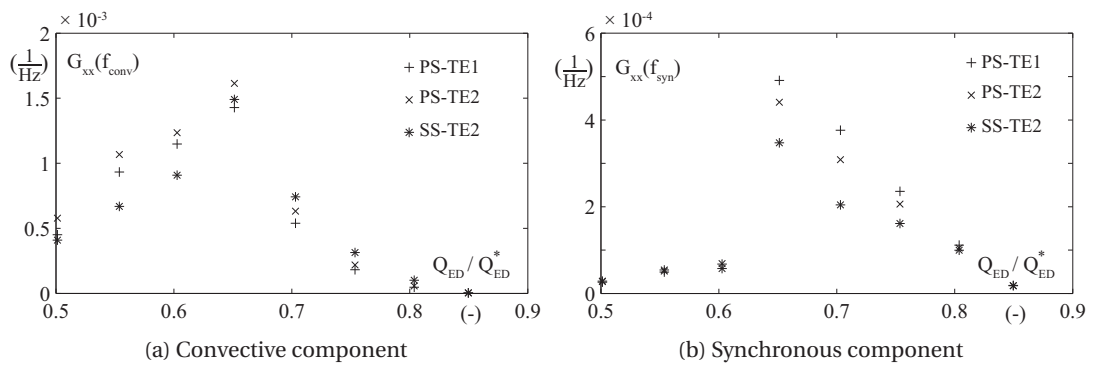


Figure 6.5: Auto-spectra amplitude at  $f_{syn}$  and  $f_{conv}$  as a function of the discharge factor for three pressure signals measured on the runner blade 1 in cavitation-free conditions.

The results are similar to those obtained with pressure sensors in the draft tube cone (see Section 3.3). The amplitude of the convective pressure fluctuations, observed at the frequency

## Chapter 6. Impact on the runner mechanical behavior

$f_{conv} = n - f_{rope}$  in the rotating frame, increases as the discharge factor decreases in the range of values  $Q_{ED}/Q_{ED}^* = [0.85 - 0.65]$  and, then, starts decreasing when the discharge factor value is less than 65 %. The amplitude of the synchronous pressure fluctuations, observed at the precession frequency  $f_{rope}$  in the rotating frame, follows a similar evolution although its value is much smaller than that of the convective fluctuations amplitude. This difference is also observed in the draft tube cone and is explained by the fact that the measurements are carried out in cavitation-free conditions, for which the synchronous pressure component is not amplified.

### 6.3.2 Strain fluctuations on the runner blades

Strain measurements are performed on the runner blade 5 in cavitation conditions for a discharge factor equal to  $Q_{ED} = 0.128$ . The auto-spectral density function of strain fluctuations measured on the runner blade 5 by two distinct strain gauges is given in Figure 6.6. The signals are made dimensionless by their mean value.

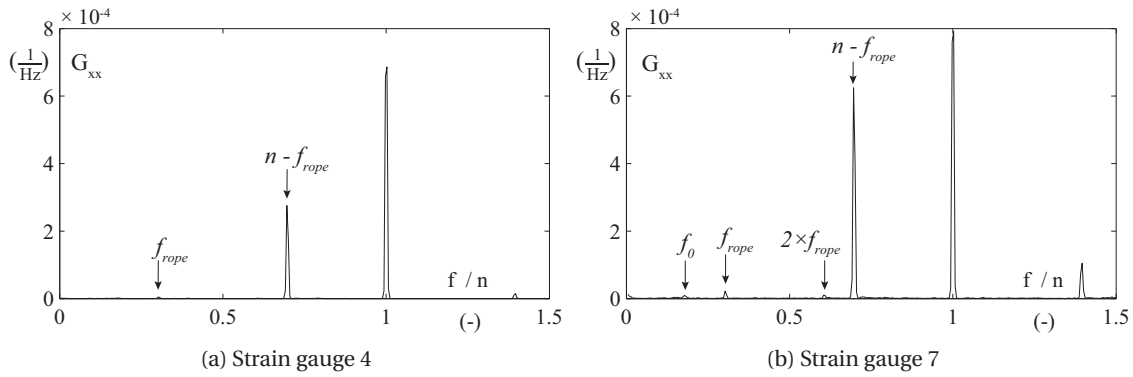


Figure 6.6: Auto-spectral density function of signals measured on the runner blade 5 by two different strain gauges ( $Q_{ED} = 0.128$ ,  $\sigma = 0.11$ ).

Surprisingly, the dominating frequency component corresponds to the rotational frequency of the runner, which is not in agreement with past experiences. It is suggested that this component is induced by a distortion from the telemetry system and signal transfer. It will be checked during the next experimental campaign in the framework of the HYPERBOLE research project.

The auto-spectral density functions feature two other main peaks, the first one at the precession frequency  $f_{rope}$  and the second one at the frequency  $f_{conv} = n - f_{rope}$ . A third peak can also be observed at the natural  $f_0$  for the strain gauge 7. However, the level of the peaks at the frequencies  $f_{rope}$  and  $f_0$ , which correspond to the frequencies of synchronous pressure fluctuations, is much smaller than that at the frequency  $f_{conv}$ . It is concluded that the propagation of synchronous pressure fluctuations in the blade channels almost does not impact the

## 6.4. Impact of resonance conditions on the mechanical behavior

mechanical behavior of the runner and is not able to generate consequent fluctuating stresses on the runner blades. On the contrary, the convective pressure component at the precession frequency represents the main source of mechanical load for the runner from the precessing vortex core.

The evolution of the auto-spectra amplitude at both frequencies  $f_{syn}$  and  $f_{conv}$  is reported in Figure 6.7 for two different strain gauges located on the runner blade 5 (gauge 4 - suction side - and gauge 7 - pressure side). The evolution for both components is similar to those observed for the pressure signals measured on the runner blade. However, the amplitude of the convective component is much greater than the amplitude of the synchronous component for all operating conditions, confirming the fact that the convective pressure component is the predominant contribution for the generation of fluctuating stresses.

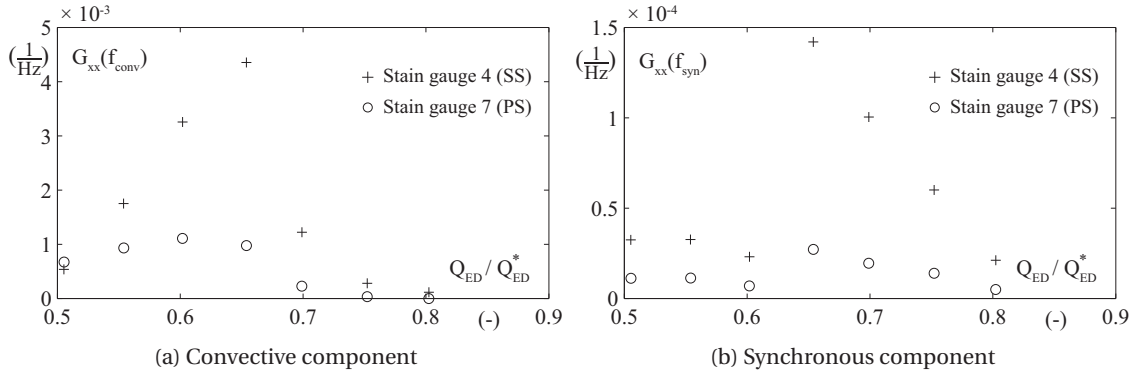


Figure 6.7: Auto-spectra amplitude at  $f_{syn}$  and  $f_{conv}$  as a function of the discharge factor for two strain gauges located on the runner blade 5 in cavitation-free conditions.

## 6.4 Impact of resonance conditions on the mechanical behavior

### 6.4.1 Pressure and strain fluctuations

The influence of the Thoma number on the runner mechanical behavior is now investigated by increasing step by step the value of  $\sigma$  from the prototype conditions  $\sigma = 0.11$  to the cavitation-free conditions  $\sigma_{atm} = 0.34$  at the operating point  $Q_{ED} = 0.128$ . The speed factor is equal to the rated value  $n_{ED} = 0.288$ . For each value of  $\sigma$ , on-board pressure and strain measurements are performed, as well as pressure measurements in the draft tube cone. The evolution of the auto-spectra amplitude at the different frequencies of interest with the Thoma number is presented in Figure 6.8 for pressure signals measured in the draft tube cone and on the runner blade 1, as well as for the fluctuating strain measured on the runner blade 5.

The resonance conditions are met for a value of  $\sigma$  approximately equal to 0.16, as seen previously in Chapter 4. They are characterized by a remarkable increase of the pressure

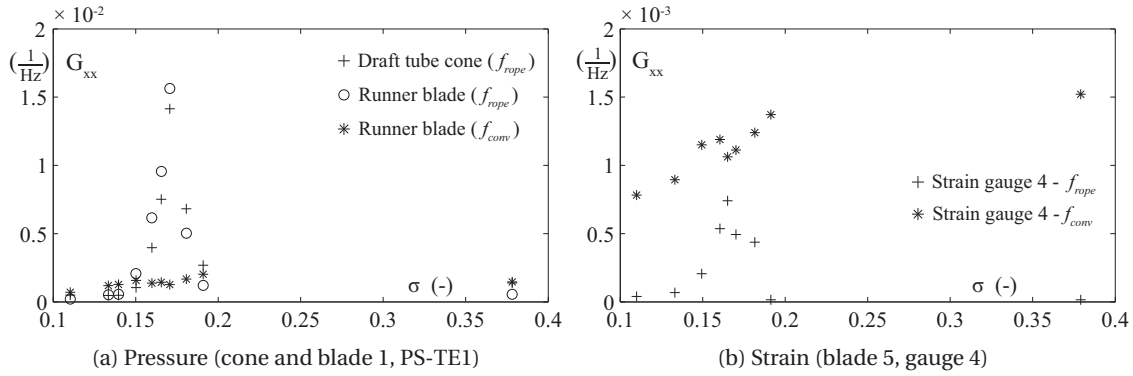


Figure 6.8: Amplitude of the auto-spectral density function at the frequencies  $f_{rop}$  and  $f_{conv} = n - f_{rop}$  as a function of  $\sigma$  for pressure signals measured in the cone and on the blade 1 (a) and for fluctuating strain measured on the blade 5 (b).

fluctuations amplitude in the draft tube cone. The amplitude of the pressure fluctuations at  $f_{rop}$  measured on the runner blade 1 follows the same evolution, as the latter corresponds to the synchronous pressure fluctuations which are greatly amplified in case of resonance.

The amplitude of the convective pressure fluctuations experienced by the runner blades at the frequency  $f_{conv} = n - f_{rop}$  follows an evolution similar to that observed in the draft tube cone (see Chapter 3). In terms of strain experienced by the runner blades, the resonance conditions induces a slight increase of the amplitude of the fluctuations at  $f_{rop}$  whereas the amplitude of the fluctuations at  $f_{conv}$  follows the same evolution than the amplitude of the convective pressure fluctuations. However, the impact of the resonance conditions on the fluctuating strain experienced by the runner blade remains negligible. Indeed, it only affects the synchronous pressure fluctuations whose effects on the runner are very low compared to those of the convective one.

### 6.4.2 Torque fluctuations

The torque applied to the runner shaft is measured at the operating point  $Q_{ED} = 0.128$  in cavitation conditions for two different values of Thoma number. The first value corresponds to the prototype value  $\sigma = 0.11$  whereas the second one corresponds to the value for which the resonance conditions are met ( $\sigma = 0.1625$ ). The time-history of the torque is given in Figure 6.9 for both values of  $\sigma$ , as well as the corresponding auto-spectral density functions. The torque signal is made dimensionless by its mean value, which is equal for this operating point to  $T = 669 \text{ N} \cdot \text{m}$  and  $T = 663 \text{ N} \cdot \text{m}$  for  $\sigma = 0.11$  and  $\sigma = 0.1625$ , respectively.

Out of resonance, the auto-spectral density function of the torque signal exhibits an important contribution at the natural frequency  $f_0$  whereas no peak at the precession frequency is observed. This observation is quite surprising as it means that the synchronous pressure

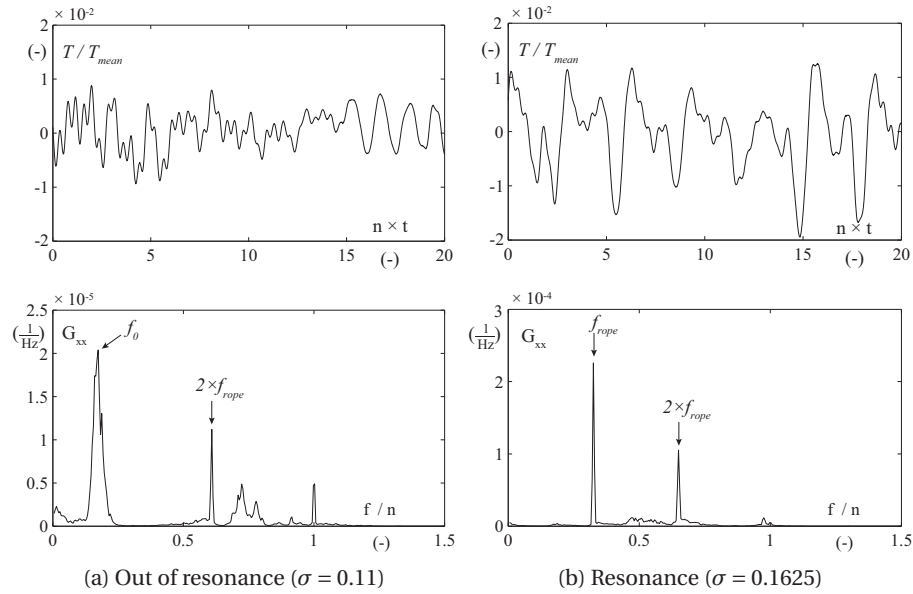


Figure 6.9: Time-history of the torque measured on the runner shaft, together with the corresponding auto-spectral density function, for two values of Thoma number ( $Q_{ED} = 0.128$ ).

fluctuations at  $f_0$  have an impact on the shaft torque contrary to the synchronous pressure fluctuations at  $f_{rope}$ , whereas the amplitudes of these two contributions are similar for this value of  $\sigma$ . Moreover, the first harmonics of the precession frequency  $f = 2 \times f_{rope}$  has an important contribution.

On the contrary, in resonance conditions, the great synchronous pressure fluctuations at  $f_{rope}$  induces torque fluctuations of high amplitude at the precession frequency. It means that the occurrence of resonance condition has a direct impact on the torque applied to the shaft and is therefore able to induce output power fluctuations. However, the peak-to-peak value is equal to nearly 2 % of the mean torque value, which is well below the peak-to-peak value potentially observed during full load instabilities, which can reach 6 % of the mean torque value.

## 6.5 Summary

The impact of the pressure fluctuations induced by the precessing vortex rope on the mechanical behavior is investigated by performing pressure and strain measurements on the blades of an instrumented runner reproducing exactly the geometry of the original one. Pressure fluctuations measurement reveals that the convective pressure component induced by the rotation of the vortex are seen in the rotating frames at a frequency equal to  $f_{conv} = n - f_{rope}$  whereas the synchronous one is seen at the precession frequency. This natural decomposition enables to directly analyse the impact of both components on the runner mechanical behavior.

## Chapter 6. Impact on the runner mechanical behavior

---

The measurements performed with strain gauges placed on the surface of the runner blades reveal that the synchronous pressure component has a low impact on the stress fluctuations experienced by the runner blades compared to that of the convective one. The latter is the main source of mechanical load from the vortex rope precession for the runner and its impact increases as the discharge factor is decreased within the flow regime 2. From past experience, the precession of the vortex rope represents however a minor contribution to the total fatigue damage cumulation, compared to other phenomena such as Rotor-Stator Interaction (RSI), transient or deep part load operations.

In case of hydro-acoustic resonance, the amplitude of the synchronous pressure component measured on the runner blade strongly increased. However, it has a very low impact on the amplitude of the dynamic strain experienced by the runner blade. Thus, these measurements reveals that the mechanical excitation induced by the precessing vortex rope is much more affected by the operating conditions (e.g. the value of the discharge factor) which strongly affects the amplitude of the convective pressure component. On the contrary, the occurrence of resonance and the value of the Thoma number have a very low impact on the runner mechanical behaviour for a given operating point. However, the occurrence of resonances produces great torque fluctuations at the precession frequency and therefore output power pulsations which can affect the stability of the electrical system at the prototype scale.



## 7 Conclusions and Perspectives

### 7.1 Conclusions

At part load conditions, Francis turbines experience the development of a precessing vortex rope in the draft tube, which acts as an excitation source for the hydraulic system via physical mechanisms which are only partially understood. Moreover, the low pressure level in the diffuser of the machine often leads to the development of cavitation in the vortex core. As a result, the wave speed in the draft tube and hence the eigenfrequencies of the system decrease, resulting in the risk of hydro-acoustic resonances. The latter put at risk the system stability and the structural integrity of the hydro-mechanical equipment. Experimental investigations including flow field surveys in the draft tube and pressure fluctuations measurements are carried out on a reduced model scale to assess the influence of the operating conditions in terms of flow discharge and pressure level in the draft tube on the vortex dynamics. A better understanding of the physical mechanisms involved in the formation of the excitation source and the interaction of the latter with the surrounding system is reached.

The experimental investigations are performed on a reduced scale physical model of a Francis turbine, reproducing the geometry and the hydraulic behaviour of a real hydropower plant. The unsteady tangential velocity fields in different cross-sections of the draft tube cone are measured in cavitation-free conditions for a wide range of discharge values by means of a two-components Particle Image Velocimetry. Based on the phase averaged results, the vortex parameters, such as the circulation and the trajectory, are determined for all the investigated flow conditions. The intensity of the excitation source is estimated by measuring the amplitude of the synchronous pressure pulsations in the feeding pipe of the machine. The results reveal the development of a coherent precessing vortical structure, identified as the precessing vortex core, for discharge values between 60 % and 85 % of the value at the Best Efficiency Point, as well as a strong influence of the discharge value on the vortex parameters. In this range of operating conditions, the vortex circulation and the precession frequency increase almost linearly as the value of the discharge is decreased. In parallel, the vortex trajectory widens in all the measurement sections and its length reaches its maximum value for a discharge value

## Chapter 7. Conclusions and Perspectives

---

equal to 64 % of the nominal value. These effects are accompanied by an important increase of the excitation source intensity. Below a given value of the discharge, the vortex dynamics loose their coherence and their periodicity, resulting in a drastic reduction of the excitation intensity. A direct link between the draft tube flow characteristics and the intensity of the excitation is established for the first time. It is suggested that the the widening of the vortex trajectory leads to a growth of the fluctuating separated flow zone at the inner wall of the draft tube elbow, resulting in a rise of the amplitude of the pressure recovery fluctuations in the diffuser.

The effect of cavitation on the precessing vortex rope, and in extension on the excitation source interaction with the system, is extensively studied. Both the axial and tangential velocity components in the draft tube are therefore measured by means of Laser Doppler Velocimetry for several values of the Thoma number, combined with wall pressure measurements for the hydro-acoustic characterization. Resonance conditions are identified for two different operating points. It is shown that the development of cavitation alters the convection of the vortex by decreasing the precession frequency and the amplitude of the convective pressure components. Moreover, the flow field investigations performed in cavitation conditions reveal that neither tangential nor axial velocity fluctuations are impacted by the propagation of great synchronous pressure pulsations. The discharge velocity fluctuations which are expected to occur in resonance conditions are much smaller than the periodical axial velocity disturbances induced by the precessing vortex rope.

The occurrence of a frequency lock-in phenomenon between the precession frequency and the natural frequency of the system for low values of the Froude number is highlighted. In this case, the hydraulic system experiences resonance conditions in a wide range of Thoma number values. This effect is assumed to be a consequence of the coupling between the excitation source and the cavitation volume oscillations in resonance conditions. The reasons for which this phenomenon is particularly pronounced for low values of the Froude number may be the slower evolution of the system's eigenfrequencies with the Thoma number value for these conditions.

Finally, the hydro-mechanical response of the runner to part load excitation is assessed through measurements with sophisticated on-board instrumentation. It is shown that the convective component of the pressure fluctuations at the precession frequency represents the main source of mechanical excitation for the runner. As a consequence, the occurrence of hydro-acoustic resonance does almost not impact the dynamic mechanical load on the runner blades, since the resonance mainly amplifies the synchronous pressure component.

## **7.2 Perspectives**

This research work provides an extensive database for the validation of ongoing CFD simulations and the stability analysis of the prototype by 1D hydro-acoustic models. Moreover, with the influence of the operating conditions having been assessed, the previously unknown physical behaviours were revealed. However, different aspects remain to be clarified and deepened in view of the various results of this research work.

First, the exact physical mechanisms causing the establishment of the excitation source are to be clarified and linked with the findings of this work. This can be experimentally realized by performing stereo-PIV in the draft tube cone and at the inlet and outlet sections of the draft tube elbow. Based on the phase averaged axial and tangential flow fields, the interaction between the vortex precession and the mean flow field in the elbow can be assessed, yielding the exact mechanisms inducing the variation of pressure recovery and the propagation of the resulting synchronous pressure fluctuations. Due to the complex geometry of the reduced scale physical model of the real machine, such an investigation could be realized with a simplified model.

Similarly, the effect of cavitation on the vortex dynamics can be assessed more precisely. Moreover, in order to highlight the convective nature of the velocity fluctuations in the draft tube cone, systematic LDV measurements synchronized with pressure measurements can be realized for a limited number of radial positions along different diameters of the cone in a wide range of Thoma number values, including resonance conditions.

Finally, the different findings of the experiments described above can lead to the development of an accurate model for the excitation source, taking into account the influence of the flow discharge and the pressure level in the draft tube. It can be used to model the coupling between the excitation source and the system's oscillations occurring in resonance conditions.



# A Hill chart of the reduced scale model

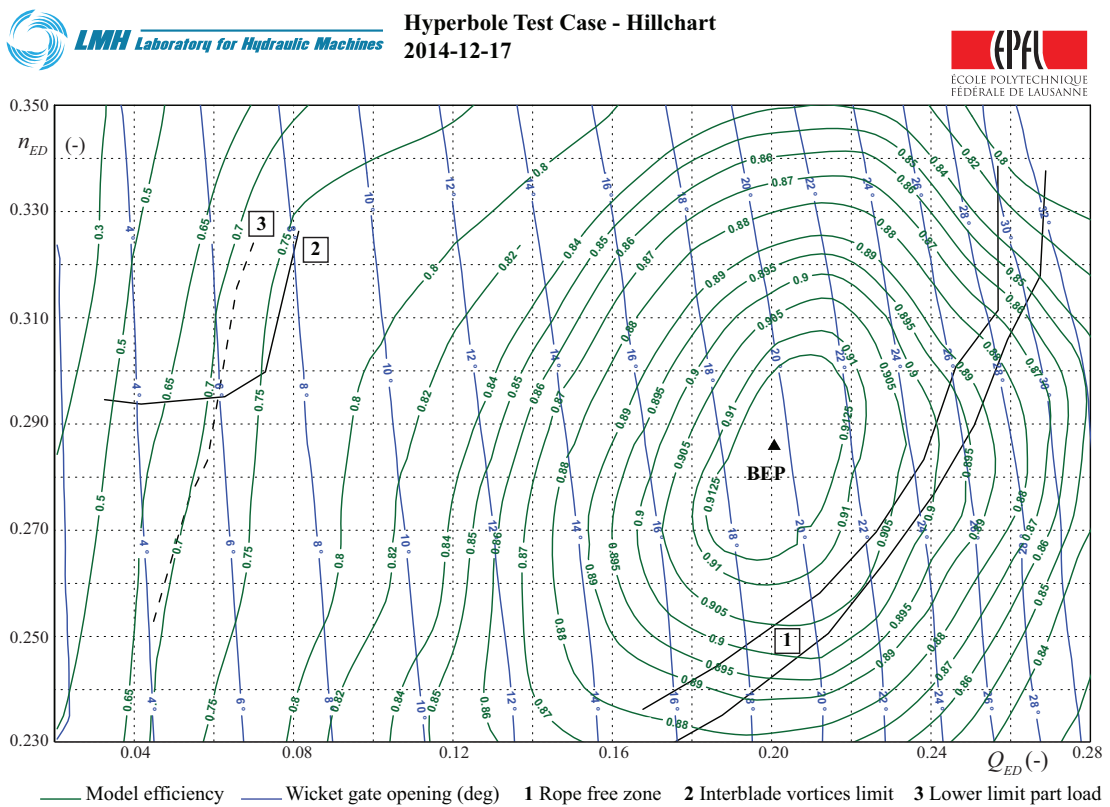


Figure A.1: Hill chart of the reduced scale physical model on the EPFL test rig PF3 as a function of the speed factor  $n_{ED}$  and the discharge factor  $Q_{ED}$ .



## B List of operating points investigated by PIV and LDV

Table B.1: List of the operating points investigated by PIV (Chapter 3).

OP	$n_{ED}$ (-)	$n$ (Hz)	$H$ (m)	$Q_{ED}$ (-)	$Q$ ( $\text{m}^3 \cdot \text{s}^{-1}$ )	$Q_{ED}/Q_{ED}^*$ (-)	$\sigma$ (-)
1				0.161	0.320	0.81	
2				0.155	0.308	0.78	
3				0.145	0.288	0.74	
4	0.288	13.33	26.8	0.135	0.268	0.68	$\sigma_{atm}$
5				0.128	0.255	0.64	
6				0.12	0.239	0.60	
7				0.11	0.319	0.55	

Table B.2: List of the operating points investigated by LDV (Chapter 4).

OP	$n_{ED}$ (-)	$n$ (Hz)	$H$ (m)	$Q_{ED}$ (-)	$Q$ ( $\text{m}^3 \cdot \text{s}^{-1}$ )	$Q_{ED}/Q_{ED}^*$ (-)	$\sigma$ (-)
1	0.288	13.33	26.8	0.161	0.320	0.81	$\sigma_{res} = 0.10$ $\sigma_{out} = 0.13$ $\sigma_{atm} = 0.31$
2	0.288	13.33	26.8	0.128	0.255	0.64	$\sigma_{out} = 0.13$ $\sigma_{res} = 0.1625$ $\sigma_{atm} = 0.38$





# C Mean phase averaged velocity profiles

## C.1 Cavitation-free conditions

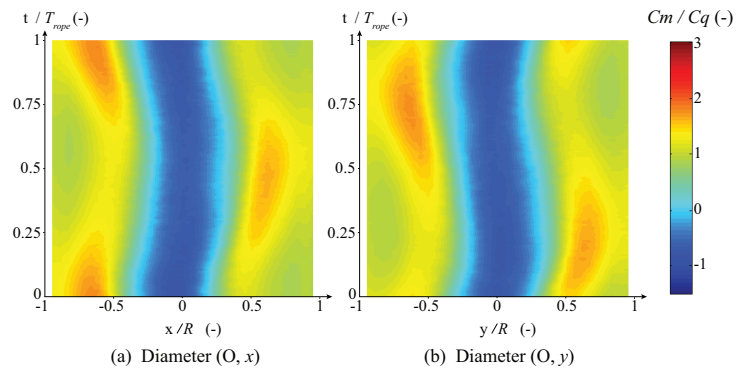


Figure C.1: Evolution of the axial velocity profile over one precession cycle in the measurement section 1 at OP#1 -  $Q_{ED} = 0.161$ ,  $\sigma = \sigma_{atm} = 0.31$ .

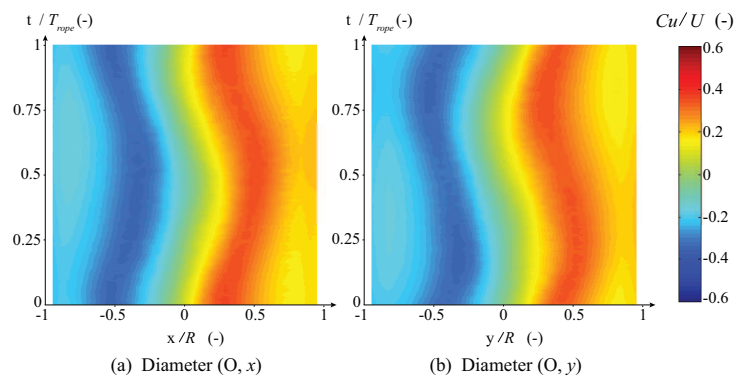


Figure C.2: Evolution of the tangential velocity profile over one precession cycle in the measurement section 1 at OP#1 -  $Q_{ED} = 0.161$ ,  $\sigma = \sigma_{atm} = 0.31$ .

## Appendix C. Mean phase averaged velocity profiles

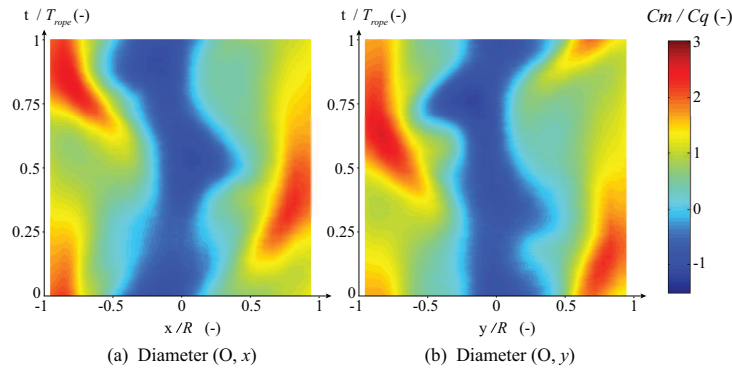


Figure C.3: Evolution of the axial velocity profile over one precession cycle in the measurement section 1 at OP#2 -  $Q_{ED} = 0.128$ ,  $\sigma = \sigma_{atm} = 0.38$ .

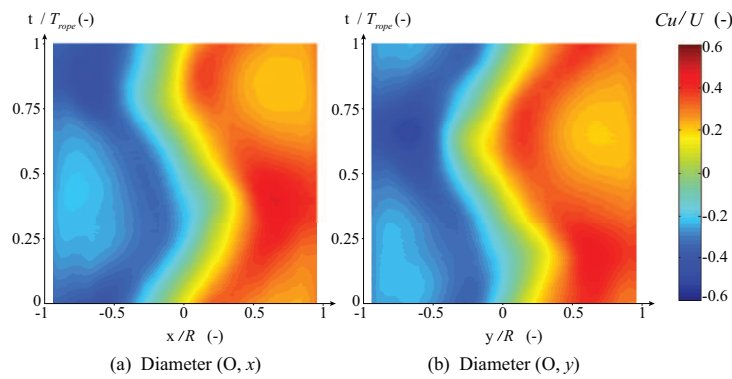


Figure C.4: Evolution of the tangential velocity profile over one precession cycle in the measurement section 1 at OP#2 -  $Q_{ED} = 0.128$ ,  $\sigma = \sigma_{atm} = 0.38$ .

### C.2 Non-resonance conditions

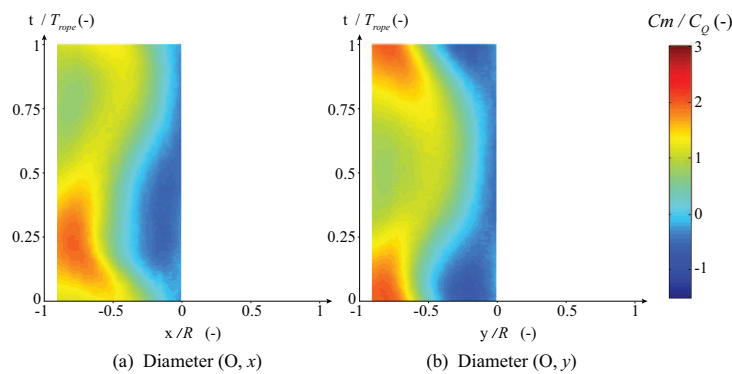


Figure C.5: Evolution of the axial velocity profile over one precession cycle in the measurement section 2 at OP#1 -  $Q_{ED} = 0.161$ ,  $\sigma = \sigma_{out} = 0.13$ .

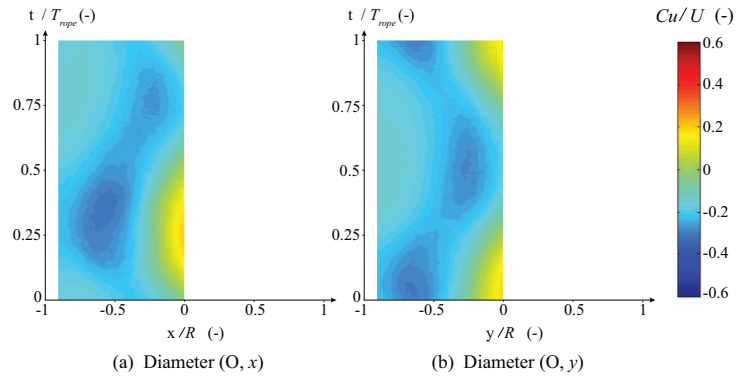


Figure C.6: Evolution of the tangential velocity profile over one precession cycle in the measurement section 2 at OP#1 -  $Q_{ED} = 0.161$ ,  $\sigma = \sigma_{out} = 0.13$ .

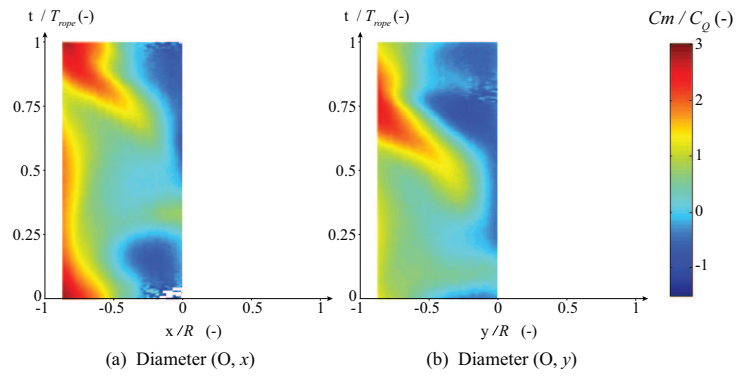


Figure C.7: Evolution of the axial velocity profile over one precession cycle in the measurement section 2 at OP#2 -  $Q_{ED} = 0.128$ ,  $\sigma = \sigma_{out} = 0.13$ .

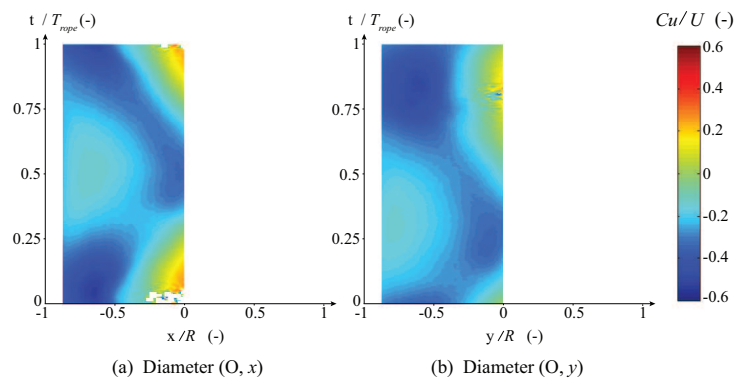


Figure C.8: Evolution of the tangential velocity profile over one precession cycle in the measurement section 2 at OP#2 -  $Q_{ED} = 0.128$ ,  $\sigma = \sigma_{out} = 0.13$ .



# D Decomposition of the pressure fluctuations

## D.0.1 Description of the problem

Pressure fluctuations induced by the precessing vortex core in the draft tube are composed of two different components, the convective and the synchronous one [66]. The convective component is a local pressure fluctuation induced by the precession of the vortex in the cone. The pressure pattern in a given section of the cone rotates with the precessing vortex core. On the contrary, the synchronous component features equal phase and amplitude in the same cross-section of the cone. The latter has been identified by Dörfler [19] as the result from the excitation source and the hydro-acoustic response of the test rig. Usually, a set of sensors regularly distributed in the same cross-section of the cone is used to identify both components. Angelico et al. [5] proposed a vector analysis in the frequency domain by using three pressure sensors to compute both components. Nishi et al. [66] developed an analytical method to compute the convective and the synchronous components in the time domain by using only two sensors spaced by 90 degrees in the same cross-section of the cone. However, this method provides reliable results only if the trajectory of the vortex is perfectly circular and centered on the cone centerline. In the present manuscript, four pressure sensors regularly spaced by 90° are used to decompose the pressure fluctuations in the time domain. The synchronous component is computed by averaging the 4 pressure signals  $C_p^j(t)$  at each instant  $t$ :

$$C_p^{syn}(t) = \frac{1}{4} \sum_{j=1}^4 C_p^j(t) \quad (D.1)$$

with  $j = 1...4$  the index of the pressure sensors. For each pressure sensor  $j$ , the convective component  $C_p^{conv,j}(t)$  is then determined as following:

$$C_p^{conv,j}(t) = C_p^j(t) - C_p^{syn}(t) \quad (D.2)$$

## Appendix D. Decomposition of the pressure fluctuations

The following section proposes a mathematical demonstration of this computation. The idea is based on the Spatial Harmonic Decomposition method proposed by Duparchy et al. [23].

### D.0.2 Mathematical demonstration

At a given time  $t$  of the precession cycle, the fluctuating component of the pressure along the perimeter of the cross-section can be written as a function of the angular position  $\theta$  by a Fourier series decomposition:

$$\tilde{p}(\theta, t) = \sum_{n=0}^{+\infty} a_n \cos(n\theta_i) + b_n \sin(n\theta_i) \quad (\text{D.3})$$

where  $\theta$  is the angular position along the perimeter of the section. The synchronous component  $\tilde{p}_{syn}(\theta, t)$ , which has equal phase and amplitude at a given time in the entire cross-section, is equal to the first component  $a_0$  of the Fourier series decomposition, whereas the convective component at a given angular position  $\theta$  is equal to:

$$\tilde{p}_{conv}(\theta, t) = \sum_{n=1}^{+\infty} a_n \cos(n\theta_i) + b_n \sin(n\theta_i) = \tilde{p}(\theta, t) - \tilde{p}_{syn}(\theta, t) \quad (\text{D.4})$$

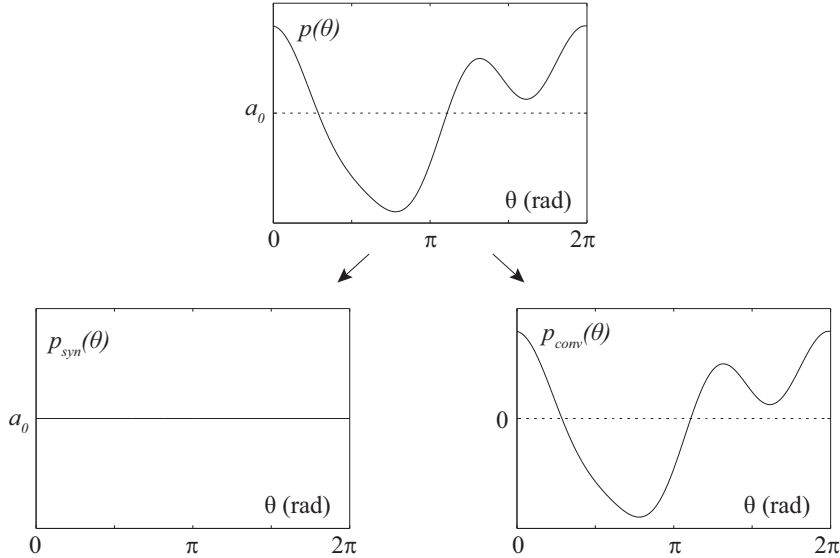


Figure D.1: Illustration of the spatial decomposition of the pressure field  $p(\theta)$  into synchronous component  $p_{syn}(\theta)$  and convective component  $p_{conv}(\theta)$  for a given time  $t$ .  $\theta$  corresponds to the angular position along the perimeter of the cone section.

---

The decomposition is illustrated in Figure 3.14 for the case of a continuous distribution of pressure. The real case of a discrete distribution of pressure  $\tilde{p}(\theta_j, t)$  with  $N$  points evenly spaced by an angle of  $\Delta\theta$  is now considered. The set of points can be seen as  $N$  pressure sensors regularly distributed along the perimeter of the cone section. At a given time  $t$ , the pressure can be written as a function of the angular position  $\theta_j$ :

$$\tilde{p}(\theta_j, t) = \sum_{n=0}^{+\infty} a_n \cos(n\theta_j) + b_n \sin(n\theta_j) \quad (\text{D.5})$$

with  $\theta_j = 0 \dots \frac{2\pi}{N} j \dots 2\pi$ . By summing all the values of pressure  $\tilde{p}(\theta_j, t)$ , it gives:

$$\begin{aligned} I &= \sum_{j=1}^N \sum_{n=0}^{+\infty} a_n \cos\left(n \frac{j2\pi}{N}\right) + b_n \sin\left(n \frac{j2\pi}{N}\right) \\ &= \sum_{n=0}^{+\infty} \sum_{j=1}^N a_n \cos\left(n \frac{j2\pi}{N}\right) + b_n \sin\left(n \frac{j2\pi}{N}\right) \\ &= \sum_{n=0}^{+\infty} I_n \end{aligned} \quad (\text{D.6})$$

The sum  $I_n$  can be decomposed into two different sums, as following:

$$I_n = \underbrace{\sum_{j=1}^N a_n \cos\left(n \frac{j2\pi}{N}\right)}_{I_{n,1}} + \underbrace{\sum_{j=1}^N b_n \sin\left(n \frac{j2\pi}{N}\right)}_{I_{n,2}} \quad (\text{D.7})$$

- For  $n = 0$ :

$$I_n = \sum_{j=1}^N a_0 = N a_0 \quad (\text{D.8})$$

- For  $n \neq 0$ :

In this case, it can be shown that the individual sums  $I_{n,1}$  and  $I_{n,2}$  are equal to 0 if  $n \neq N$ , with  $n$  the number of harmonics and  $N$  the number of angular positions taking into account (or number of sensors). To demonstrate it, the sum  $I_{n,1}$  is considered and a second sum

## Appendix D. Decomposition of the pressure fluctuations

---

$J_{n,1} = \sum_{j=1}^N a_n \sin(n \frac{j2\pi}{N})$  is introduced. A new sum  $T_{n,1} = I_{n,1} + i \cdot J_{n,1}$  can be computed as following,  $i$  being the imaginary unit:

$$\begin{aligned} T_{n,1} &= \sum_{j=1}^N a_n \cos(n \frac{j2\pi}{N}) + i \sum_{j=1}^N a_n \sin(n \frac{j2\pi}{N}) \\ &= \sum_{j=1}^N a_n e^{i(\frac{jn2\pi}{N})} \end{aligned} \quad (D.9)$$

$$\begin{aligned} T_{n,1} &= \sum_{j=1}^N a_n e^{j(i \frac{n2\pi}{N})} = a_n \frac{1 - e^{in2\pi}}{1 - e^{i \frac{n2\pi}{N}}} \\ &= a_n e^{in\pi \frac{(N-1)}{N}} \frac{\sin(n\pi)}{\sin(\frac{n\pi}{N})} \end{aligned} \quad (D.10)$$

The sum  $I_{n,1}$  is equal to the real part of  $T_{n,1}$ :

$$I_{n,1} = \Re(T_{n,1}) = a_n \cos(n\pi \frac{N-1}{N}) \frac{\sin(n\pi)}{\sin(\frac{n\pi}{N})} \quad (D.11)$$

In the case  $n \neq N$ , the sum  $I_{n,1}$  is equal to 0. However, in the particular  $n = N$ , the sum  $I_{n,1}$  is undefined. The same demonstration can be performed for the sum  $I_{n,2}$  and leads to the same result. Finally, the results show that in the case of a discrete distribution ( $N$  pressure sensors regularly distributed), the synchronous component can be computed as following:

$$\tilde{p}_{syn}(\theta) = a_0 \approx \frac{1}{N} \sum_{i=1}^N \tilde{p}(\theta_i) \quad (D.12)$$

The asynchronous (or convective) component for each sensor  $i$  can be deduced by:

$$\tilde{p}_{conv}(\theta_i, t) \approx \tilde{p}(\theta_i, t) - \tilde{p}_{syn}(\theta_i, t) \quad (D.13)$$

Therefore, the use of  $N$  pressure sensors evenly distributed in one cross-section of the cone permits to correctly reconstruct the convective and synchronous components until the  $(N - 1)^{th}$  harmonic, as the decomposition breaks down for  $n = N$ .



# Bibliography

- [1] R.J. Adrian and C.S. Yao. Power spectra of fluid velocities measured by Laser Doppler Velocimetry. *Experiments in Fluids*, 5(1):p.17–28., 1987.
- [2] S. Alligné. *Forced and Self Oscillations of Hydraulic Systems Induced by Cavitation Vortex Rope of Francis Turbines*. PhD thesis, EPFL, 2011.
- [3] S. Alligné, C. Nicolet, Y. Tsujimoto, and F. Avellan. Cavitation surge modelling in francis turbine draft tube. *Journal of Hydraulic Research*, 52(3):399–411, 2014.
- [4] K. Amiri, M.J. Cervantes, and B. Mulu. Experimental investigation of the hydraulic loads on the runner of a Kaplan turbine model and the corresponding prototype. *Journal of Hydraulic Research*, 53(4):1–14, 2015.
- [5] G. Angelico, F. Muciaccia, and Rossi G. Part load behaviour of a turbine: a study on a complete model of a hydraulic power plant. In *Proceedings of the 13th IAHR Symposium on Hydraulic Machinery and Systems, Beijing, China*, 1986.
- [6] J. Arpe. *Analyse du champ de pression pariétale d'un diffuseur coudé de turbine Francis*. PhD thesis, EPFL, Lausanne, Switzerland, 2003.
- [7] P. Ausoni, M. Farhat, X. Escaler, E. Egusquiza, and F. Avellan. Cavitation influence on Von Kármán vortex shedding and induced hydrofoil vibrations. *Journal of Fluids Engineering, Transactions of the ASME*, 129(8):966–973, 2007.
- [8] F. Avellan. Flow investigation in a Francis turbine: The FLINDT project. In *Proceedings of the 20th IAHR Symposium on Hydraulic Machinery and System, Charlotte, USA*, 2000.
- [9] J.S. Bendat and A.G. Piersol. *Random Data: Analysis and Measurement Procedures*. Wiley, fourth edition, 2011.
- [10] T.B. Benjamin. Theory of the vortex breakdown phenomenon. *Journal of Fluid Mechanics*, 14:593–629, 1962.
- [11] M.J. Bhagwat and M. Ramasamy. Effect of tip vortex aperiodicity on measurement uncertainty. *Experiments in Fluids*, 53(5):1191–1202, 2012.

## Bibliography

---

- [12] C. Brennen and A.J. Acosta. Dynamic transfer function for a cavitating inducer. *Journal of Fluids Engineering, Transactions of the ASME*, 98 Ser 1(2):182–191, 1976.
- [13] C.E. Cala, E.C. Fernandes, M.V. Heitor, and S.I. Shtork. Coherent structures in unsteady swirling jet flow. *Experiments in Fluids*, 40(2):267–276, 2006.
- [14] J.J. Cassidy and H.T. Falvey. Observations of unsteady flow arising after vortex breakdown. *Journal of Fluid Mechanics*, 41(4):727–736, 1970.
- [15] R.C. Chanaud. Observations of oscillatory motion in certain swirling flows. *Journal of Fluid Mechanics*, 21:111–127, 1965.
- [16] G.D. Ciocan, M.S. Iliescu, T.C. Vu, B. Nennemann, and F. Avellan. Experimental study and numerical simulation of the FLINDT draft tube rotating vortex. *Journal of Fluids Engineering, Transactions of the ASME*, 129(2):146–158, 2007.
- [17] M. Couston and R. Philibert. Partial load modelling of gaseous Francis turbine rope. *The International Journal on Hydropower and Dams*, 1:146–158, 1998.
- [18] E. de Langre. Frequency lock-in is caused by coupled-mode flutter. *Journal of Fluids and Structures*, 22(6-7):783–791, 2006.
- [19] P. Dörfler. System dynamics of the Francis turbine half load surge. In *Proceedings of the 11th IAHR Symposium on Operating Problem of Pump Stations and Powerplants, Amsterdam, Netherlands*, 1982.
- [20] P. Dörfler and N. Ruchonnet. A statistical method for draft tube pressure pulsation analysis. *IOP Conference Series: Earth and Environmental Science*, 15(6), 2012.
- [21] M. Dreyer. *Mind The Gap: Tip Leakage vortex dynamics and cavitation in axial turbines*. PhD thesis, EPFL, Lausanne, Switzerland, 2015.
- [22] M. Dreyer, J. Decaix, C. Münch-Alligné, and M. Farhat. Mind the gap: a new insight into the tip leakage vortex using stereo-PIV. *Experiments in Fluids*, 55(11), 2014.
- [23] A. Duparchy, J. Guillozet, T. De Colombel, and L. Bornard. Spatial harmonic decomposition as a tool for unsteady flow phenomena analysis. *IOP Conference Series: Earth and Environmental Science*, 22, 2014.
- [24] F. Duparchy, A. Favrel, P-Y. Lowys, C. Landry, A. Müller, K. Yamamoto, and F. Avellan. Analysis of the part load helical vortex rope of a Francis turbine using on-board sensors. *Journal of Physics: Conference Series*, 656(1):012061, 2015.
- [25] M. Escudier. Confined vortices in flow machinery. *Annual Review of Fluid Mechanics*, 19: 27–52, 1987.
- [26] European Parliament and Council of the European Union. Directive 2009/28/ec. *Official Journal of the European Union*, 52:L140/16–62, 2009.

- 
- [27] J.H. Faler and S. Leibovich. Disrupted states of vortex flow and vortex breakdown. *Physics of Fluids*, 20:1385–1400, 1977.
- [28] M. Fanelli. Vortex rope in the draft tube of francis turbines operating at partial load. a proposal for a mathematical model. *Journal of Hydraulic Research*, 27(6):769–807, 1989.
- [29] M. Farhat, S. Natal, F. Avellan, F. Paquet, P.Y. Lowys, and M. Couston. Onboard measurements of pressure and strain fluctuations in a model of low head Francis turbine - Part 1: Instrumentation. In *Proceedings of the 21th IAHR Symposium on Hydraulic Machinery and Systems, Lausanne, Switzerland*, 2002.
- [30] S. Farokhi, R. Taghavi, and E.J. Rice. Effect of initial swirl distribution on the evolution of a turbulent jet. *AIAA Journal*, 27(6):700–706, 1989.
- [31] A. Favrel, C. Landry, A. Müller, and F. Avellan. Experimental identification and study of hydraulic resonance test rig with Francis turbine operating at partial load. *IOP Conference Series: Earth and Environmental Science*, 15(6), 2012.
- [32] A. Favrel, C. Landry, A. Müller, K. Yamamoto, and F. Avellan. Hydro-acoustic resonance behavior in presence of a precessing vortex rope: Observation of a lock-in phenomenon at part load Francis turbine operation. *IOP Conference Series: Earth and Environmental Science*, 22, 2014.
- [33] A. Favrel, A. Müller, C. Landry, K. Yamamoto, and F. Avellan. Study of the vortex-induced pressure excitation source in a Francis turbine draft tube by particle image velocimetry. *Experiments in Fluids*, 56(12), 2015.
- [34] E.C. Fernandes, M.V. Heitor, and S.I. Shtork. An analysis of unsteady highly turbulent swirling flow in a model vortex combustor. *Experiments in Fluids*, 40(2):177–187, 2006.
- [35] J.P. Franc, F. Avellan, B. Belahadji, J.Y. Billard, L. Briançon-Marjollet, D. Fréchou, D.H. Fruman, A. Karimi, J.L. Kueny, and J.M. Michel. *La cavitation: mécanismes physiques et aspects industriels*. Collection Grenoble sciences. Presses universitaires de Grenoble, 1995.
- [36] L. Graftieaux, M. Michard, and G. Nathalie. Combining PIV, POD and vortex identification algorithms for the study of unsteady turbulent swirling flows. *Measurement Science and Technology*, 12(9):1422–1429, 2001.
- [37] A.J. Griffiths, P.A. Yazdabadi, and N. Syred. Alternate eddy shedding set up by the non-axisymmetric recirculation zone at the exhaust of a cyclone dust separator. *Journal of Fluids Engineering, Transactions of the ASME*, 120(1):193–199, 1998.
- [38] A. K. Gupta, D. G Lilley, and N. Syred. *Swirl flows*, volume 1. Abacus Press, UK, 1984.
- [39] J.K. Harvey. Some observations of the vortex breakdown phenomenon. *Journal of Fluid Mechanics*, 14:585–592, 1962.

## Bibliography

---

- [40] M.V. Heitor and J.H. Whitelaw. Velocity, temperature, and species characteristics of the flow in a gas-turbine combustor. *Combustion and Flame*, 64(1):1–32, 1986.
- [41] S. Houde, R. Fraser, G. Ciocan, and C. Deschênes. Experimental study of the pressure fluctuations on propeller turbine runner blades: part 2, transient conditions. *IOP Conference Series: Earth and Environmental Science*, 15(6):062061, 2012.
- [42] IEC Standards. *60193: hydraulic turbines, storage pumps and pump-turbines - model acceptance tests*. International Electrotechnic Commission, second edition, 1999.
- [43] M. Iliescu, S. Houde, S. Lemay, R. Fraser, and C. Deschênes. Investigation of the cavitation behavior of an axial hydraulic turbine operating at partial discharge by 3D-PIV. In *Proceedings of the 9th International Symposium on Particle Image Velocimetry, Kobe, Japan, July, 2011*.
- [44] M.S. Iliescu, G.D. Ciocan, and F. Avellan. Analysis of the cavitating draft tube vortex in a francis turbine using particle image velocimetry measurements in two-phase flow. *Journal of Fluids Engineering, Transactions of the ASME*, 130(2):0211051–02110510, 2008.
- [45] K.M. Ingvorsen, K.E. Meyer, J.H. Walther, and S. Mayer. Turbulent swirling flow in a model of a uniflow-scavenged two-stroke engine. *Experiments in Fluids*, 54(3), 2013.
- [46] T. Jacob. *Evaluation sur modèle réduit et prédiction de la stabilité de fonctionnement des turbines Francis*. PhD thesis, EPFL, Lausanne, Switzerland, 1993.
- [47] T. Jacob and J.E. Prenat. Identification of a hydraulic turbomachine’s hydro-acoustic transmission parameters. In *Proceedings of the 5th IAHR International Meeting of the Workgroup on the Behaviour of Hydraulic Machinery under Steady Oscillatory conditions, Milano, Italy, 1991*.
- [48] J. Jeong and F. Hussain. On the identification of a vortex. *Journal of Fluid Mechanics*, 285: 69–94, 1995.
- [49] O. Kirschner, A. Ruprecht, E. Göde, and S. Riedelbauch. Experimental investigation of pressure fluctuations caused by a vortex rope in a draft tube. *IOP Conference Series: Earth and Environmental Science*, 15, 2012.
- [50] J. Koutnik, P. Faigle, and W. Moser. On cavitating vortex rope form stability during Francis turbine part load operation. In *Proceedings of the IAHR International Meeting of the Workgroup on Cavitation and Dynamic Problems in Hydraulic Machinery and Systems, Barcelona, Spain, 2006*.
- [51] J. Koutnik, P. Faigle, and W. Moser. Pressure fluctuations in Francis turbines - theoretical prediction and impact on turbine. In *Proceedings of the 24th Symposium on Hydraulic machinery and Systems, Foz do Iguassu, Brazil, 2008*.

- 
- [52] P.A. Kuibin, R.F. Susan-Resiga, and S. Muntean. A model for precessing helical vortex in the turbine discharge cone. *IOP Conference Series: Earth and Environmental Science*, 22, 2013.
- [53] C. Landry. *Hydroacoustic Modeling of a Cavitation Vortex Rope for a Francis Turbine*. PhD thesis, EPFL, Lausanne, Switzerland, 2015.
- [54] C. Landry, A. Favrel, A. Müller, C. Nicolet, K. Yamamoto, and F. Avellan. Experimental investigation of the local wave speed in a draft tube with cavitation vortex rope. *IOP Conference Series: Earth and Environmental Science*, 22, 2014.
- [55] P.Y. Lowys, J. Doyon, M. Couston, and G. Vuillerod. Dynamic behavior of low head Francis turbine. In *Proceedings of the 10th IAHR Workgroup on the Behavior of Hydraulic machinery under Steady Oscillatory Conditions, Trondheim, Norway*, 2001.
- [56] P.Y. Lowys, F. Paquet, M. Couston, M. Farhat, S. Natal, and F. Avellan. Onboard measurements of pressure and strain fluctuations in a model of low head Francis turbine - Part 2: Measurements and preliminary results. In *Proceedings of the 21th IAHR Symposium on Hydraulic Machinery and Systems, Lausanne, Switzerland*, 2002.
- [57] O. Lucca-Negro and T. O'Doherty. Vortex breakdown: A review. *Progress in Energy and Combustion Science*, 27(4):431–481, 2001.
- [58] F. Martinelli, F. Cozzi, and A. Coghe. Phase-locked analysis of velocity fluctuations in a turbulent free swirling jet after vortex breakdown. *Experiments in Fluids*, 53(2):437–449, 2012.
- [59] A. Müller. *Physical Mechanisms governing Self-Excited Pressure Oscillations in Francis Turbines*. PhD thesis, EPFL, Lausanne, Switzerland, 2014.
- [60] A. Müller, A. Bullani, M. Dreyer, S. Roth, A. Favrel, C. Landry, and F. Avellan. Interaction of a pulsating vortex rope with the local velocity field in a Francis turbine draft tube. *IOP Conference Series: Earth and Environmental Science*, 15(3), 2012.
- [61] A. Müller, M. Dreyer, N. Andreini, and F. Avellan. Draft tube discharge fluctuation during self-sustained pressure surge: Fluorescent Particle Image Velocimetry in two-phase flow. *Experiments in Fluids*, 54(4), 2013.
- [62] A. Müller, K. Yamamoto, S. Alligné, K. Yonezawa, Y. Tsujimoto, and F. Avellan. Measurement of the self-oscillating vortex rope dynamics for hydroacoustic stability analysis. *ASME J. Fluids Eng.*, 2015.
- [63] C. Nicolet. *Hydroacoustic modelling and numerical simulation of unsteady operation of hydroelectric systems*. PhD thesis, EPFL, Lausanne, Switzerland, 2007.
- [64] M. Nishi and S. Liu. An outlook on the draft-tube-surge study. *International Journal of Fluid Machinery and Systems*, 6(1):33–48, 2013.

## Bibliography

---

- [65] M. Nishi, S. Matsunaga, and Senoo Y. Kubota, T. Flow regimes in an elbow-type draft tube. In *Proceedings of the 11th IAHR Symposium on Hydraulic Machinery and Systems, Amsterdam, Netherlands, 1982*.
- [66] M. Nishi, S. Matsunaga, and Senoo Y. Kubota, T. Surging characteristics of conical and elbow-type draft tubes. In *Proceedings of the 12th IAHR Symposium on Hydraulic Machinery and System, Stirling, Scotland, 1984*.
- [67] M. Nishi, S. Matsunaga, and Senoo Y. Kubota, T. Effect of draft tube shape on the characteristics of pressure surge and swirl flow. In *Proceedings of the 13th IAHR Symposium on Hydraulic Machinery and Systems, Montreal, Canada, 1986*.
- [68] Obser'ER et la Fondation Energies pour le Monde. Worldwide electricity production from renewable energy sources, 2013.
- [69] M. Raffel, C.E. Willert, and J. Kompenhans. *Particle Image Velocimetry: A Practical Guide*. Springer, 1998.
- [70] W. C. Reynolds and A. Hussain. The mechanics of an organized wave in turbulent shear flow. part 3. theoretical models and comparisons with experiments. *Journal of Fluid Mechanics*, 54:263–288, 1972.
- [71] W.J. Rheingans. Power swings in hydroelectric power plants. *Transactions of the ASME*, 62:171–184, 1940.
- [72] P. Rudolf, V. Haban, F. Pochyly, J. Koutnik, and K. Kruegler. Collapse of cylindrical cavitating region and conditions for existence of elliptical form of cavitating vortex rope. In *Proceedings of the 2nd IAHR International Meeting of the Workgroup on Cavitation and Dynamic Problems in Hydraulic Machinery and Systems, Timisoara, Romania, 2007*.
- [73] T. Sarpkaya. On stationary and travelling vortex breakdowns. *Journal of Fluid Mechanics*, 45:545–559, 1971.
- [74] R. Susan-Resiga, G.D. Ciocan, I. Anton, and F. Avellan. Analysis of the swirling flow downstream a Francis turbine runner. *Journal of Fluids Engineering, Transactions of the ASME*, 128(1):177–189, 2006.
- [75] N. Syred. A review of oscillation mechanisms and the role of the precessing vortex core (PVC) in swirl combustion systems. *Progress in Energy and Combustion Science*, 32(2): 93–161, 2006.
- [76] H. Takamura, S. Ebara, H. Hashizume, K. Aizawa, and H. Yamano. Flow visualization and frequency characteristics of velocity fluctuations of complex turbulent flow in a short elbow piping under high reynolds number condition. *Journal of Fluids Engineering, Transactions of the ASME*, 134(10), 2012.
- [77] I.K. Toh, D. Honnery, and J. Soria. Axial plus tangential entry swirling jet. *Experiments in Fluids*, 48(2):309–325, 2010.

- [78] G. H. Vatistas, V. Kozel, and W. Mih. A simple model for concentrated vortices. *Experiments in Fluids*, 11(1), 1991.
- [79] C.H.K. Williamson and R. Govardhan. Vortex-induced vibrations. *Annual Review of Fluid Mechanics*, 36:413–455, 2004.
- [80] K. Yamamoto, A. Müller, A. Favrel, C. Landry, and F. Avellan. Pressure measurements and high speed visualizations of the cavitation phenomena at deep part load condition in a Francis turbine. *IOP Conference Series: Earth and Environmental Science*, 22(2):022011, 2014.
- [81] K. Yamamoto, A. Müller, A. Favrel, C. Landry, and F. Avellan. Guide vanes embedded visualization technique for investigating Francis runner inter-blade vortices at deep part load operation. In *Proceedings of the 6th IAHR International Meeting of the Workgroup on Cavitation and Dynamic Problems in Hydraulic Machinery and Systems, Ljubljana, Slovenia*, 2015.
- [82] Z. Zhang. *LDA Application Methods: Laser Doppler Anemometry for Fluid Dynamics*. Experimental Fluid Mechanics. Springer, 2010.





## Favrel Arthur

Mechanical engineer

Born in 1988, French citizen

Rue de l'Industrie 2

1020, Renens, Switzerland

E-mail : arthurfavrel@gmail.com

## Education

---

<b>2011 - 2016</b>	<b>PhD</b> Ecole Polytechnique Fédérale de Lausanne (EPFL), Switzerland
<b>2008 – 2011</b>	<b>Master of Science MSc</b> (Mechanical engineering) Ecole Polytechnique Universitaire de l'UCBL, France
<b>2006 - 2008</b>	<b>Bachelor of Science BSc – First and second years</b> (Physics) Université Claude Bernard de Lyon (UCBL), France

## Professional Experiences

---

<b>2011 - 2015</b>	<b>Doctoral assistant</b> – EPFL Laboratory for Hydraulic Machines (LMH) <ul style="list-style-type: none"><li>• Experimental investigation of flow instabilities involving cavitation and hydro-acoustic resonances in hydraulic machines</li><li>• Participation in teaching activities as an assistant and supervision of Master/Bachelor projects</li><li>• Participation in the HYPERBOLE research project (ERC/FP7-ENERGY-2013-1-Grant 608532) involving industrial and academic partners</li></ul>
<b>2011</b> (6 months)	<b>Master thesis</b> – Laboratoire de Mécanique des Fluides et d'Acoustique (LMFA), Ecole Centrale de Lyon, France. Theoretical and experimental study of noise propagation induced by a fan in conducts in collaboration with Airbus and Technofan

## Skills and Languages

---

<b>Programming</b>	Matlab, C, C++, Delphi, Labview
<b>Theory</b>	Aero-acoustics, Fluid mechanics, Signal processing, Hydraulic machines
<b>Languages</b>	French – Native proficiency English – Professional working proficiency Italian – Elementary proficiency

## Interests / Activity

---

- Sport (football, running, winter sports), travel, reading
- Participation in Shell eco-marathon 2010 with the team *Timistil*
- Teaching activities in the framework of the *Methodia* program for college and high-school students

## Journal Papers

---

A. Favrel, A. Müller, C. Landry, K. Yamamoto and F. Avellan, F. (2015) Study of the vortex-induced pressure excitation source in a Francis turbine draft tube by particle image velocimetry. *Experiments in Fluids*, volume 56, issue 12.

C. Landry, A. Favrel, A. Müller, C. Nicolet and F. Avellan (2016). Local wave speed and bulk viscosity in Francis turbines at Part load operation, *Journal of Hydraulic Research* (Article in press)

## Conference Papers

---

F. Duparchy, A. Favrel, P.Y. Lowys, C. Landry, A. Müller, K. Yamamoto and F. Avellan (2015) Analysis of the part load helical vortex rope of a Francis turbine using on-board sensors. *Journal of Physics: Conference Series*, volume 656, issue 1.

S. Alligné, C. Landry, A. Favrel, C. Nicolet and F. Avellan (2015), Francis turbine draft tube modelling for prediction of pressure fluctuations on prototype. *Journal of Physics: Conference Series*, volume 656, issue 1.

K. Yamamoto, A. Müller, A. Favrel, C. Landry and F. Avellan (2015) Guide vanes embedded visualization technique for investigating Francis turbine runner inter-blade vortices at deep part load operation. *Proceedings of the 6<sup>th</sup> IAHR International Meeting of the Workgroup on Cavitation and Dynamics Problems in Hydraulic Machinery and Systems*, Ljubljana, Slovenia.

A. Favrel, C. Landry, A. Müller, K. Yamamoto and F. Avellan (2014) Hydro-acoustic resonance behaviour in presence of a precessing vortex rope: Observation of a lock-in phenomenon at part load Francis turbine operation. *IOP Conference Series: Earth and Environmental Science*, volume 22.

C. Landry, A. Favrel, A. Müller, C. Nicolet and F. Avellan (2014). Experimental investigation of the local wave speed in a draft tube with cavitation vortex rope. *IOP Conference Series: Earth and Environmental Science*, volume 22.

A. Müller, A. Favrel, C. Landry, K. Yamamoto and F. Avellan (2014) On the physical mechanisms governing self-excited pressure surge in Francis turbines. *IOP Conference Series: Earth and Environmental Science*, volume 22.

K. Yamamoto, A. Müller, A. Favrel, C. Landry and F. Avellan (2014) Pressure measurements and high speed visualizations of the cavitation phenomena at deep part load condition in a Francis turbine. *IOP Conference Series: Earth and Environmental Science*, volume 22.

A. Favrel, C. Landry, A. Müller and F. Avellan (2012) Experimental identification and study of hydraulic resonance test rig with Francis turbine operating at partial load. *IOP Conference Series: Earth and Environmental Science*, volume 15.

A. Müller, A. Bullani, M. Dreyer, S. Roth, A. Favrel, C. Landry and F. Avellan (2012) Interaction of a pulsating vortex rope with the local velocity field in a Francis turbine draft tube. *IOP Conference Series: Earth and Environmental Science*, volume 15.

